THE CHARACTERISATION AND SURFACE ELECTROCHEMISTRY OF A CORROSION PRODUCT (αFeOOH).

by

KEITH ROBERT ROGAN

(B.Sc. University of Liverpool)

A thesis submitted to the Council for National and Academic Awards in partial fulfilment of the requirements for the degree of Doctor of Philosophy.

Department of Chemistry and Biochemistry,
Liverpool Polytechnic
in collaboration with
British Nuclear Fuels Limited.

June 1988

ABSTRACT

αFeOOH (goethite), in its natural state, has been identified in the rust nodules and sludge of a typical industrial cooling system. These deposits and a synthetic αFeOOH were characterised by X-ray and thermal methods, infrared spectroscopy, gas adsorption and electron microscopy. The natural αFeOOH was most concentrated in the rust nodules; the water insoluble residue of the sludge was predominantly quartz. The synthetic αFeOOH had a virtually uncontaminated surface, a lath-like particle morphology and a small measure (ca. 10 m^2 g^{-1}) of microporosity, and contained amorphous material (ca. 15 %). The dehydration of synthetic αFeOOH to αFe_2O_3 was shown to involve an initial homogenous decomposition followed by recrystallisation.

The sludge filtrate was found to contain a high level of chloride and, accordingly, the interactions of αFeOOH (synthetic) with Cl^- ions were investigated, using particle electrophoresis, ion chromatography, potentiometric titrations and salt titrations; an observed interference by OH^- ions on the Cl^- ion potential response of a Cl^- ion selective electrode prohibited the use of this electrode at variable pH. The electrokinetic charge and potential of the colloid αFeOOH/NaCl aq. were determined using the most recent solutions to the equations of electrophoretic mobility and zeta potential, based upon a cylindrical geometry (Stigter, D., J. Phys. Chem., 82, 1417 and 1424 (1978)). Charge densities and potentials of the αFeOOH-NaCl aq. interface were obtained by combining electrophoretic and chromatographic data. Cl^- ions were shown to have a specificity for the αFeOOH surface while the proportion of this surface that is apparently accessible to such ions is only ca. 70 % of that accessible to H^+ and OH^- ions. The titrimetric data were interpreted in terms of a triple layer surface ionisation and complexation model (Davis, J. A., et. al., J. Colloid Interface Sci., 63, 480 (1978)) which was elaborated to yield quantitative information. The tendency towards ion-pair formation was shown to be dependent on the density of ion-pairs already formed, whilst a predominance of surface complexation over surface ionisation was indicated by the magnitude of the Cl^- ion and Na^+ ion binding constants. The calculation of integral capacities indicated a very close association between surface and counterions at high NaCl concentration. At elevated temperatures the analysis indicated an increased affinity of H^+ ions for the surface and that those ion-pairs involving a Cl^- ion became more abundant.

AND SURFACE-ELECTROCHEMISTRY
OF A CORROSION PRODUCT (αFeOOH).

by

KEITH ROBERT ROGAN

ABSTRACT

αFeOOH (goethite), in its natural state, has been identified in the rust nodules and sludge of a typical industrial cooling system. These deposits and a synthetic αFeOOH were characterised by X-ray and thermal methods, infrared spectroscopy, gas adsorption and electron microscopy. The natural αFeOOH was most concentrated in the rust nodules; the water insoluble residue of the sludge was predominantly quartz. The synthetic αFeOOH had a virtually uncontaminated surface, a lath-like particle morphology and a small measure (ca. 10 m^2 g^{-1}) of microporosity, and contained amorphous material (ca. 15 %). The dehydration of synthetic αFeOOH to αFe_2O_3 was shown to involve an initial homogenous decomposition followed by recrystallisation.

The sludge filtrate was found to contain a high level of chloride and, accordingly, the interactions of αFeOOH (synthetic) with Cl^- ions were investigated, using particle electrophoresis, ion chromatography, potentiometric titrations and salt titrations; an observed interference by OH^- ions on the Cl^- ion potential response of a Cl^- ion selective electrode prohibited the use of this electrode at variable pH. The electrokinetic charge and potential of the colloid αFeOOH/NaCl aq. were determined using the most recent solutions to the equations of electrophoretic mobility and zeta potential, based upon a cylindrical geometry (Stigter, D., J. Phys. Chem., 82, 1417 and 1424 (1978)). Charge densities and potentials of the αFeOOH-NaCl aq. interface were obtained by combining electrophoretic and chromatographic data. Cl^- ions were shown to have a specificity for the αFeOOH surface while the proportion of this surface that is apparently accessible to such ions is only ca. 70% of that accessible to H^+ and OH^- ions. The titrimetric data were interpreted in terms of a triple layer surface ionisation and complexation model (Davis, J.A., et. al., J. Colloid Interface Sci., 63, 480 (1978) which was elaborated to yield quantitative information. The tendency towards ion-pair formation was shown to be dependent on the density of ion-pairs already formed, whilst a predominance of surface complexation over surface ionisation was indicated by the magnitude of the Cl^- ion and Na^+ ion binding constants. The calculation of integral capacities indicated a very close association between surface and counterions at high NaCl concentration. At elevated temperatures the analysis indicated an increased affinity of H^+ ions for the surface and that those ion-pairs involving a Cl^- ion became more abundant.

ACKNOWLEDGEMENTS

I wish to express my thanks to Dr. J. Pearce and Dr. P. A. Sewell for their encouragement and support. I am indebted to Dr. A. Wood and Dr. D. J. Shaw for their guidance. I would also like to thank Dr. P. A. Owens and Dr. S. A. Jones for their friendly help and advice. I acknowledge the financial support of British Nuclear Fuels Limited. I am also indebted to English China Clays International, and particularly Dr. R. Bown, for encouraging me to complete this work. Finally, I wish to express my sincere gratitude to my wife Lynne for her support and for typing this thesis.

CONTENTS

-o0o-o0o-o0o-

INTRODUCTION

This thesis is about αFeOOH, one of the main products of the corrosion of mild steel, and the interaction at the solid/solution interface between αFeOOH and Cl^- ion, an aggressive anion implicated in the initiation of corrosion.

The genesis of this work is a problem encountered whenever cooling water is circulated in steel pipes. Typically, cooling water is drawn from a lake and is delivered to site via a mild steel supply pipework. The mild steel pipework is corroded by the water, and produces corrosion products (sludge) which may deposit on the inner surfaces of the cooling system, including stainless steel in-tank coolers.

Leaks have been known to occur in the stainless steel cooling systems and it has been suggested that such failures may be partly due to the corrosion of metal from the cooling water side, accelerated by the release of aggressive ions, such as Cl^- ion, from the sludge found on the inner walls of the stainless steel coils. Following the discovery of leaks in the cooling coils of a typical cooling system, samples of cooling water and sludge were collected and analysed. A high level of chloride was found in the sludge. This discovery has initiated this investigation into the mechanism by which a high level of chloride is generated in the vicinity of a cooling coil sludge.

It is well known that the main products of the generalised and localised corrosion of mild steel, and low alloy steels, are the oxyhydroxides αFeOOH (goethite) and γFeOOH (lepidocrocite), the oxide Fe_3O_4 (magnetite) and amorphous material; β FeOOH (akaganeite) is sometimes found in the corrosion products of the steels when relatively large quantities of chloride are present (e.g., in seawater). Recent investigations of the adsorptive properties of the products of corrosion reported by several groups of authors (Hingston et. al., Int. Congr. Soil Sci. Trans., 1, 669 (1968)and Hingston et. al., J. Soil Sci., 23, 177 (1972)) have shown that chloride is quite efficiently adsorbed from aqueous solution by the oxides and oxyhydroxides of iron. This, in view of the known involvement of chloride in the corrosion process (Foley, Corrosion, 26, 58 (1970) and Pourbaix, Int. Corros. Conf. Ser. 1971, NACE-3 (Localised Corros.), 12 (1974)) and the more recent discovery of the chloride adsorbing properties of the products of corrosion it would seem reasonable to suggest that the mechanism by which a high level of

chloride is generated in the vicinity of a cooling coil sludge involves an interaction at the solid-solution interface between corrosion product(s) and Cl^- ion. This interaction has been investigated in this work, in which a typical corrosion product is represented by αFeOOH.

The thesis is presented in two parts. In the first part the physical and chemical characteristics of both a synthetic and a corrosion product αFeOOH have been elucidated, and further information has been obtained concerning the structural changes that occur during the thermal transformation of αFeOOH to αFe_2O_3. In the second part a greater understanding of the interaction between αFeOOH and Cl^- ion has been sought by means of a comprehensive investigation of the electrical double layer at the αFeOOH/Cl^- ion interface. In an addendum, the adverse influence of OH^- ions on a chloride ion selective electrode has been recorded.

PART A

THE CHARACTERISATION

OF A CORROSION PRODUCT (αFeOOH).

ABBREVIATIONS AND SYMBOLS

ABBREVIATIONS

DSC	differential scanning calorimetry.
fps	fragmentation pattern series.
GC-MS	gas chromatography-mass spectrometry.
HPLC	high performance liquid chromatography.
IR	infrared.
NMR	nuclear magnetic resonance.
SEM	scanning electron microscopy.
TGA	thermogravimetric analysis.
WCAIR	water, chloroform and acid insoluble residue.
WCAIRH	heated, water, chloroform and acid insoluble residue.
WCIASE	water and chloroform insoluble/acid soluble extract.
WCIASEH	heated, water and chloroform insoluble/acid soluble extract.
WCIR	water and chloroform insoluble residue.
WCIRME	water and chloroform insoluble residue/magnetic extract.
WIBSE	water-insoluble/base-soluble extract.
WICSE	water insoluble/chloroform-soluble extract.
WIR	water insoluble residue.
WWSC	water plus water soluble content.
XRD	X-ray diffraction.
XRDLPA	XRD line profile analysis.
XRF	X-ray fluorescence.

SYMBOLS

[Unless stated, values given are according to Weast, R.C., "CRC Handbook of Chemistry and Physics", 59th Edition, 1978.]

Symbols based on the Roman alphabet.

a	half of particle width; m.
a_G	a unit cell dimension of $\alpha FeOOH$; m.
a_H	a unit cell dimension of αFe_2O_3; m.
b	particle thickness.
b_G	b unit cell dimension of $\alpha FeOOH$; m.
c_G	c unit cell dimension of $\alpha FeOOH$; m.
c_H	c unit cell dimension of αFe_2O_3; m.
$\bar{D}$	volume averaged crystallite size (also called the size of the scatterer); m.
d	width of slit-shaped pores; m.

d_{KS}	width of the core condensate inside a slit-shaped pore; m.
$d_{(hk\ell)}$	XRD perpendicular spacing for any plane of Miller indices (hkℓ); m.
$\bar{E}$	mean lattice distortion (or microstrain).
f	XRD structural profile.
g	XRD instrument dependent profile.
h	Miller indice h.
$I_{(hk\ell)}$	XRD peak intensity of reflections from planes of Miller indices (hkℓ); counts s^{-1}.
K	shape factor; 0.9 (Klug, H.P. and Alexander, L.E., "X-Ray Diffractions Procedures", John Wiley and Sons, Inc., New York, 1959.
k	Miller indice k.
L_p	micropore dimension; m.
ℓ	Miller indice ℓ.
m/z	ratio of molecular mass to valency; g mol^{-1}.
n	number of adsorbed layers.
p	pressure; mm Hg.
pH_o	pH of an aqueous suspension whose solid surface is at its point of zero charge.
p_{SAT}	saturated vapour pressure; 765.3 mm Hg (N_2 at 77.4K) (Micromeritics Instrument Corporation, Atlanta, Georgia).
R	molar gas constant; 8.31441 J mol^{-1} K^{-1}.
r_{KC}	radius of core condensate inside a cylindrical pore; m.
r_{KS}	radius of the core condensate inside a slit-shaped pore; m.
r_p	pore radius; m.
r_1 and r_2	principal radii, at right angles, of a curved surface; m.
S_{BET}	specific surface area (BET, N_2 at 77K); m^2 g^{-1}.
S_{CYL}	surface area of a cylindrical particle with hemispherical ends; m^2.
S_t^{EX}	external, specific surface area (t-plot analysis); m^2 g^{-1}.
S^{MICR}	micropore, specific surface area; m^2 g^{-1}.
S_{REC}	surface area of a rectangular particle; m^2 g^{-1}.
S_p^{MESO}	specific surface area, obtained by summation across the mesopore size range in a pore size calculation; m^2 g^{-1}.
S_t^{TOT}	specific surface area (t-plot analysis); m^2 g^{-1}.
T	absolute temperature; K.
t	statistical thickness of adsorbed layer: m.

t_I	t-value at the change in slope of a t-plot; m.
t_{MONO}	average thickness of a single layer of adsorbed molecules; m.
V	specific volume of gas adsorbed (at STP); $cm^3\ g^{-1}$.
V_{CYL}	volume of a cylindrical particle with hemispherical ends; m^3.
V_G	unit cell volume of αFeOOH; m^3.
V_{REC}	volume of a rectangular particle; m^3.
V^{TOT}	specific volume of gas adsorbed at $p/p_{SAT} = 0.95$; $cm^3\ g^{-1}$.
V_p^{MESO}	specific volume of adsorbed gas, obtained by summation across the mesopore size range in a pore size distribution calculation; $cm^3\ g^{-1}$.
V_t^{MICR}	specific volume of micropores; $cm^3\ g^{-1}$.
Vol_M	molar volume of an ideal gas; 22413.83 $cm^3\ mol^{-1}$.
$Vol_M^{N_2}$	molar volume of adsorbed and/or capillary condensed N_2; 34.67 $cm^3\ mol^{-1}$.
w	weight fraction.

Symbols based on the Greek alphabet.

β	integral breadth (of a peak is defined as the width of a rectangle having the same area and height as the peak); degrees.
γ	surface tension of liquid N_2 at 77.4K; 8.84 mN m^{-1}.
Δr_p	change in pore radius; m.
ΔS_p	specific surface area of pore walls, corresponding to the decremental volume ΔV_p; $m^2\ g^{-1}$.
Δt	diminution in adsorbed layer thickness; m.
ΔV	total decrement in the specific volume of gas adsorbed; $cm^3\ g^{-1}$.
ΔV_f	amount desorbed from the film on the pore walls during a desorption step; $cm^3\ g^{-1}$.
ΔV_K	decrement in the amount of capillary condensed material; $cm^3\ g^{-1}$.
ΔV_p	decrement in pore volume; $cm^3\ g^{-1}$.
Δv_p	decrement in pore volume expressed as a liquid; $mm^3\ g^{-1}$.
$\theta_{(hk\ell)}$	Bragg angle of reflections from planes of Miller indices (hkℓ); degrees.
λ	X-ray wavelength; 0.1540562 nm (Philips N.V., Eindhoven, Holland).
μ	linear mass absorption coefficient.
ρ_G	density of αFeOOH; kg m^{-3}.

ϕ angle of contact; degrees.

Other symbols.

$2W_{\frac{1}{2}}$ peak width at half maximum height; degrees.

$\mathcal{F}$ conversion factor from volume of gas (at STP) to volume of liquid (at STP); $\mathcal{F} = Vol_M^{N_2} / Vol_M = 15.5 \times 10^{-4}$.

h XRD observed (or analysed)profile.

ℓ particle length; m.

$(hk\ell)$ Miller indices describing a plane.

$(\bar{r}_p)_{MAX}$ $\bar{r}_p$ value at the maximum in a pore size distribution plot; m.

$(S_{SEM})_{CYL}$ specific surface area (SEM dimensional information) of a cylindrical particle with hemispherical ends; $m^2\ g^{-1}$.

$(S_{SEM})_{REC}$ specific surface area (SEM dimensional information) of a rectangular particle; $m^2\ g^{-1}$.

Subscripts.

A relating to amorphous material.

c relating to the Cauchy part of the Voigt function.

G relating to $\alpha FeOOH$.

GP relating to pure $\alpha FeOOH$.

H relating to αFe_2O_3.

i relating to phase i.

ip relating to pure phase i.

Rem relating to remaining phases.

g relating to the Gaussian part of the Voigt function.

Superscripts.

f relating to the XRD structural profile.

g relating to the XRD instrumental dependent profile.

h relating to the XRD observed (or analysed) profile.

- mean.

INTRODUCTION

The characterisation of the corrosion product αFeOOH was performed on both αFeOOH-containing industrial cooling system deposits and a synthetic αFeOOH, using X-ray and thermal methods, infrared spectroscopy, gas adsorption and electron microscopy. The characterisation of αFeOOH-containing deposits is given in Chapter A2 and the characterisation of a synthetic αFeOOH is given in Chapters A1 and A3.

SUMMARY

αFeOOH was prepared by a modified version of the preparation given by Brauer ("Handbook of Preparative Inorganic Chemistry", Vol. 2, Academic Press, London, 1965). This synthetic αFeOOH was identified, characterised and assessed for its chloride contaminating ability of αFeOOH - suspending aqueous solutions. Such an αFeOOH (structure confirmed by X-ray diffraction (XRD) and infrared (IR) spectroscopy) had a virtually uncontaminated surface, an acicular particle morphology (which was best described as lath-like), a small measure of microporosity and contained the omnipresent adsorbed water. When it was heated, the separate endothermic dehydroxylations of the differently coordinated surface hydroxyls of this αFeOOH were clearly apparent in its differential scanning calorimetric thermogram. On suspending this synthetic αFeOOH in water, it did slightly contaminate such water with chloride (from its preparation) that had been, presumably, desorbed from its surface.

Rust nodules, sludge and a piece of piping, all containing at least one corrosion product such as αFeOOH, were obtained from a typical industrial cooling system and subjected to a visual examination, an instrumental analysis and a chemical analysis. The rust nodules were composed mainly of αFeOOH in a stable crystalline form and with a surface (specific area 26.8 $m^2\ g^{-1}$) that was non-porous, virtually uncontaminated and (presumed to be) negatively charged. The sludge was an heterogenous, dark brown viscous slurry, 83.5% of which was water plus water soluble material. The water insoluble residue (WIR) of the sludge was composed of SiO_2 (ca. 40%) with minor amounts of other inorganic phases such as αFeOOH, Fe_3O_4, $FeCO_3$, γFeOOH and metallic iron. The WIR also contained minor amounts of a thermally - unstable acid - insoluble material (presumed to be cellulose), chloroform - soluble long - chain hydrocarbons and base soluble constituents. The surface (specific area 25.7 $m^2\ g^{-1}$) of the WIR was non-porous and (presumed to be) negatively charged. The water plus water soluble content of the sludge contained relatively high levels (ca. 1mmol dm^{-3}) of three monovalent anions, one of which was chloride. The piece of piping was 1.2 cm thick 'Grey' cast iron with a corrosion depth of 2mm.

The structural changes that take place when αFeOOH is thermally dehydrated to αFe_2O_3 were studied by means of a stopped reaction experiment in which quantities of a prepared αFeOOH were heated from ambient to several temperatures up to 850°C, in a dynamic atmosphere of air, and cooled

ballistically. The products of this thermal treatment, and their precursor, were submitted to XRD, the low temperature sorption of N_2 and IR absorption spectroscopy; the products formed at 400 and 850°C were also subjected to scanning electron microscopy. The prepared αFeOOH contained an estimated 14.8% of amorphous material which was mostly adsorbed water with the remainder (presumed to be) amorphous iron oxyhydroxide. On heating this αFeOOH up to 300°C, the proportion of amorphous material originally present was reduced and the αFeOOH crystallinity was improved. With further heating up to 400°C the αFeOOH crystal structure was completely decomposed and over 80% of the original αFeOOH was transformed into a high specific surface area, microporous, amorphous material. The remainder of the original αFeOOH was apparently transformed directly into an unusual αFe_2O_3 phase that gave rise to a non-uniform line-broadened XRD profile and whose crystal structure contained an appreciable degree of microstrain. The αFe_2O_3 XRD peak intensities of the initial dehydration products of the prepared αFeOOH increased with increasing preheat-treatment temperature. It was concluded, therefore, that the non-uniform line-broadening phenomenon of the XRD profiles of such products was better explained by the incomplete Fe^{3+} ion arrangement theory of Francombe and Rooksby (Clay Minerals Bull., 21, 1 (1959)) rather than the direct αFe_2O_3 formation theory of Watari et.al. (Phys. Status Solidi A, 73, 215 (1982)). t-plot and mesopore analyses, and a pore size distribution calculation, were carried out using the N_2 desorption data. The thickness of the adsorbed layer of N_2 present on either the prepared αFeOOH or products of its thermal treatment was better estimated by reference to the desorption data of one of these (non-porous) products, such as that formed at 250°C, than by the use of an empirical relation such as that of Halsey (J. Chem. Phys., 16, 931 (1948)). The prepared αFeOOH and the products formed by its thermal treatment to between 300 and 450°C were microporous, with slit-shaped pores. In contrast, the products formed between 500 and 705°C possessed both regions of mesoporosity and microporosity. Indeed, the evidence suggested that during the thermal treatment (from 400 to 500°C) of the prepared αFeOOH, micropores were transformed into mesopores such that the principal type of porosity of the product formed at 500°C was mesoporosity. The pores of the product formed at 705°C were slit-shaped and of a size which indicated that they each had been formed by the coalescence of two smaller slit-shaped micropores. The lath-like morphology of the prepared αFeOOH particles was unaffected by heating up to 500°C. Consequently, the observed high specific surface area of

products formed at temperatures up to 500°C was attributed entirely to pore formation within the particles and not to any visible change of particle shape. However, there was a change of particle shape on heating the prepared αFeOOH to temperatures above 500°C. Indeed, the product particles formed at 850°C had a regular size and shape which was best described as cylindrical with hemispherical ends. Similarly, the structures of the IR absorbing groups present in the product formed at 375°C were unaffected by further heating up to 500°C, while these structures were altered by heating the prepared αFeOOH to temperatures above 500°C. The results of this study suggest that the thermal dehydration of an αFeOOH particle occurs by an homogenous mechanism in which the decomposition of FeOOH, and the concomittant loss of water, occurs throughout the greater extent of the particle. Furthermore, αFeOOH was observed to decompose to amorphous material which then remained the principal phase over a relatively wide temperature range before its crystallisation to αFe_2O_3. Apparently, the dehydration of $\alpha FeOOH$ to αFe_2O_3 is not a simple two phase topotactic transformation as suggested by Bernal (Schweiz. Arch. Wiss. Tech., 26, 69 (1960)) but rather a two stage process involving an intermediate amorphous phase.

CHAPTER A1

THE INSTRUMENTAL IDENTIFICATION AND CHARACTERISATION, AND AN ASSESSMENT OF THE CHLORIDE CONTAMINATING ABILITY, OF A SYNTHETIC αFeOOH.

1. RESUME

αFeOOH was prepared using a modified version of the preparation given by Brauer. This synthetic αFeOOH was identified by X-ray diffraction (XRD) and infrared (IR) absorption spectroscopy. Further characterisation was carried out by XRD, the low temperature adsorption of N_2, scanning electron microscopy (SEM), thermogravimetric analysis (TGA) and differential scanning calorimetry (DSC). The ability, if any, of this αFeOOH to chloride contaminate αFeOOH-suspending aqueous solutions was assessed by X-ray fluorescence (XRF) and high performance liquid chromatography (HPLC).

2. METHODS AND RESULTS.

2.1. The preparation of αFeOOH.

A solution of iron (III) nitrate (1 mol dm^{-3} $Fe(NO_3)_3.9H_2O$ aq.) at ca. 10°C was slowly poured into a vigorously stirred ammonia solution (3.6 mol dm^{-3} NH_3 aq.). The precipitated dark brown, amorphous iron (III) oxyhydroxide was washed four times with 4 dm^3 portions of distilled water at ca. 10°C and a fifth time with a 4 dm^3 portion of double distilled water, each portion being decanted as completely as possible. The residual slurry was stirred with sufficient potassium hydroxide solution (5 mol dm^{-3} KOH aq. 20 cm^3) to give a solution of pH 12.5. The suspension was allowed to stand overnight and its pH checked and adjusted if necessary. Steam (100°C) was bubbled through the basic slurry for 4 hours, thereby transforming the amorphous oxyhydroxide into bright yellow, crystalline αFeOOH. The αFeOOH particles were flocculated, to aid dewatering, by the adjustment of the solution pH (using ca. 20 cm^3 of 5 mol dm^{-3} HNO_3 aq.) to a value that was within the range of αFeOOH pH_o values (i.e., pH 7.5 to pH 8.7) (Atkinson et.al., Hingston et.al., Yates and Healy, Madrid and de Arambarri). The clear supernatant, so produced, was decanted as completely as possible. The flocculated αFeOOH was dialysed against 25 dm^3 of distilled water, filtered and finally dried in a vacuum desiccator. The synthetic αFeOOH, so prepared, was ground to a fine powder and stored in a screw-top jar.

2.2. The identification of αFeOOH by XRD and IR absorption spectroscopy.

All the XRD perpendicular spacings ($d_{(hk\ell)}$) recorded for the prepared αFeOOH (the profile is shown in Fig. A1.1) were corrected by a comparison of the $d_{(hk\ell)}$ values recorded for NaCl with published (Morris et.al.) data. The corrected $d_{(hk\ell)}$ values and the associated intensities of the prepared

FIGURE A1.1

X-RAY DIFFRACTION PROFILE

OF A SYNTHETIC ∝FeOOH.

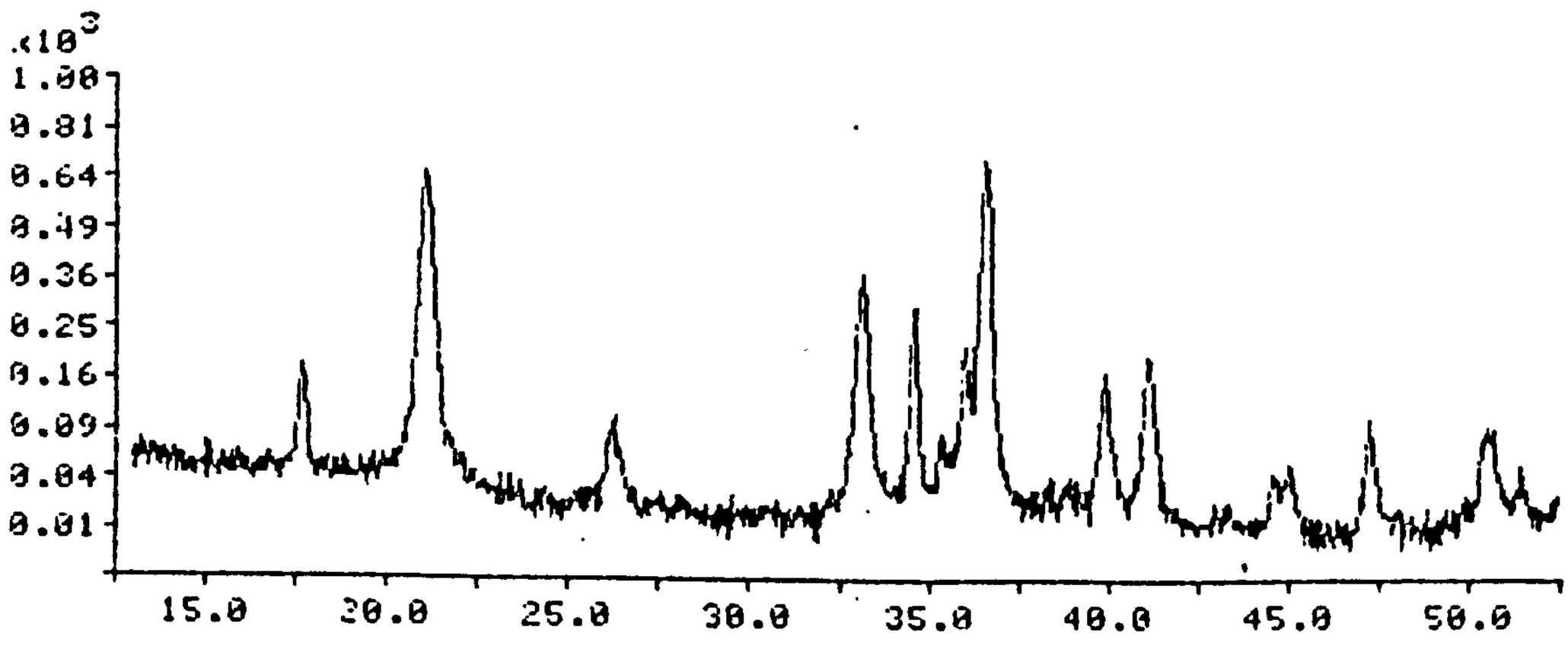

αFeOOH corresponded to the $d_{(hk\ell)}$ values and associated intensities of αFeOOH (Joint Committee On Powder Diffraction Standards, mineral αFeOOH card number 29-713).

The wavenumbers and associated intensities of the absorption bands of the IR spectrum of the prepared αFeOOH (shown in Chapter A3) are given, along with the corresponding published values, in Table A1.1. The excellent correlation between the wavenumbers and associated intensities of the corresponding absorption bands listed in this table confirmed the identity of the prepared sample.

2.3. The characterisation of αFeOOH by XRD, the low temperature adsorption of N_2, SEM, TGA and DSC.

The unit cell dimensions (a_G, b_G and c_G), unit cell volume (V_G) and density (ρ_G) of the prepared αFeOOH were obtained from the corrected $d_{(hk\ell)}$ values of the recorded XRD profile (see Chapter A3). The values of these parameters were determined to be as follows (corresponding literature (Weast) value of mineral αFeOOH in parentheses):- a_G = 0.4646 nm (0.4596 nm), b_G = 0.9960 nm (0.9957 nm), c_G = 0.3026 nm (0.3021 nm), V_G = 140.1 x 10^{-3} nm^3 (138.2 x 10^{-3} nm^3) and ρ_G = 4.213 g cm^{-3} (4.269 g cm^{-3}).

The low temperature sorption isotherms (shown in Chapter A3) of N_2 onto the prepared αFeOOH are of Type II in the BDDT classification (Brunauer et.al.) and they exhibit a slight hysteresis which extends down to low relative pressure (ca. 0.4). The desorption isotherm was reduced to a t-plot (shown in Chapter A3) by reference to the desorption data of a non-porous αFeOOH (see Chapter A3). This t-plot exhibits a change in slope, i.e., a downward deviation, that is indicative of a microporous solid, while the slope of the line after the change in slope relates to an external specific surface area (S_t^{Ex}) value of 35.03 m^2g^{-1} for the prepared αFeOOH.

A scanning electron micrograph of the prepared αFeOOH is shown in Plate A1.1. This αFeOOH was composed of very small, acicular particles having an average length (ℓ) and width (2a) of 587 nm and 87.6 nm, respectively.

A simple geometric shape for the observed acicular particles is cylindrical with hemispherical ends. The surface area (S_{CYL}), volume

Table A1.1

Infrared absorption bands of αFeOOH:
each band is listed as a wavenumber/cm^{-1}
and an intensity (i.e., S-strong, M-moderate,
W-weak and VW-very weak).

This work	Russell et.al.	Gast. et.al.	Shokarev et. al.
	3660 (VW)		
3450 (VW)	3486 (VW)		
3350 (M)		3350 (M)	
3100 (S)	3145 (S)		3145 (S)
		1630 (W)	
892 (S)			888 (S)
792 (S)			792 (S)
631 (M)			623 (M)
453 (M)			456 (M)
402 (S)			405 (S)
below			370 (M)
scan range.			270 (S)

PLATE A1.1

αFeOOH (synthetic).

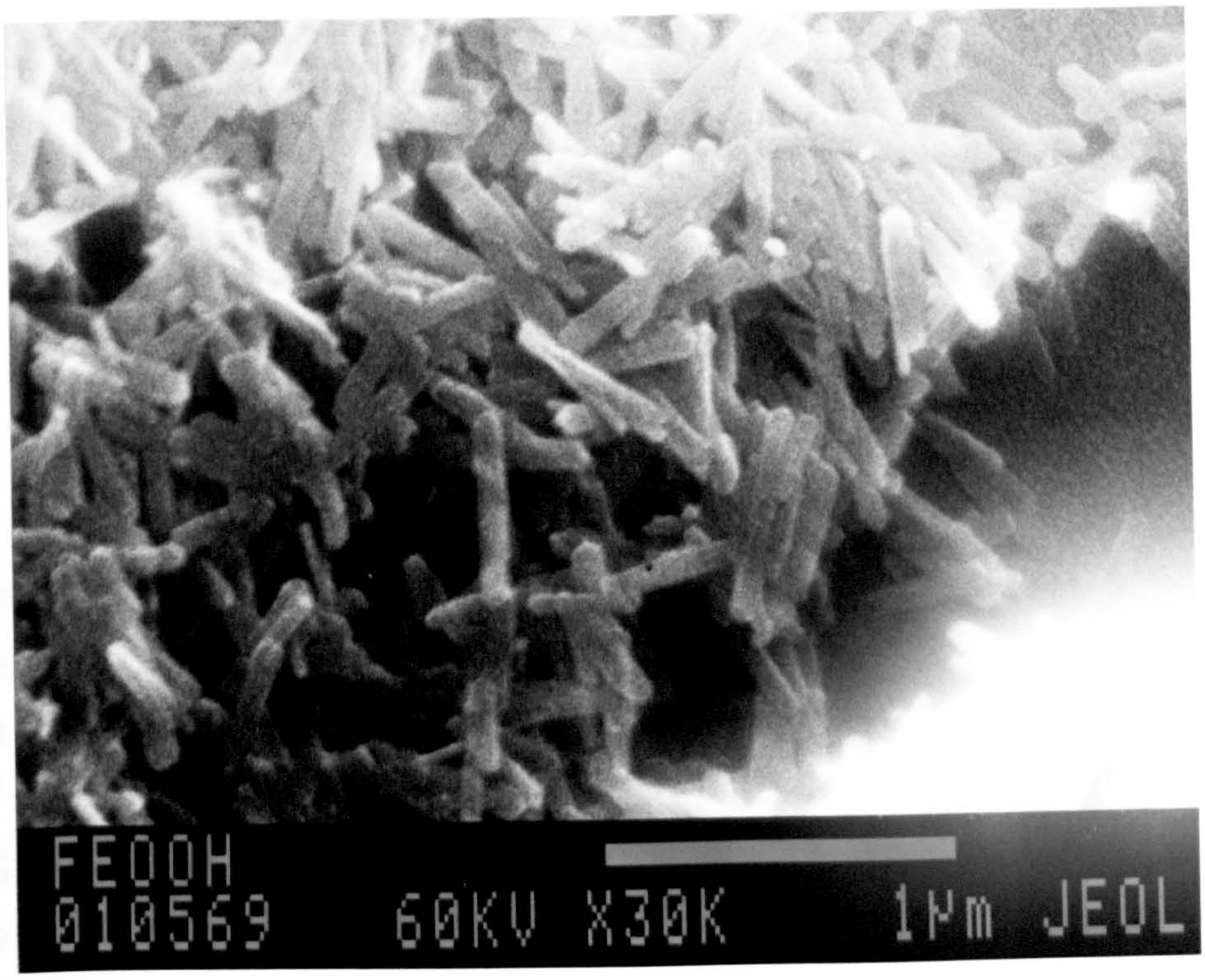

Magnification:- x 30000

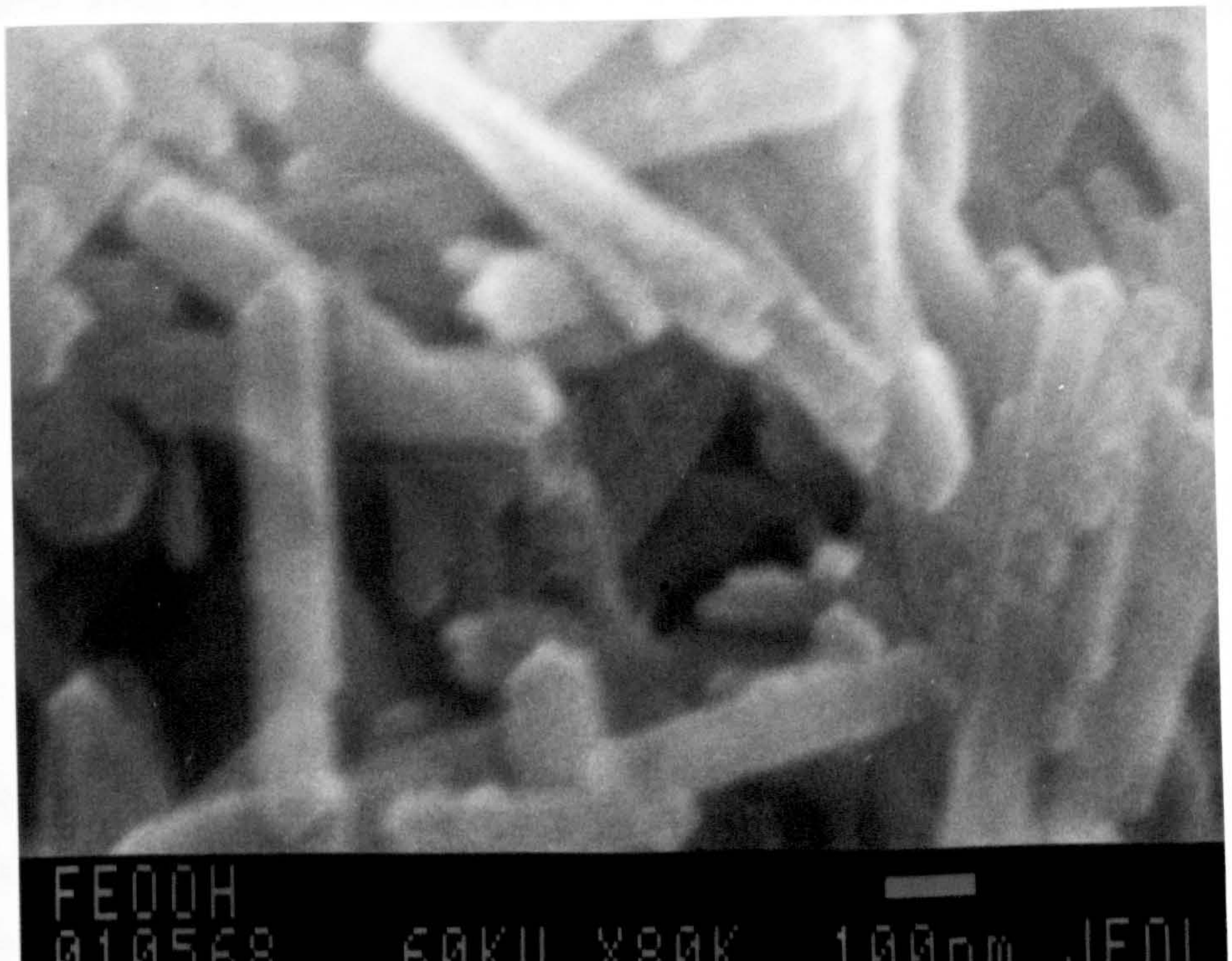

Magnification:- x 80000

(V_{CYL}) and specific surface area ((S_{SEM})$_{CYL}$) of such an αFeOOH shaped particle are given by the relations

$$S_{CYL} = 4 \pi a^2 \left(\frac{\ell}{2a} + 1\right) \qquad \text{A1.1}$$

$$V_{CYL} = 4 \pi a^2 \left(\frac{\ell}{4} + \frac{a}{3}\right) \qquad \text{A1.2}$$

$$\text{and} \qquad (S_{SEM})_{CYL} = \frac{S_{CYL}}{V_{CYL}} \cdot \frac{1}{\rho_G} \quad , \qquad \text{A1.3}$$

while the insertion of the measured dimensions and density of the αFeOOH particles into these relations gives a specific surface area of 11.33 $m^2 g^{-1}$. This areal value is, however, vastly different from the S_t^{Ex} value of 35.03 $m^2 g^{-1}$ obtained for this αFeOOH from low temperature gas adsorption data. Such a disparity discredits a cylindrical shape for these αFeOOH particles.

Another simple geometric shape for the observed acicular particles is rectangular (or lath-like) with a thickness (b) which is much smaller than the other two dimensions and, apparently, not readily observable by SEM. The surface area (S_{REC}), volume (V_{REC}) and specific surface area ((S_{SEM})$_{REC}$) of such an αFeOOH shaped particle are given by the relations

$$S_{REC} = 2 (2 a\ell + b\ell + 2 a\ell) \qquad \text{A1.4}$$

$$V_{REC} = 2 ab\ell \qquad \text{A1.5}$$

$$\text{and} \qquad (S_{SEM})_{REC} = \frac{S_{REC}}{V_{REC}} \cdot \frac{1}{\rho_G} \quad , \qquad \text{A1.6}$$

while the insertion of the measured dimensions, ρ_G and S_t^{Ex} values of the αFeOOH particles into these relations gives the smaller thickness of a lath-like αFeOOH particle as 16.5 nm. A lath-like morphology for αFeOOH particles has also been suggested by the work of Rendon et.al., while Jung et.al have measured the average smaller thickness of rectangular

αFeOOH particles, observed by transmission electron microscopy, to be 16 nm.

The TGA, at 3°C minute^{-1}, of 886mg of the prepared αFeOOH is shown in Fig. A1.2. This αFeOOH incurred losses of mass at 88.5°C and ca. 251°C that represented, respectively, 8.4% and 10.0% of the original mass of αFeOOH. The first mass loss was almost certainly due to the desorption of physically adsorbed water, while the second mass loss, which actually began at ca. 220°C and was complete at ca. 310°C, was due to the loss of structural water from the dehydrating αFeOOH.

The DSC, at 20°C minute^{-1}, of 10mg of the prepared αFeOOH is shown in Fig. A1.3. This αFeOOH registered a major endothermic event that began at ca. 200°C and was complete at ca. 320°C. The temperature corresponding to the maximum in the reaction rate of this endothermic event was 294°C and three smaller maxima occurred at 258, 237 and 200°C. This major endothermic event can be readily attributed to the loss of structural water from the dehydrating αFeOOH, while the three smaller maxima (or shoulders) are generally attributed (Paterson and Swaffield) to the separate dehydroxylations of the differently coordinated hydroxyls at the surface of αFeOOH (see section 4.).

2.4. An assessment of the ability of αFeOOH to chloride contaminate αFeOOH - suspending aqueous solutions, using XRF and HPLC.

An XRF analysis of the prepared αFeOOH showed no element other than iron, and with an atomic number > 12, having a major or minor concentration. However, a trace amount (< 10 μmol g^{-1}) of chlorine was detected in this αFeOOH.

The concentrations of simple anionic species present in 200 cm^3 of double distilled water, that was contained under a slight positive pressure of N_2 and maintained at pH 7.00 and 25°C, were determined by ion chromatography. 2g of the prepared αFeOOH was added to this water and after 2 hours the pH of the, so formed, αFeOOH aqueous suspension was raised to a value that was within the range of αFeOOH pH_o values (i.e., pH 7.5 to 8.7) (Atkinson et.al., Hingston et.al., Yates and Healy, Madrid and Arambarri).

The concentration of simple anionic species present in filtered samples of the αFeOOH-suspending aqueous solution were determined by ion chromatography.

FIGURE A1.2

THERMOGRAVIMETRIC ANALYSIS OF A SYNTHETIC ∝FeOOH, AT 3 °C min.$^{-1}$

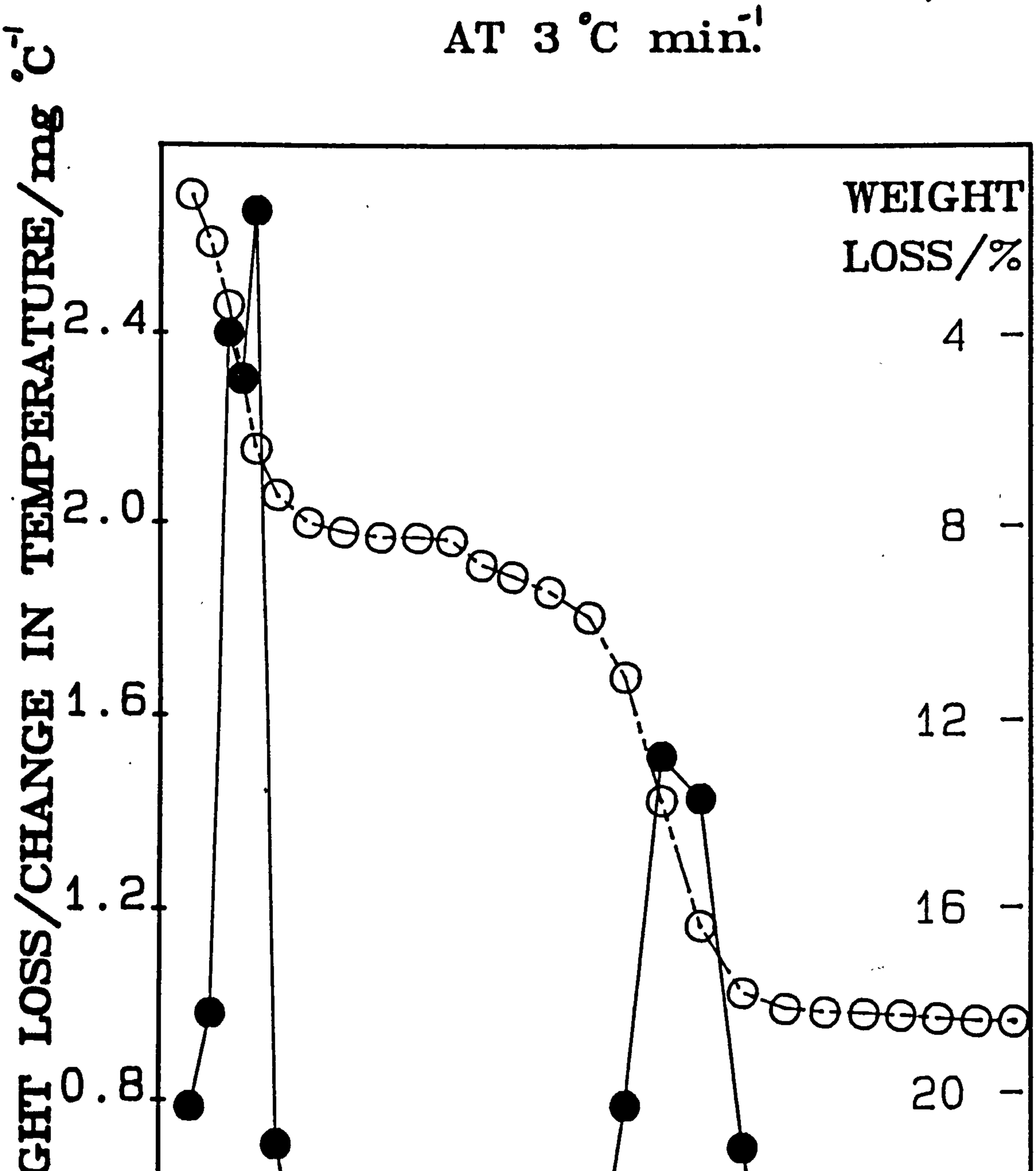

FIGURE A1.3

DIFFERENTIAL SCANNING CALORIMETRY OF A SYNTHETIC αFeOOH.

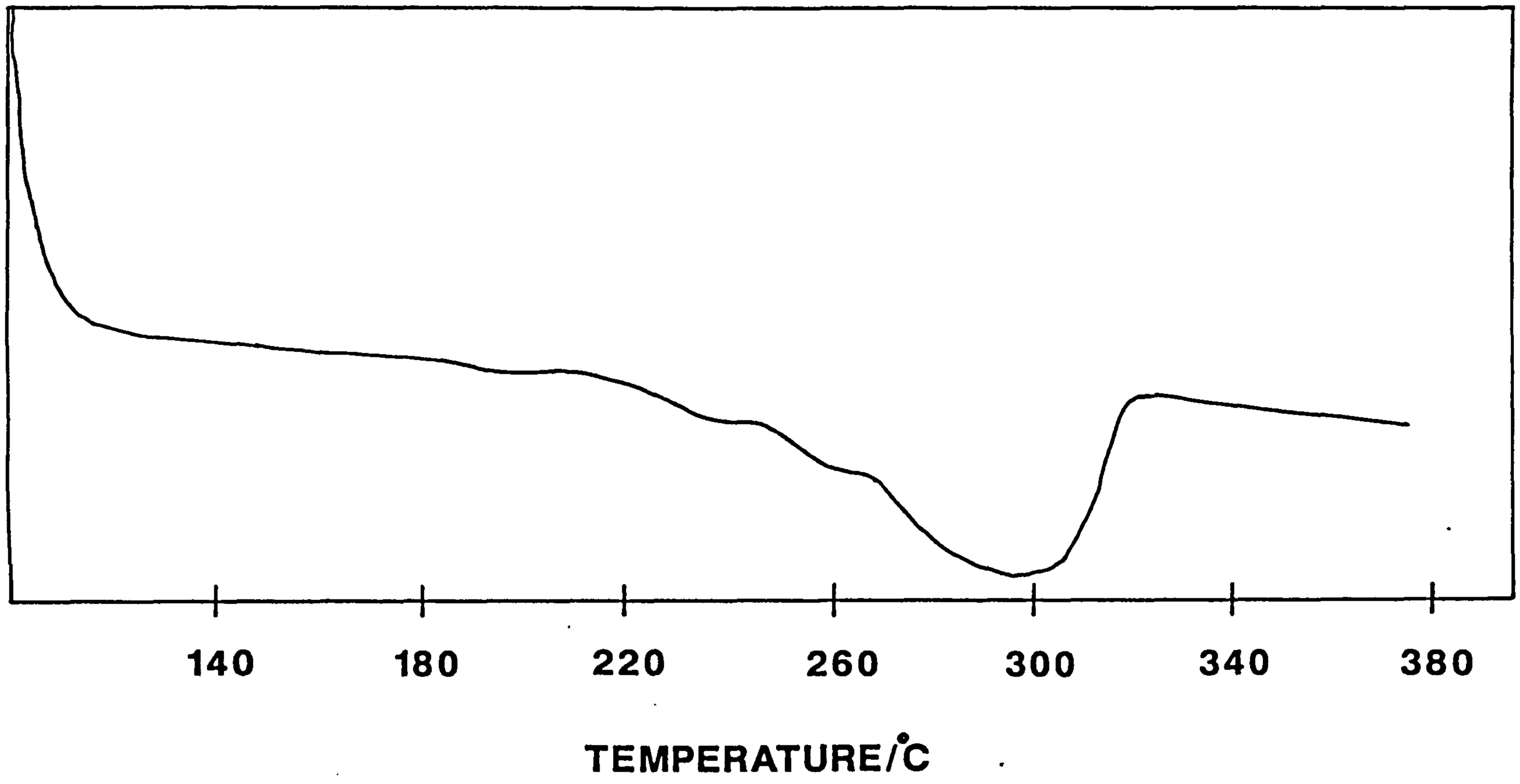

It was found that the 200 cm^3 of double distilled water did not contain any simple anionic species having a concentration > 10 $\mu mol\ dm^{-3}$, while 1.049 μmol Cl^- ion and 5.171 μmol NO_3^- ion were detected in the αFeOOH-suspending aqueous solution. It was considered, however, that this slight chloride contamination would not seriously inhibit the range of chloride concentration over which electrokinetic and adsorption experiments could be conducted on αFeOOH aqueous suspensions.

3. CONCLUSIONS.

Synthetic αFeOOH (structure confirmed by XRD and IR spectroscopy), with a virtually uncontaminated surface and an acicular particle morphology which is best described as lath-like (length/width/thickness ratio of 36:5:1), can be prepared by a modified version of the preparation given by Brauer. Such an αFeOOH is slightly microporous, with a BET (N_2) specific surface area that is ca. 10 $m^2\ g^{-1}$ larger than its t-plot external specific surface area, and contains 8.4% adsorbed water. On heating, the separate endothermic dehydroxylations of the differently coordinated surface hydroxyls of this αFeOOH are clearly apparent in its DSC thermogram. When this synthetic αFeOOH is suspended in water there is a slight contamination of the water by chloride ions that are, presumably, desorbed from the αFeOOH surface.

4. APPENDIX: THE SURFACE STRUCTURE OF αFeOOH.

At the surface of αFeOOH there are three types of hydroxyl groups designated A, C and B which are coordinated to one, two and three Fe^{3+} lattice ions, respectively (Russell et.al). Only A type hydroxyls can form hydrogen bonds with oxygen sites within the surface structure. B and C type hydroxyls cannot form hydrogen bonds because all such, adjacent, hydroxyls are coordinated to a common Fe^{3+} lattice ion.

Significant quantities of residual water remain on the surface of αFeOOH even after extended evacuation (1 nm Hg for 5 days) at room temperature (Gast et.al.).

REFERENCES

Atkinson, R. J., Posner, A. M. and Quirk, J. P., J. Phys. Chem., 71, 550 (1967).

Brauer, G., "Handbook of Preparative Inorganic Chemistry", Vol. 2, Academic Press, London, 1965.

Brunauer, S., Deming, L. S., Deming, W. E. and Teller, E., J. Amer. Chem. Soc., 62, 1723 (1940).

Gast, R. G., Landa, E. R. and Meyer, G. W., Clays and Clay Minerals, 22, 31 (1974).

Hingston, F. J., Posner, A. M. and Quirk, J. P., J. Soil Sci., 23, 177 (1972).

Jung, R. F., James, R. O. and Healy, T. W., J. Colloid Interface Sci., 118, 463 (1987).

Madrid, L. and de Arambarri, P., Geoderma, 21, 199 (1978).

Morris, M. C., McMurdie, H. F., Evans, E. H., de Groot, J. and Paretzkin, B., "Powder Diffraction data", 1st Edition, Joint Committee on Powder Diffraction Standards, Pennsylvania, 1976.

Paterson, E. and Swaffield, R., J. Thermal Anal., 18, 161 (1980).

Rendon, J. L., Cornejo, J., de Arambarri, P. and Serna, C. J., J. Colloid Sci., 92, 508 (1983).

Russell, J. D., Parfitt, R. L., Fraser, A. R. and Farmer, V. C., Nature, 248, 220 (1974).

Shokarev, M. M., Margulis, E. V., Vershinina, F. I., Beisekeera, L. I. and Sarchenko, L. A., Zh. Neorg. Khim., 17, 9, 2474 (1972).

Weast, R. C., "Handbook of Chemistry and Physics", 59th Edition, 1978.

Yates, D. E. and Healy, T. W., J. Colloid Interface Sci., 52, 222 (1975).

CHAPTER A2

CORROSION PRODUCT αFeOOH

1. INTRODUCTION

Corrosion product αFeOOH is found, with γFeOOH, in the outer region of the rust layer formed on unalloyed steel (Suzuki et.al). The inner region of such a rust layer consists primarily of amorphous αFeOOH with some crystalline Fe_3O_4. αFeOOH and the other corrosion products are formed from unalloyed steel in many environments because iron, the principal constituent of steel, is a fairly reactive metal; in thermodynamic terms all the compounds of iron are formed with a resulting decrease in free energy, so it may be anticipated that reaction with other compounds can occur in almost any environment. Metals, such as iron and aluminium, that react with water and oxygen in combination, more rapidly than with either water or oxygen in isolation, readily form corrosion products (Ross). In the corrosion of iron the friable corrosion products so formed afford little protection against continued corrosion. Indeed, the deposition of layers of corrosion products can actually assist in the corrosion of unalloyed steel by restricting the access of electrolyte, leading to the formation of an occluded cavity (Pourbaix); the solution inside the cavity becomes very acidic (due to the hydrolysis of Fe^{2+} and Fe^{3+} ions) and dissolves further steel.

The most common environments to which metallic products of iron are exposed are the atmosphere, domestic and industrial water and sea-water. The use of industrial water, primarily as a coolant, gives rise to much corrosion (Ross) and, consequently, appreciable quantities of corrosion products. In the following study samples were obtained from a typical, industrial cooling system and subjected to a visual inspection, and instrumental and chemical analyses (Fig. A2.1). The samples were:-

i) a rust nodule detached from the inside surface of a cooling pipe,
ii) a cooling pipe sludge, and
iii) a piece of cooling pipe (through which had flowed high-quality water).

2. RESULTS.

2.1. Visual examination.

2.1.1. Rust nodules

These were heterogenous structures mainly composed of yellow/brown

FIGURE A2.1

INSTRUMENTAL AND CHEMICAL ANALYSES OF DEPOSITS FROM A TYPICAL INDUSTRIAL COOLING SYSTEM.

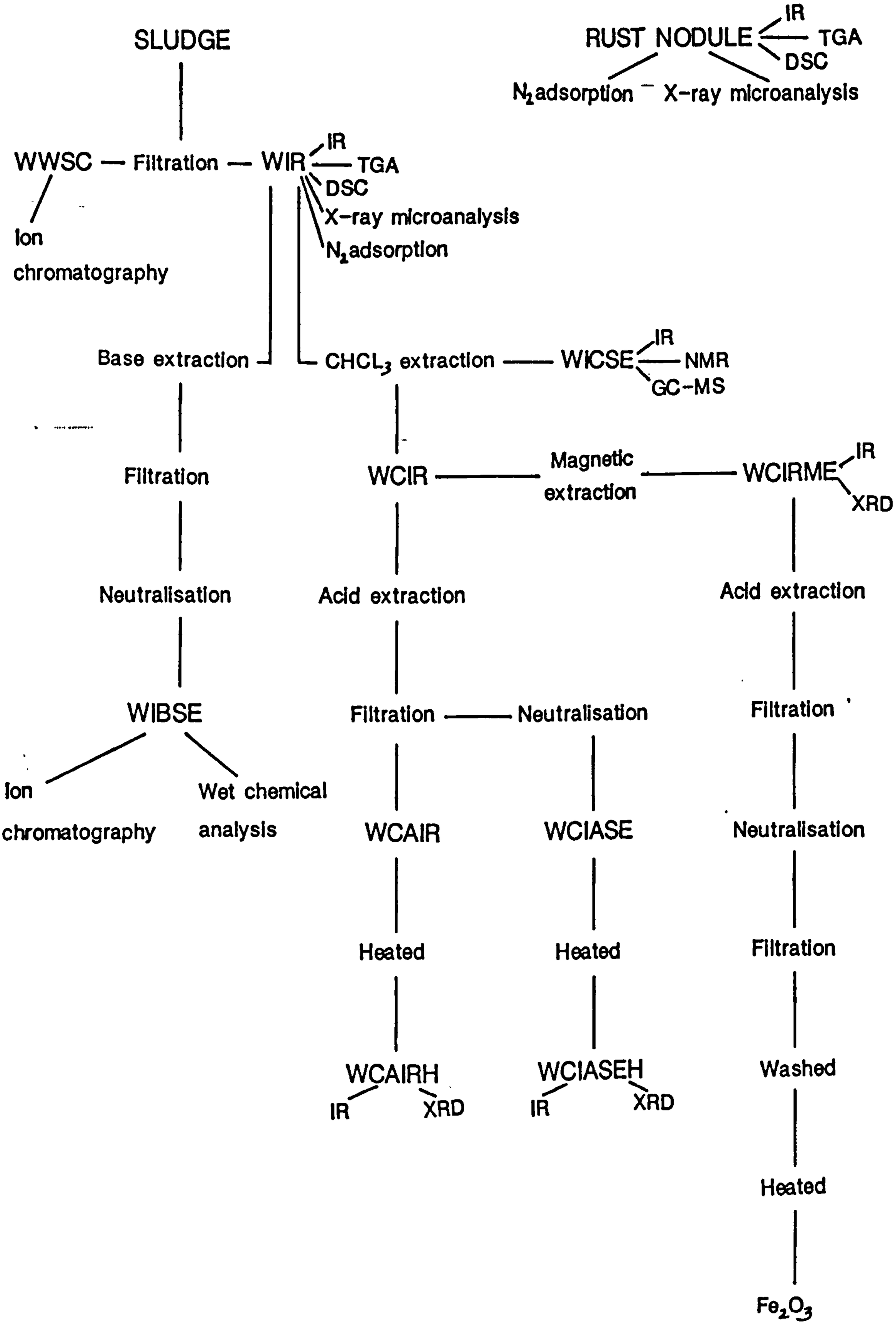

particles and a small amount of metallic material. Strands of glass fibre were adhering to the nodules. A photograph of a section through a rust nodule is shown in Plate A2.1.

2.1.2. Sludge

This was a dark brown, viscous slurry with a pungent odour.

2.1.3. Piping (6" diameter water main)

The piping was identified as 'Grey' Cast iron, having a wall thickness of about 1.2cm. The depth of corrosion, displayed as a zone containing only graphite with no iron, was approximately 2mm from the inside surface of the pipe. A photograph of a section through the piping wall is shown in Plate A2.2.

2.2. Instrumental and chemical analyses.

2.2.1. Rust nodules

a) Infrared (IR) spectrum, Figs. A2.2 and A2.3.

A strong doublet at 890 cm^{-1} and 798 cm^{-1} confirmed the presence of αFeOOH in the rust nodules, while an increased intensity of the higher frequency band, relative to the lower frequency band, suggested that this particular αFeOOH had, on the basis of differential thermal analysis, a relatively stable structure (Kalinskaya et.al.). The next strong absorption band on the longer wavelength side of this doublet occurred at a frequency of approx. 593 cm^{-1} which is characteristic of naturally produced αFeOOH samples (Estep et.al., White and Roy). The absence of a peak at approx. 1018 cm^{-1} indicated that γFeOOH was not present in the rust nodules (Shokarev et.al.).

b) Thermogravimetric analysis (TGA).

On heating a rust nodule from ambient to 760°C at 3°C per minute, a single major loss in mass (8.7%, corrected for mass losses occurring at temperatures < 195°C) was observed centred around 268°C. A single major loss in mass occurring at 268°C was consistent with the IR assignment for the chemical composition of the rust nodules; however, the corresponding percentage mass loss was lower than the theoretical value of 10.14% for the total thermal dehydroxylation of FeOOH. Differences between the mass loss of an FeOOH sample and the theoretical mass loss are normally

PLATE A2.1

A section through a rust nodule (magnification x 7.4).

PLATE A2.2

A section through a piece of piping wall (magnification x 6.9).

FIGURE A2.2

INFRARED ABSORPTION SPECTRUM OF A RUST NODULE

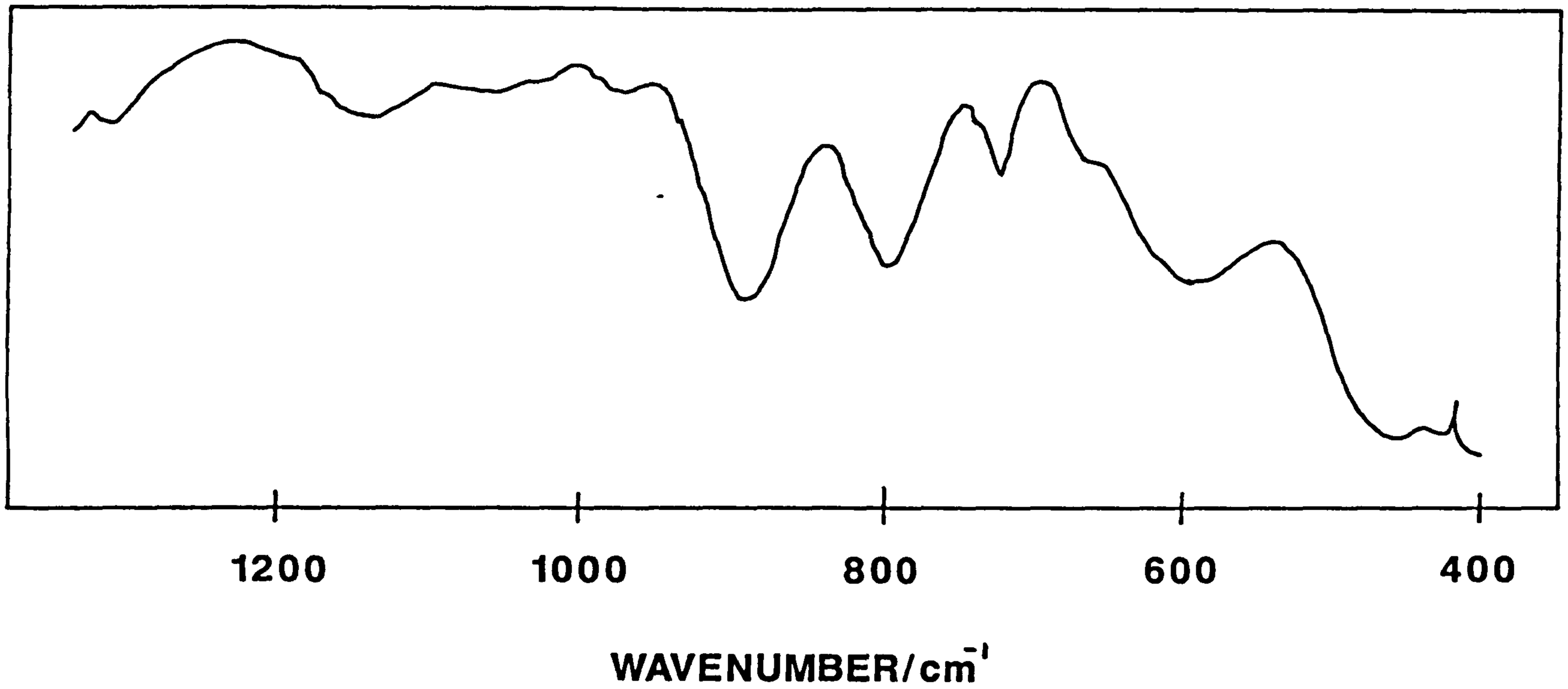

attributed to the stoichiometry of the FeOOH surface (Paterson and Swaffield, Paterson). Thus, whereas a mass loss of > 10.14% reflects an excess hydroxyl content of a protonated (positively charged) surface, a mass loss of < 10.14% is indicative of an ionised (negatively charged) FeOOH surface.

c) Differential scanning calorimetry (DSC), Fig. A2.4.

The DSC of a rust nodule, over the temperature range ambient to 500°C at a heating rate of 20°C per minute, showed two major endothermic events, one at 135°C and the other at 296°C plus a shoulder at 258°C. The endothermic event at 135°C was almost certainly due to adsorbed water. The endothermic event at 296°C, with the appearance of a shoulder at 258°C, was consistent with the IR assignment for the chemical composition of the rust nodules.

It is known that the surface of the predominant (100) face of αFeOOH contains singly, doubly and triply coordinated hydroxyl groups (Russell et.al.). The DSC curve for the dehydroxylation of αFeOOH is a series of small shoulders, before the principal peak, which are generally attributed to the separate dehydroxylations of these differently coordinated surface hydroxyls (Paterson and Swaffield). Thus, the absence of two out of three expected shoulders on the major endothermic event at 296°C of the rust nodule would suggest a reduced surface hydroxyl content (Paterson). Such an observation is consistent with the earlier interpretation of the TGA data in terms of the αFeOOH of the rust nodules possessing an ionised, or hydroxyl deficient, surface.

d) Physical and chemical surface characteristics.

The specific surface area of the ground rust nodules, as evaluated by N_2 adsorption at 77.4K, was 26.8 $m^2\ g^{-1}$. Although the type II adsorption/ desorption isotherms displayed a slight hysteresis, a t-curve analysis indicated that the rust nodules were non-porous.

An X-ray microanalysis of the particles constituting the rust nodules showed their surface to be free of any non-iron contamination, other than a very small amount of sulphur. No surface chloride was detected.

FIGURE A2.4

DIFFERENTIAL SCANNING CALORIMETRY OF A RUST NODULE.

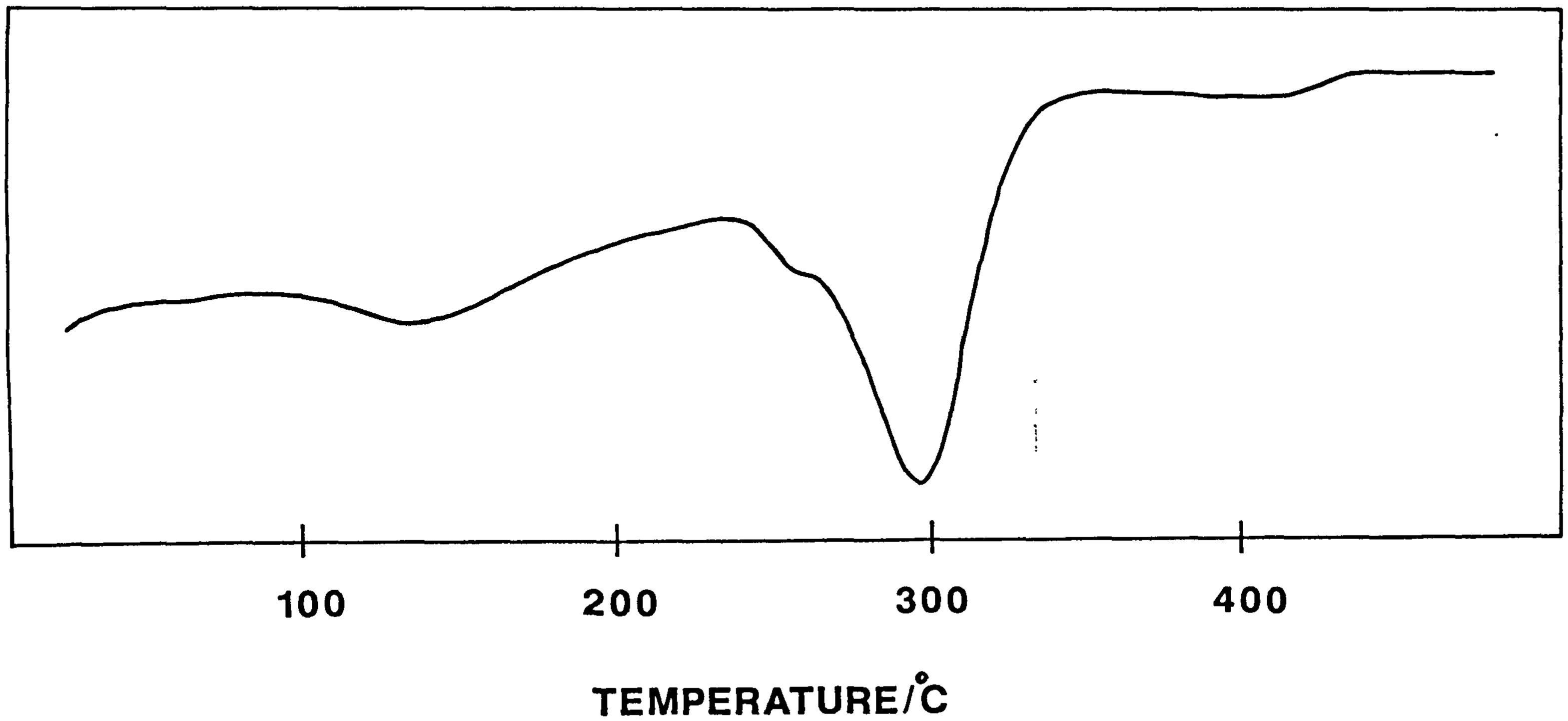

2.2.2. Sludge

A portion of the sludge was filtered by suction through a Hartley funnel. The remaining water of the semi-dry residue was removed by vacuum desiccation. From a knowledge of the weight of the portion of sludge and the weight of the dry, water insoluble residue (WIR) remaining after filtration and desiccation, the water plus water soluble content (WWSC) of the sludge was estimated to be 83.5%.

2.2.2.1. WIR

a) IR spectrum.

The IR absorption bands for the WIR are tabulated in Table A2.1, together with those for the two naturally occurring crystalline forms of SiO_2, quartz and cristobalite (Taylor et.al.). The excellent correspondence between the IR absorption bands of quartz and the WIR confirmed the presence, in the WIR, of a large amount of quartz. It was noted that the strong, broad band at approx. 1030 cm^{-1} would appear to have no counter-part in the IR spectra of quartz or cristobalite. The assignment of this band to the absorption of energy by a particular functional group must await further investigation. The absence of strong absorption doublets at 900 cm^{-1}/800 cm^{-1} and 1020 cm^{-1}/740 cm^{-1}, and an absorption band at 570 cm^{-1}, suggested that the WIR did not contain large amounts of $\alpha FeOOH$, $\gamma FeOOH$ or Fe_3O_4.

b) TGA

On heating the WIR from ambient to 620°C at 3°C per minute, several major losses in mass occurred at 103°C, 193.5°C and 242.5°C, and a less pronounced loss in mass occurred from 280°C up to 460°C. A clear separation of these losses in mass was achieved by heating the WIR from ambient to 390°C at the slower heating rate of 1°C per minute (Fig. A2.5). The first major loss in mass (6.60%) was almost certainly due to the evaporation of physically adsorbed water. The second and third major losses in mass represented, respectively, 6.87% and 3.44% of the total mass of solid, while the mass loss occurring from 280°C to 460°C represented 4.30% of the total mass of solid.

A TGA of a sample of pure synthetic $\alpha FeOOH$ was obtained at 3°C per minute. This analysis showed, besides the loss in mass due to physically adsorbed water (occurring at 88.5°C), a single major loss in mass at 251°C. Such

Table A2.1

Infrared absorption bands.

WIR cm^{-1}		Quartz cm^{-1}	Cristobalite cm^{-1}
3600→3100	(b)		
1630	(b)		
1163	(sh)	1165 (sh)	1195 (sh)
1145	(sh)	1140 (sh)	1150 (sh)
1080		1085	1095
1030	(b)		
860			
797		798	798
778		779	
765	(sh)		
695		694	
515	(sh)	512	490
460		460	
		397	385
		370	297
			274

FIGURE A2.5

THERMOGRAVIMETRIC ANALYSIS OF THE WATER INSOLUBLE RESIDUE OF A SLUDGE, AT 1°C min^{-1}.

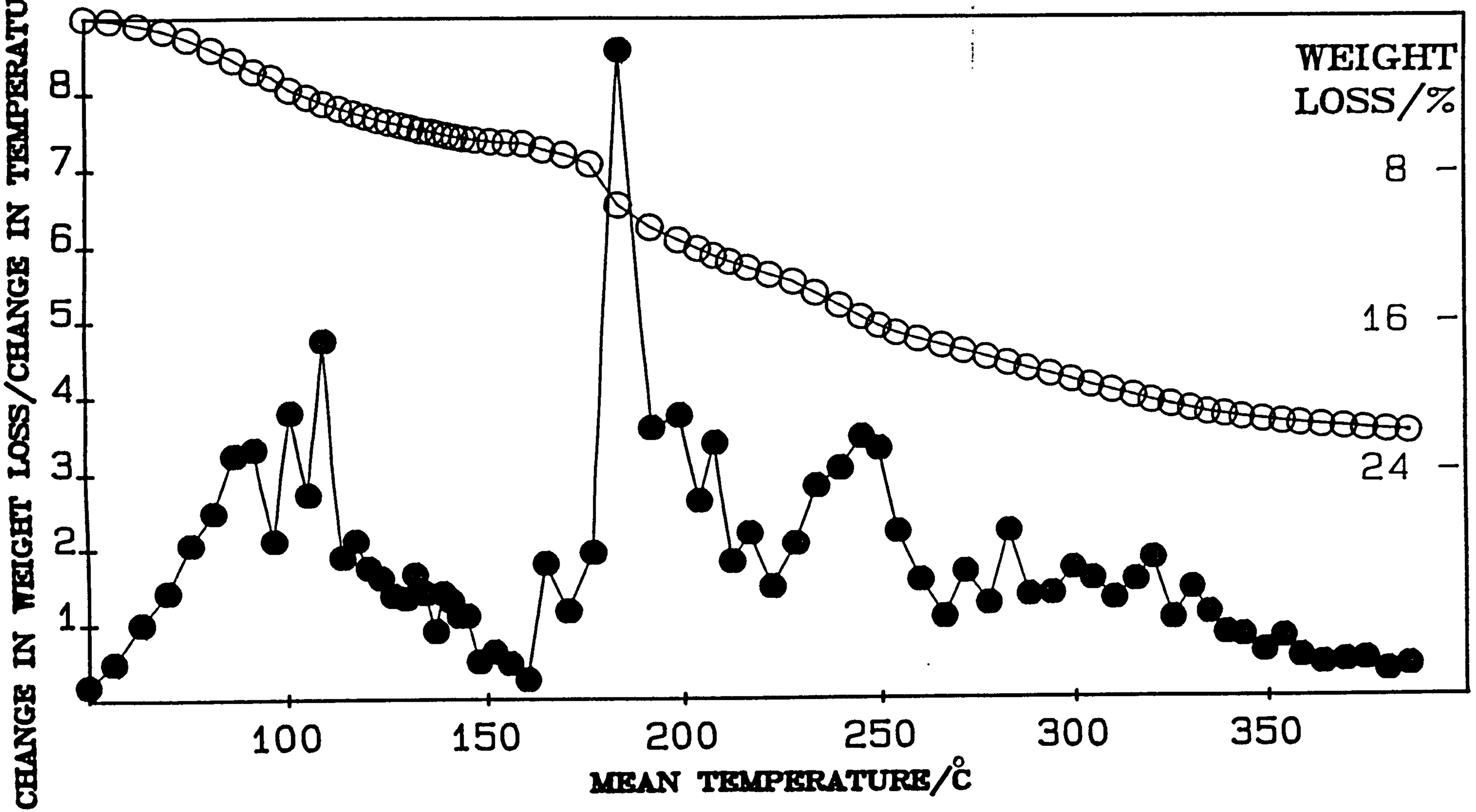

a temperature was similar to the temperature of the third major mass loss of the WIR, and constituted slight evidence for the presence of iron (III) oxyhydroxide in the WIR. If iron (III) oxyhydroxide was present, and the 3.44% mass loss at 242.5°C was the loss of structural water, then it is possible to estimate the proportion of compounds with the generic formula FeOOH in the WIR as 33.9%.

c) DSC

Two different WIR's (one obtained from the sludge sample immediately after its removal from the cooling pipe, and another obtained from the same sample several months later) gave different DSC thermograms. In general, the DSC of the WIR showed an endotherm at about 130°C, three exothermic events at about 265°C, 340°C and 425°C, and a small endothermic event at 587°C (Fig. A2.6a). The endothermic event at about 130°C was almost certainly due to adsorbed water. The strong exothermic event at about 265°C could possibly be due to the oxidation, to CO_2 and H_2O, of organic material. However, a DSC (at 20°C min^{-1}) of the WIR after a chloroform extraction, using both cold and boiling $CHCl_3$, still displayed a strong exothermic event at 290°C and a shoulder at 360°C (Fig. A2.6b). The DSC thermogram of the WIR displayed a similarity with that obtained (in an atmosphere of oxygen) for wood products, such as lignin and cellulose (water and chloroform insoluble)(Tang), suggesting the presence of such organic materials in the WIR. The strong exothermic peaks at about 265°C and at 340°C in the DSC thermogram for the WIR prohibited the detection of endothermic peaks, in this temperature interval, arising from the loss of structural water from iron (III) oxyhydroxide. However, the small exothermic event at 440°C was slight evidence for the phase transition

$$\gamma Fe_2O_3 \rightarrow \alpha Fe_2O_3$$

and, consequently, the presence in the WIR of γFeOOH and/or γFe_2O_3 (Subrt et.al.). The very small endothermic event at 587°C was possibly due to the magnetic transition, ferromagnetism to paramagnetism, of Fe_3O_4 (Chaklader and Blair).

d) Physical and chemical surface characteristics.

The specific surface area of the WIR, after a chloroform extraction, was 25.7 m^2 g^{-1}.

FIGURE A2.6

DIFFERENTIAL SCANNING CALORIMETRY OF THE WATER INSOLUBLE RESIDUE OF A SLUDGE.

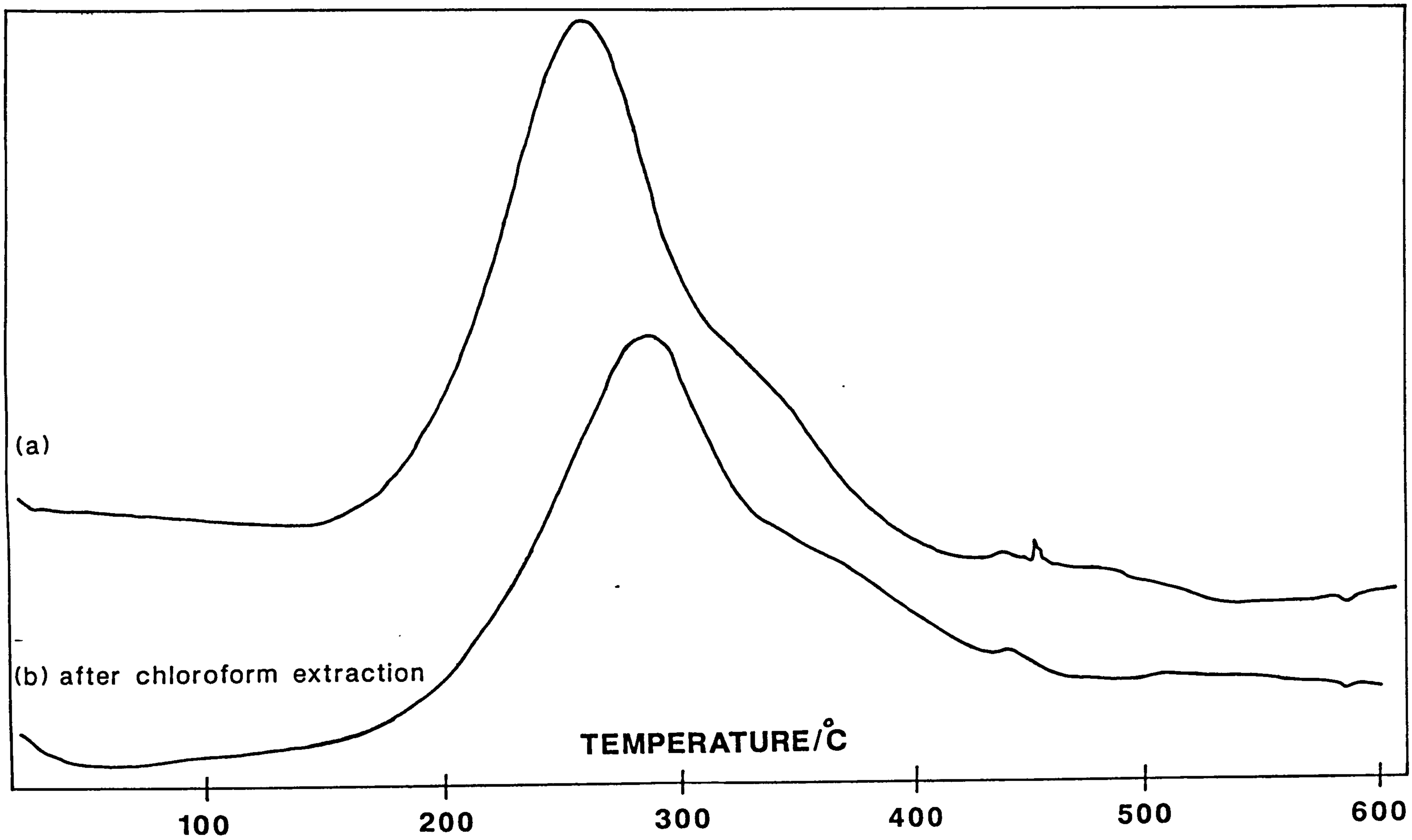

Although the type II adsorption/desorption isotherms displayed a hysteresis, a t-curve analysis indicated that the WIR was non-porous.

The X-ray microanalysis of the surface of the WIR is shown in Fig. A2.7. This surface analysis of the particles showed a high proportion of Fe and a small proportion of Si, with trace amounts of K, Al and Ti, i.e., elements having a tendency to form cations. No surface chlorine was detected. It is possible, therefore, to conjecture that, in view of the very probable presence of surface cations the surface of the particles constituting the WIR possessed a negative charge.

e) X-ray diffraction (XRD) analysis.

Quartz (αSiO_2), siderite ($FeCO_3$) and magnetite (Fe_3O_4) gave good identification patterns; the values of the remaining d-spacings corresponded to the more intense lines of the XRD patterns of $\alpha FeOOH$ and $\gamma FeOOH$.

f) Chloroform extraction.

A known weight of the WIR was shaken with chloroform in a separating funnel for 30 minutes. After filtration, all the chloroform was removed from the water-insoluble/chloroform-soluble extract (WICSE) (4.44% of the WIR). The dark coloured, viscous extract was analysed by IR spectroscopy, ^{13}C and ^{1}H nuclear magnetic resonance (NMR) spectroscopy and gas chromatography-mass spectrometry (GC-MS).

The IR absorption bands and assignments (Smalley and Wakefield) are tabulated in Table A2.2. The IR spectrum over the range 4000 cm^{-1} to 1300 cm^{-1} is shown in Fig. A2.8. The spectrum was principally composed of saturated C-H absorptions, which confirmed the presence of an alkane structure in the extract. Other absorptions in the spectrum suggested the presence of different types of carbonyl groups, $\begin{matrix} R \\ R \end{matrix}\!\!>\!C = O$, and possibly a poly-chlorinated structure in the extract (although this may have been due to traces of $CHCl_3$ on the KBr plates).

The ^{1}H NMR spectrum, over the scan range 0 to 14 ppm, showed two intense high field resonances and two weak resonances to the low field side of

FIGURE A2.7

X-RAY MICROANALYSIS OF THE SURFACE OF THE WATER INSOLUBLE RESIDUE OF A SLUDGE.

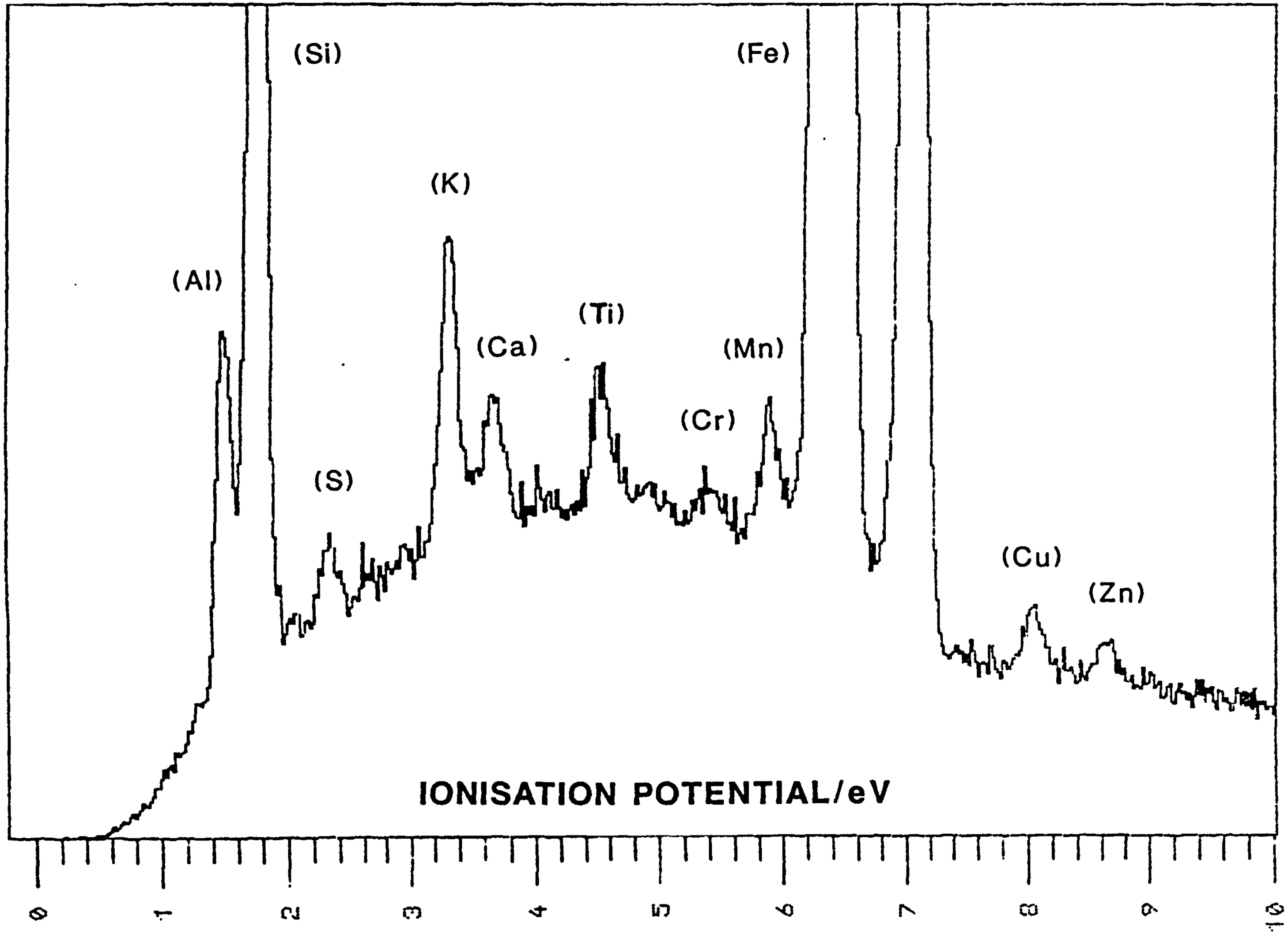

Table A2.2

IR absorption bands of WICSE

Absorption frequency / cm^{-1}	Assignment
3500→3200	Intermolecular hydrogen bonded OH (polymeric OH)
2945 (sh)	$-CH_3$ asym. stretch
2915	$-CH_2-$ asym. stretch
2885 (sh)	$-CH_3$ sym. stretch
2855 (sh)	?
2840	$-CH_2-$ sym. stretch
2810 (sh)	?
1710 (b)	C=O stretch
1595 (b)	aromatic C=C skeletal stretch
1460	$-CH_3$ asym. bending
1435 (sh)	$-CH_3$ asym. bending
1375	$-CH_3$ sym. bending
1365 (sh)	$-CH_3$ sym. bending
1020	?
810	?
760	C-Cl stretch in polychlorinated compounds (possibly residual cleaning solvent, $CHCl_3$, on I.R. plates)
720	$-CH_2)n-$ rock, only appears when $n \geqslant 4$.

FIGURE A2.8

INFRARED ABSORPTION SPECTRUM OF THE CHLOROFORM EXTRACT OF THE WATER INSOLUBLE RESIDUE OF A SLUDGE.

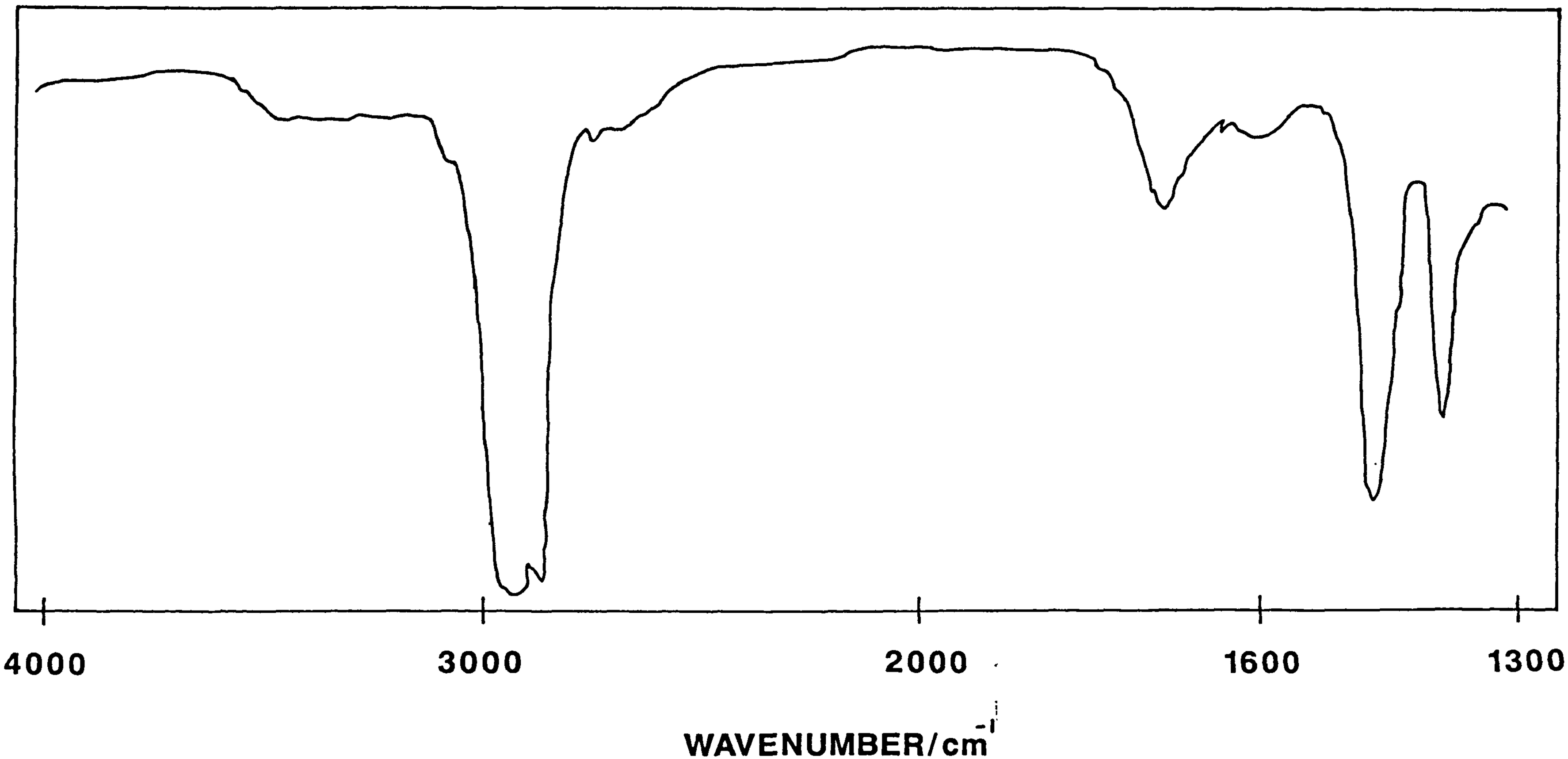

the intense resonances (Table A2.3). The intense resonances were almost certainly generated by the absorption of energy by methyl and methylene protons, while the weak resonances were very probably due to the absorption of energy by methine protons (Williams and Fleming). Such high field resonances, indicative of alkane protons, were consistent with the IR spectrum of the extract. It is noteworthy that no resonances were observed having a chemical shift indicative of acidic or aldehydic protons, or protons attached to unsaturated structures.

The ^{13}C NMR spectrum of the WICSE is shown in Fig. A2.9 and those resonances that were readily assignable are tabulated in Table A2.3. The spectrum, over the scan range 0 to 250 ppm, showed several high field resonances of saturated, sp^3 carbon atoms. Four such resonances were identified as being generated by the absorption of energy by the first three, and subsequent methylene, carbon atoms of a normal alkane. Such high field resonances, indicative of saturated carbon atoms, were consistent with the IR spectrum of the WICSE. The remaining sp^3 resonances suggested the presence of sp^3 carbon atoms involved in branching and/or attached to atoms such as halide, sulphur or nitrogen (Wehrli and Wirthlin). No resonances were observed having a chemical shift indicative of sp^2 or sp hybridised carbon atoms, which is not consistent with the IR evidence for the presence of different types of carbonyl structures. Such a disparity amongst the analytical evidence must await clarification.

The GC-MS data pertaining to the extract, including the reconstructed ion chromatogram and the mass spectra of several selected (apparently pure) components (from 50 amu to 500 amu) is shown in Figs. A2.10 to A2.13. The reconstructed ion chromatogram showed the chromatographic separation of the different components of the WICSE, while a quantitation report gave the percentage amount of each component (each component being categorised as a scan number, eg. #385). The WICSE was chromatographically separated into about a dozen major and minor components, whose combined amount represented about 90% of the WICSE. The mass spectra of the two major components, scan numbers #385 and #509, and two minor components, #352 and #358, displayed the same fragmentation pattern, especially at low m/z values. This fragmentation pattern can be expressed as the series of m/z values

57 · 71 · 85 · 55

Table A2.3

Assignments

^{13}C NMR resonances

No.	ppm	Assignment	
19	14.126	methyl	$\underline{C}H_3$-
17	22.705	methylene	CH_3-$\underline{C}H_2$-
13	29.727	methylene	CH_3-CH_2-CH_2-$(\underline{C}H_2)_n$-
12	30.051	methylene	CH_3-CH_2-CH_2-

^{1}H NMR resonances

No.	ppm	Intensity	Assignment	
1	2.55	weak	methine	$\underline{H}C$ -
2	2.28	weak	methine	$\underline{H}C$ -
3	1.28	strong (broad at base)	methylene	-$C\underline{H}_2$-
4	0.88	strong (broad at base)	methyl	$C\underline{H}_3$-

FIGURE A2.9

CARBON-13 NUCLEAR MAGNETIC RESONANCE SPECTRUM OF THE WATER-INSOLUBLE/CHLOROFORM-SOLUBLE EXTRACT OF A SLUDGE.

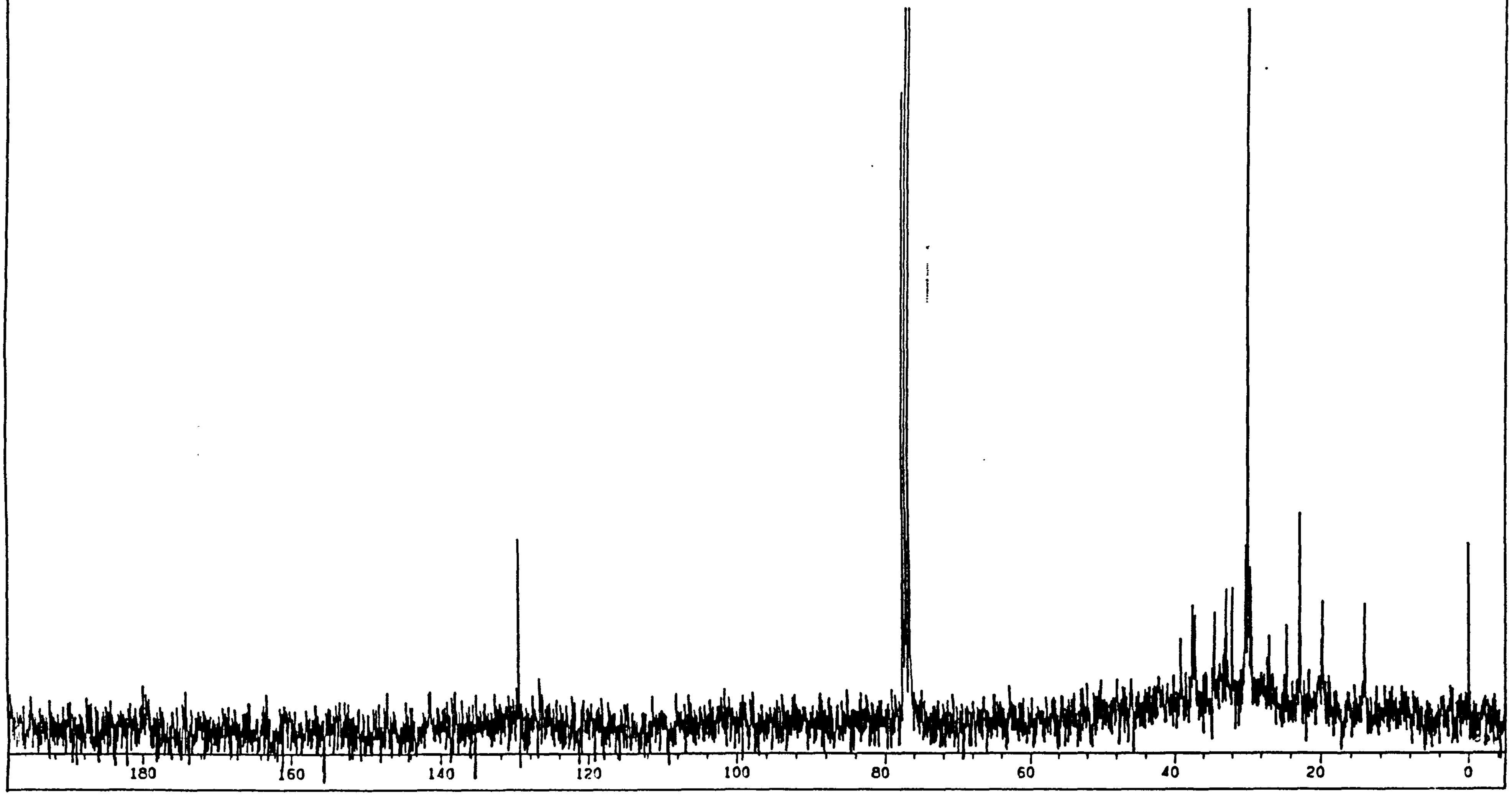

FIGURE A2.10

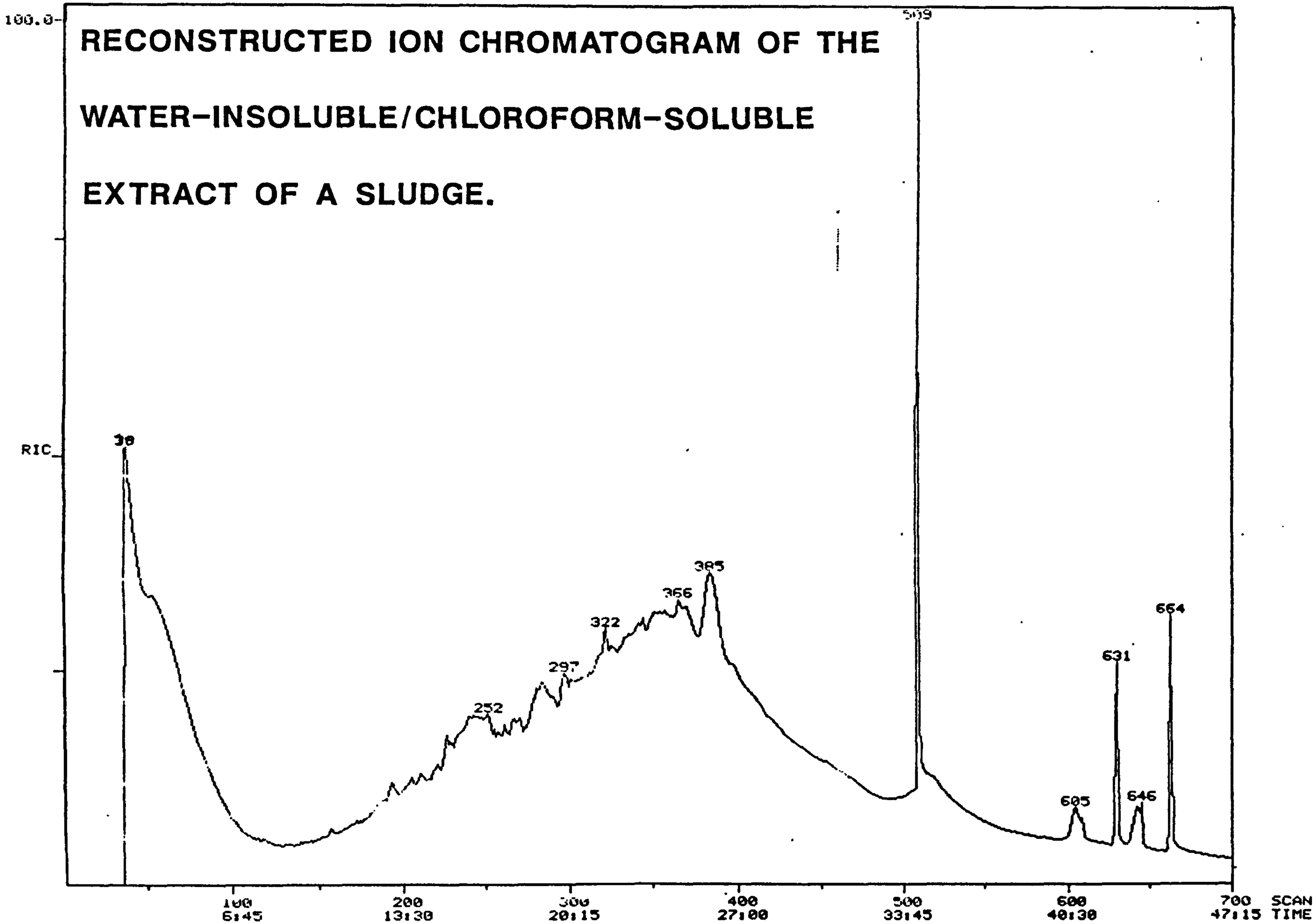
RECONSTRUCTED ION CHROMATOGRAM OF THE
WATER-INSOLUBLE/CHLOROFORM-SOLUBLE
EXTRACT OF A SLUDGE.
100.0
RIC
509
38
252
297
322
366
385
605
631
646
664
100
6:45
200
13:30
300
20:15
400
27:00
500
33:45
600
40:30
700
47:15
SCAN
TIME

FIGURE A2.11

MASS SPECTRUM OF A MAJOR COMPONENT OF THE WATER-INSOLUBLE/CHLOROFORM-SOLUBLE EXTRACT OF A SLUDGE.

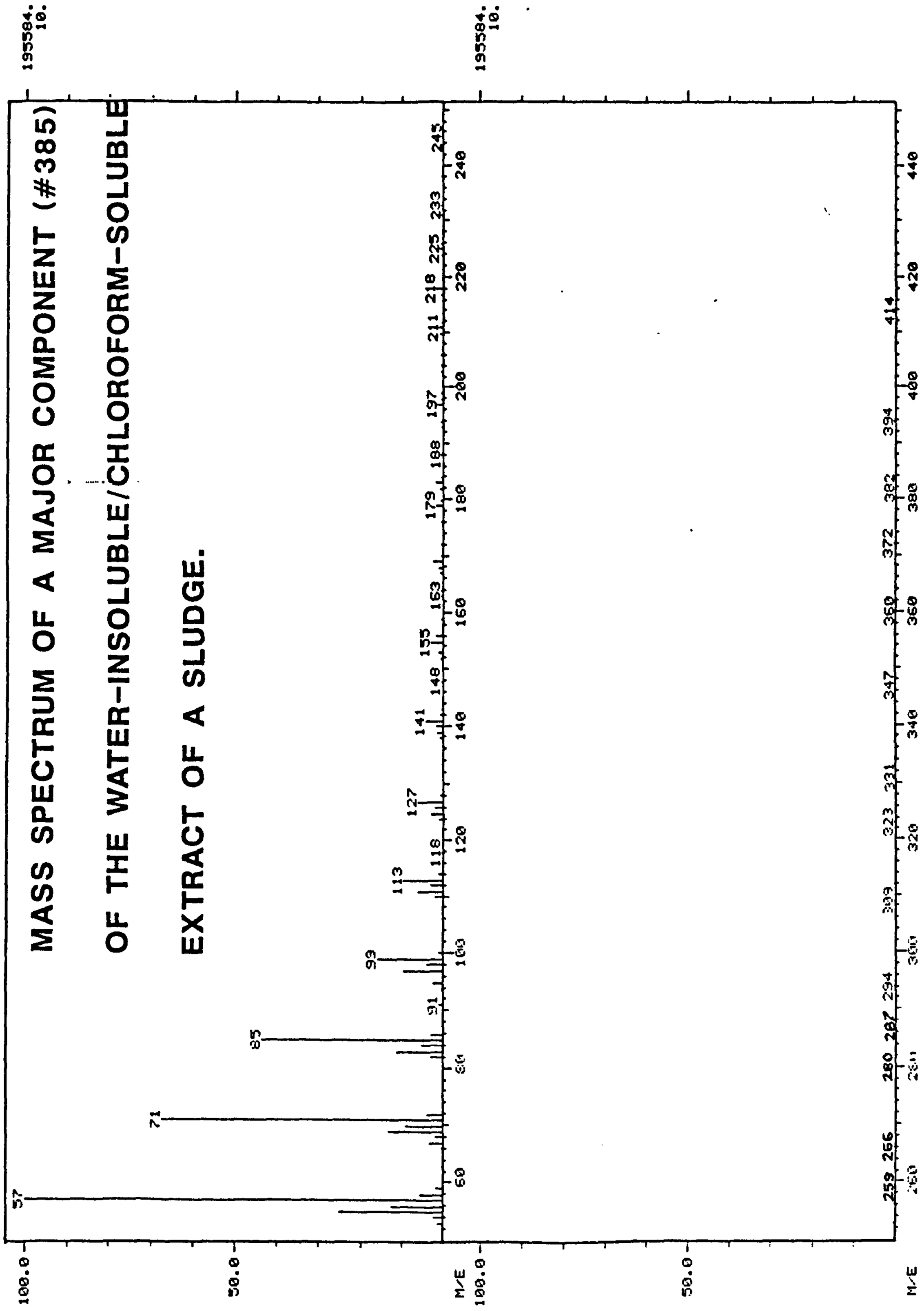

FIGURE A2.12

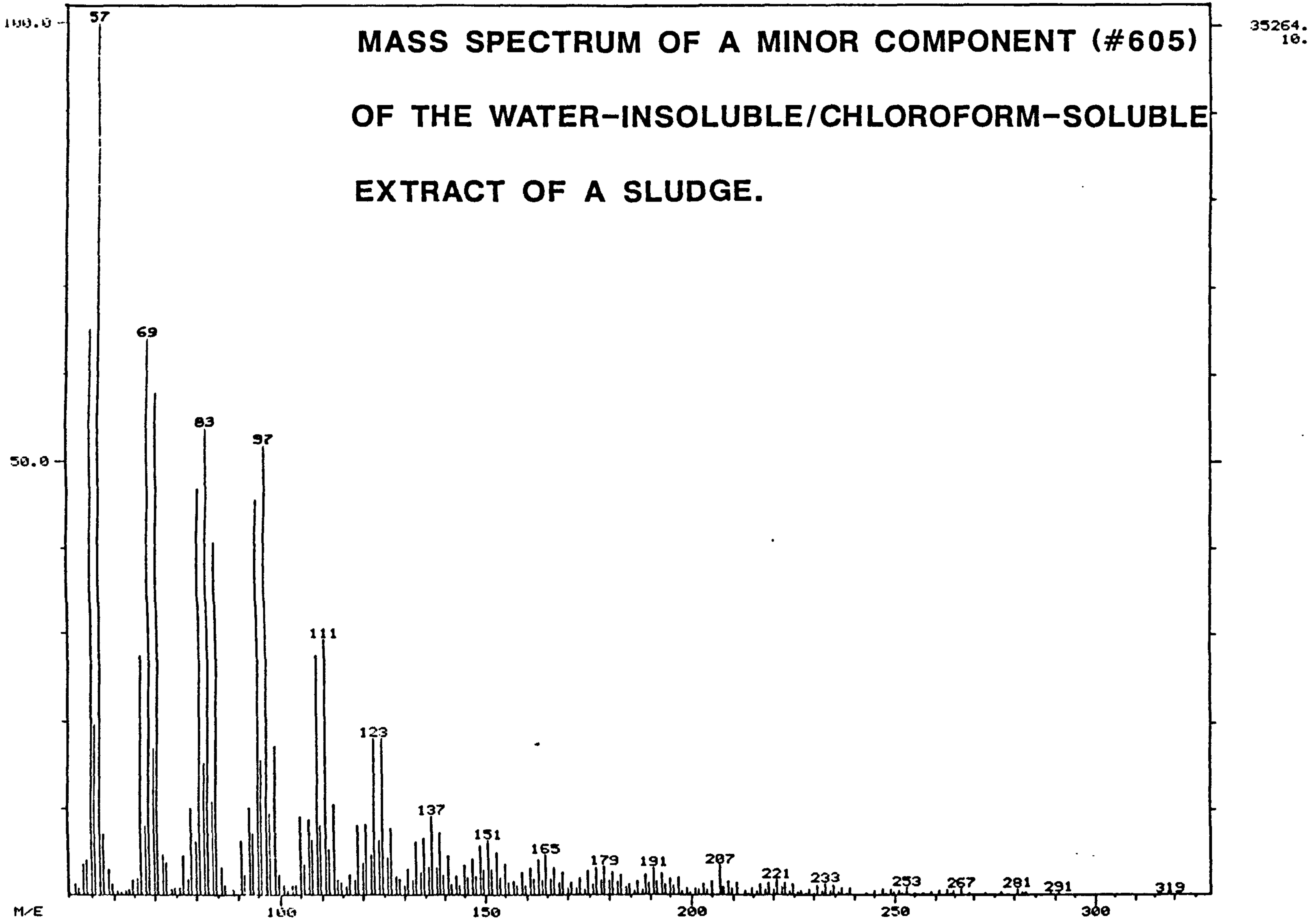
MASS SPECTRUM OF A MINOR COMPONENT (#605)
OF THE WATER-INSOLUBLE/CHLOROFORM-SOLUBLE
EXTRACT OF A SLUDGE.
100.0
50.0
35264.
10.
57
69
83
97
111
123
137
151
165
179
191
207
221
233
253
267
281
291
319
M/E
100
150
200
250
300

FIGURE A2.13

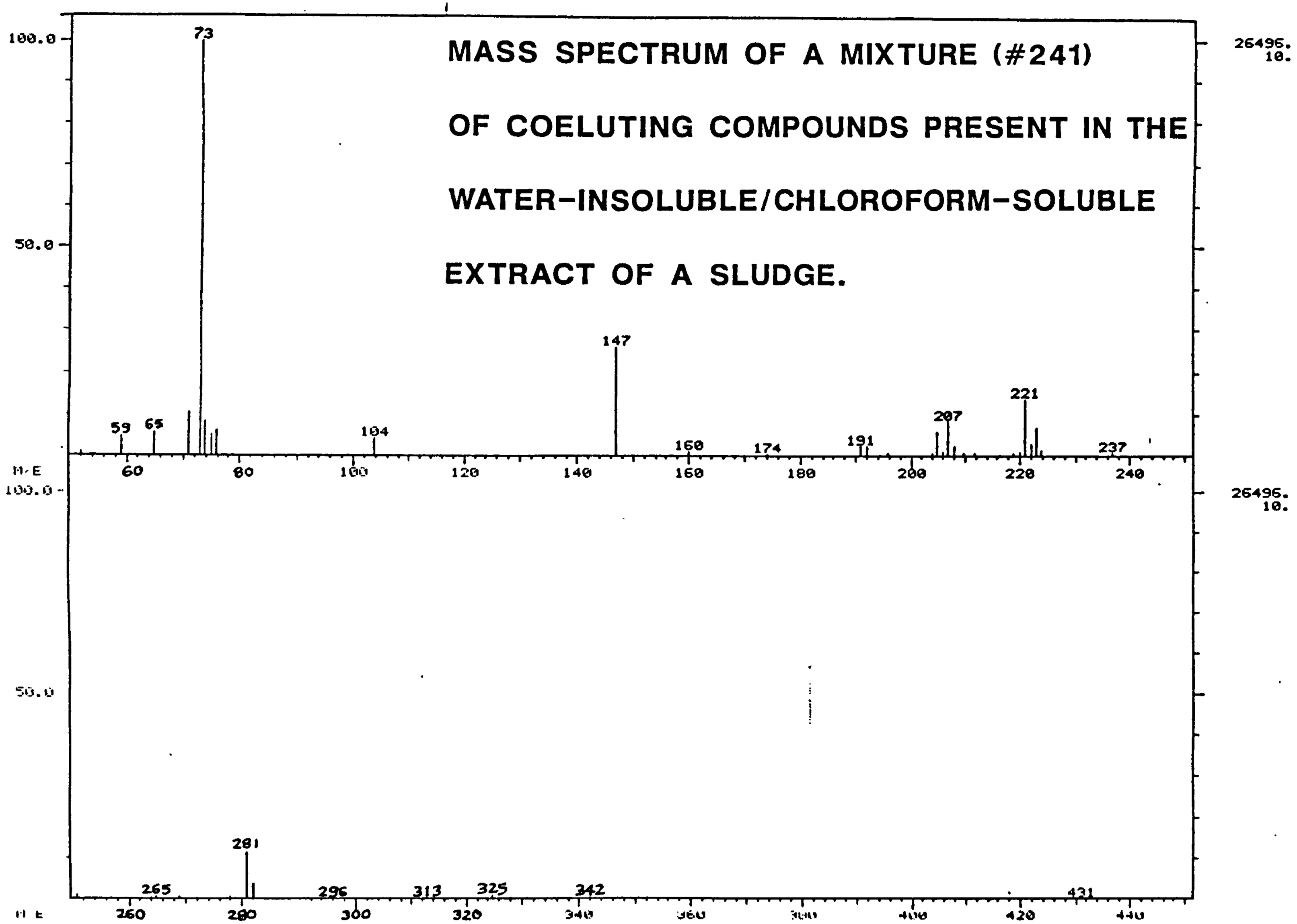
MASS SPECTRUM OF A MIXTURE (#241)
OF COELUTING COMPOUNDS PRESENT IN THE
WATER-INSOLUBLE/CHLOROFORM-SOLUBLE
EXTRACT OF A SLUDGE.
100.0
50.0
M/E
26496.
10.
73
147
221
207
59
65
104
160
174
191
237
281
265
296
313
325
342
431

in which the intensity decreases from left to right. This fragmentation pattern series (fps) is given by alkanes (Cornu and Massot). On closer examination of the common fragmentation pattern of #385, #509, #352 and #358, it was possible to augment this fps to the following, more definitive series

$$57 \cdot 71 \cdot 85 \cdot 55 \cdot \begin{matrix}\text{not}\\56\end{matrix}$$

which is not the fps given by normal (straight chain) alkanes. Thus, the components #385, #509, #352 and #358, which constituted 38.2% of the WICSE, were alkanes, and very probably branched alkanes. There is very facile fragmentation in branched hydrocarbons and therefore no molecular ion peak (Williams and Fleming). The highest m/z values of #385, #509, #352 and #358 were 414, 498, 364 and 384 respectively. Thus, it was assumed that these m/z values did not represent the respective molecular ions, and the actual mass numbers of the four components were in the range 380 to 520. Consequently, it was deduced that the molecular formulae of #385, #509, #352 and #358 were in the range $C_{27}H_{56}$ to $C_{37}H_{76}$.

The mass spectra of the last four components of the extract to be eluted, viz. #605, #631, #646 and #664, had the same fps at low m/z values:

$$57 \cdot 55 \cdot \begin{matrix}69\\\text{or}\\71\end{matrix}$$

This fps is given by compounds of the following generic molecular formulae

$$C_nH_{2n} \;;\; C_nH_{2n+1}X \;;\; C_nH_{2n}O_2 \;;\; C_nH_{2n+2}O_2$$

(involving a cyclic structure)

Thus, the components #605, #631, #646 and #664, constituting 12.6% of the extract, were essentially long chain saturated hydrocarbons incorporating one or more of the following entities:- an alicyclic side chain, a halide substituent, an ether linkage, an hydroxyl substituent or a carboxyl group. The highest m/z values for these four components were 319, 498, 278 and 445, respectively, which, because of the possibility that such m/z values were not the respective molecular ions, only served as a guideline to the actual mass numbers of these components.

The fragmentation patterns of the remaining minor components of the extract, whose combined amount represented 40.2% of the WICSE, were not consistent with any of the fragmentation patterns of the more common organic compounds (Budzikiewicz et.al.). This suggested that these remaining components, notably #241, #284, #322, #345 and #366, had not been successfully chromatographically separated; i.e., each chromatographic peak designated by one of these scan numbers represented a mixture of co-eluting organic compounds. It was noted that the mass spectra of these components did show a degree of similarity, particularly in the acquisition of an intense peak at m/z = 147 which is commonly observed in the mass spectra of organo-silicon-oxygen compounds (Williams and Fleming).

g) Base extraction.

A portion of the WIR was shaken with base (0.1 mol dm^{-3} NaOH aq.) for 30 minutes. After filtration the basic solution was neutralised with acid (0.1 mol dm^{-3} HNO_3 aq.), and evaporated to a small volume (rotary evaporator at 80°C). The yellow/brown water-insoluble/base-soluble extract (WIBSE) was analysed qualitatively by ion chromatography and classical 'wet' chemical analysis (Vogel).

The ion chromatograms of water samples almost invariably display a peak at a long retention time, generated by the CO_3^{2-} ion; in the particular ion chromatographic system being employed, such a peak occurred at about 24 minutes. The injection of the WIBSE into the ion chromatographic system did produce a shoulder on this carbonate peak, having a retention time of about 22 minutes and a broad base commencing at about 15 minutes. A peak occurring at such a relatively long retention time in an ion chromatographic system is usually generated by a highly charged species. Thus it would appear that the base extraction had removed a highly charged molecule from the WIR, such as a highly charged carboxylic acid or inorganic anion.

The classical 'wet' chemical analysis of the WIBSE is tabulated in Table A2.4.

h) Acid extraction.

A known weight of the water and chloroform insoluble residue (WCIR) was

Table A2.4

Test	Observation	Inference
H_2SO_4 (conc.)	immediate charring	organic
NH_4Cl	no precipitate	no silicates
$HgO + H_2SO_4$ (dil.)	no precipitate	no formates
$La(NO_3)_3 + I_2$ + NH_3 (aq.dil.)	no blue colour	no acetates or propionates
$HgSO_4$ + H_2SO_4 + $KMnO_4$	no precipitate	no citrates
Resorcinol + H_2SO_4 (conc.)	no green fluorescence	no succinates
$FeSO_4 + H_2O_2$	no blue colour	no tartrates
$BaCl_2$ + HCl (dil.)	no precipitate	no sulphates
$(NH_4)_6Mo_7O_{24}$ + NH_3 (aq. conc.) + NH_4NO_3 + HNO_3 (aq. conc.)	canary yellow, fine crystalline precipitate after several days	orthophosphates in presence of large amount of chloride (Holness)
H_2SO_4 (dil.) + Mg^{2+} + resorcinol + H_2SO_4 (conc.) as a bottom layer	red layer at junction of two liquids on warming	colour is due to condensation product of resorcinol and glycollic aldehyde, this latter species arising from the action of sulphuric acid on a α-hydroxy carboxylic acid type compound

shaken with cold, strong acid (conc. HCl aq.) for 10 minutes. After separation of the water, chloroform and acid insoluble residue (WCAIR) by filtration, the strongly acidic filtrate was neutralised with cold, strong base (conc. NH_3 aq.) yielding a precipitate of the water and chloroform insoluble/acid soluble extract (WCIASE). The WCAIR and accompanying dry filter papers were placed in a crucible of known weight. The crucible and its contents were weighed and then heated to 800°C/900°C on a bunsen. After cooling, the weight of the heated water, chloroform and acid insoluble residue (WCAIRH) was obtained. Similarly, the WCIASE and accompanying dry filter papers were placed in a crucible of known weight. The crucible and its contents were weighed and then heated to 800°C/900°C on a bunsen. After cooling, the weight of the heated, water and chloroform insoluble/acid soluble extract (WCIASEH) was obtained.

Weighings:

weight of WCIR	=	7.9751 g
∴ weight of WIR	=	8.3456 g
approx. weight of WCAIR	=	4.2980 g
approx. weight of WCIASE	=	3.3729 g
weight of WCAIRH	=	3.3385 g
weight of WCIASEH	=	3.1165 g
∴ approx. loss in mass on heating the WCAIR	=	0.9595 g
∴ approx. loss in mass on heating the WCIASE	=	0.2564 g

The WCAIRH and the WCIASEH were analysed by IR spectroscopy and XRD. The IR absorption bands and d-spacings given by the WCAIRH confirmed it to be almost exclusively quartz (SiO_2). Thus, it was possible to calculate the proportion of Si in the WIR to be 18.7%. In addition, on the assumption that all this silicon was occurring in the WIR as SiO_2, it was possible to make the tentative estimation of 40.0% for the proportion of SiO_2 in the WIR. The loss in mass incurred on heating the WCAIR was significant, 11.50% of the WIR, and represented that portion of the WIR that was both acid insoluble and thermally unstable, such as, for example, cellulose. The IR absorption bands of the WCIASEH are tabulated in Table A2.5, together with those presented in the literature by two authors for samples of iron (III) oxyhydroxides heated to >300°C (Vlasov et.al., Yariv and Mendelovici). The good agreement between the IR absorption bands of WCIASEH and those of iron (III) oxyhydroxides heated to >300°C, and the XRD analysis of WCIASEH, confirmed WCIASEH to be largely Fe_2O_3. The

Table A2.5

Infrared absorption bands of WCIASEH

WCIASEH cm^{-1}	Vaslov et. al. cm^{-1}	Yariv and Mendelovici cm^{-1}
640	645	~630
550	540	543
480	475	468
440	445	~440

proportion of Fe in the WIR was, therefore, calculated to be 26.1%. It must be noted that this figure for the Fe content of the WIR can only be an approximation since the XRD pattern of the WCIASEH did, rather surprisingly, include two moderately intense lines at those d-spacings characteristic of metallic iron.

i) Magnetic extraction

A known weight of the WCIR was placed on one half of a previously weighed sheet of shiny paper. A magnet, covered with paper, was moved in the space above the solid such that the distance between it and the WCIR was never less than 1 cm. After collecting strongly magnetic particles, the magnet plus covering paper were moved to the other half of the shiny paper, at which point the magnet was lifted clear of its covering thereby allowing the water and chloroform insoluble residue, magnetic extract (WCIRME)(11.1% of WIR) to fall onto this half of the shiny paper. The WCIRME was significantly darker in colour than the non-magnetic portion of the WCIR.

The WCIRME was analysed by IR spectroscopy and XRD. An absorption of energy at 570 cm^{-1} indicated the presence of compounds with the ferrite structure, such as Fe_3O_4 (Grimes and Collett, Jirgensons). In complete agreement with this IR assignment, the XRD analysis displayed a good identification pattern for the inverse spinel structure of ferrite compounds (Wells). In view of the X-ray microanalysis of the WIR, it was possible to conclude that the WCIRME contained a high proportion of the inverse spinel structured ferrite compound of iron, Fe_3O_4. The XRD analysis of the WCIRME did contain a weak line at a d-spacing (2.03) characteristic of metallic iron. Thus, it was deduced that a small proportion of the WCIRME was metallic iron.

A known mass of the WCIRME was shaken with cold, conc. acid (HCl aq.) for 10 minutes. It was observed that a small portion of the WCIRME was insoluble in the acid, and apparently not magnetic. This acid insoluble non-magnetic portion was presumably wood or a wood product adhering to the magnetic particles, and was removed from the strongly acidic solution by filtration. The strongly acidic solution was neutralised with strong base (conc. NH_3 aq.) to yield a precipitate. This precipitate (oxyhydroxides of iron) was removed from solution by filtration, washed to remove NH_4Cl, placed in a crucible of known mass and heated to 800°C/900°C on a bunsen.

After cooling, the weight of the thermally produced oxide of iron, Fe_2O_3, was obtained. From a knowledge of the mass of Fe contained in the WCIRME and the proportion of the WIR that was magnetically extracted, it was possible to calculate the proportion of magnetic Fe (i.e., Fe incorporated in magnetic compounds) in the WIR as 7.0%. In view of the XRD analyses performed on the WIR and the WCIRME it was deemed reasonable to assume that the magnetic Fe in the WIR was occurring almost exclusively in the compound Fe_3O_4.

2.2.2.2. WWSC

Ion chromatographic analysis.

The ion chromatographic analysis, at an attenuation indicative of analyte concentrations in the 0.1 mmol dm^{-3} to 10 mmol dm^{-3} range, showed three closely grouped peaks occurring at short retention times. Peaks occurring at short retention times, in the ion chromatographic system employed, are usually generated by monovalent species such as (in elution order)

$$H_2PO_4^- \approx SO_3^- \approx HCO_3^- < Cl^- < NO_2^- \quad Br^- << NO_3^-$$

(retention time increasing across the series from left to right).

The retention time of the peak generated by the injection of a standard chloride solution (1 mmol dm^{-3}) was very similar to that for the second peak of the WWSC and thereby strongly suggested the presence of chloride at an estimated concentration of 0.790 mmol dm^{-3} (28 ppm Cl^-).

Although standard solutions of other common anions were also injected into the chromatographic system, it was not possible to positively identify the other two monovalent anions present. However, it can be stated that one of these anions was possibly $H_2PO_4^-$, or HCO_3^- while the other was possibly NO_2^- or Br^-, and that their concentration was in the range 0.1 mmol dm^{-3} to 10 mmol dm^{-3}.

3. CONCLUSIONS

3.1. Rust Nodules.

a) The rust nodules are heterogenous but principally composed of particles of naturally produced αFeOOH, in a relatively stable crystalline form,

and physically adsorbed water.

b) The surface of the rust nodules has a specific area of 26.8 m^2 g^{-1}, is non-porous, is free from non-iron contamination (other than a small amount of sulphur) and possesses a negative charge (indicative of a low surface hydroxyl content).

3.2. Sludge

The sludge is a dark brown, viscous slurry, 83.5% of which is water plus water soluble material, and is extremely heterogenous (or not stable over a period of several months).

3.2.1. WIR

a) The surface of the WIR has a specific area of 25.7 m^2 g^{-1}, is non-porous, and is largely composed of Fe with a small amount of Si and trace amounts of those elements which have a tendency to form cations (indicative of a negatively charged surface).

b) The WIR is principally composed of quartz (approx. 40%), magnetite and siderite, with other inorganic phases such as goethite (αFeOOH) and lepidocrocite (γFeOOH) also present.

c) A dark coloured, viscous chloroform extract (4.44%) is obtained consisting of about a dozen different compounds. Several structurally related compounds, constituting almost 40% of the extract, are branched alkanes having molecular formulae in the range $C_{27}H_{56}$ to $C_{37}H_{76}$. Another group of structurally related compounds constituting more than 10% of the extract, and having molecular masses in the range 300 to 500, also contain hydrocarbon structures but with the incorporation of one or more of the following entities:- an alicyclic side chain, a halide substituent, an hydroxyl group or a carboxyl group. There was evidence to suggest that several of the remaining unresolvable compounds of the extract contain organo-silicon-oxygen type structures. IR evidence for the presence of different types of carbonyl groups in the extract was not substantiated by NMR analysis.

d) The WIR contains the following:-

i) Physically adsorbed water (6.60%) and loses structural volatiles

representing 6.87%, 3.44% and 4.30% of the total mass of solid at 193.5°C, 242.5°C and 280°C up to 460°C, respectively. If the loss in mass at 246°C is the loss of structural water from FeOOH, then the proportion of compounds with this formula in the WIR is 33.9%.

ii) A chloroform insoluble component which undergoes oxidation in the temperature interval 150°C to 430°C and displays a DSC thermogram that is very similar to wood and wood products (such as cellulose). There was evidence for the presence of γFeOOH and Fe_3O_4.

iii) Base extractable constituents, viz., a high charged structure, phosphate, an organic structure prone to charring, and an organic structure that yields glycollic aldehyde upon its reaction with sulphuric acid. [If cellulose was present then the action of dilute base would have removed associated molecules such as lignin, acidic polysaccharides and proteins (Jirgensons)].

iv) Approx. 11.5% of an acid insoluble, thermally unstable portion, which is very possibly cellulose.

v) 11.1% of a darkly coloured, strongly magnetic material which is mostly Fe_3O_4 with small amounts of metallic iron and adhered non-magnetic, acid insoluble material.

vi) 7.0% and 19.1% of magnetic Fe and non-magnetic Fe, respectively. If the magnetic Fe is occurring exclusively in the compound Fe_3O_4, then the proportion of this inorganic phase is 9.7%.

The proportions of the components of the WIR are given in Table A2.6.

3.2.2. WWSC

Chloride is present at a concentration of 0.790 mmol dm^{-3} (28 μg cm^{-3}). Two other monovalent anions are also present at concentrations similar to that for chloride. One of these anions is possibly $H_2PO_4^-$ or HCO_3^- while the other is possibly NO_2^- or Br^-.

3.3. Piping

The piping is 'Grey' cast iron, having a wall thickness of approx. 1.2 cm

Table A2.6

The proportions of the components present in the WIR.

Component	Proportion %
a) SiO_2	~40.0
b) Total Fe	~26.1
c) Fe incorporated in non-magnetic compounds (identified as $FeCO_3$, $\alpha FeOOH$ and $\gamma FeOOH$)	~19.1
d) Total Si	18.7
e) Acid insoluble thermally unstable material (possibly cellulose)	~11.5
f) Strongly magnetic material (identified as mostly Fe_3O_4)	~11.1
g) Fe incorporated in magnetic compounds (identified as Fe_3O_4)	~ 7.0
h) Structural volatile I, volatilisation temp. 185°C (possibly incorporated in cellulose)	6.9
i) Physically adsorbed water	6.6
j) Chloroform extractable material; 40% are branched alkanes (C_{27} to C_{37}), 10% contain alkane structures plus a functional group, and several of the remaining compounds contain C-Si-O structures	4.4
k) Structural volatile III, volatilisation temp. 266°C to 460°C	4.3
l) Structural volatile II, volatilisation temp. 246°C (possibly incorporated in FeOOH)	3.4
m) Trace components, K, Al, Ti and base extractable (total) material:	< 5%
i) water soluble, highly charged structure	
ii) phosphate	
iii) an organic structure prone to charring	
iv) an organic structure that yields glycollic aldehyde upon its reaction with sulphuric acid.	

and a depth of corrosion, from the inside surface of the pipe, of 0.2 cm.

REFERENCES

Budzikiewicz, H., Djerassi, C., and Williams, D.H., "Interpretation of Mass Spectra of Organic Compounds", Holden-Day, San Francisco, 1964.

Chaklader, A.C.D., and Blair, G.R., J. Thermal Anal., 2, 165 (1970).

Cornu, A., and Massot, R.,"Compilation of Mass Spectral Data", Heyden, London, 1966.

Estep, P.A., Kovach, J.J., Karr, C., Childers, E.E., and Hiser, A.L., Am. Chem. Soc. Div. Fuel Chem. Prepr., 13, 1, 18 (1969).

Grimes, N.W., and Collett, A.J., Nature, 230, 158 (1971).

Holness, H., "Advanced Inorganic Qualitative Analysis by Semi-micro Methods", Pitman, London, 1957.

Jirgensons, B., "Natural Organic Macromolecules", Pergamon, London, 1962.

Kalinskaya, T.V., Lobanova, L.B., Pologikh, I.V., and Kotikov, V.A., Zh. Prikl, Khim., 53, 9, 2097 (1980).

Paterson, E., Anal. Proc. (London), 17, 6, 234 (1980).

Paterson, E., and Swaffield, R., J. Thermal Anal., 18, 161 (1980).

Pourbaix, M., Int. Corros. Conf. Ser. 1971, NACE-3 (Localised Corros.), 12 (1974).

Ross, T.K., "Engineering Design Guides 21 Metal Corrosion", Oxford University Press, 1977.

Russell, J.D., Parfitt, R.L., Fraser, A.R., and Farmer, V.C., Nature, 248, 220 (1974).

Shokarev, M.M., Margulis, E.V., Vershinina, F.I., Beisekeera, L.I., and Sarchenko, L.A., Zh Neorg. Khim., 17, 9, 2474 (1972).

Smalley, R.F., and Wakefield, B.J., in "An Introduction to Spectroscopic Methods for the Identification of Organic Compounds", Scheinmann, F., Editor, Vol. 1, Pergamon, Oxford, 1970.

Subrt, J., Hanousek, F., Zapletal, V., Lipka, J., and Hucl, M., J. Thermal Anal., 20, 61 (1981).

Suzuki, I., Hisamatsu, Y., and Masuko, N., J. Electrochem. Soc., 127, 2210 (1980).

Tang, W.K., in "Differential Thermal Analysis", Mackenzie, R.C.; Editor, 2, Chap. 45, Academic Press, London, 1972.

Taylor, D.G., Nenadic, C.M., and Crable, J.V., Amer. Ind. Hyg. Ass. J., 31, 1, 100 (1970).

Vlasov, A. Ya., Loseva, G.V., Sakash, G.S., and Solntseva, L.S., Zh. Prik. Spectrosk., 12, 6, 1130 (1970).

Vogel, A.I., "A Text-Book of Macro and Semimicro Qualitative Inorganic Analysis", 4th Edition, Longmans; London, 1969.

Wehrli, F.W., and Wirthlin, T., "Interpretation of Carbon -13 NMR Spectra", Heyden, Bristol, 1976.

Wells, A.F., "Structural Inorganic Chemistry", 4th Edition, Oxford . University, London, 1975.

Williams, D.H., and Fleming, I., "Spectroscopic Methods in Organic Chemistry", 2nd Edition, Chap. 3, McGraw-Hill, London, 1973.

Yariv, Sh. and Mendelovici, E., Appl. Spectros., 33, 4, 410 (1979).

CHAPTER A3

A STUDY OF THE STRUCTURAL CHANGES THAT TAKE PLACE WHEN αFeOOH IS THERMALLY DEHYDRATED TO αFe_2O_3.

1. INTRODUCTION

The αFeOOH crystal structure undergoes thermally induced dehydration to αFe_2O_3 without any major breakdown of the atomic patterns (Francombe and Rooksby). In particular, the framework of hexagonally close-packed hydroxyl/oxygen ions of αFeOOH suffers comparatively little disturbance during the transformation. Thus, the majority of the atomic positions in αFeOOH and αFe_2O_3 are substantially the same, and, for example, the X-ray diffraction (XRD) profiles before and after dehydration show a common orientation with the (100), (010) and (001) directions of αFeOOH becoming the (001), (010) and 210) directions, respectively, of αFe_2O_3 (Dasgupta). Accordingly, the change from αFeOOH to αFe_2O_3 is considered a (two-phase) topotactic transformation (Bernal). [A characteristic of a topotactic transformation is that the new phase is usually formed at a temperature far below its melting point or even its normal recrystallisation temperature. Consequently, such a phase cannot show normal crystal growth and is likely to be small-grained, heavily distorted or both (Bernal).]

1.1. The manifestations of the structural changes.

1.1.1. Topotaxy.

The topotactic nature of the αFeOOH→ αFe_2O_3 transformation is exhibited visually, in that a single crystal of αFeOOH appears outwardly to retain its single-crystal form during dehydration. However, a small change in volume is expected to occur during the transformation on the basis of the relationship between the unit cell dimensions of αFeOOH (a_G, b_G and c_G) and those of αFe_2O_3 (a_H and c_H) (Lima-de-Faria). Since the molecular unit cell contents of αFeOOH and αFe_2O_3 are four and six, respectively, then every nine unit cells of αFeOOH will correspond to three unit cells of αFe_2O_3. Thus, according to the orientational relationship of the transformation, a slight contraction (0.09%), a slight expansion (1.29%) and a measurable contraction (3.60%) are expected along the a_G, b_G and c_G directions, respectively; such changes arising from the non-zero values of the differences

$$(3a_G - c_H)$$

$$(b_G - 2a_H)$$

and $$(3c_G - a_H\sqrt{3}).$$

1.1.2. XRD non-uniform line-broadening.

The material produced from αFeOOH immediately after dehydration gives an αFe_2O_3 - like XRD profile but some lines are sharp and some are broad (Brindley and Brown); for example, the lines arising from (110), (113) and (116) reflections give rise to sharp lines, while (102), (104) and (204) reflections are very broad (Rendon et.al.). On further heating, the reflections gradually produce sharper lines until at ca. 800°C the typical profile of αFe_2O_3 is observed. This unusual line-broadening effect has been attributed by Francombe and Rooksby to the formation of a super-lattice (referred to an hexagonal anion lattice sub-unit), which is common to both αFeOOH and αFe_2O_3. Thus immediately after dehydration the ordering of Fe^{3+} ions in the structure is incomplete so that the superlattice required to perfect the αFe_2O_3 arrangement is not yet fully developed. However, according to Watari et.al. the effect of an incomplete Fe^{3+} ion arrangement would lead to a change of peak position and intensity as well as the occurrence of new (superlattice) reflections, other than those of αFe_2O_3. These authors found constant peak intensities and no non-αFe_2O_3 peaks throughout the heating temperature range. Watari et.al. explain the phenomenon of non-uniform line broadening in terms of twin formation in αFe_2O_3 and that the initial dehydration product is already the final product, αFe_2O_3; in this event, the peak positions will remain constant but broadening will occur. These authors explain that there are two equivalent possibilities for the arrangement of the cations, namely the obverse and reverse twins of αFe_2O_3. Thus, the appearance of a peak in the αFe_2O_3 XRD profile depends on whether the reflections giving rise to that peak belong to only one of the twin crystallites (non-common reflections) or are common to both (common reflections); non-common reflections (observed at the Miller ℓ indice values not equal to 3n) will give rise to line broadening because the X-rays diffracted by each crystallite are out-of-phase with each other. Furthermore, Watari et.al. interpret the observed change of peak width with dehydration temperature as an increase of the αFe_2O_3 crystallite size, effected by surface diffusion and coalescence.

1.1.3. The development of pore structure.

αFeOOH exhibits an increase in surface area when heated to temperatures in the range 200 to 450°C. However, beyond this temperature range a gradual decline in surface area is observed, until at ca. 800°C the

αFe_2O_3 product so formed may have a surface area about one-quarter of that of the original αFeOOH. Electron microscopic studies (Hirokawa et.al.) of αFeOOH heated to between 200 to 300°C have clearly shown the presence of micropores in the dehydrated microcrystals, while the overall shape of such microcrystals has been observed to remain essentially unchanged. Furthermore, this microporosity has been manifested in the development of hysteresis loops, i.e., low pressure retention, in the low temperature N_2 sorption isotherms (Rendon et.al.) of these dehydrated products. Thus, it has become accepted that the surface area increase observed on heating αFeOOH is due to micropore formation. Rendon et.al. have observed these micropores to be slit-shaped, of width about 1.4nm, with their longest axis running parallel to the elongated direction (i.e., the c_G direction or the 110 direction of αFe_2O_3) of the heated acicular microcrystals; the distance between slits was determined to be less than 3nm. Rendon et.al., Duvigneaud and Derie attribute the reduction in surface area observed on heating αFeOOH to progressively higher temperatures to the transformation of the microcrystal pore structure to a closed, spherical mesopore structure; t-plots (Rendon et.al.) corroborate the absence of micropores above 300°C. Such a transformation in pore structure with increasing temperature can be readily attributed to the occurrence of internal sintering.

Interestingly, Garcia-Gonzalez et.al. have shown that the porosity of the dehydrated product of αFeOOH is dependent upon the atmosphere in which the dehydration process occurred. These authors found that the dehydration of αFeOOH in an atmosphere of N_2 or in a vacuum yielded a microporous product, while an essentially non-porous product was formed if the αFeOOH dehydration was conducted in an atmosphere of water vapour. Garcia-Gonzalez et. al. conclude that the presence of water vapour modifies the process of water diffusion in the αFeOOH structure.

1.1.4. Changes in infrared (IR) absorption frequencies.

The initial dehydration product of αFeOOH, formed by heating to temperatures below 600°C, is a multidomain of extremely small, poorly crystallised particles (Yariv and Mendelovici). If the dimensions of a polar crystal are not very large compared to the IR phonon wavelength, then the frequencies of IR-active lattice mode vibrations are dependent on particle size and shape (Ruppin and Englman). Thus, a departure from bulk-mode

frequencies is expected (Farmer and Russell) for the extremely small, initial dehydration product of αFeOOH, and only absorptions due to surface modes should appear in its IR spectrum (Ruppin and Englman); these absorptions lying between the crystal transverse and longitudinal absorptions.

The crystallinity of the initial dehydration products of αFeOOH improves with increasing formation temperature, but the particle size and shape of such products, formed at temperatures up to 600°C, are very similar (Rendon and Serna). Consequently, the IR spectra of such products are also very similar and the only effect of temperature is a sharpening of the absorption bands (Yariv and Mendelovici). At temperatures between 600°C and 900°C crystallisation is virtually complete, i.e., the αFe_2O_3 structure of the dehydration product is perfected (Yariv and Mendelovici), and the αFeOOH-shaped particle morphology (acicular) has disappeared, whilst interparticle sintering takes place in this temperature range leading to an heterogeneity in particle size and shape (Rendon et.al.). Importantly, the difference in particle size and shape of dehydration products formed either below or above ca. 600°C is manifested as a difference between the IR spectra of such products. Thus, the values of the important band frequencies and general appearance of the IR spectrum of an αFeOOH dehydration product will depend upon the temperature of formation and the general heat treatment employed. This dependency has led to the appearance in the literature of many discrepancies on the wavenumber values of the characteristic IR absorption bands of αFeOOH dehydration products (McDevitt and Baun, Liese, Schwertmann and Taylor, Bogdanovitch et.al., Estep).

2. THEORY

2.1. The application of XRD.

Information such as unit cell dimensions, non-uniform line-broadening, crystallite size, crystal strain and the estimation of phase concentration can be obtained from an XRD study of a powder synthetically prepared from high purity reagents. Single crystal diffraction techniques can give information which is of particular relevance to topotactic changes. In this study accurate crystallographic information was obtained by the XRD analysis of powder specimens; the topotactic nature of the dehydration of αFeOOH was not studied.

2.1.1. The relationship between the dimensions of the orthorhombic αFeOOH unit cell, and the hexagonal αFe_2O_3 unit cell, and the measured Bragg angles.

The relationship between a_G, b_G and c_G of the αFeOOH orthorhombic unit cell and the measured Bragg angle $\theta_{(hk\ell)}$ (where $hk\ell$ are the Miller indices) is (D'eye and Wait)

$$\frac{4 \sin^2\theta_{(hk\ell)}}{\lambda^2} = \frac{h^2}{a_G^2} + \frac{k^2}{b_G^2} + \frac{\ell^2}{c_G^2} \qquad \text{A3.1}$$

Combining this with the Bragg equation gives the perpendicular spacing ($d_{(hk\ell)}$) for any plane of Miller indices ($hk\ell$) in the αFeOOH orthorhombic unit cell:

$$\frac{1}{d^2_{(hk\ell)}} = \frac{h^2}{a_G^2} + \frac{k^2}{b_G^2} + \frac{\ell^2}{c_G^2} \qquad \text{A3.2}$$

For the series of planes of Miller indices (0k0) and 00ℓ), eqn. A3.2 becomes respectively,

$$\frac{1}{d^2_{(0k0)}} = \frac{k^2}{b_G^2} \qquad \text{A3.3}$$

and

$$\frac{1}{d^2_{(00\ell)}} = \frac{\ell^2}{c_G^2} \qquad \text{A3.4}$$

Similarly, $d_{(hk\ell)}$ for any ($hk\ell$) plane in the αFe_2O_3 hexagonal unit cell is given by (hexagonal indexing) (D'eye and Wait)

$$\frac{1}{d^2_{(hk\ell)}} = \frac{4(h^2 + hk + k^2)}{3a_H^2} + \frac{\ell^2}{c_H^2} \qquad \text{A3.5}$$

for the series of planes of Miller indices (h00) eqn. A3.5 becomes

$$\frac{1}{d^2_{(h00)}} = \frac{4h^2}{3a_H^2} \qquad \text{A3.6}$$

In this study b_G and c_G values were readily obtained from $d_{(060)}$ and $d_{(002)}$ spacings, respectively, using eqns. A3.3 and A3.4, while a_G values were obtained by means of eqn. A3.2. Similarly, a_H values were readily obtained from $d_{(300)}$ spacings using eqn. A3.6, while c_H values were obtained by means of eqn. A3.5.

2.1.2. XRD line profile analysis (XRDLPA).

XRDLPA is a technique to extract information on the microstructure of crystalline material from the shape of peaks in an XRD profile.

All XRD peaks are broadened to a minor extent by instrumental effects such as diffractometer broadening, the presence in the X-ray spectrum of the K_α doublet, and the surface roughness of (and absorption by) the specimen. However, significant broadening of all, or some, of the peaks of the XRD profile of a specimen can occur if its crystal structure contains any one, or a combination of, the following imperfections:- small crystallite size (< 1 μm), lattice distortions (for example, microstrain from mechanical deformation or concentration variations), stacking faults or microtwins. Thus, the XRD profile of a specimen which contains such crystal imperfections will contain peaks whose shape (i.e., the extent of broadening) has been influenced by both instrumental effects and crystal imperfections. In a mathematical sense the observed (or analysed) profile (called the ~~h~~-profile) is the result of an instrumental dependent profile (called the g-profile) and a structural profile (called the f-profile), such that (Delhez)

$$\text{~~h~~} = g + f \qquad \text{A3.7}$$

The individual contributions of two structural line-broadening effects, viz., small crystallite size and lattice distortions, to the parameters of the f-profile can be obtained on the basis of an assumption concerning the shape of the profile resulting from each effect. From practical experience it has become clear that a small crystallite size often yields a Cauchy-shaped profile, whereas a Gaussian-shaped profile is often found to be the result of lattice distortions (Delhez). This implies that the f-profile resulting from both effects can be described by a convolution of Cauchy and Gaussian functions, i.e., a Voigt function; it is further

assumed that the g and h-profiles can also be represented sufficiently accurately by Voigt functions. The assumption concerning the shape of profiles resulting from structural imperfections is the basis of a Voigt deconvolution method (approximate, single-line method) developed by Langford. In this method, which is very useful for comparing analogous specimens, the shape of a Voigt function can be described by its peak width at half maximum height ($2W_{\frac{1}{2}}$) and its integral breadth (β). Then, the integral breadth of the Cauchy part of the Voigt function, describing the f-profile, is given by

$$\beta_C^f = \beta_C^h - \beta_C^g \qquad \text{A3.8}$$

and the integral breadth of the Gaussian part of the Voigt function, describing the f-profile, is given by

$$\beta_g^f = \beta_g^h - \beta_g^g \qquad \text{A3.9}$$

Thus, from measurement of $2W_{\frac{1}{2}}$ and β of each g (i.e., $2W_{\frac{1}{2}}^g$ and β^g) and h (i.e., $2W_{\frac{1}{2}}^h$ and β^h) profile the integral breadths of the Cauchy (i.e., β_C^g and β_C^h) and Gaussian (i.e., β_g^g and β_g^h) components of the Voigt function describing the f-profile can be obtained using the empirical equations

$$\beta_C = \beta\left[2.0207 - 0.4803\left(\frac{2W_{\frac{1}{2}}}{\beta}\right) - 1.7756\left(\frac{2W_{\frac{1}{2}}}{\beta}\right)^2\right] \qquad \text{A3.10}$$

and

$$\beta_g = \beta\left[0.642 + 1.4187\left[\left(\frac{2W_{\frac{1}{2}}}{\beta}\right) - \frac{2}{\pi}\right]^{\frac{1}{2}} - 2.2043\left(\frac{2W_{\frac{1}{2}}}{\beta}\right) + 1.8706\left(\frac{2W_{\frac{1}{2}}}{\beta}\right)^2\right] \qquad \text{A3.11}$$

[An appropriate g-profile can be obtained from an XRD analysis of a highly crystalline, strain-free, specimen, such as NaCl.] Finally, the magnitudes of the two structural line-broadening effects are given by the volume averaged crystallite size (also called the size of the scatterer) ($\overline{D}$) and the mean lattice distortion (or microstrain) ($\overline{E}$) using the relations

$$\overline{D} = \frac{K\lambda}{\beta_C^f \cos\theta_{(hk\ell)}} \qquad \text{(Scherrer)} \qquad \text{A3.12}$$

$$\text{and} \quad \overline{E} = \frac{\beta_g^f}{4 \tan \theta_{(hk\ell)}} \qquad \text{A3.13}$$

(β in radians)

In this study, the Cauchy and Gaussian integral breadths were calculated by the insertion of the measured $2W_{\frac{1}{2}}$ and β of each recorded profile into both eqn. A3.10 and eqn. A3.11. Then, the Cauchy and Gaussian integral breadths of the f-profiles were obtained using eqns. A3.8 and A3.9, while values of $\overline{D}$ and $\overline{E}$ were obtained by insertion of the appropriate f-profile integral breadth into eqns. A3.12 and A3.13.

2.1.3. The estimation of phase concentration.

For an homogenous specimen containing a phase i, of linear mass absorption coefficient μ_i, and other (remaining) phases Rem, of linear mass absorption coefficient μ_{Rem}, the weight fraction w_i is related to the intensity $(I_{(hk\ell)})_i$ and the intensity of pure i $(I_{(hk\ell)})_{ip}$ by the equation (Jenkins and de Vries)

$$w_i = \frac{\dfrac{(I_{(hk\ell)})_i}{(I_{(hk\ell)})_{ip}} \quad \mu_{Rem}}{\mu_i - \left[(I_{(hk\ell)})_i \, (\mu_i - \mu_{Rem}) \Big/ (I_{(hk\ell)})_{ip}\right]} \qquad \text{A3.14}$$

For $\mu_i = \mu_{Rem}$, eqn. A3.14 becomes

$$w_i = \frac{(I_{(hk\ell)})_i}{(I_{(hk\ell)})_{ip}} \qquad \text{A3.15}$$

In this study the weight fractions of $\alpha FeOOH$ in specimens having no XRD-detectable αFe_2O_3 were calculated using eqn. A3.15. Similarly, the weight fractions of αFe_2O_3 in specimens having no XRD-detectable $\alpha FeOOH$ were also calculated using eqn. A3.15. For those specimens containing XRD-detectable quantities of both $\alpha FeOOH$ and αFe_2O_3, however, the weight fractions of $\alpha FeOOH$ and αFe_2O_3 were calculated by means of eqn. A3.14.

2.2. The evaluation of pore structure from an analysis of gas adsorption data.

2.2.1. Capillary condensation.

When a solid containing pores is exposed to an increasing pressure of vapour adsorbate an adsorbed layer is built up on exposed surfaces. The adsorbed layer on the non-porous surfaces of the solid will be many molecules thick and condensation of the vapour adsorbate will occur when the saturated vapour pressure (p_{SAT}) is reached. However, the thickness of the adsorbed layer on the surfaces (or walls) of the pores will be limited to the width of the pores. In this event, capillary condensation of vapour adsorbate is believed to occur onto an existing adsorbed layer (Gregg and Sing) when the pressure of the adsorbate reaches a value significantly below p_{SAT}. Conversely, when a solid containing pores is exposed to a decreasing pressure of adsorbate the bulk liquid within the pores will not begin to evaporate until the pressure of the adsorbate reaches a value that is, once again, significantly below p_{SAT}. Thus, the presence of pores in a solid can modify both the adsorption and desorption of a gas onto and off the solid, and cause a departure from BET (i.e., Brunauer et.al. 1938) behaviour.

The relationship between the pressure p at which condensation of N_2 vapour to bulk liquid (of surface tension γ and molar volume $Vol_M^{N_2}$) takes place on a curved surface (eg. the liquid meniscus in a pore) and the radius of curvature of that surface is given by the Kelvin equation; this equation also gives the relationship between the pressure at which evaporation of bulk liquid to vapour takes place on a curved surface and the radius of curvature of that surface. Huckel provides a rigorous derivation of this equation for a curved surface of principal radii r_1 and r_2 (at right angles) which leads to

$$RT \ln\left[\frac{p_{SAT}}{p}\right] = \gamma Vol_M^{N_2}\left(\frac{1}{r_1} + \frac{1}{r_2}\right) + Vol_M^{N_2}(p_{SAT} - p) \qquad A3.16$$

If the second term of eqn. A3.16 is neglected and the angle of contact (Ø) between the bulk liquid and the curved surface substituted (Dollimore and Heal 1978), then

$$RT \ln\left[\frac{p_{SAT}}{p}\right] = \gamma \, Vol_M^{N_2} \cos\phi \left(\frac{1}{r_1} + \frac{1}{r_2}\right) \qquad A3.17$$

In order to apply eqn. A3.17 to the condensation/evaporation at the curved meniscus in pores of radius r_p a geometrical shape has to be assumed for the pores. From this assumption, the shape of the meniscus at the mouth of the pores can be deduced. The most common pore shape assumed is cylindrical, which then has a hemispherical meniscus at the pore mouth such that $r_1 = r_2$; eqn. A3.17 becomes, therefore,

$$\ln\left[\frac{p}{p_{SAT}}\right] = -\frac{2\gamma \, Vol_M^{N_2}}{r_1 RT} \cdot \cos\phi \qquad A3.18$$

When allowance is made for the existing adsorbed layer of thickness t, then

$$\ln\left[\frac{p}{p_{SAT}}\right] = -\frac{2\gamma \, Vol_M^{N_2}}{r_{KC} RT} \cdot \cos\phi \qquad A3.19$$

which is known as the Kelvin equation; where r_{KC} is commonly referred to as the "core" condensate inside the pore (equal to the difference r_p - t). If the pores are assumed to be slit shaped then a point on the surface of the meniscus of such a pore has two principal radii of curvature (at right angles), one equal to the radius of the "core" condensate (r_{KS}) and the other to infinity. Then eqn. A3.17 becomes

$$\ln\left[\frac{p}{p_{SAT}}\right] = -\frac{\gamma \, Vol_M^{N_2}}{r_{KS} RT} \cdot \cos\phi \qquad A3.20$$

Since, the width (d_{KS}) of the core condensate is equal to $2r_{KS}$, the Kelvin equation for this shape of pore is usually expressed as

$$\ln\left[\frac{p}{p_{SAT}}\right] = -\frac{2\gamma \, Vol_M^{N_2}}{d_{KS} RT} \cdot \cos\phi \qquad A3.21$$

[The negative sign of the Kelvin equation implies that p will be lower than p_{SAT} if $\phi < 90°$ (Gregg and Sing) i.e., the vapour pressure over a liquid contained in a pore will be lower than that over a plane surface of the liquid at the same temperature.]

In order to make quantitative use of the Kelvin equation it is necessary to assign a value to ϕ, a quantity which is extremely difficult to determine for porous solids (Gregg and Sing). To make progress it is usual to make the simplifying, though not always justified, assumption that $\phi = 0$ i.e., that the bulk liquid wets the walls of the pores.

For a solid containing pores that are neither cylindrical nor slit shaped the relationship between r_{KC} and the pore size parameter or parameters, which describe the actual pores, can be worked out from geometrical principles (Everett).

In this study r_{KC} (equivalent to d_{KS}) was calculated using eqn. A3.19 (analogous to eqn. A3.21), with ϕ set to zero.

2.2.2. The t-plot analysis of gas adsorption data.

The porosity of a solid adsorbent may be qualitatively assessed by means of the t-plot method of Lippens and de Boer. Furthermore, if a solid adsorbent is assessed to contain a degree of microporosity then this method can give quantitative information regarding the micropores of such an adsorbent. The t-plot method involves the use of a reduced isotherm, where V is plotted as a function of t. The reduced isotherm of a non-porous adsorbent, on which adsorption has resulted entirely from the formation of physically adsorbed layers of adsorbate molecules, will be a straight line passing through the origin with a slope proportional to the surface area (S_t^{TOT}) of the solid:

$$S_t^{TOT} = \mathcal{F} \cdot \frac{\Delta V}{\Delta t} \qquad \text{A3.22}$$

[If t is the statistical thickness of the adsorbed layer on a non-porous reference solid, rather than that given empirically (see later), then an equality between S_{BET} and S_t^{TOT} will indicate a correctness in the choice of the non-porous reference solid.] The reduced isotherm of a porous

solid will, however, show characteristic deviations from an initial linear plot, passing through the origin, with the possible occurrence of valuable (extrapolated) intercepts on the ordinate or absissa; such non-linearity is a qualitative assessment of porosity. These deviations appear as a change in slope at a particular t value (t_I) i.e., a change in the rate at which vapour is adsorbed for a given change in pressure, and are due to the onset of capillary condensation of vapour adsorbate into pores having a radius, or width related to t_I. Thus, the radius of the cylindrical pores of a material will be equal to t_I, whereas for a material possessing slit-shaped pores of width d the value of t_I will be equal to $^d/_2$. An upward deviation (enhanced adsorption) corresponds to the onset of capillary condensation of vapour into mesopores, whereas a downward deviation (depressed adsorption) corresponds to the onset of condensation into micropores. Thus, the reduced isotherm of a solid possessing a degree of microporosity will have an initial straight line (TOT) passing through the origin and intersecting, at t_I, with another straight line (MICR) of different slope. The slope of the line TOT will, as for a non-porous solid, be proportional to S_t^{TOT}, which in this case is the sum of the area (S_t^{Ex}) of the external surface of the solid plus the surface area (S^{MICR}) of the pores. S_t^{Ex} can be directly obtained from the slope of the line MICR. To avoid any uncertainty in S_t^{TOT}, S^{MICR} is usually obtained from S_{BET}:

$$S^{MICR} = S_{BET} - S_t^{Ex} \qquad \text{A3.23}$$

The intercept of the line MICR to the ordinate will be equal to the volume of the micropores (V_t^{MICR}). The dimension (L_p) of the micropores can be obtained from the ratio $2V_t^{MICR}/S^{MICR}$, and this will be equal to t_I or $2t_I$ depending upon whether the pores have a cylindrical geometry or are slit-shaped, respectively.

2.2.2.1. Estimation of t.

The most direct way of estimating t is to measure the desorption isotherm on a non-porous reference substance having a surface as nearly identical in nature as possible with the porous solid in question; in this way it is assumed that, at the same pressure, the thickness of the adsorbed layer on the non-porous solid is the same at that on the porous solid. Then, t is the product of the average thickness t_{MONO} of a single layer of adsorbed

molecules and the number (n) of such layers:

$$t = nt_{MONO} \qquad \text{A3.24}$$

If the volume of gas adsorbed (at STP) is V and the volume of a single layer of adsorbed gas is V_{MONO} then

$$t = \frac{V}{V_{MONO}} \cdot t_{MONO} \qquad \text{A3.25}$$

For the case of adsorbed N_2, Lippenset.al. obtained a value of 0.354 nm for t_{MONO} by assuming an hexagonal close packing of adsorbate molecules of area 0.162 nm^2 in the successive molecular layers of the adsorbed film; this value is supported by the work of Dollimore and Heal 1970.

Wheeler suggested that the adsorption on the walls of fine pores is probably greater than on an open surface at low relative pressure; he therefore proposed the use of the Halsey equation in the form

$$t = t_{MONO} \left(\frac{-5}{\ell n \left[\frac{p}{p_{SAT}} \right]} \right)^{\frac{1}{3}} \qquad \text{A3.26}$$

In this study t values were estimated both by the Halsey equation (eqn. A3.26) and eqn. A3.25 in which volumetric values were obtained from a non-porous αFeOOH. The choice of the most appropriate estimation of t-values was made by comparison of the derived surface areas with corresponding BET areas.

2.2.3. Estimation of pore size distribution.

The estimation of pore size distribution is complicated by the fact that after the loss of condensed liquid from pores, a multilayer film is left behind. Thus, a pore is not truly emptied in a desorption step and the real pore volume has to be calculated from the apparent pore volume by allowing for the adsorbed film left behind.

An estimation of the distribution of the different sized pores of a porous solid can be made from desorption isotherm data, i.e., V at $\frac{p}{p_{SAT}}$, by application of the method of Gregg and Sing. [It is common practice to estimate a pore size distribution from desorption isotherm data on the grounds that this data, in preference to adsorption isotherm data, is more likely to correspond to a condition of true equilibrium (Gregg and Sing). Furthermore, Cohan has shown that adsorption condensation occurs at a cylindrical meniscus (i.e., $r_1 \neq r_2$), whereas desopption takes place from a spherical meniscus (i.e., $r_1 = r_2$) to which the Kelvin equation is readily applicable.] Thus, for each reduction in p (more commonly called a step down the desorption isotherm) the following, in conjunction with a calculated r_{KC} value (by means of eqn. A3.19) and an estimated t value (see earlier), can be calculated:- the total decrement in the amount adsorbed (ΔV), r_p, the mean values $\bar{r}_{KC}$ and $\bar{r}_p$, the diminution in film thickness (Δt), and the change in pore radius (Δr_p). The decrement in the amount of capillary condensed material (ΔV_K) is given by the difference ($\Delta V - \Delta V_f$); where ΔV_f is the amount desorbed from the film on the pore walls during a desorption step. ΔV_K is related to the decrement in pore volume (ΔV_p) by

$$\Delta V_p = \Delta V_K \left(\frac{\bar{r}_p}{\bar{r}_{KC}} \right)^2 \qquad \text{A3.27}$$

If the shape of the pores is assumed to be cylindrical, then the area of the pore walls (ΔS_p), corresponding to the decremental volume ΔV_p, is given by

$$\Delta S_p = 2 \mathcal{H} \frac{\Delta V_p}{\bar{r}_p} \qquad \text{A3.28}$$

whereas if the pores are assumed to be slit shaped, then

$$\Delta S_p = 2 \mathcal{H} \frac{\Delta V_p}{d} \qquad \text{A3.29}$$

where $d = d_{KS} + 2t$. The summation of the individual decrements ΔS_p up to the desorption step x in the pore size distribution calculation is related to the ΔV_f of step (x + 1) by

$$\Delta V_f = 0.064 \Delta t \lesssim \Delta S_p \qquad \text{A3.30}$$

Thus, the calculation of ΔV_K at the first desorption step (x = 1) requires, via ΔV_f, a knowledge of $\lesssim \Delta S_p$. In practice it is usually adequate to assume that $\lesssim \Delta S_p = 0$ at the highest relative pressure, so that $\Delta V_f = 0$ for the first desorption step. The calculation is usually stopped when, either, the step-by-step summation $\lesssim \Delta V_p$ exceeds V^{TOT}, or at the lower limit of the mesopore size range where eqns. A3.28 and A3.29 are still applicable (Dollimore and Heal 1978). Then, for each desorption step, the decrement in pore volume expressed as a liquid (Δv_p) is obtained from ΔV_p by means of the factor $\mathcal{F}$, and the distribution of pore sizes is given by a plot of $\Delta v_p / \Delta r_p$ as a function of $\bar{r}_p$. In addition, the summation of the individual decrements ΔV_p and ΔS_p in the mesopore size range gives the mesopore volume (V_p^{MESO}) and surface area (S_p^{MESO}), respectively.

In this study the method of Gregg and Sing was used to estimate the distribution of differently sized mesopores from desorption isotherm data.

2.3. The IR absorption spectroscopy of αFeOOH and the products of its thermal treatment.

In the early stages of the dehydration of αFeOOH, ca. 235°C, there is a monotonic reduction in the intensity of the OH stretching (at ca. 3150 cm^{-1}) and bending (at 892 cm^{-1} and 795 cm^{-1}) bands as OH groups are lost from the αFeOOH structure (Vlasov et.al.). The IR spectrum of the dehydration products formed at temperatures below 600°C is characterised (in the range 1000 cm^{-1} to ca. 390 cm^{-1}) by two strong absorption bands at 530 cm^{-1} and 445 cm^{-1}, which Farmer has assigned as O^{2-} displacements. There are also two weak absorption bands in the IR spectra of such products, at about 650 cm^{-1} and 400 cm^{-1}, and Wilson et.al. have shown that the vibrations giving rise to these absorptions occur parallel to the C_H axis of the αFe_2O_3 unit cell; Wilson et.al. have also shown that the 530 cm^{-1} and 445 cm^{-1} absorption bands are due to vibrations that are perpendicular to the C_H axis. On the basis of these features, Rendon et.al. have suggested

that the acicular crystals observed by electron microscopy have really a lath-like morphology, with their thickness much smaller than the other two dimensions.

In the IR spectra of dehydration products formed at temperatures above 600°C the 530 cm^{-1} and 445 cm^{-1} bands are shifted to higher frequencies (i.e., 543 cm^{-1} and 486 cm^{-1}, respectively) (Yariv and Mendelovici), whereas the 650 cm^{-1} and 400 cm^{-1} bands are shifted to lower frequencies on the disappearance of the acicular (or lath-like) morphology (Rendon et.al.).

2.4. The mechanism of dehydration.

Although the crystal structures of αFeOOH and its eventual dehydration product (αFe_2O_3) are very similar as regards the oxygen framework (see section 6.), on dehydration one quarter of the oxygen atoms must leave the αFeOOH structure (Mackay). Whether this happens regularly, by the coalescence of layers, or by the total destruction of certain regions of the crystal, with the migration of Fe^{3+} ions into (and H^+ ions out of) the remainder, is not clear.

Two main types of mechanism have been proposed to explain the dehydration process (Lima-de-Faria) a) an homogenous mechanism in which water is considered to be lost uniformly from all parts of the crystal (Goodman), and b) an inhomogenous mechanism in which water is only released from certain regions of the crystal (called donor regions), other parts of the same crystal (called acceptor regions) preserving the oxygen close-packed structure (Ball and Taylor); in the donor regions water is lost by the combination of the hydroxyls with the protons that have migrated from the acceptor regions, and, consequently, the donor regions gradually transform into pores.

In an homogenous mechanism the loss of water from all parts of the αFeOOH crystal structure can hardly be expected to cause only a little disturbance to the framework of hexagonally close-packed hydroxyl/oxygen ions. The inhomogenous mechanism, which is based on the stability of the oxygen close-packed framework, appears, therefore, as the more appropriate to describe the $\alpha FeOOH \rightarrow \alpha Fe_2O_3$ transformation. Two implications of the inhomogenous mechanism are pore formation and proton migration. The occurrence of the latter event is supported by the reasonable agreement between the activation energy for the dehydration process, 82.8 kJ mol^{-1} (Lima-de-Faria), and the

activation energy for the diffusion of protons, 69.0 kJ mol^{-1} (Feitknecht et.al.).

3. METHOD

700 mg quantities of a prepared αFeOOH (the preparation is given in Chapter A1) were heated from ambient to several temperatures up to 850°C, at a heating rate of 20°C $minute^{-1}$. The quantities of αFeOOH were contained in platinum crucibles, heated in a dynamic atmosphere of air (25 $cm^3 . minute^{-1}$) and allowed to cool ballistically. In this way products were formed at each of the following temperatures:- 250, 300, 350, 375, 400, 425, 450, 500, 705 and 850°C. The identifying nomenclature of the products, used hereafter, indicates both the preheat-treatment temperature reached in their production and the principal phases as indicated by XRD, i.e., G (for αFeOOH) and/or H (for αFe_2O_3). [The prepared (unheated) αFeOOH is also treated as a product and designated amb. G.]

The products were submitted to XRD, the low temperature sorption of N_2, and IR absorption spectroscopy. In addition, the products formed at 400 and 850°C were submitted to scanning electron microscopy (SEM). XRD profiles of the products and (as a reference) a highly crystalline solid (NaCl) were measured with Cu K_α radiation, while the low temperature sorption of N_2 by a product was measured in a conventional volumetric apparatus in which the product had been previously equilibrated in a vacuum better than 10^{-4} mm Hg for several hours at 60°C. IR absorption spectra were recorded with the products dispersed in liquid paraffin (Nujol), and electron micrographs were obtained of the previously, ultrasonically, dispersed products.

4. RESULTS

A colour photograph of the products is shown in Plate A3.1, where the preheat-treatment temperature of the products increases from left to right; amb. G and 850H are positioned in the top-left and bottom-right corners of the photograph, respectively.

4.1. XRD data.

4.1.1. Unit cell dimensions.

All $d_{(hk\ell)}$ values obtained for the products were corrected by a comparison

PLATE A3.1

αFeOOH (top left) and the products formed by its thermal treatment to various temperatures up to 850°C (bottom right); preheat-treatment temperature increases from left to right.

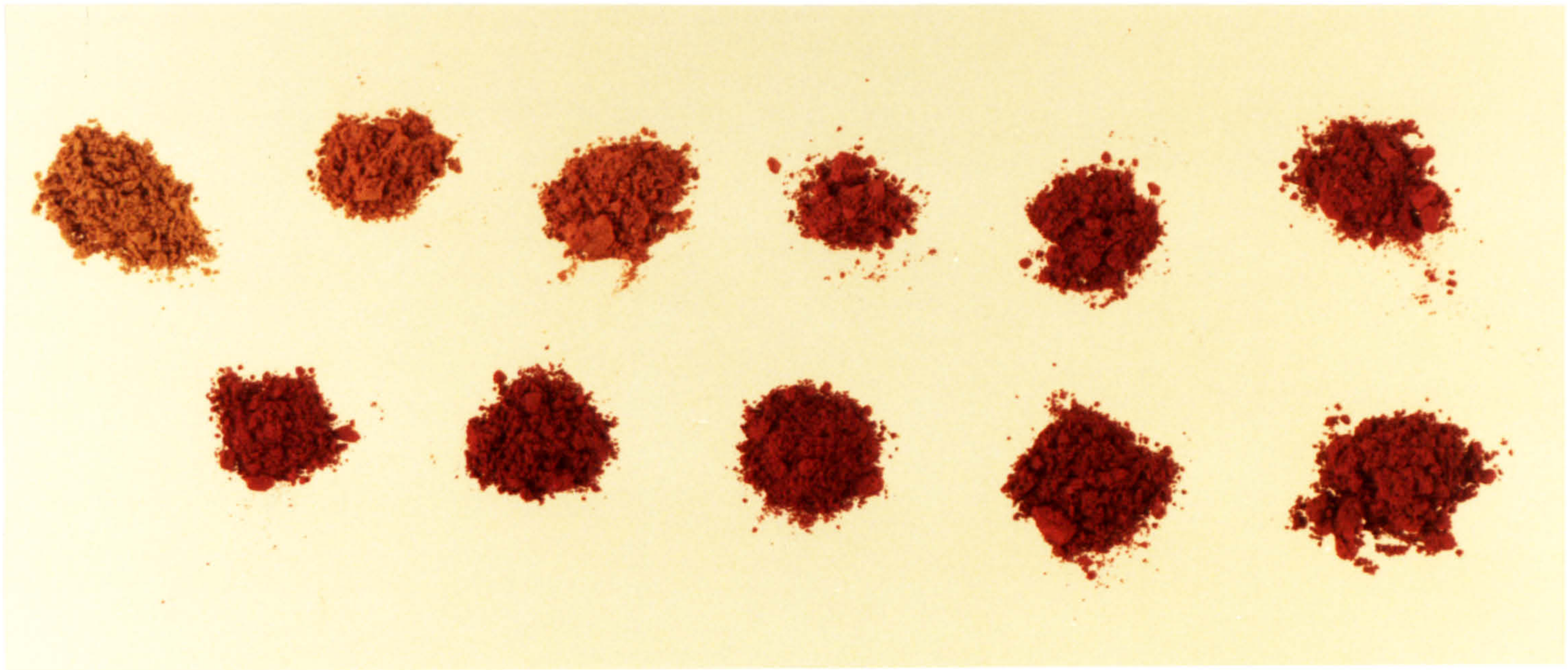

of the measured NaCl $d_{(hk\ell)}$ values with published (Morris et.al.) data.

For amb. G, 250G, 300G and 350GA, b_G and c_G values were readily obtained from the $d_{(060)}$ and $d_{(002)}$ spacings, respectively, of the corresponding αFeOOH profiles. An average a_G value of each αFeOOH containing product was obtained from the intercepts of least-squares-fits to eqn. A3.2 for the values 1, 2 and 3 of the Miller h indice. The $d_{(060)}$ spacing of 375A was not detected and, consequently, only the c_G value was obtained for this product. The three αFeOOH unit cell dimensions of those products formed on heating αFeOOH to temperatures up to 300°C expanded with increasing preheat-treatment temperature. Consequently, the αFeOOH unit cell volume and density of such products increased and decreased, respectively, with increasing preheat-treatment temperature up to 300°C. The expected contraction of a_G and c_G and the expansion of b_G, as αFeOOH was transformed to αFe_2O_3, were only observed in those products formed at temperatures > 350°C.

For 375A, 400A, 425A, 705H and 850H, a_H values were readily obtained from the $d_{(300)}$ spacings of the corresponding αFe_2O_3 profiles. An average c_H value for each of these products was obtained from the intercepts of least-squares-fits to eqn. A3.5 for the values 2, 4 and 6 of the Miller ℓ indice.

a_G, b_G and c_G values and, where possible, the derived parameters, viz., unit cell volume and density, for amb. G, 250G, 300G, 350GA and 375A, together with a_H and c_H values for 375A, 400A, 425A, 705H and 850H, are given in Table A3.1. Also included in this table are the published (Weast) values of the unit cell dimensions of mineral αFeOOH and mineral αFe_2O_3.

4.1.2. XRD line-broadening data.

The profiles of 250G (being a representative αFeOOH profile), 375A, 400A, 425A, 450A, 500A, 705H and 850H are shown in Figs. A3.1 to A3.4. Non-uniform line broadening is clearly apparent in the profiles of 375A, 400A, 425A, 450A and 500A. In particular, and for a given profile, the lines arising from (110), (006) and (116) reflections (i.e., reflections having a Miller ℓ indice value of 3n) are noticeably sharper than the lines arising from (012), (104) and (024) reflections (i.e., reflections having a Miller ℓ indice value $\neq$ 3n). In contrast, the lines in the profile of

Table A3.1

The unit cell dimensions and derived parameters of a prepared αFeOOH and products formed by preheating this αFeOOH to various temperatures.

Preheat-treatment temperature / °C	Unit cell dimensions a_G / nm	b_G / nm	c_G / nm	Volume of Unit cell / 10^{-3} nm³	Density / g cm⁻³
[(Ref. (Weast)	0.4596	0.9957	0.3021	138.2	4.269]
ambient	0.4646	0.9960	0.3026	140.1	4.213
250	0.4687	0.9978	0.3030	141.7	4.165
300	0.4716	0.9996	0.3030	142.8	4.133
350	0.4665	1.0002	0.3016	140.7	4.195
375	-	-	0.2998	-	-

	c_H / nm	a_H / nm
375	1.3658	0.5085
400	1.3491	0.5061
425	1.3481	0.5068
705	1.3891	0.5040
850	1.4015	0.5047
[(Ref. (Weast)	1.3749	0.5033	301.6	5.275]

FIGURE A3.1

X-RAY DIFFRACTION PROFILES OF THE PRODUCTS OF THE THERMAL TREATMENT OF ∝FeOOH TO 250°C AND 375°C.

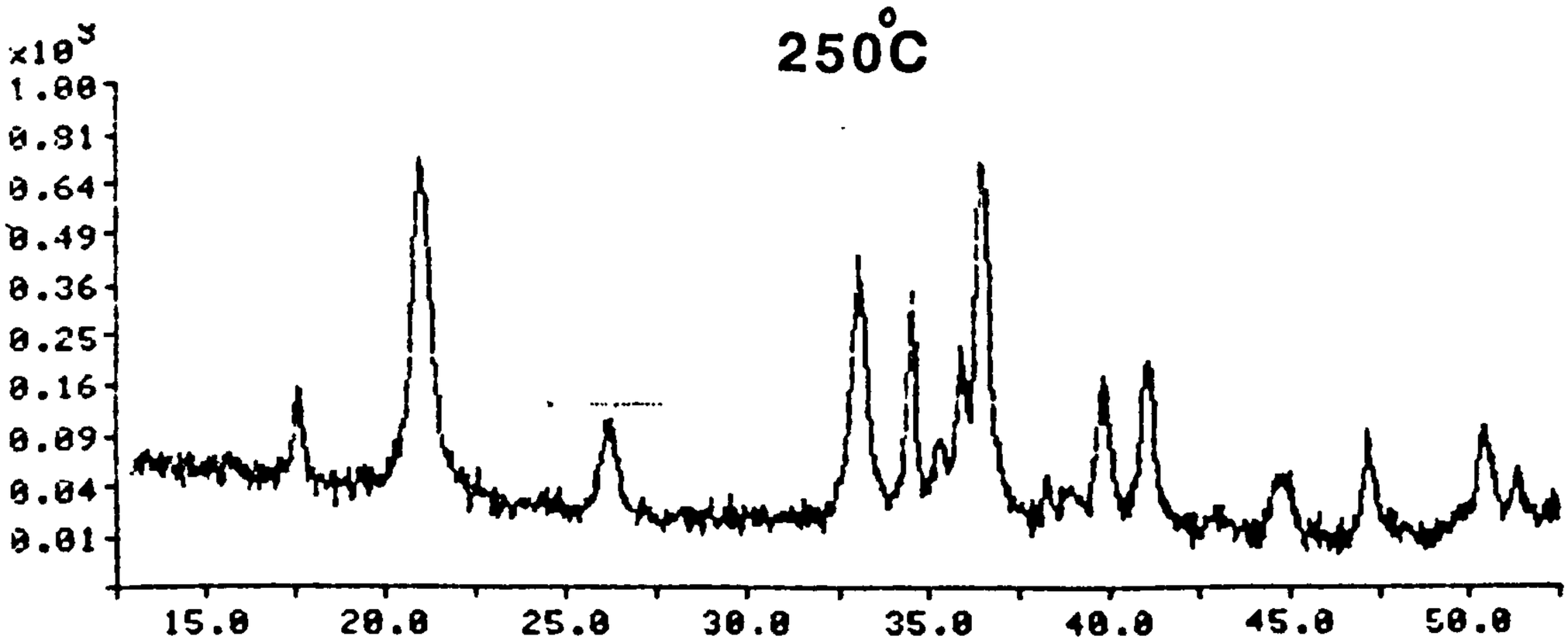

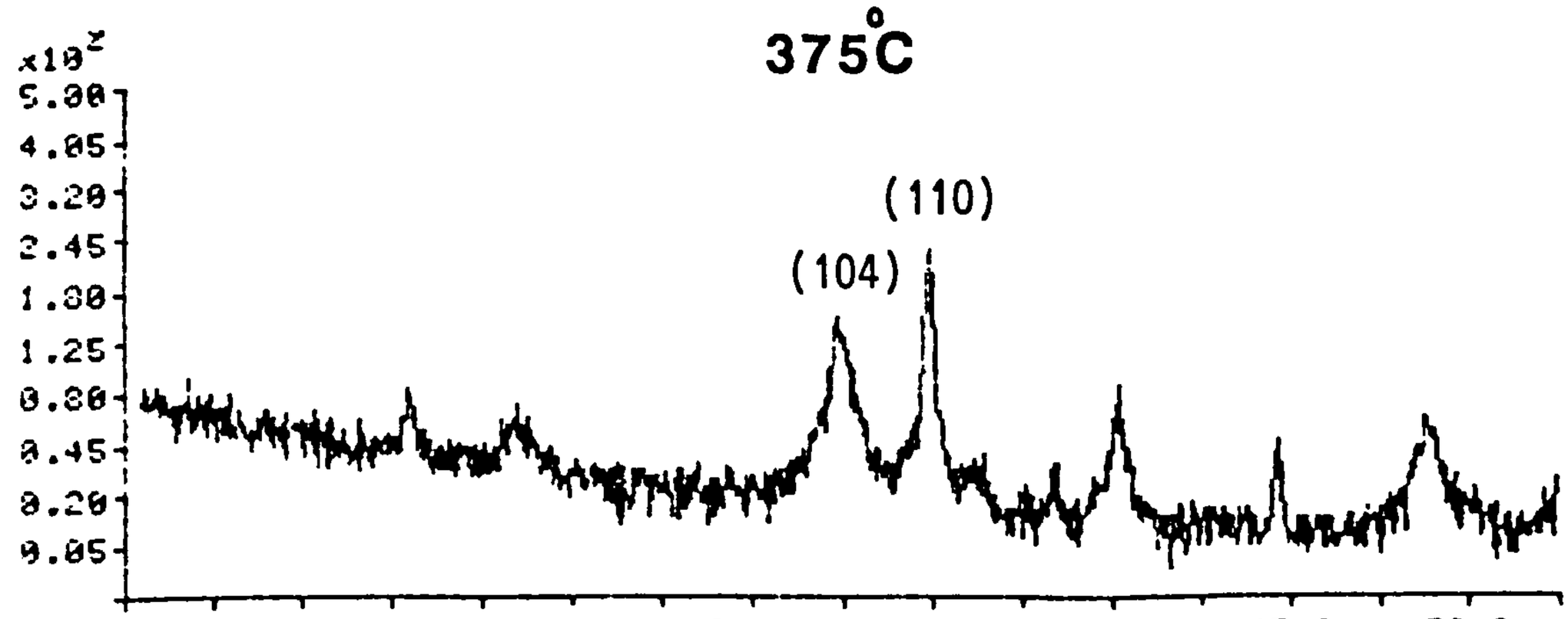

FIGURE A3.2

X-RAY DIFFRACTION PROFILES OF THE PRODUCTS OF THE THERMAL TREATMENT OF ∝FeOOH TO 400°C AND 425°C.

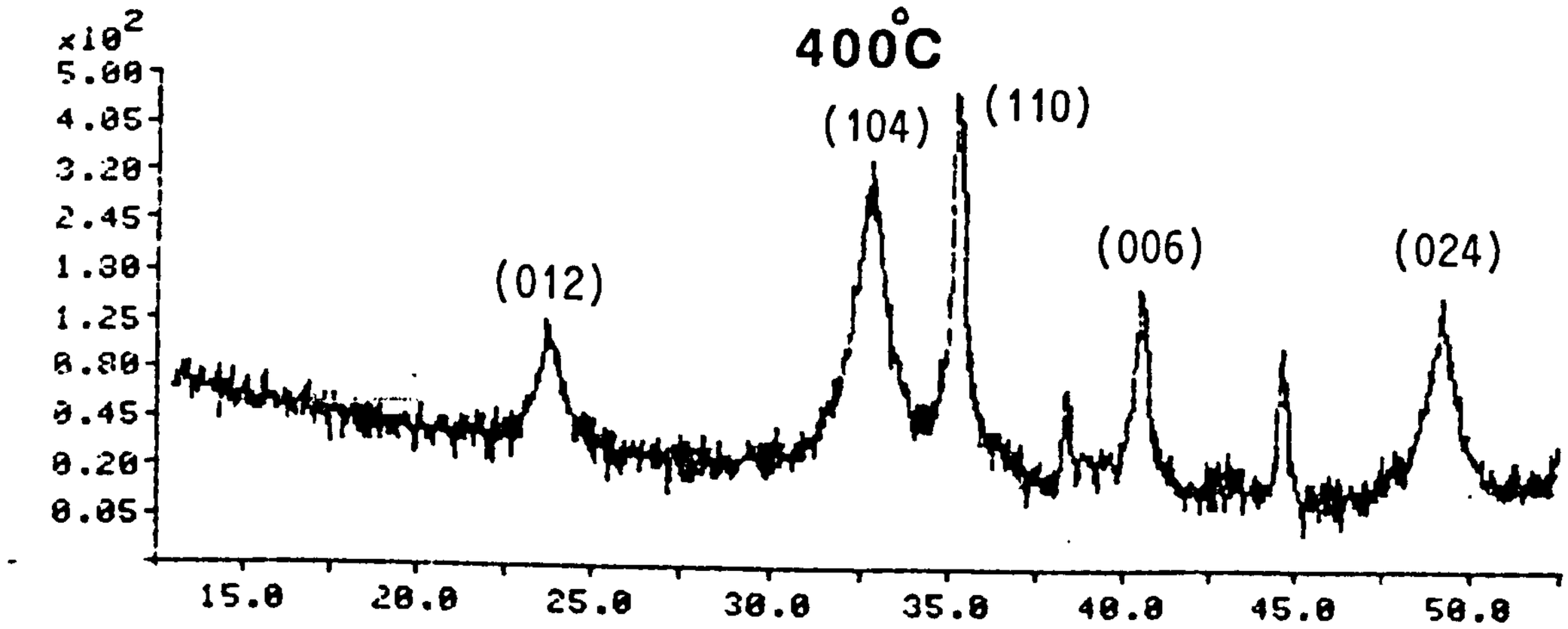

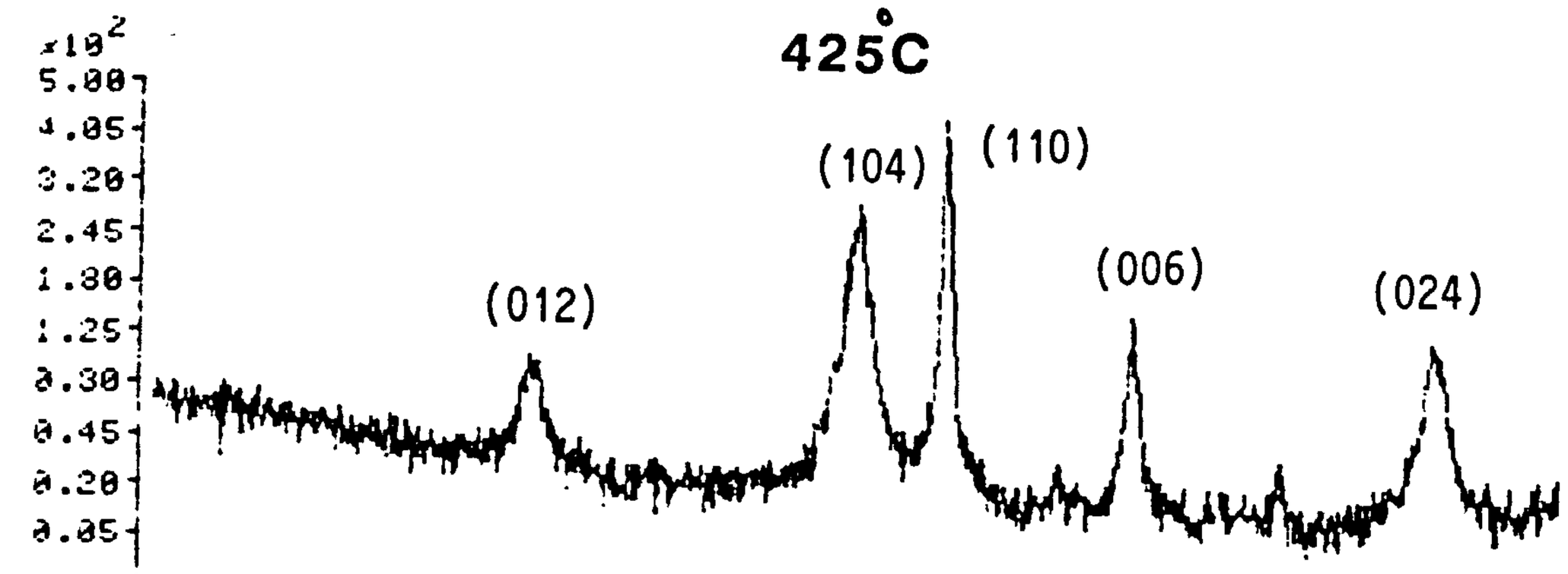

FIGURE A3.3

X-RAY DIFFRACTION PROFILES OF THE PRODUCTS OF THE THERMAL TREATMENT OF ∝FeOOH TO 450°C AND 500°C.

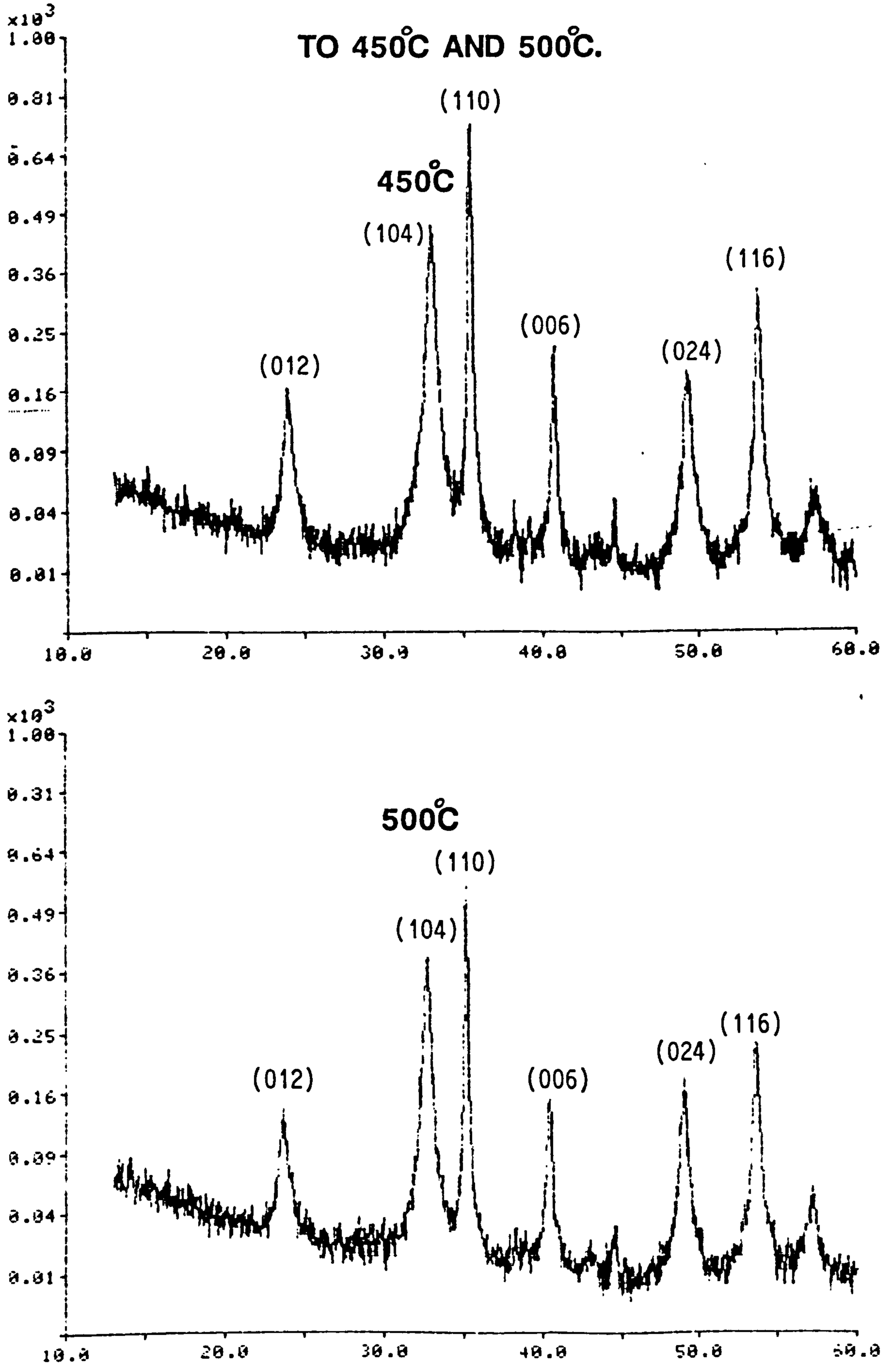

FIGURE A3.4

X-RAY DIFFRACTION PROFILES OF THE PRODUCTS OF THE THERMAL TREATMENT OF αFeOOH TO 705°C AND 850°C.

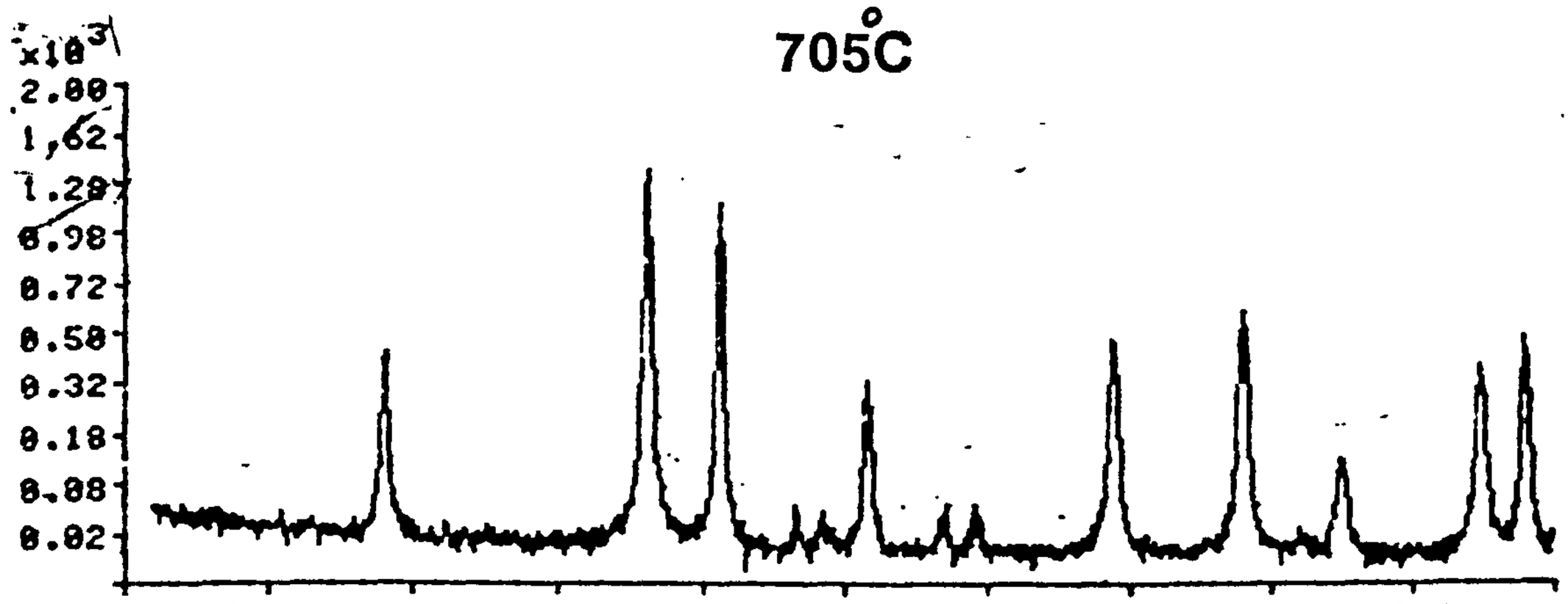

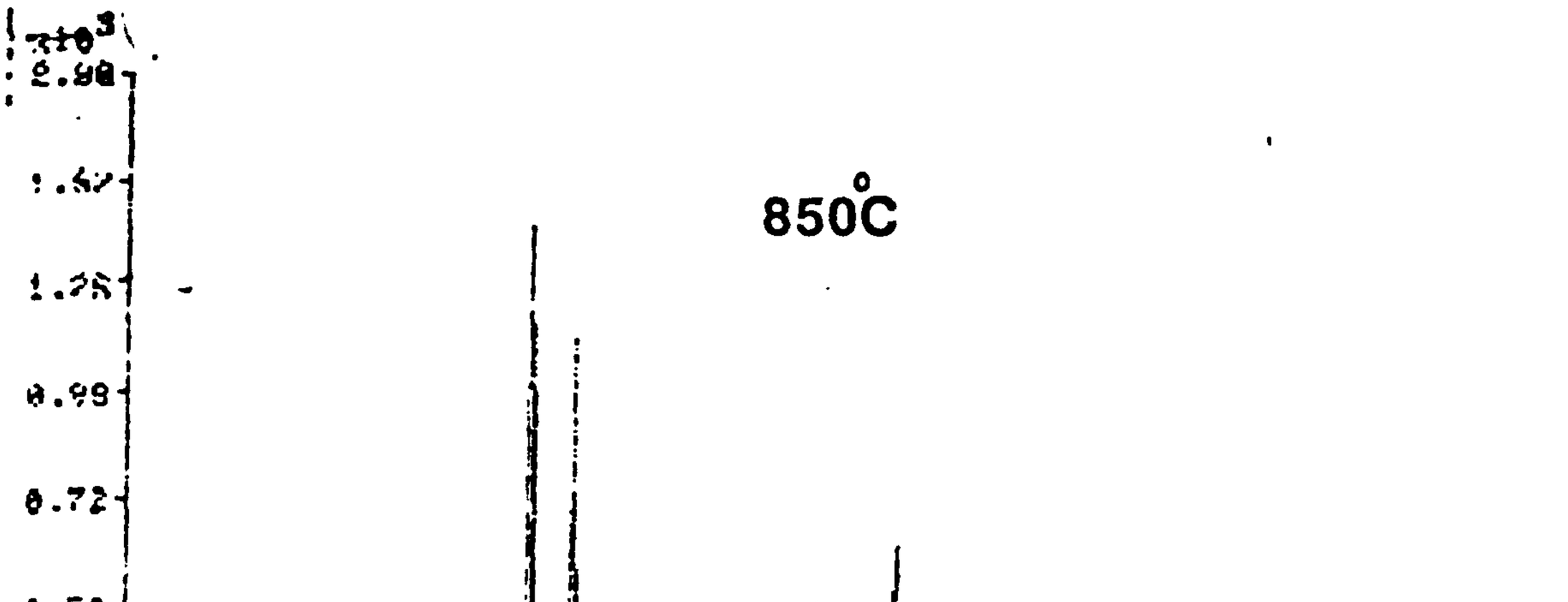

250G are uniformly broad, while the lines in the profile of 850H are uniformly sharp.

The $2\theta_{(110)}$ angles of the profiles of amb. G, 250G, 300G, 350GA and 375A, together with the $2\theta_{(024)}$ angles of the profiles of 400A, 425A, 500A, 705H and 850H, were corrected (via the measured $d_{(110)}$ and $d_{(024)}$ values) by a comparison of the measured NaCl $d_{(hk\ell)}$ values with published (Morris et.al.) data. The XRD profile of this solid also served as a g-profile, and the value of each of the shape parameters, $2W_{\frac{1}{2}}^{g}$ and β^{g}, of one of the peaks (the (111) peak) in this profile were obtained; the (111) peak of NaCl was chosen because it was of the same order of intensity as that of the (110) and (024) peaks of the $\alpha FeOOH$ and αFe_2O_3 products, respectively. From these values, β_C^g and β_G^g were calculated using eqns. A3.10 and A3.11, respectively. For each product, the value was obtained of each of the shape parameters, $2W_{\frac{1}{2}}^{h}$ and β^{h}, characterising a single peak in the corresponding XRD profile (i.e., the h-profile); for amb. G, 250G, 300G, 350GA and 375A, the (110) peaks of the corresponding profiles were characterised, while for 400A, 425A, 450A, 500A, 705H and 850H the (024) peaks of the corresponding profiles were characterised. From these values, β_C^h and β_G^h were calculated for each product using eqns. A3.10 and A3.11, respectively. Then, by means of eqns. A3.8 and A3.9 values of, respectively, β_C^f and β_G^f were obtained for each product. Finally, the $\overline{D}$ and $\overline{E}$ values of each product were calculated using eqns. A3.12 and A3.13, respectively, and the appropriate β^f value (in radians); the value of 0.9 (Philips) was used for the shape factor in all crystallite size calculations. The $\overline{D}$ and $\overline{E}$ values of each product are plotted against preheat-treatment temperature in Figs. A3.5 and A3.6.

The products formed at temperatures from 250 to 350°C had similar $\alpha FeOOH$ $\overline{D}$ values which were greater than that of the unheated $\alpha FeOOH$ sample. Similarly, the products formed at temperatures from 400 to 500°C had comparable αFe_2O_3 $\overline{D}$ values which were smaller than those of products formed at temperatures above 500°C and up to 850°C.

In general, the $\overline{E}$ values of both $\alpha FeOOH$ and αFe_2O_3 crystals present in products formed at temperatures up to, respectively, 350°C and 850°C decreased with increasing preheat-treatment temperature.

FIGURE A3.5

AVERAGED CRYSTALLITE SIZE OF ∝FeOOH AND THE PRODUCTS OF ITS THERMAL TREATMENT TO VARIOUS TEMPERATURES.

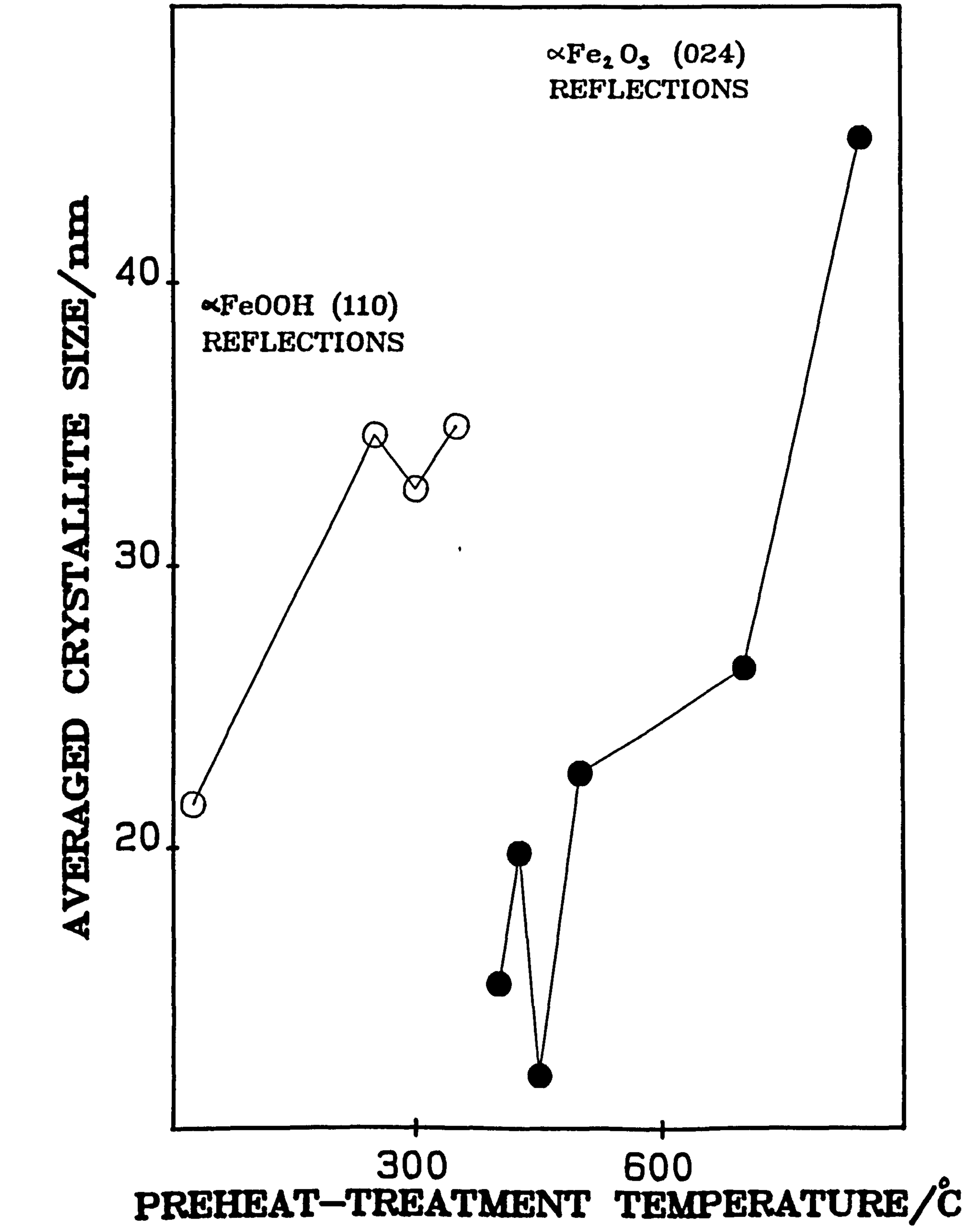

FIGURE A3.6

MEAN LATTICE DISTORTION OF ∝FeOOH AND THE PRODUCTS OF ITS THERMAL TREATMENT TO VARIOUS TEMPERATURES.

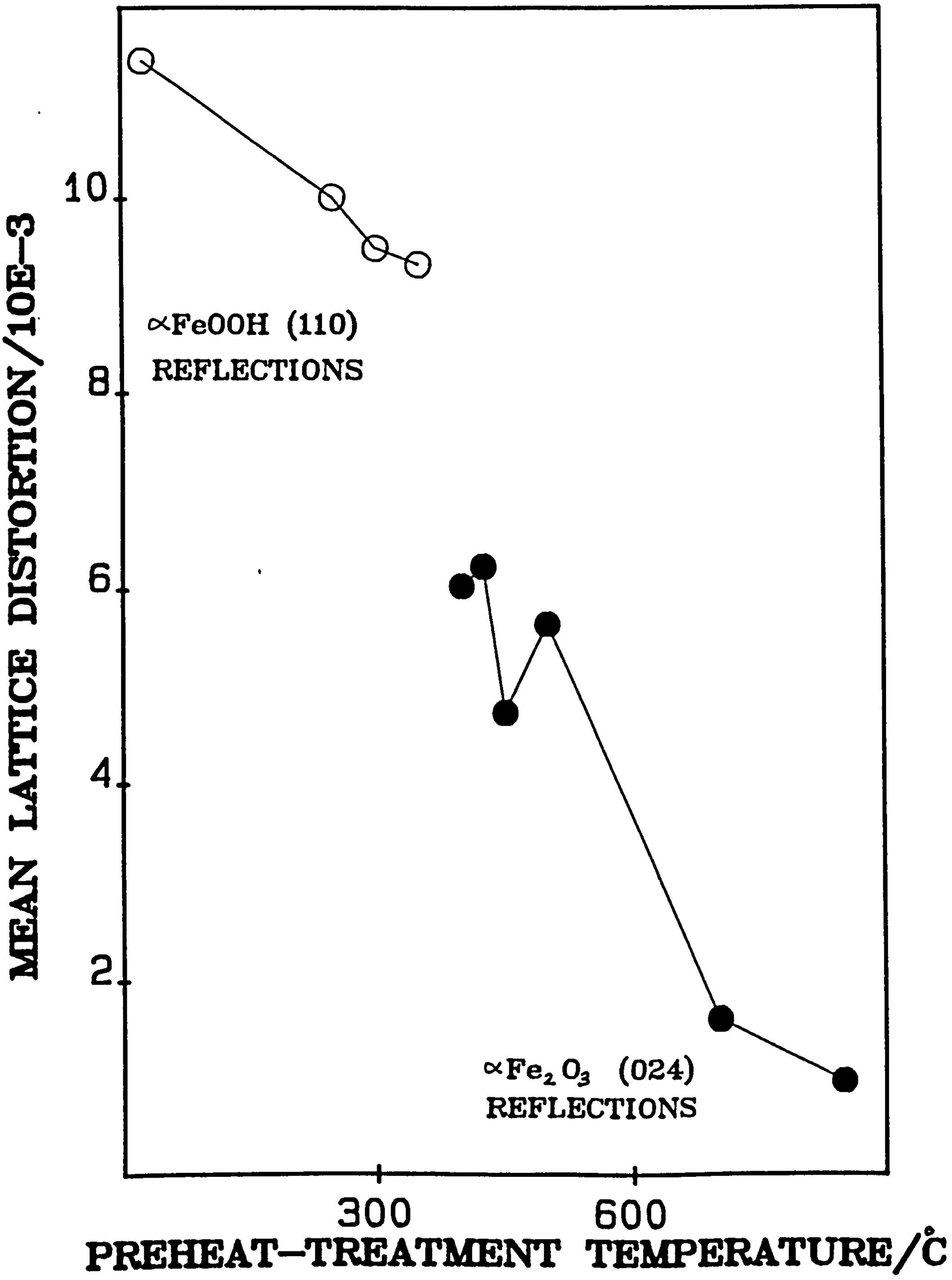

4.1.3. Estimated phase concentrations.

The intensities, $(I_{(110)})_G$, of the αFeOOH peaks in the XRD profiles of amb. G, 250G and 300G increased with increasing preheat-treatment temperature. Similarly, the intensities, $(I_{(024)})_H$, of the αFe_2O_3 peaks in the XRD profiles of 300G, 350GA, 375A, 400A, 425A, 450A, 500A, 705H and 850H also increased with increasing preheat-treatment temperature. In view of the non-zero $(I_{(024)})_H$ value for 300G it was considered reasonable to assume that the intensity, $(I_{(110)})_G$, of an idealised, pure αFeOOH (that would have been formed by heating the prepared αFeOOH to between 250 and 300°C) would have been greater than that of 300G ($(I_{(110)})_G$ = 692). From a plot of I against preheat-treatment temperature (Fig. A3.7) it was estimated that an idealised pure αFeOOH, with an associated intensity of $(I_{(110)})_{GP}$ = 730, would have been formed by heating the prepared αFeOOH to 275°C.

To progress further the following assumptions were made:-

(i) 850H was pure αFe_2O_3,

(ii) the μ_{Rem} of the non-αFeOOH portions of amb. G and 250G was equal to the absorption coefficient (μ_G) of αFeOOH,

and (iii) the μ_{Rem} of the non- αFe_2O_3 portions of those products formed at temperatures ≥ 400°C was equal to the absorption coefficient (μ_H) of αFe_2O_3.

Thus, the weight fractions (w_G) of αFeOOH in amb. G and 250G were obtained using the ratio $(I_{(110)})_G$ / $(I_{(110)})_{GP}$ and the appropriate $(I_{(110)})_G$ value, while the weight fractions (w_H) of αFe_2O_3 in those products formed at temperatures ≥ 400°C were obtained using the ratio $(I_{(024)})_H$ / $(I_{(024)})_{HP}$. For those products having non-zero $(I_{(110)})_G$ and $(I_{(024)})_H$ values (300G, 350GA and 375A) it was considered reasonable to expect that μ_{Rem} would show a gradual change from μ_G (200.18) to μ_H (221.47) with increasing preheat-treatment temperature. On the basis of this expectation and the $(I_{(hk\ell)})_H$ value of each of these products, values of w_H were inserted into eqn. A3.14 until a unique set of three w_H values gave a conforming series of μ_{Rem} values for these products; these values were 201, 212 and 221 for 300G, 350GA and 375A, respectively. Then, the w_G of each of these products was calculated by means of eqn. A3.14 and the appropriate μ_{Rem} value. The weight fraction (w_A) of the non-crystalline material present in a product was obtained by

FIGURE A3.7

X-RAY DIFFRACTION PEAK INTENSITY OF ∝FeOOH AND THE PRODUCTS OF ITS THERMAL TREATMENT TO VARIOUS TEMPERATURES.

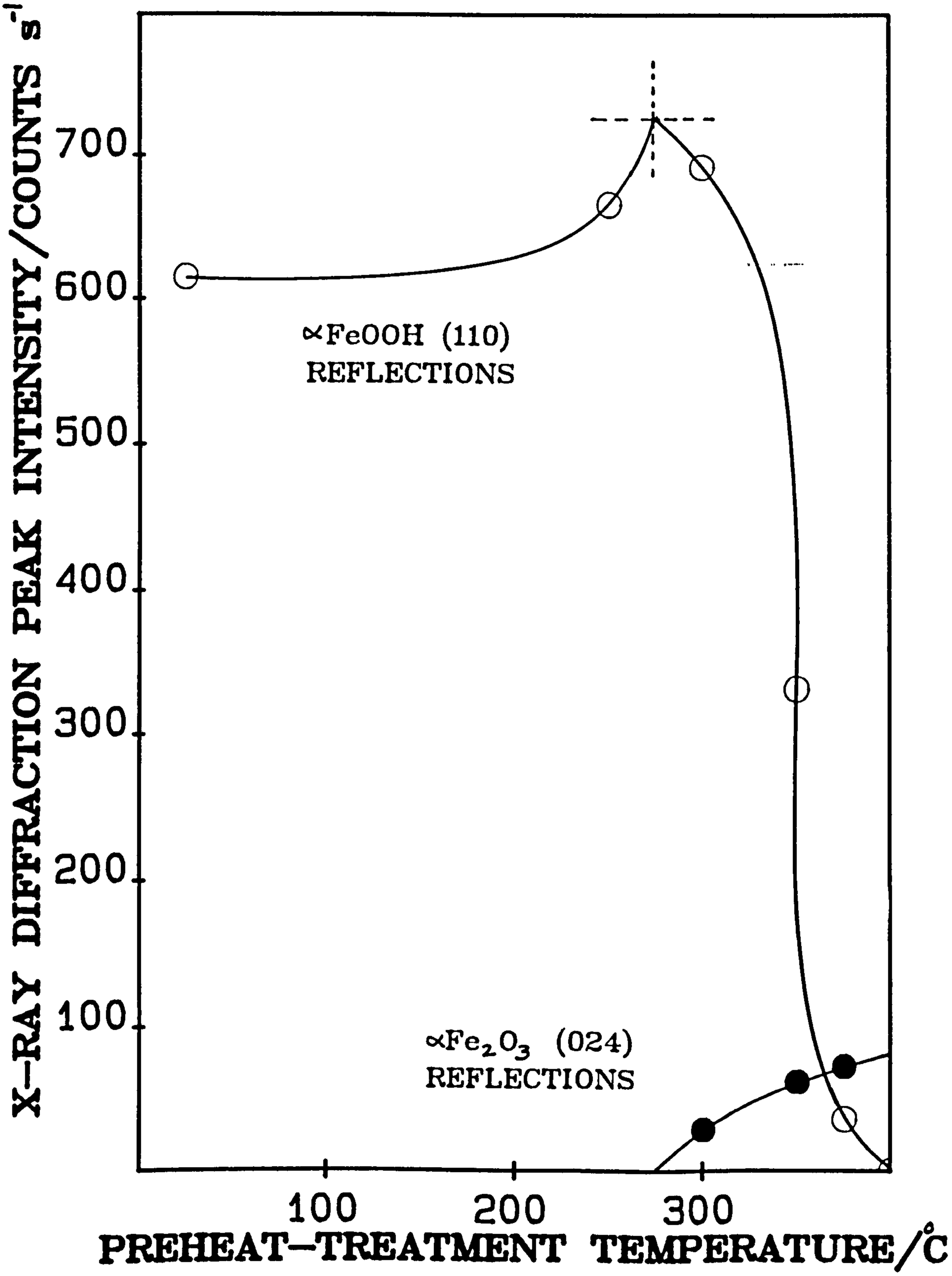

difference. The variation of the w_G, w_H and w_A of the products with preheat-treatment temperature is shown in Fig. A3.8.

The prepared αFeOOH was estimated to be composed of αFeOOH, amorphous material and αFe_2O_3 at weight concentrations of ca. 84.2, 14.8 and 1.0%, respectively. [It was shown elsewhere (Chapter A1) that the prepared αFeOOH contained 8.4% of the omnipresent adsorbed water (X-ray amorphous). Thus, it would appear that the prepared αFeOOH also contained, rather unexpectedly, 6.4% (i.e., 14.8-8.4) of amorphous material that was not adsorbed water. It may be conjectured that this unexpected material was amorphous iron oxyhydroxide.]

Although the prepared αFeOOH was not heated to 275°C, it was estimated from Fig. A3.8 that if a product had been produced at this temperature it would have contained 97.4% αFeOOH, i.e., the greatest w_G value of all products.

αFeOOH was the principal phase (either amorphous or crystalline) in those products formed at temperatures up to 350°C. The w_G and w_H values of products formed at temperatures up to 300°C increased with increasing preheat-treatment temperature. In contrast, the w_A values of these products decreased with increasing preheat-treatment temperature.

Amorphous material was the principal phase present in those products formed at temperatures from 350°C to below 575°C. 375A had, in comparison with products formed at other temperatures, the greatest w_A value (84.6%). Indeed, the w_A values of those products formed at temperatures from 375°C up to 500°C were consistently high (> 70%).

There was no XRD detectable αFeOOH present in those products formed at temperatures above 400°C, while αFe_2O_3 was the principal phase present in those products formed at temperatures above ca. 575°C.

4.2. Gas adsorption data

4.2.1. Isotherms

The adsorption isotherms of N_2 (Figs. A3.9 to A3.13) were of Type II in the BDDT classification (Brunauer et.al. 1940) and, excluding those

FIGURE A3.8

WEIGHT FRACTION OF PHASES IN ∝FeOOH AND THE PRODUCTS OF ITS THERMAL TREATMENT TO VARIOUS TEMPERATURES.

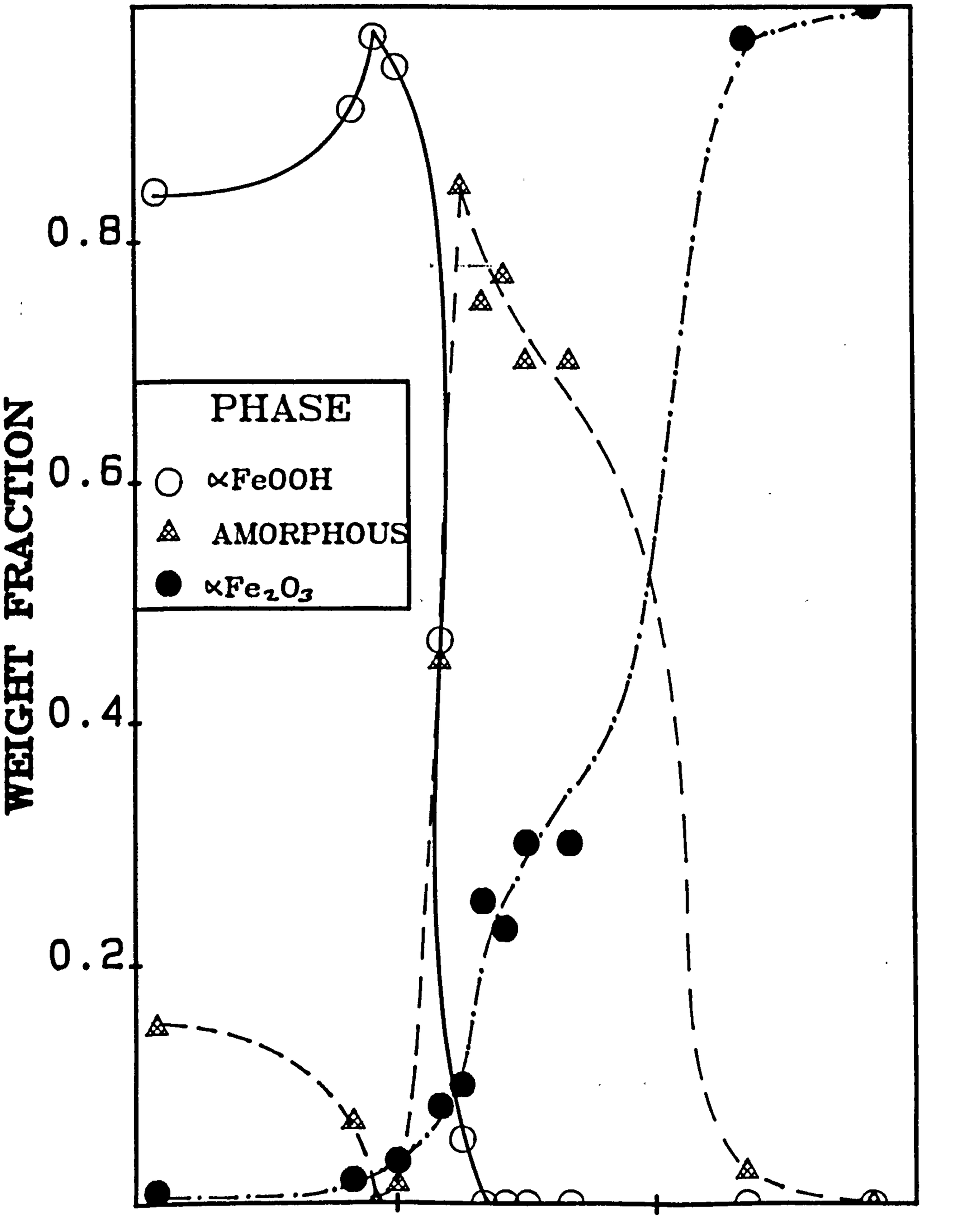

FIGURE A3.9

SORPTION ISOTHERMS OF NITROGEN ON ∝FeOOH AND THE PRODUCT OF ITS THERMAL TREATMENT TO 250°C.

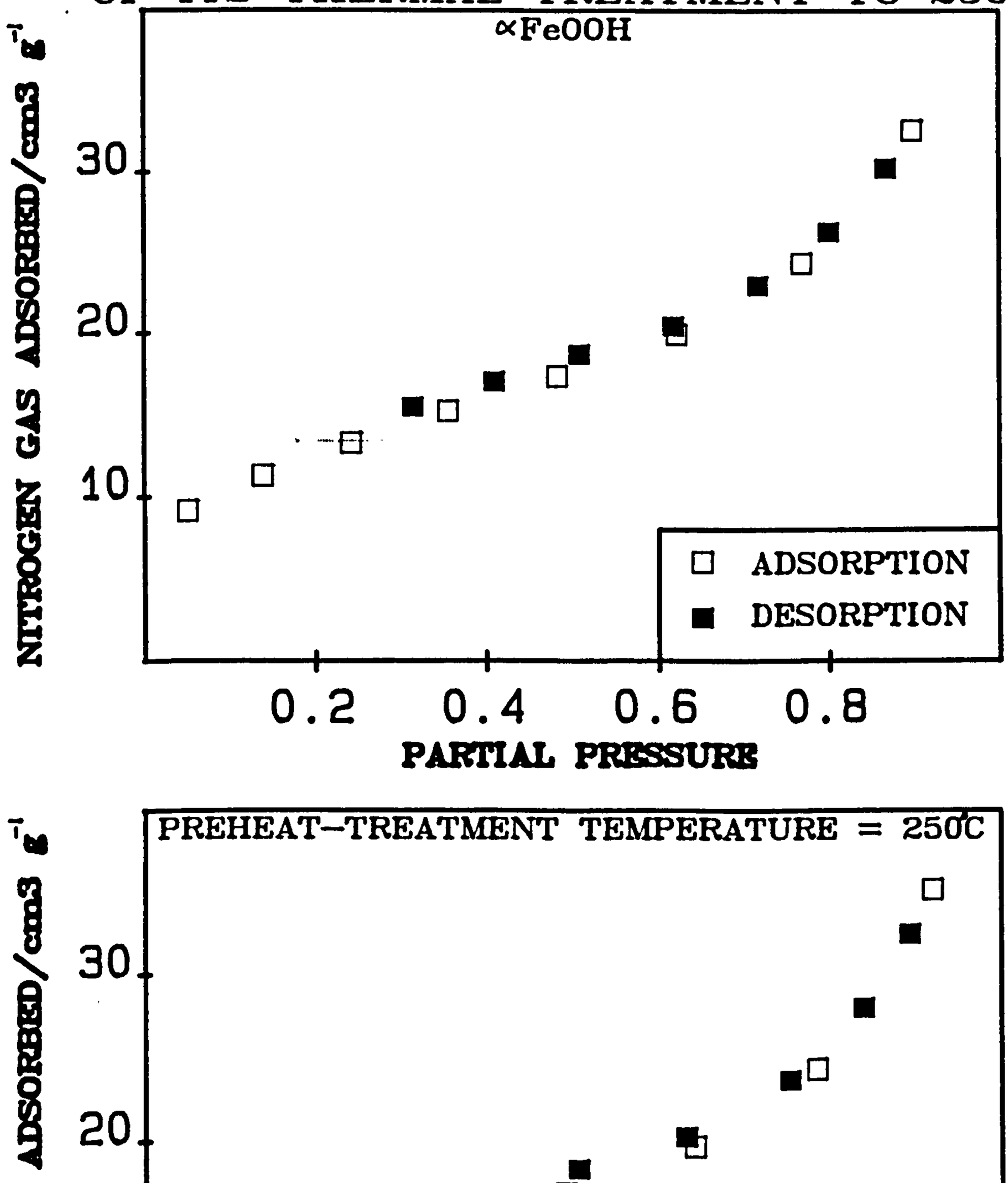

FIGURE A3.10

SORPTION ISOTHERMS OF NITROGEN ON THE PRODUCTS OF THE THERMAL TREATMENT OF ∝FeOOH TO 300 AND 350°C.

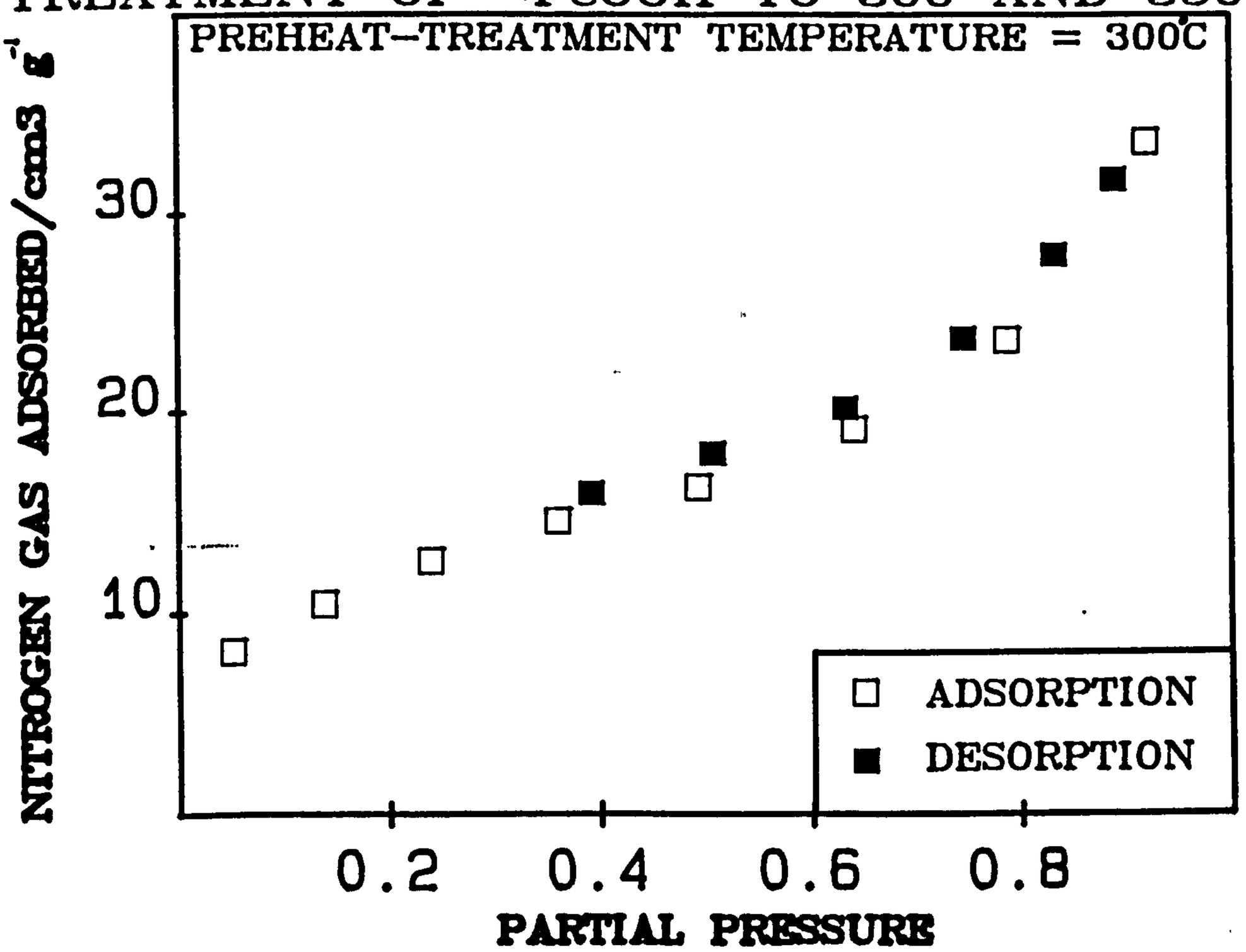

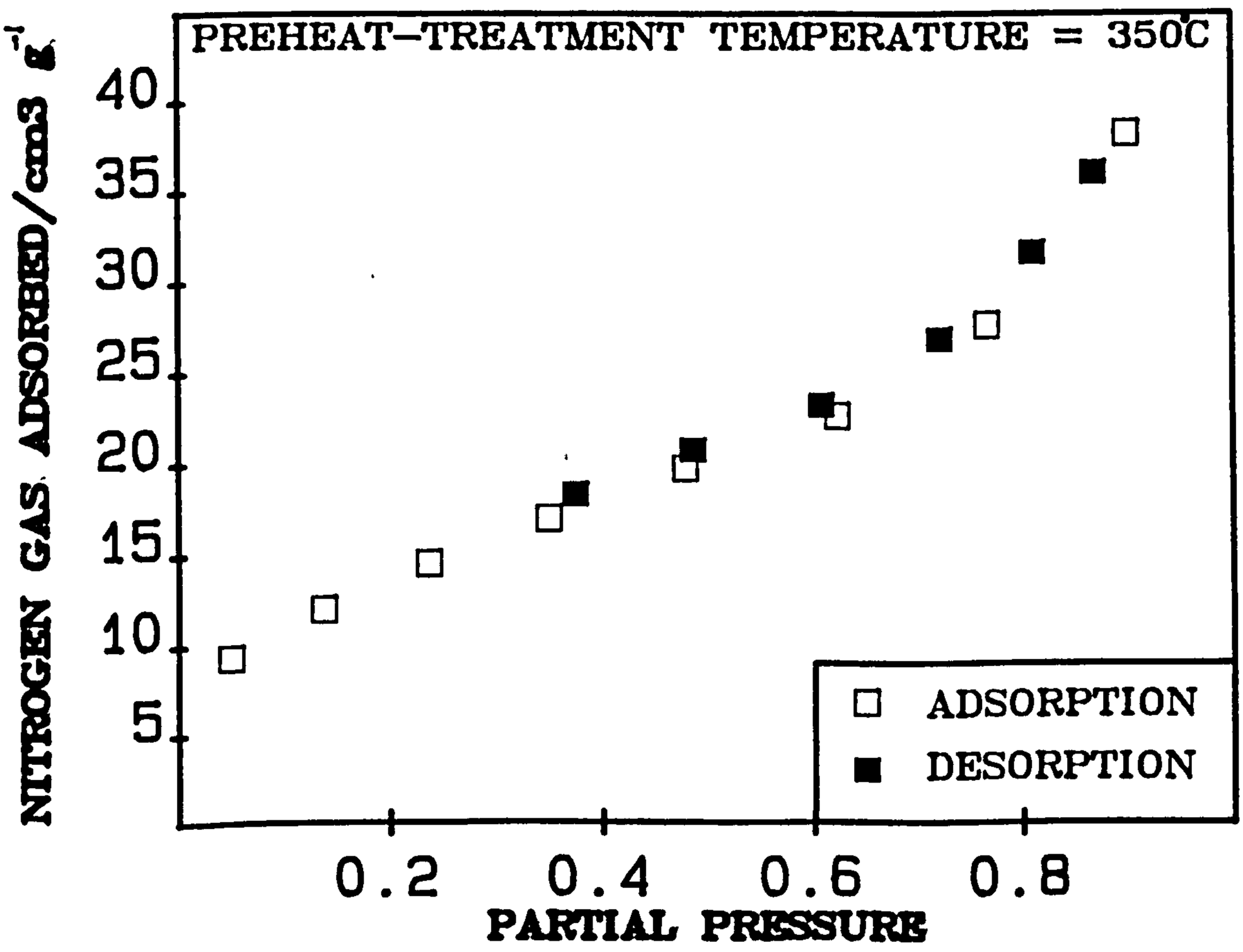

FIGURE A3.11

SORPTION ISOTHERMS OF NITROGEN ON THE PRODUCTS OF THE THERMAL TREATMENT OF ∝FeOOH TO 400 AND 450°C.

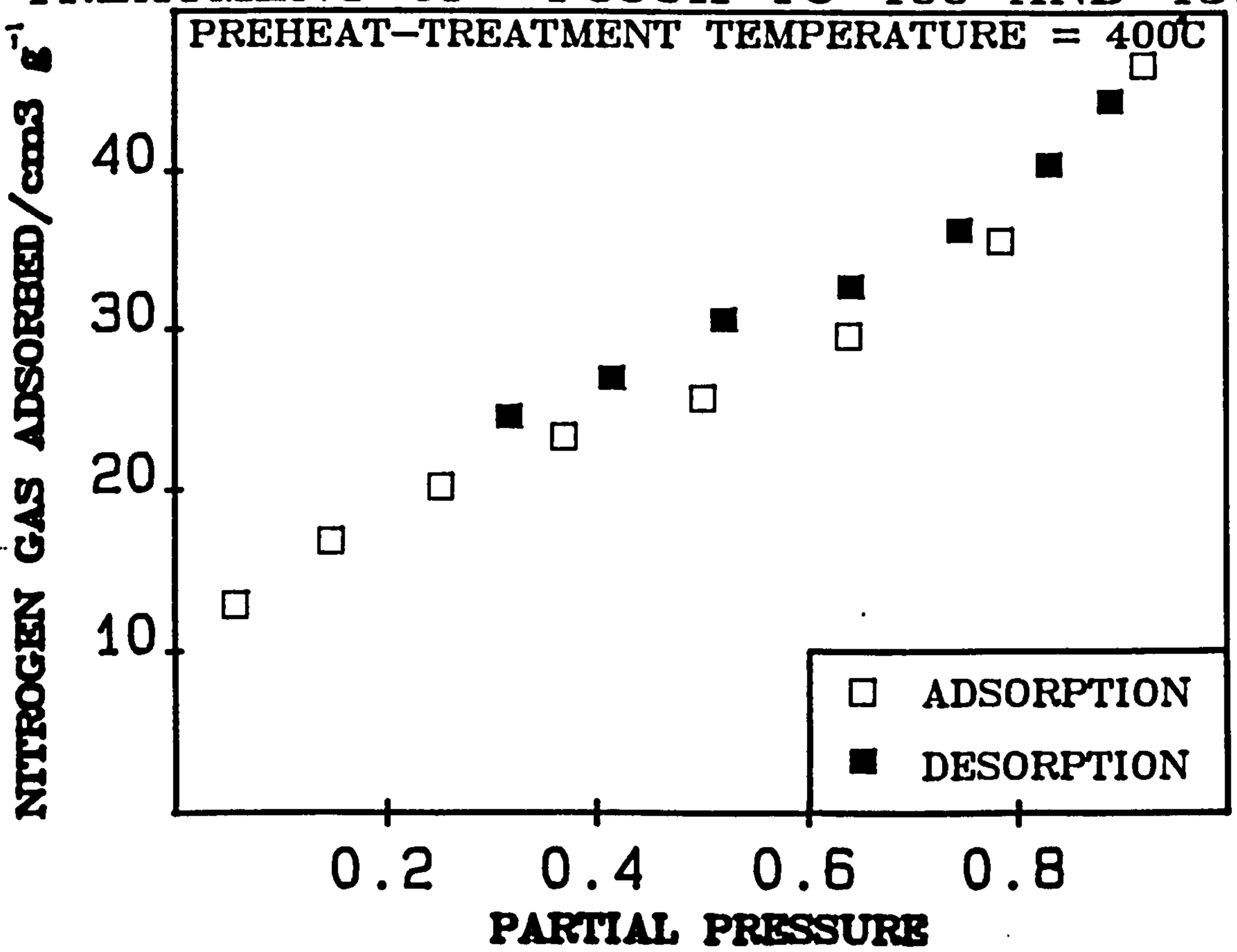

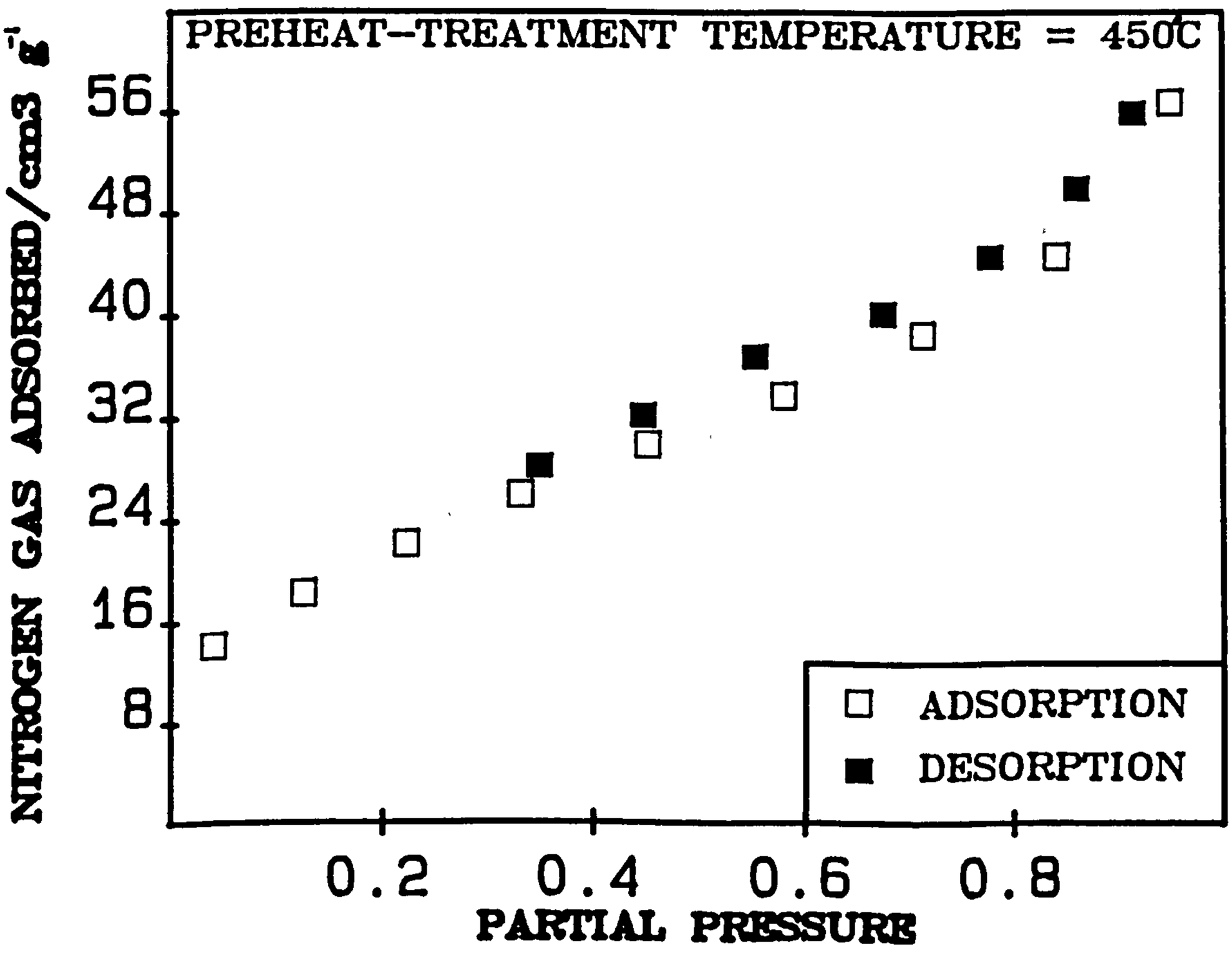

FIGURE A3.12

SORPTION ISOTHERMS OF NITROGEN ON THE PRODUCTS OF THE THERMAL TREATMENT OF ∝FeOOH TO 500 AND 705°C.

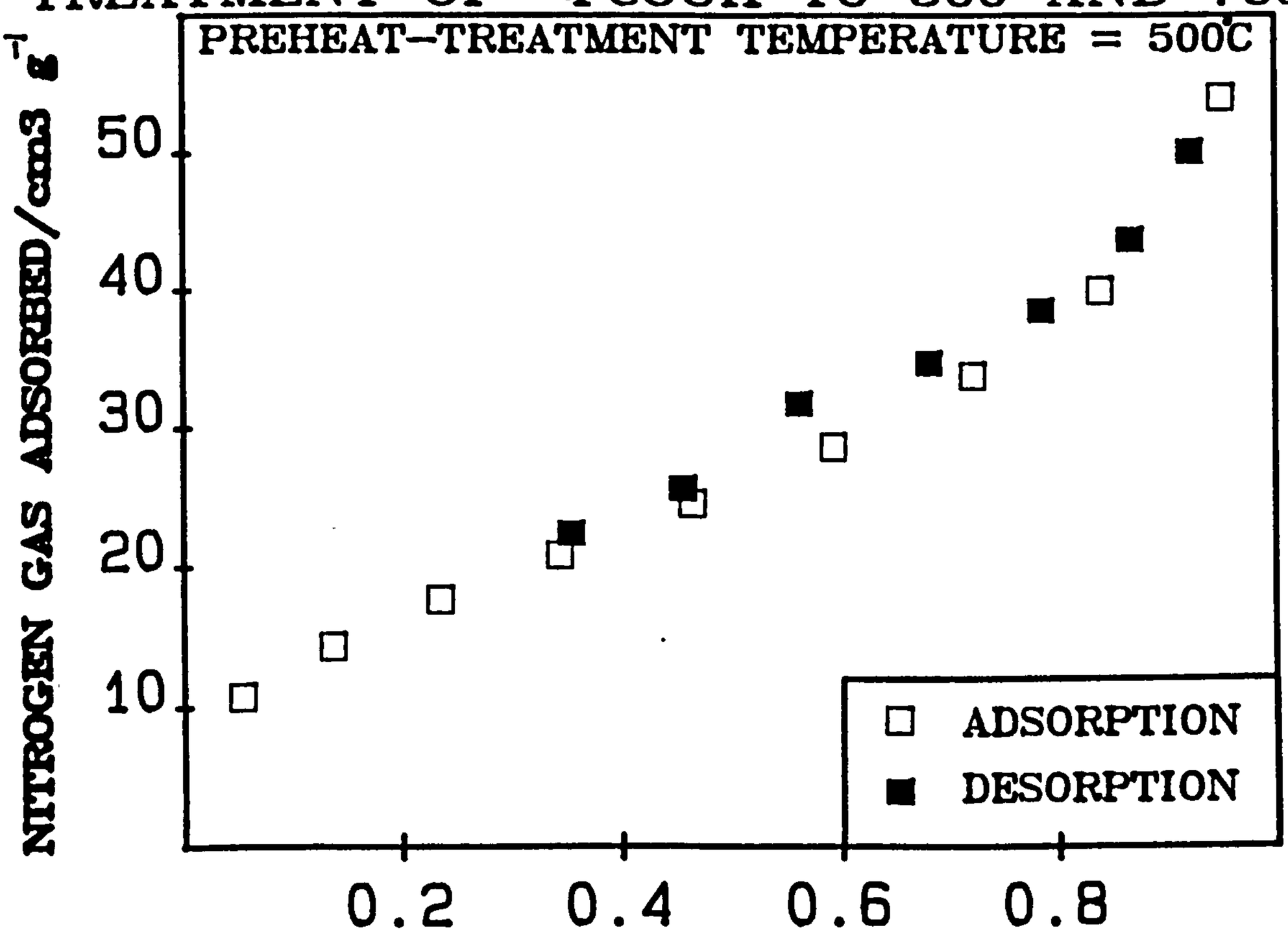

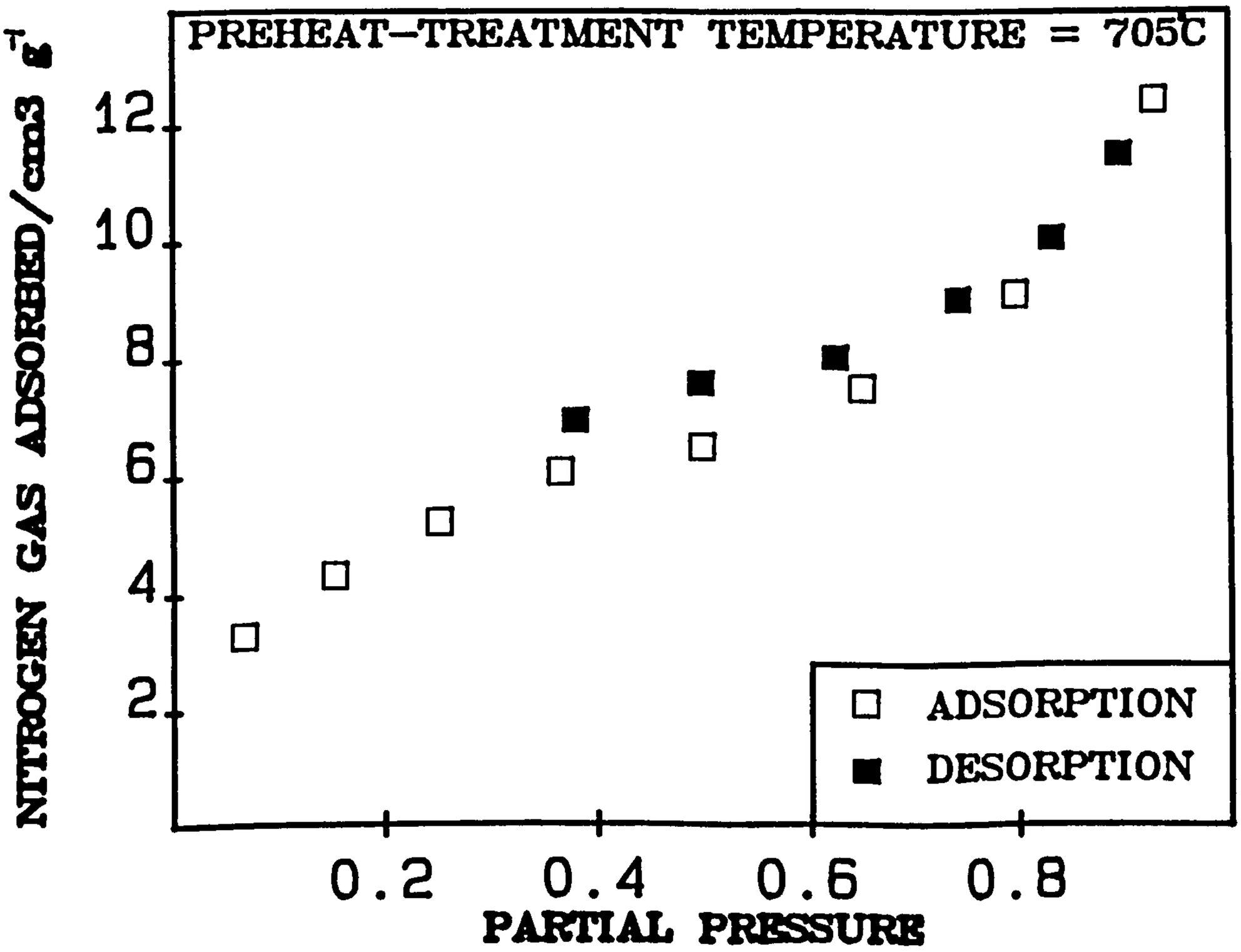

FIGURE A3.13

SORPTION ISOTHERMS OF NITROGEN ON THE PRODUCT OF THE THERMAL TREATMENT OF ∝FeOOH TO 850°C.

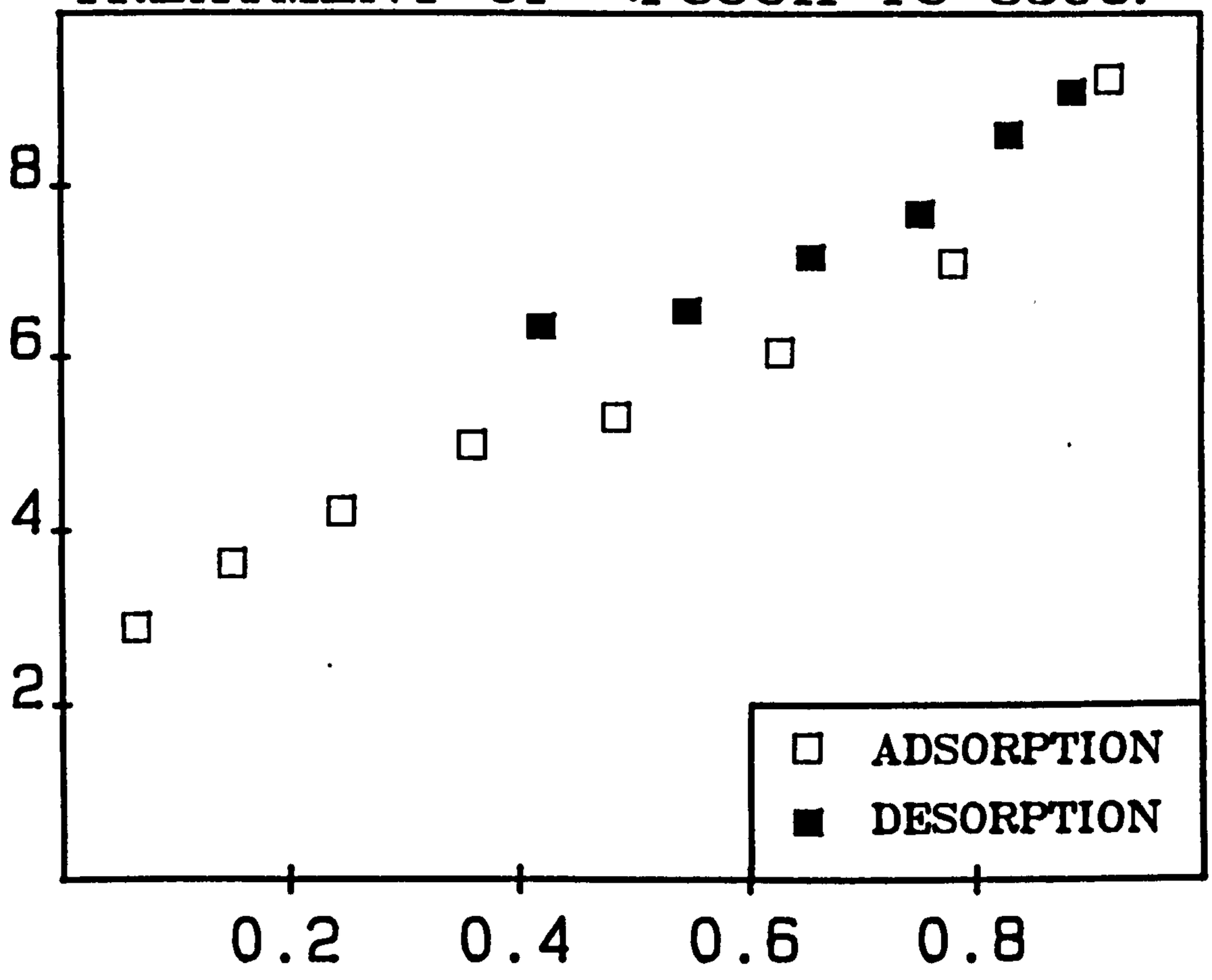

corresponding to 250G, they exhibit hysteresis which in each case extends down to low relative pressure (ca. $\frac{p}{p_{SAT}} = 0.4$).

The S_{BET} values of products formed at temperatures up to 450°C increased with increasing preheat-treatment temperature, whereas the surface areas of products formed at temperatures above 450°C and up to 850°C decreased with increasing preheat-treatment temperature.

4.2.2. Estimations of t-values and t-plot analysis.

The corresponding N_2 desorption isotherms of the products were reduced to t-plots using the Halsey equation (eqn. A3.26). The total specific surface areas ($(S_t^{TOT})_H$) obtained from the initial slopes of these plots are compared with the corresponding S_{BET} values in Table A3.2(a). For amb. G, 250G and 300G the $(S_t^{TOT})_H$ values (see Figs. A3.14 and A3.15) were, in general, comparable with the corresponding S_{BET} values. However, the $(S_t^{TOT})_H$ values obtained for the remaining products were significantly different from the corresponding S_{BET} values. This suggested that for these products (and very probably all the surfaces studied) t was incorrectly estimated by the Halsey equation. Instead, in a more direct approach, the thickness of the adsorbed layer of N_2 present on a product, in equilibrium with a particular partial pressure of N_2, was estimated to be that of the adsorbed layer present on a non-porous reference substance at the same partial pressure. In view of the relative magnitudes of the S_{BET} values of amb. G, 250G and 300G, and the absence of any strong deviation in the t-plot for 250G, 250G was considered to represent an appropriate non-porous reference substance for all the surfaces studied. Thus, values of t were obtained from the desorption data of 250G, using eqn. A3.25, and a calibration curve of t against partial pressure constructed (Fig. A3.16). Then, the value of t for a product in equilibrium with a particular partial pressure of N_2 was interpolated from the t / $\frac{p}{p_{SAT}}$ calibration curve. In this way the N_2 desorption isotherms were reduced to t-plots (Figs. A3.17 to A3.21). The S_t^{TOT} values obtained from the initial slopes of these plots are compared with the corresponding S_{BET} values in Table A3.2(a). The close similarity between these corresponding areas indicated that 250G was a good reference substance for the surfaces studied.

The t-plots corresponding to amb. G, 300G, 350GA, 400A, 450A and 850H

Table A3.2(a)

Areal, volumetric and pore size date of a prepared αFeOOH and products formed by preheating this αFeOOH to various temperatures.

Preheat-Treatment Temperature °C	S_{BET} $m^2\ g^{-1}$	$(S_t^{TOT})_H$ $m^2\ g^{-1}$	S_t^{TOT} $m^2\ g^{-1}$	t_I nm	L_p nm	$(\bar{r}_p)_{MAX}$ nm
ambient	45.1	43.9	45.3	0.99	1.98	1.98
250	43.6	45.8	44.1	-	-	1.52
300	43.7	43.7	47.6	1.02	2.24	-
350	51.0	57.9	57.1	1.01	2.30	-
400	69.5	80.5	64.2	0.82	1.70	1.98 3.75
450	78.7	105.8	88.8	0.77	1.80	1.70
500	63.4	88.0	72.4	0.90	2.23	1.92
705	18.4	14.3	13.4	0.70	1.36	2.97
850	14.6	8.3	9.6	1.03	1.91	2.40 4.55

FIGURE A3.14

t–PLOTS OF NITROGEN ON ∝FeOOH AND THE PRODUCT OF ITS THERMAL TREATMENT TO 250°C.

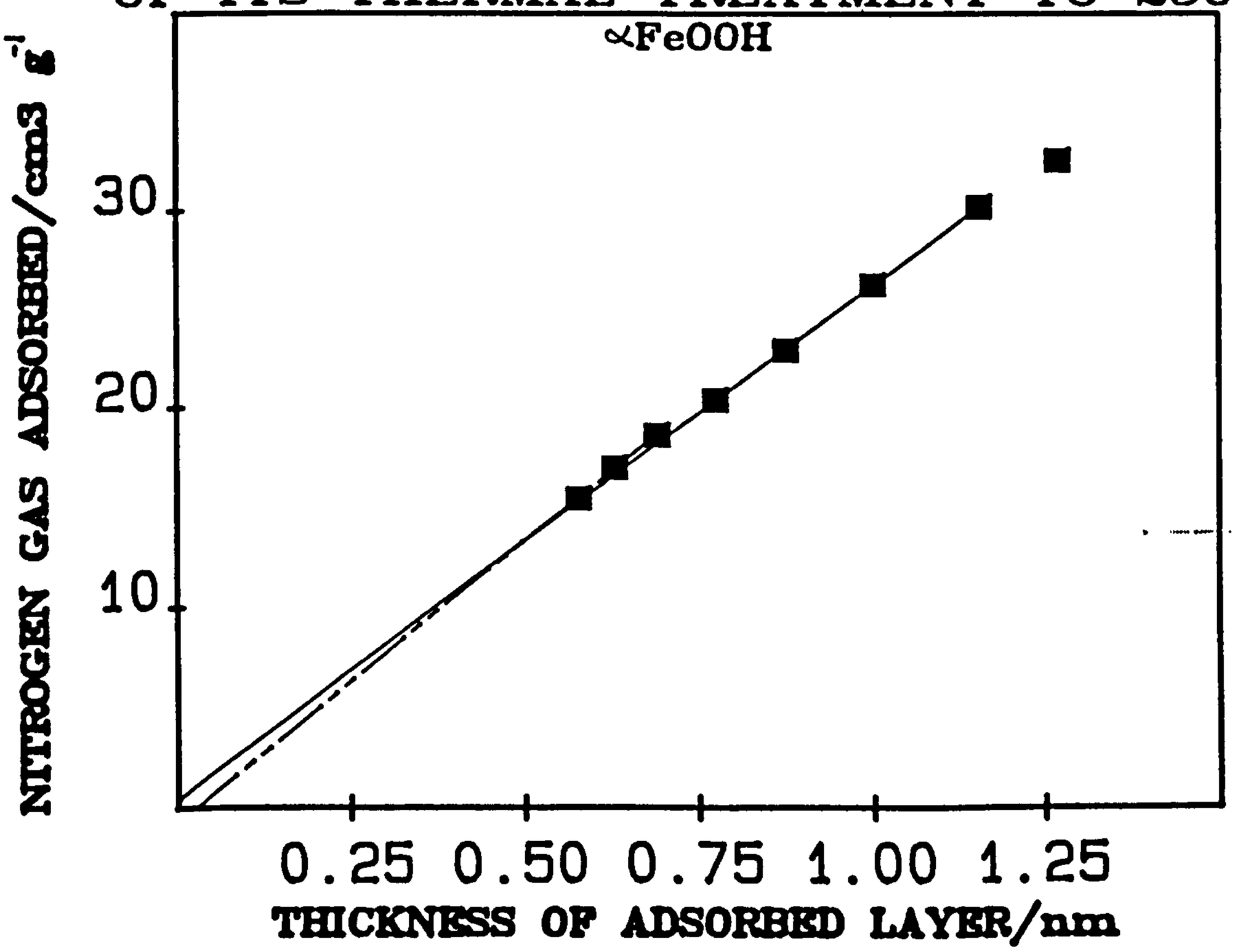

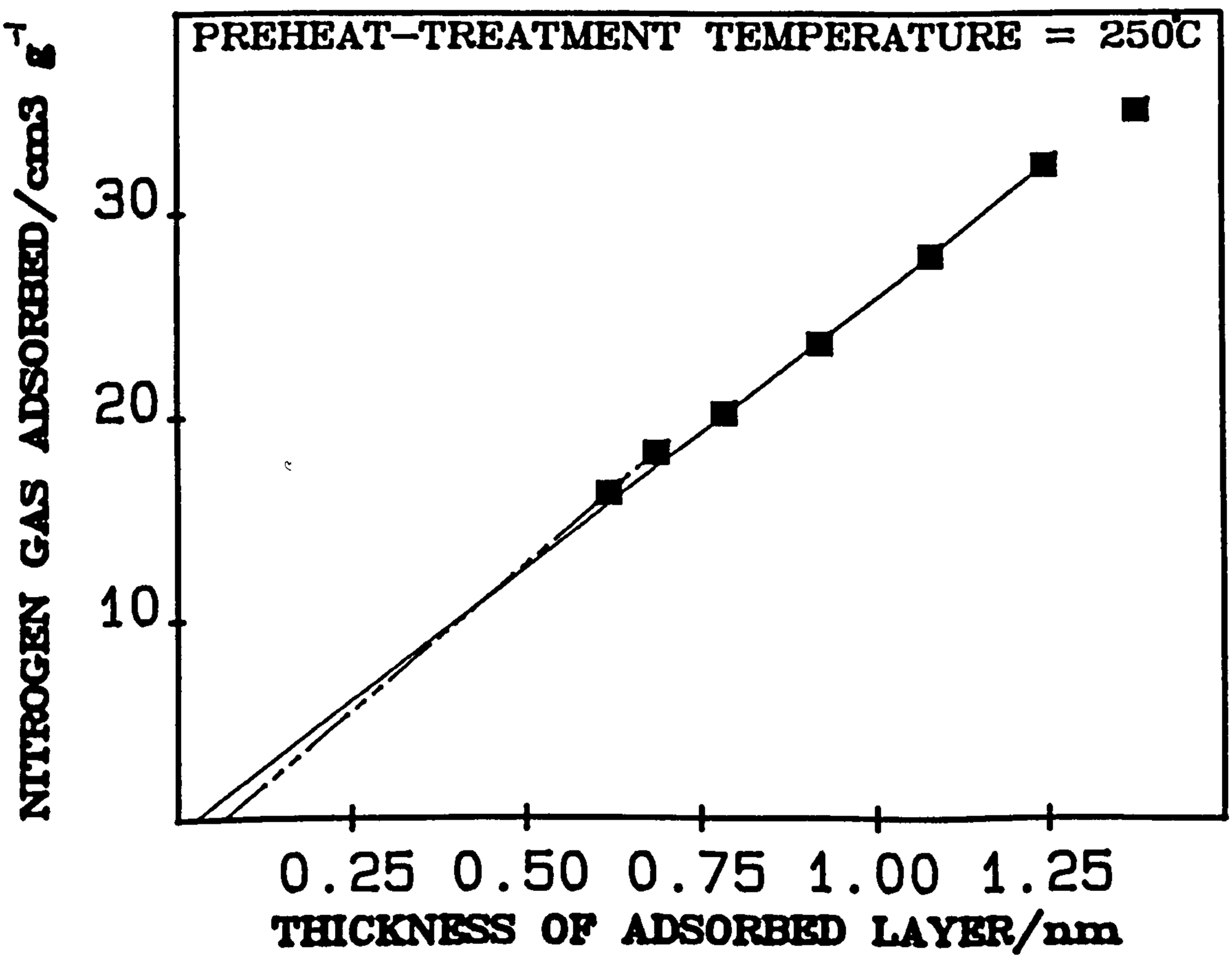

FIGURE A3.15

t–PLOT OF NITROGEN ON THE PRODUCT OF THE THERMAL TREATMENT OF ∝FeOOH TO 300°C.

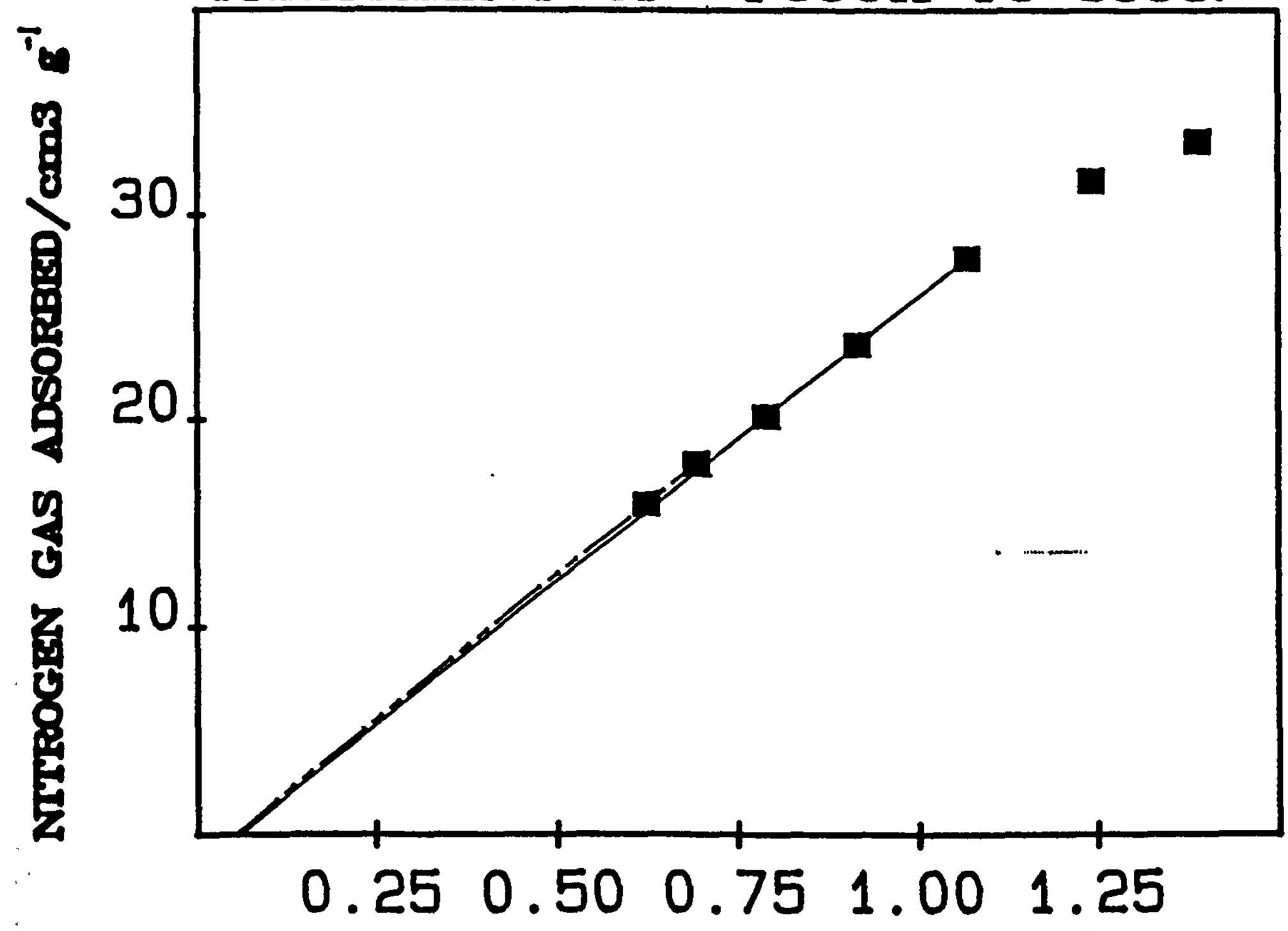

FIGURE A3.16

CALIBRATION CURVE OF THE THICKNESS OF ADSORBED NITROGEN ON A NON-POROUS ∝FeOOH AS A FUNCTION OF PARTIAL PRESSURE.

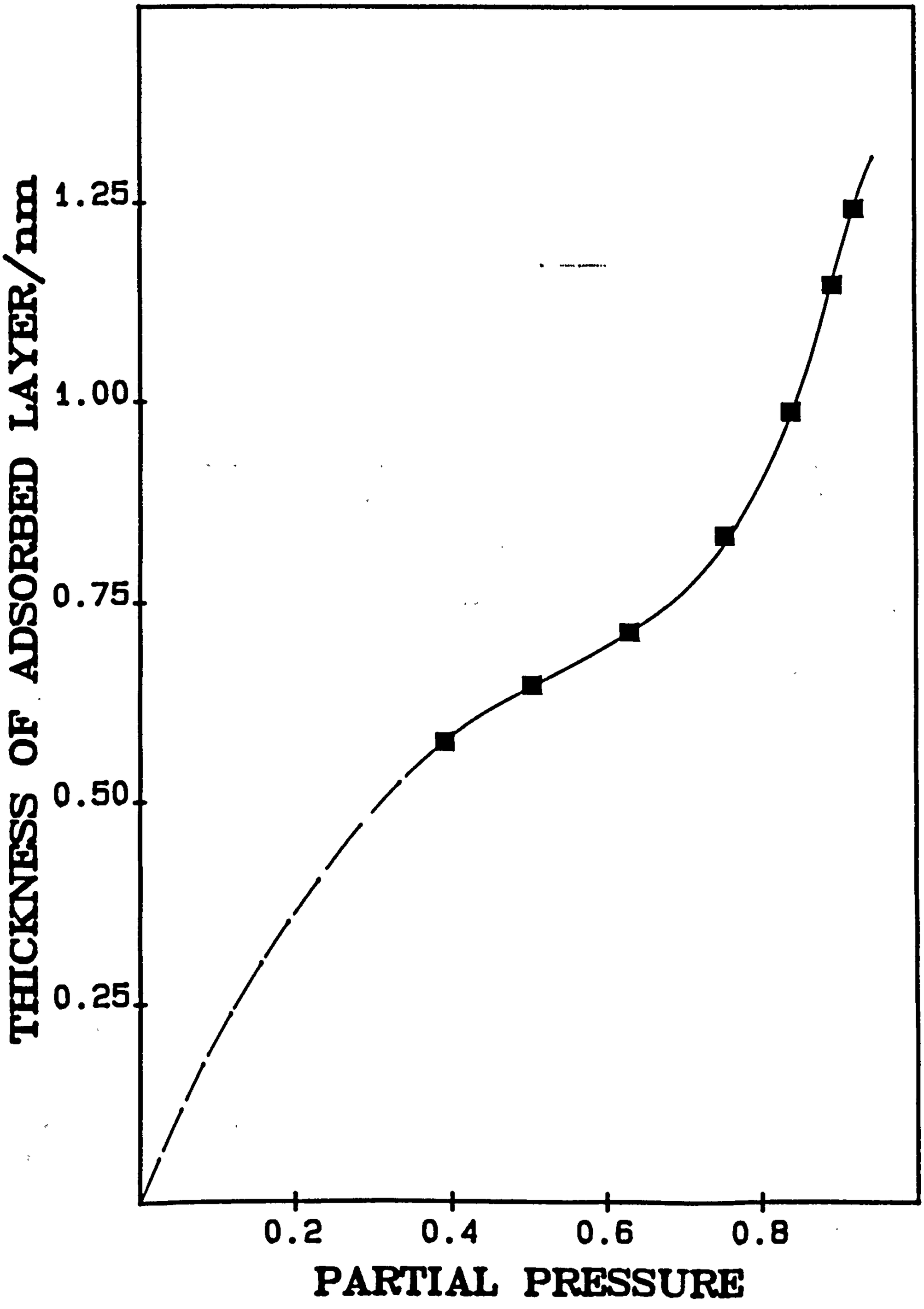

FIGURE A3.17

t–PLOTS OF NITROGEN ON ∝FeOOH AND THE PRODUCT OF ITS THERMAL TREATMENT TO 250°C.

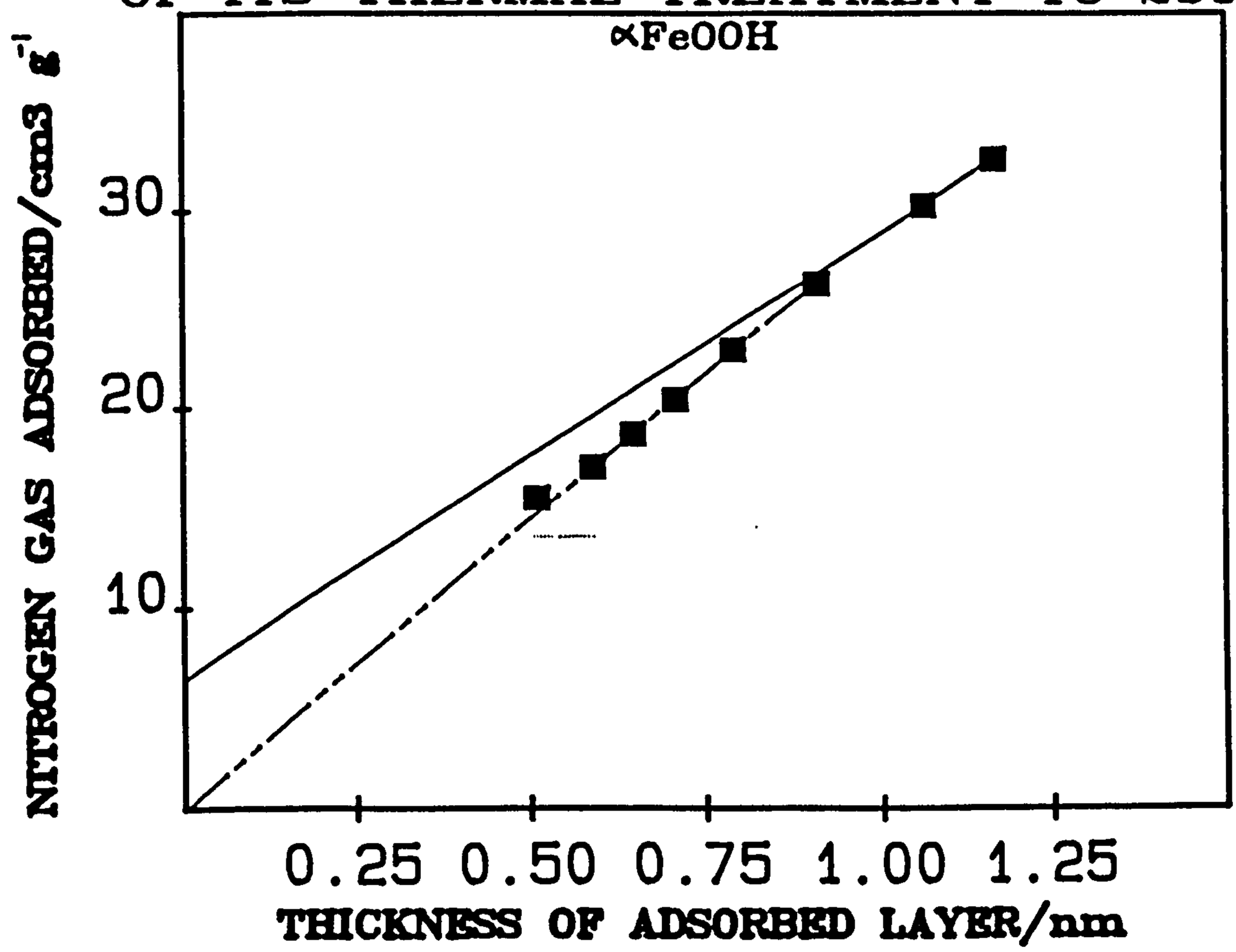

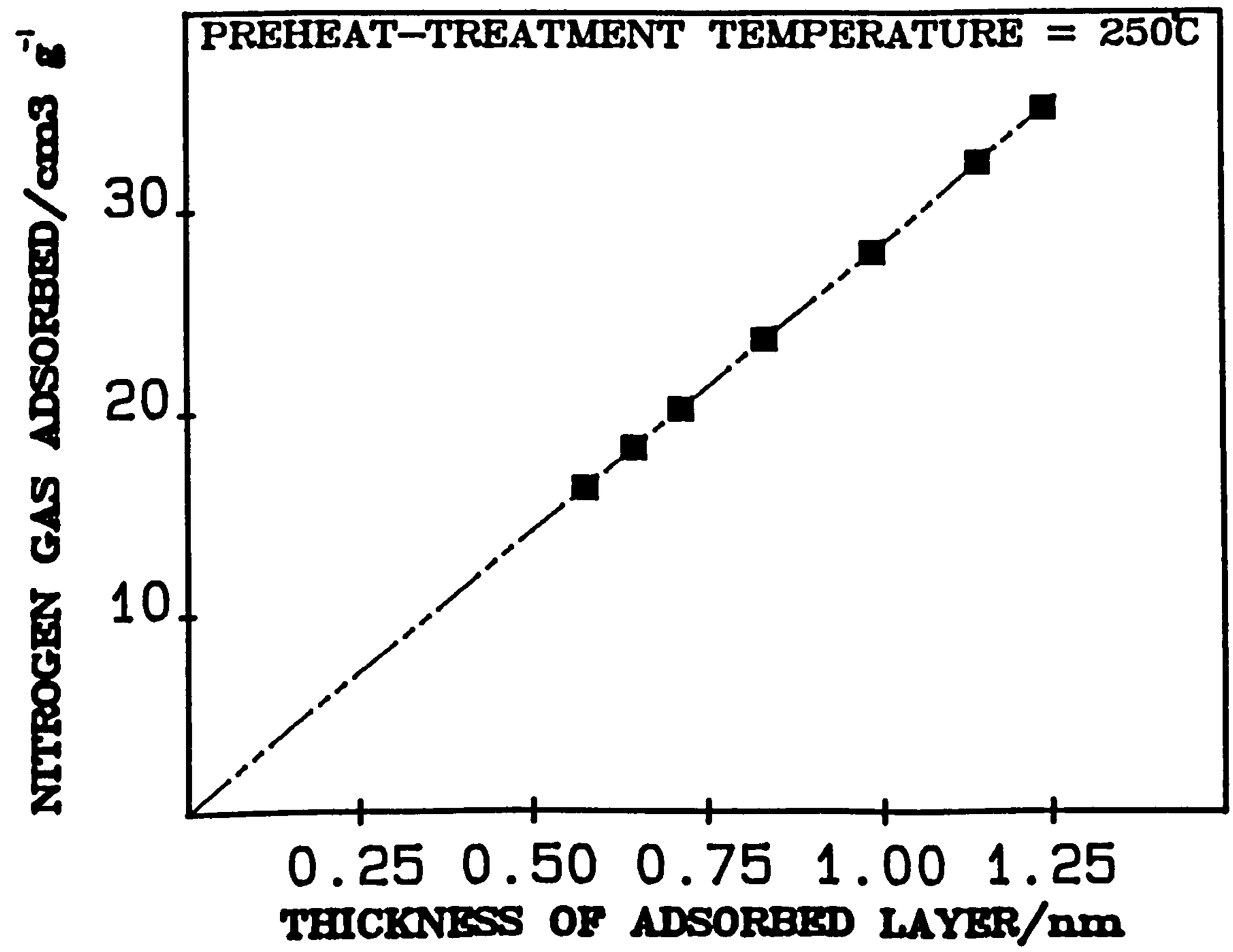

FIGURE A3.18

t–PLOTS OF NITROGEN ON THE PRODUCTS OF THE THERMAL TREATMENT OF ∝FeOOH TO 300 AND 350°C.

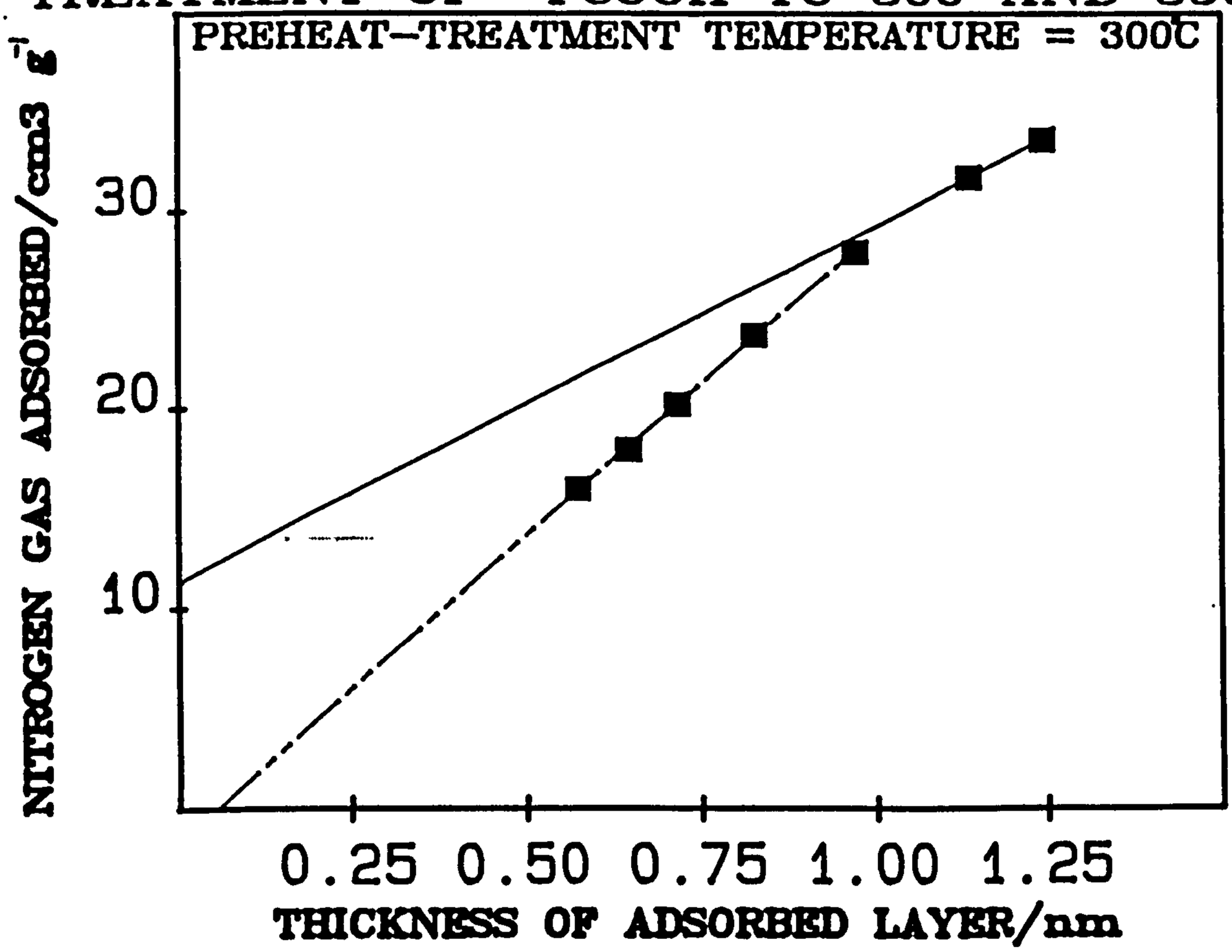

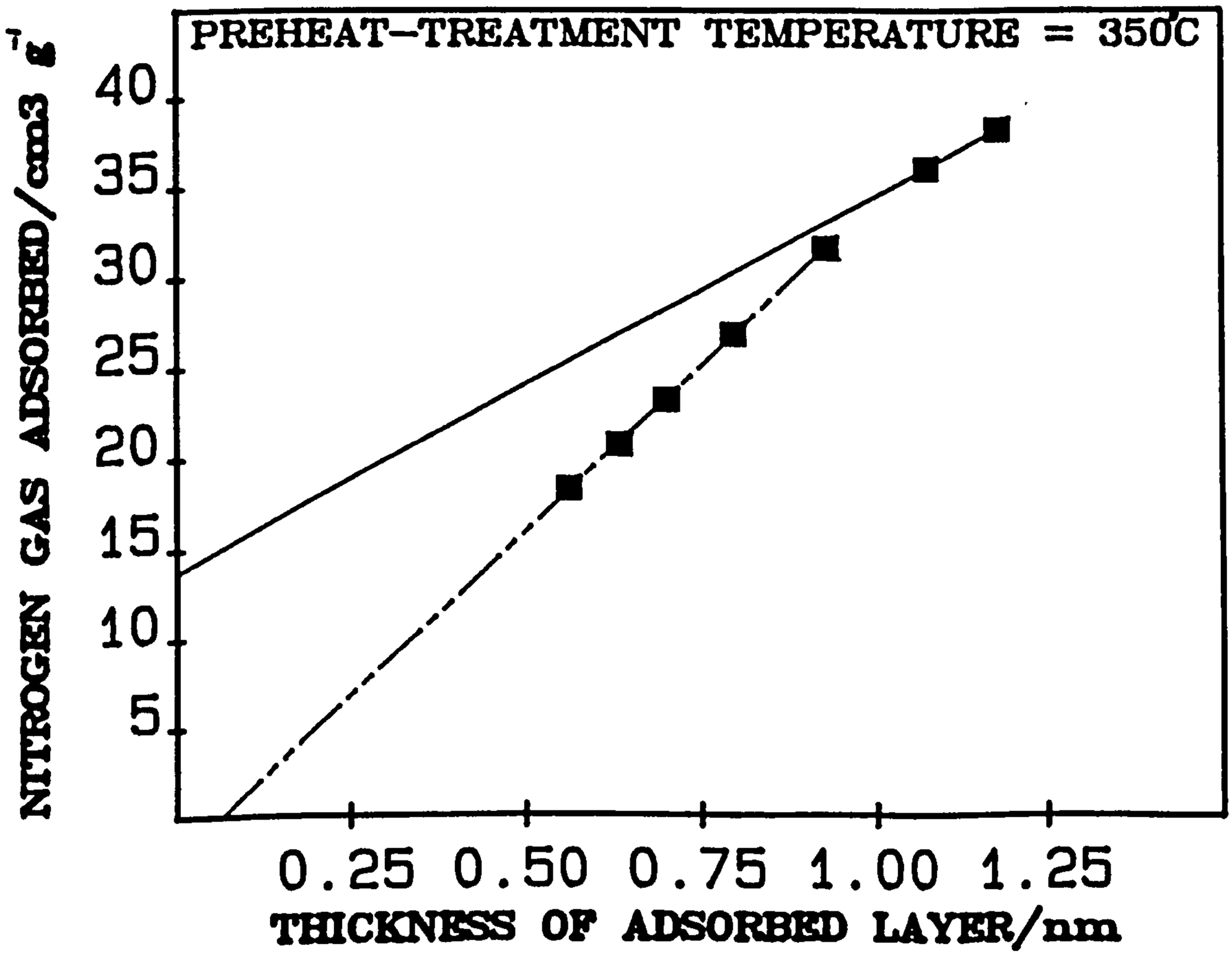

FIGURE A3.19

t–PLOTS OF NITROGEN ON THE PRODUCTS OF THE THERMAL TREATMENT OF ∝FeOOH TO 400 AND 450°C.

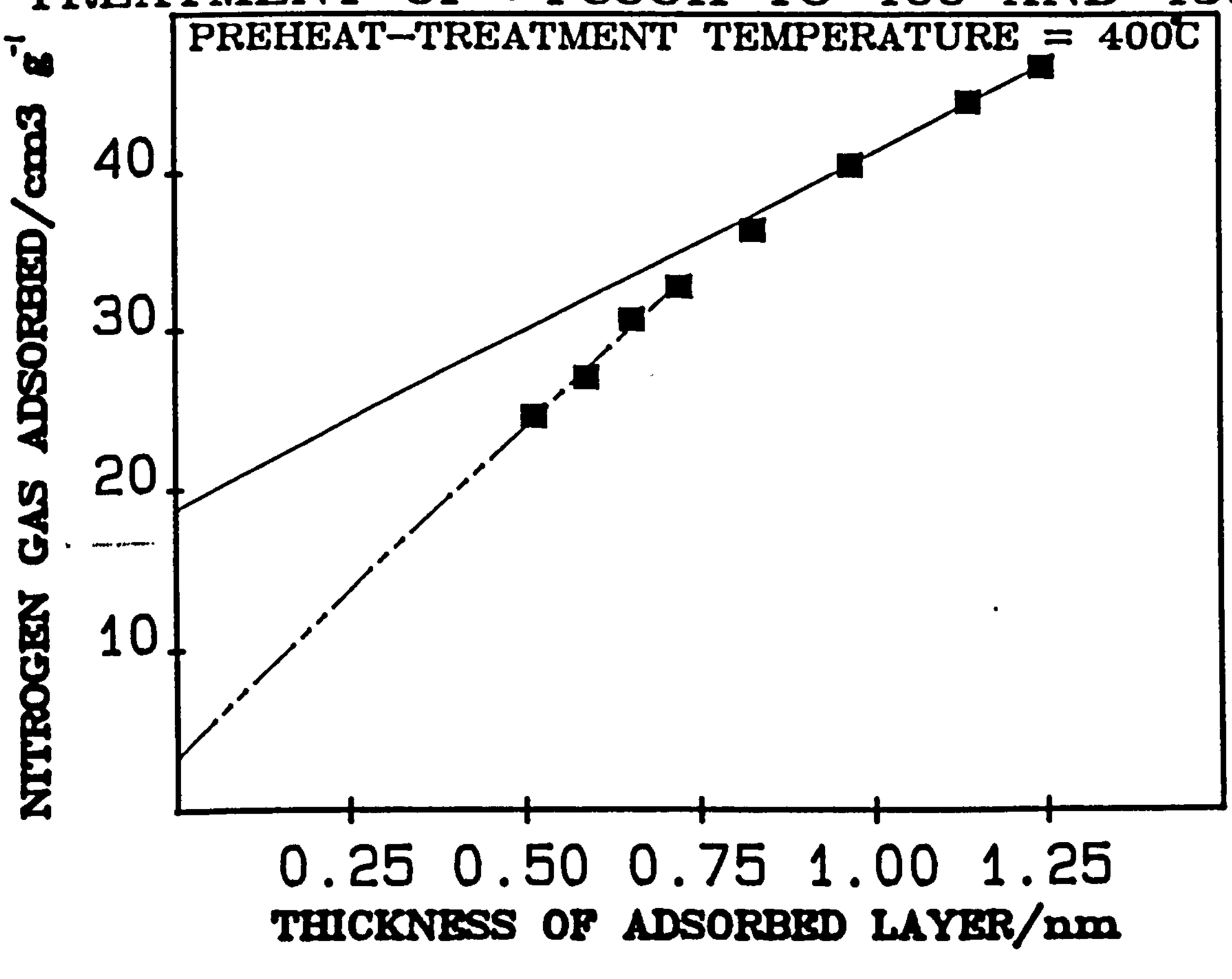

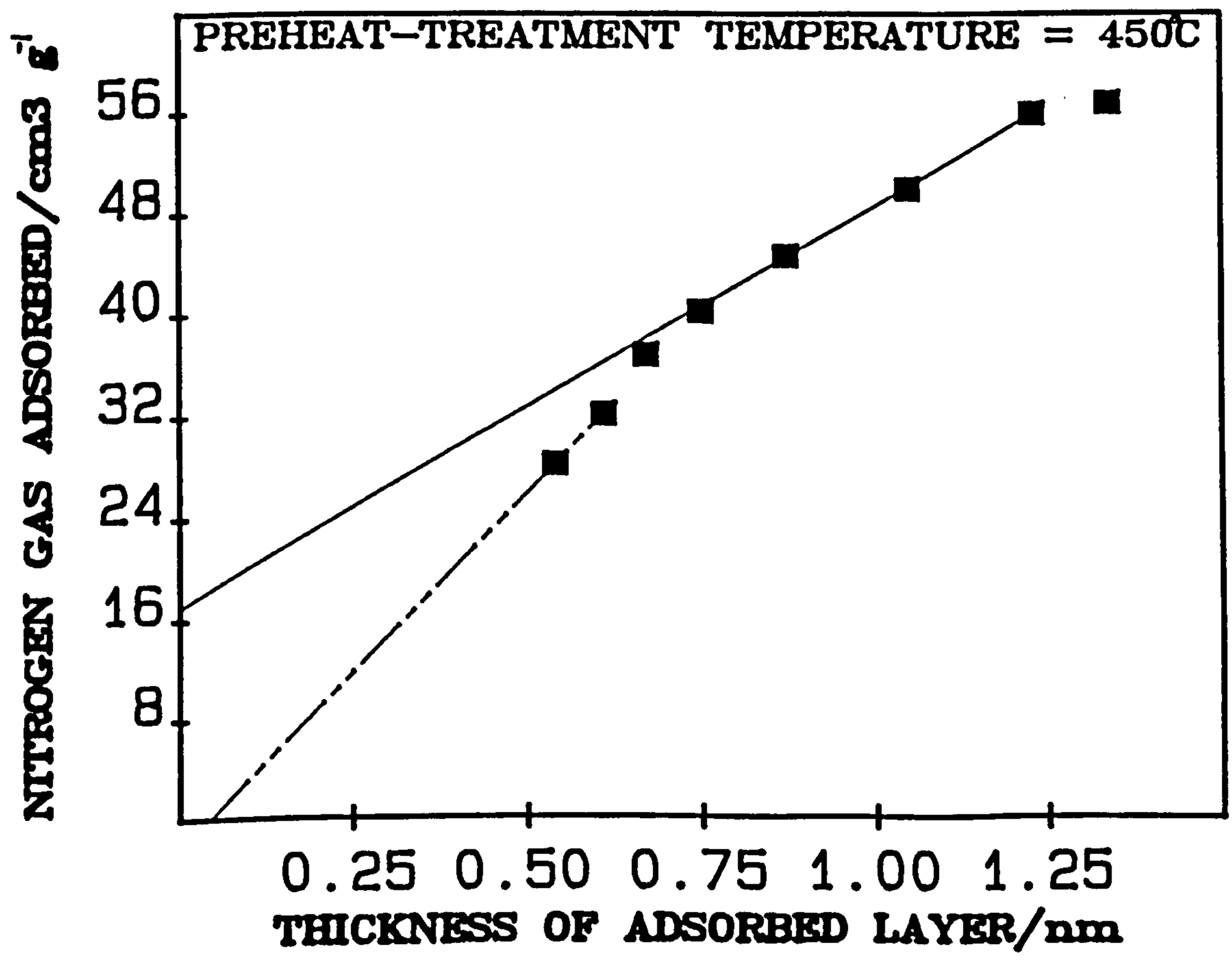

FIGURE A3.20

t–PLOTS OF NITROGEN ON THE PRODUCTS OF THE THERMAL TREATMENT OF ∝FeOOH TO 500 AND 705°C.

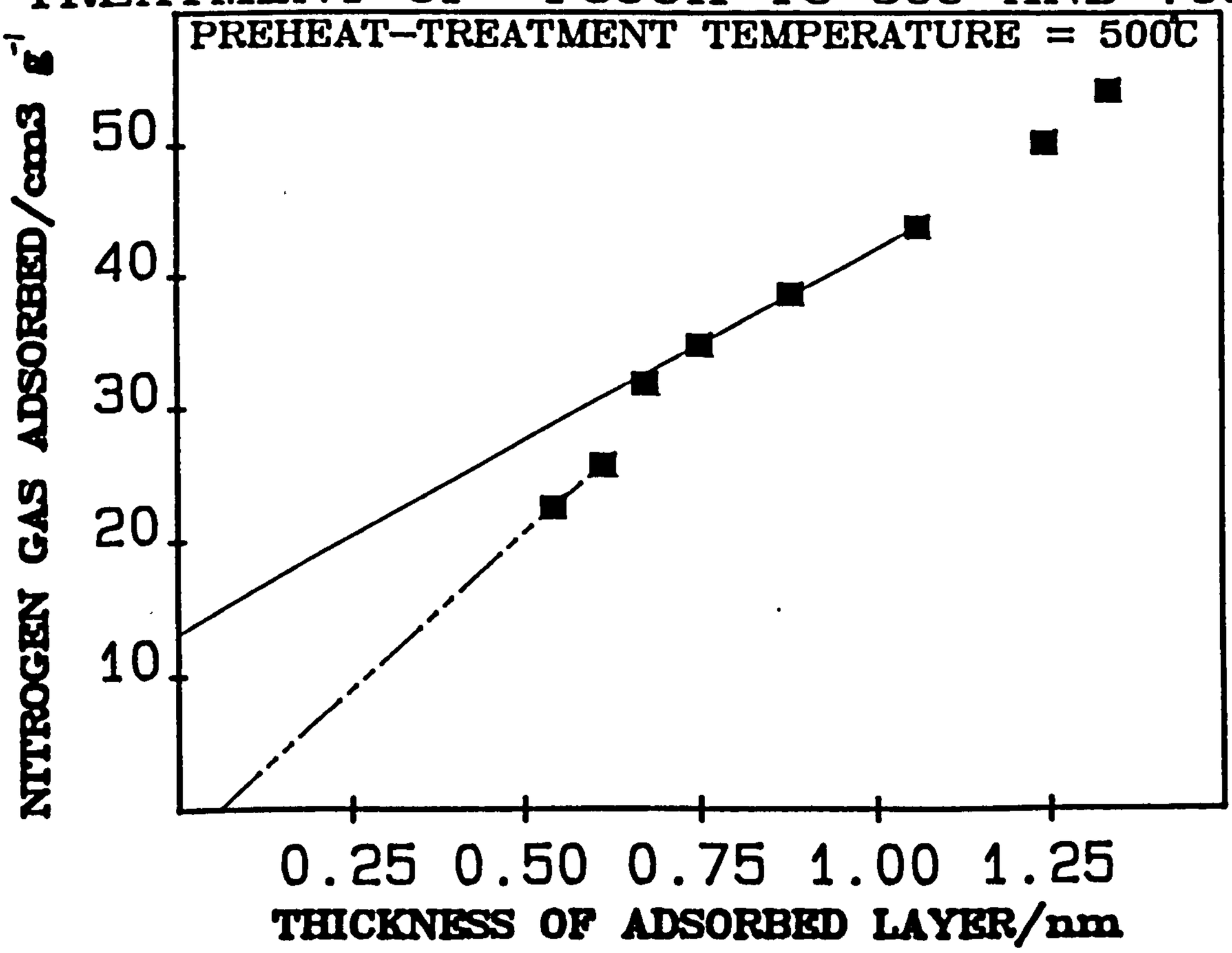

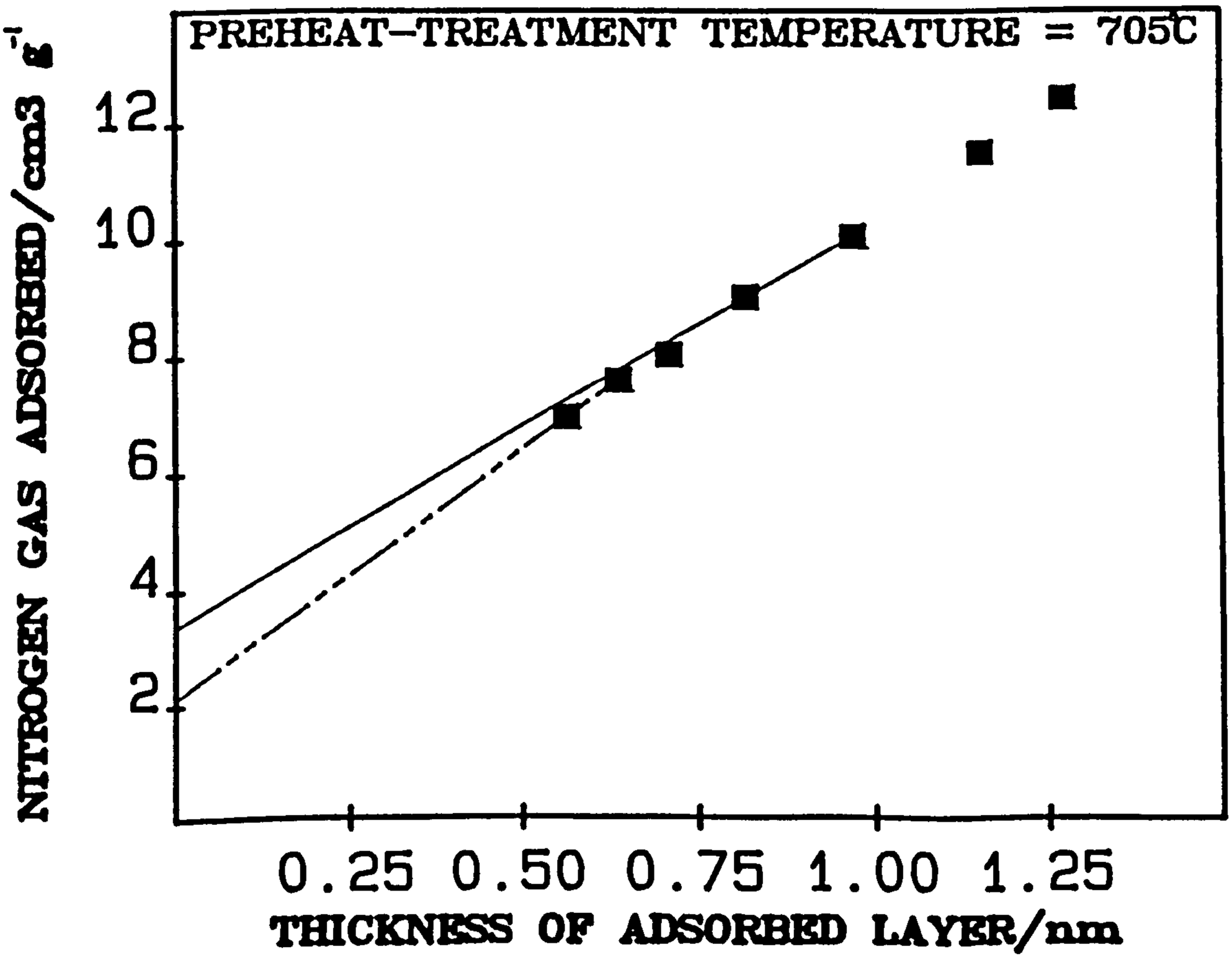

FIGURE A3.21

t–PLOT OF NITROGEN ON THE PRODUCT OF THE THERMAL TREATMENT OF αFeOOH TO 850°C.

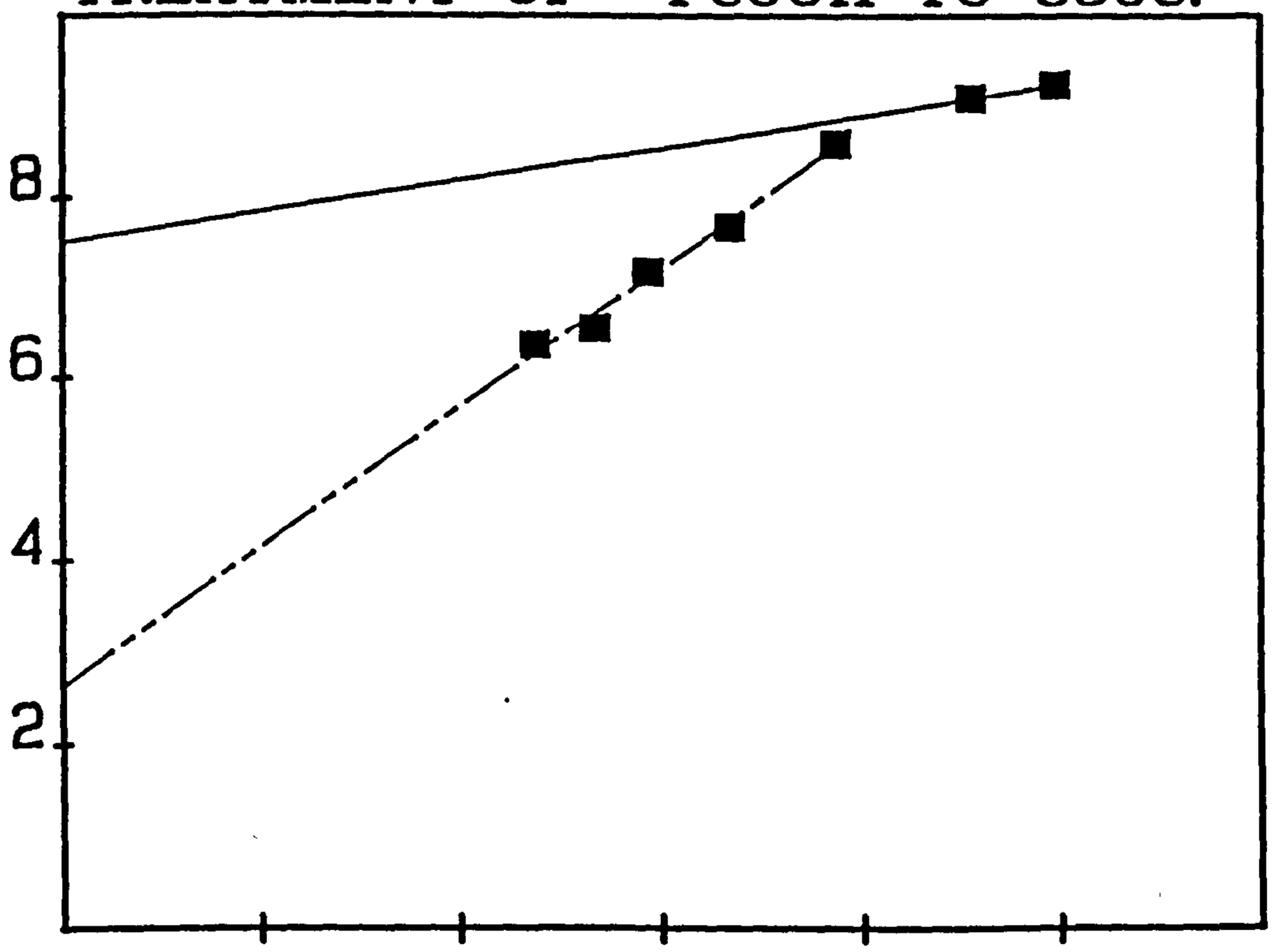

show downward deviations resulting in two straight lines per t-plot. This depressed adsorption indicates that these products, notably including the prepared αFeOOH and 850H, were microporous. In contrast, the t-plots corresponding to 500H and 705H show initial downward deviations from linearity followed, at high t-values, by upward deviations. The occurrence of both depressed and enhanced adsorption, over different ranges of t, indicates that capillary condensation of N_2 took place into both microporous and mesoporous regions of 500H and 705H.

The S_t^{Ex} and S^{MICR} values of the products, obtained from the slopes of the corresponding t-plots in conjunction with the S_{BET} values, are plotted (along with the S_{BET} values) against preheat-treatment temperature in Fig. A3.22. The S_t^{Ex} values of products formed at temperatures up to 500°C were fairly consistent at ca. 38 $m^2\ g^{-1}$, and significantly different from those of products formed at temperatures above 500°C.

The extrapolation to the ordinate of the less steep line, occurring after the initial change in slope, of the t-plot of each porous product gave the value of V_t^{MICR}.

400A had, in comparison with products formed at different temperatures, the greatest S^{MICR} and V_t^{MICR} values.

The t_I and L_p values of each porous product are given in Table A3.2(a). For each one of these products the L_p value is in close agreement with twice the value of t_I, suggesting that the pores of these products are best described as slit-shaped rather than cylindrically shaped.

4.2.3. Pore size distributions.

Mesopore analyses were carried out over the appropriate partial pressure range ($0.95 \geqslant \frac{p}{p_{SAT}} \geqslant 0.30$) using the N_2 desorption data and the t-values of the reference substance 250G. V^{TOT}, the volume of N_2 (expressed as a liquid) adsorbed over the mesopore range and the volume of liquid N_2 adsorbed by the micropores of all the products are plotted against preheat-treatment temperature in Fig. A3.23. Pore size distributions for the majority of the products are shown in Figs. A3.24 to A3.28, while the value (or values) of $\overline{r}_p$ ($(\overline{r}_p)_{MAX}$) corresponding to a maximum (or maxima) in

FIGURE A3.22

SPECIFIC SURFACE AREA OF ∝FeOOH AND THE PRODUCTS OF ITS THERMAL TREATMENT TO VARIOUS TEMPERATURES.

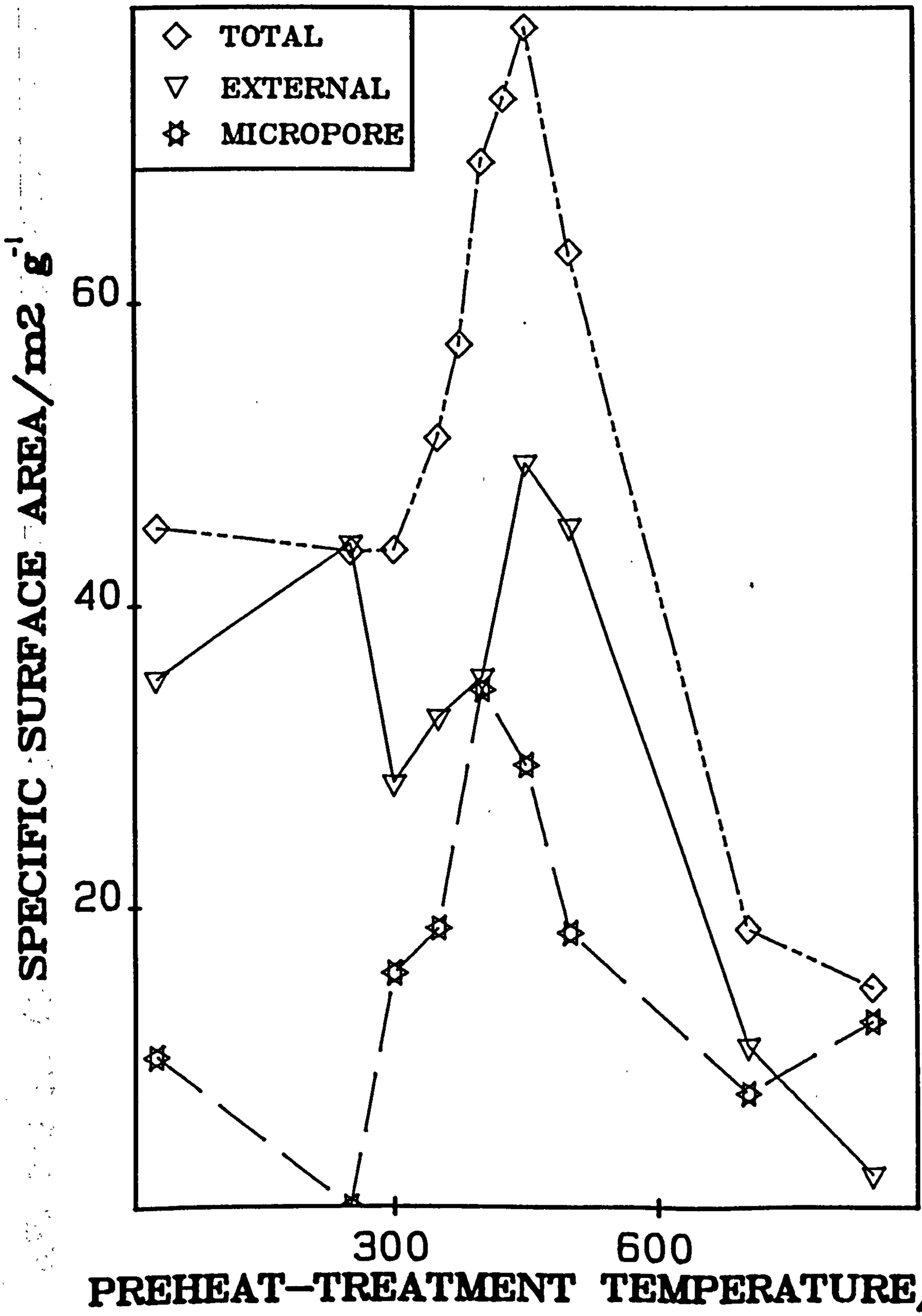

FIGURE A3.23

SPECIFIC VOLUME OF NITROGEN ADSORBED BY ∝FeOOH AND THE PRODUCTS OF ITS THERMAL TREATMENT TO VARIOUS TEMPERATURES.

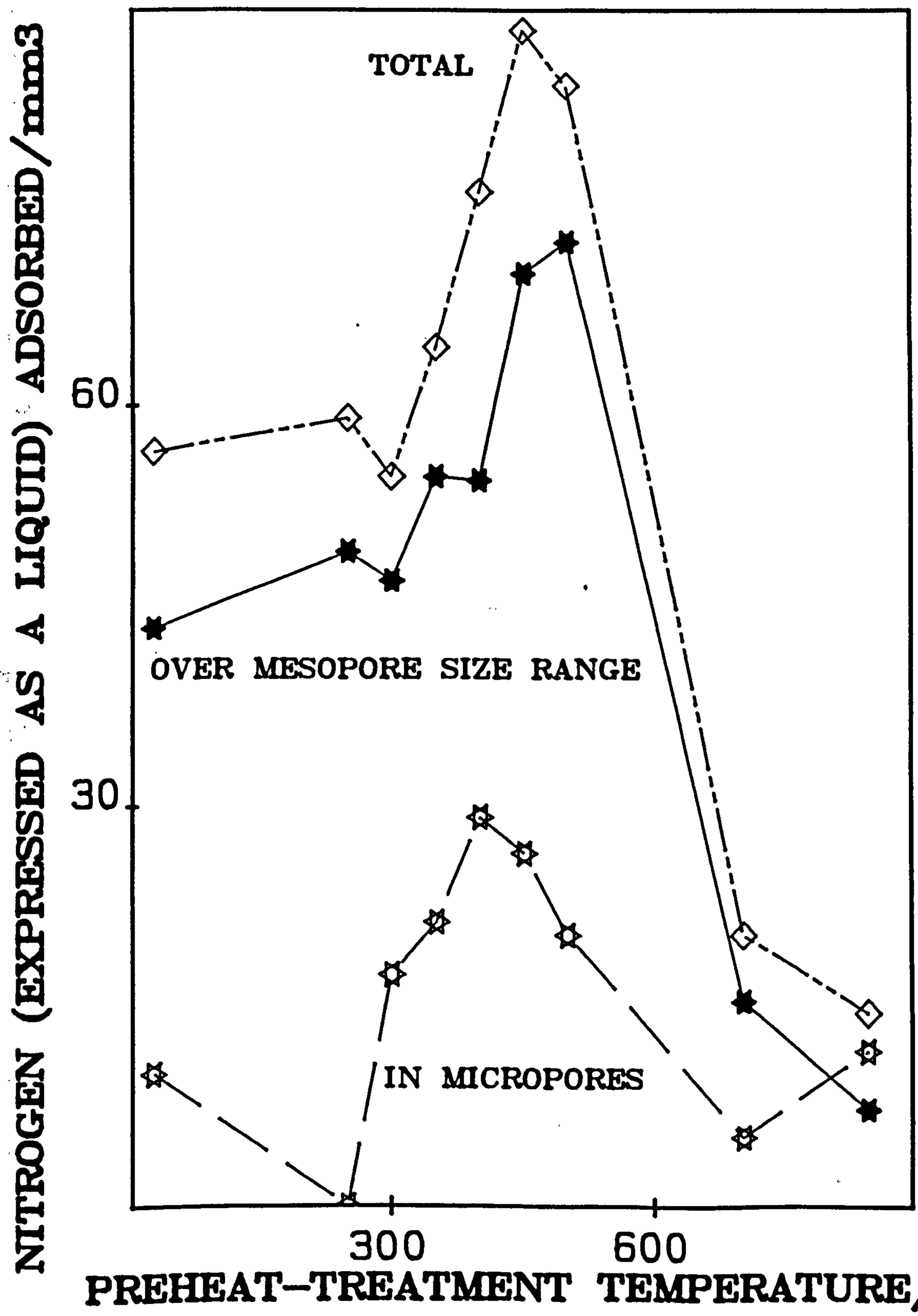

FIGURE A3.24

PORE SIZE DISTRIBUTIONS OF ∝FeOOH AND THE PRODUCT OF ITS THERMAL TREATMENT TO 250°C.

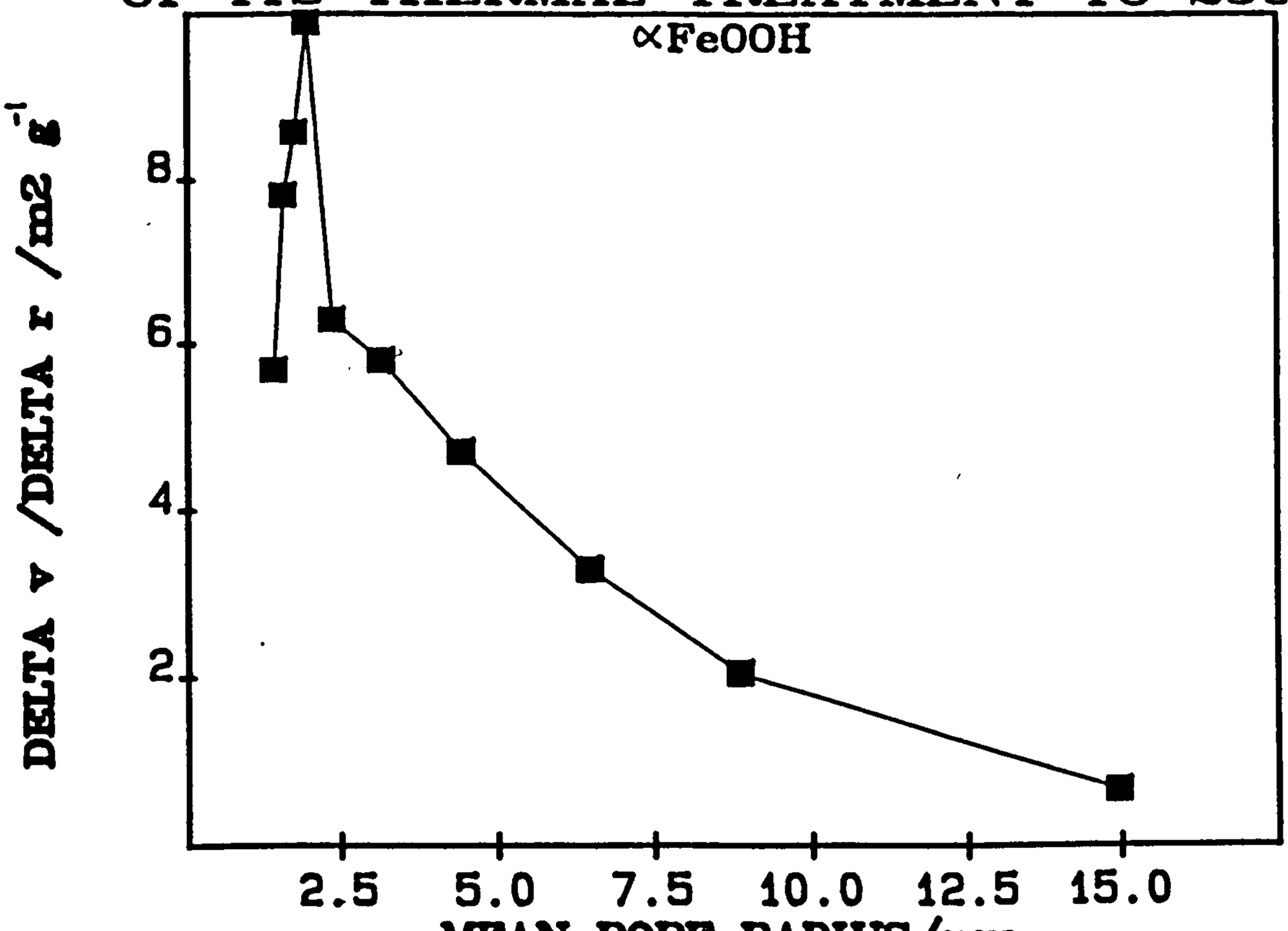

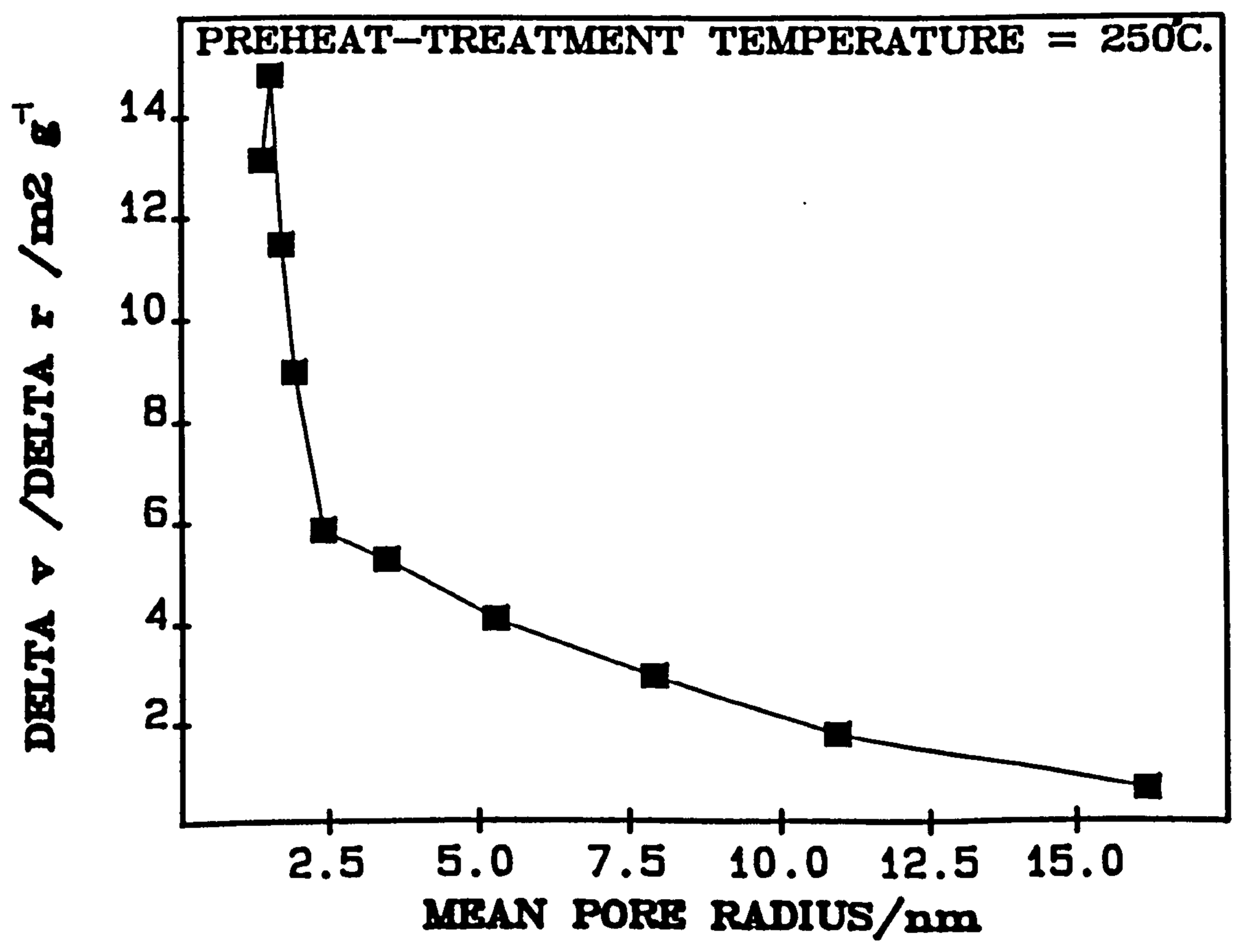

FIGURE A3.25

PORE SIZE DISTRIBUTIONS OF THE PRODUCTS OF THE THERMAL TREATMENT OF ∝FeOOH TO 300 AND 350°C.

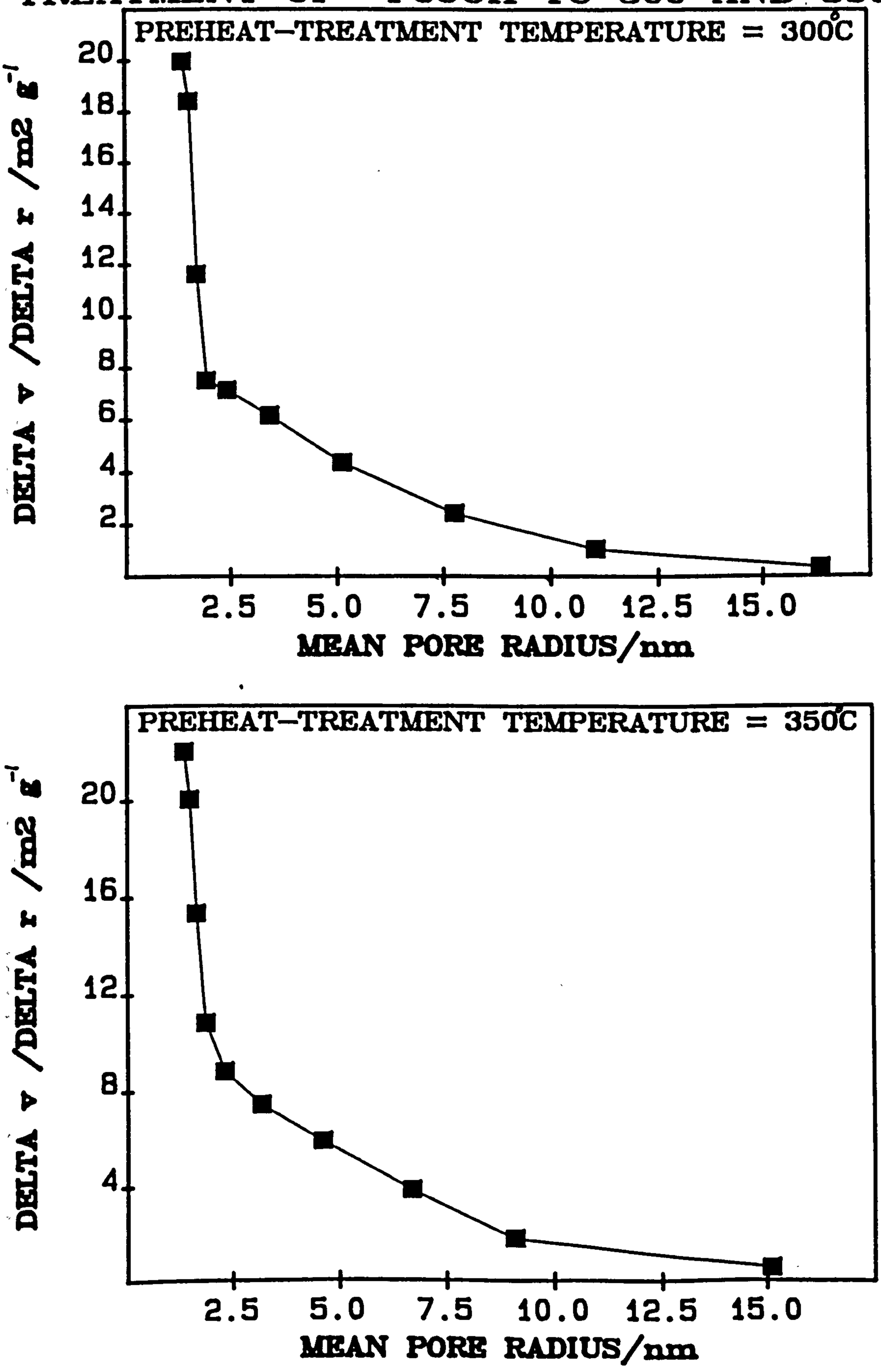

FIGURE A3.26

PORE SIZE DISTRIBUTIONS OF THE PRODUCTS OF THE THERMAL TREATMENT OF ∝FeOOH TO 400 AND 450°C.

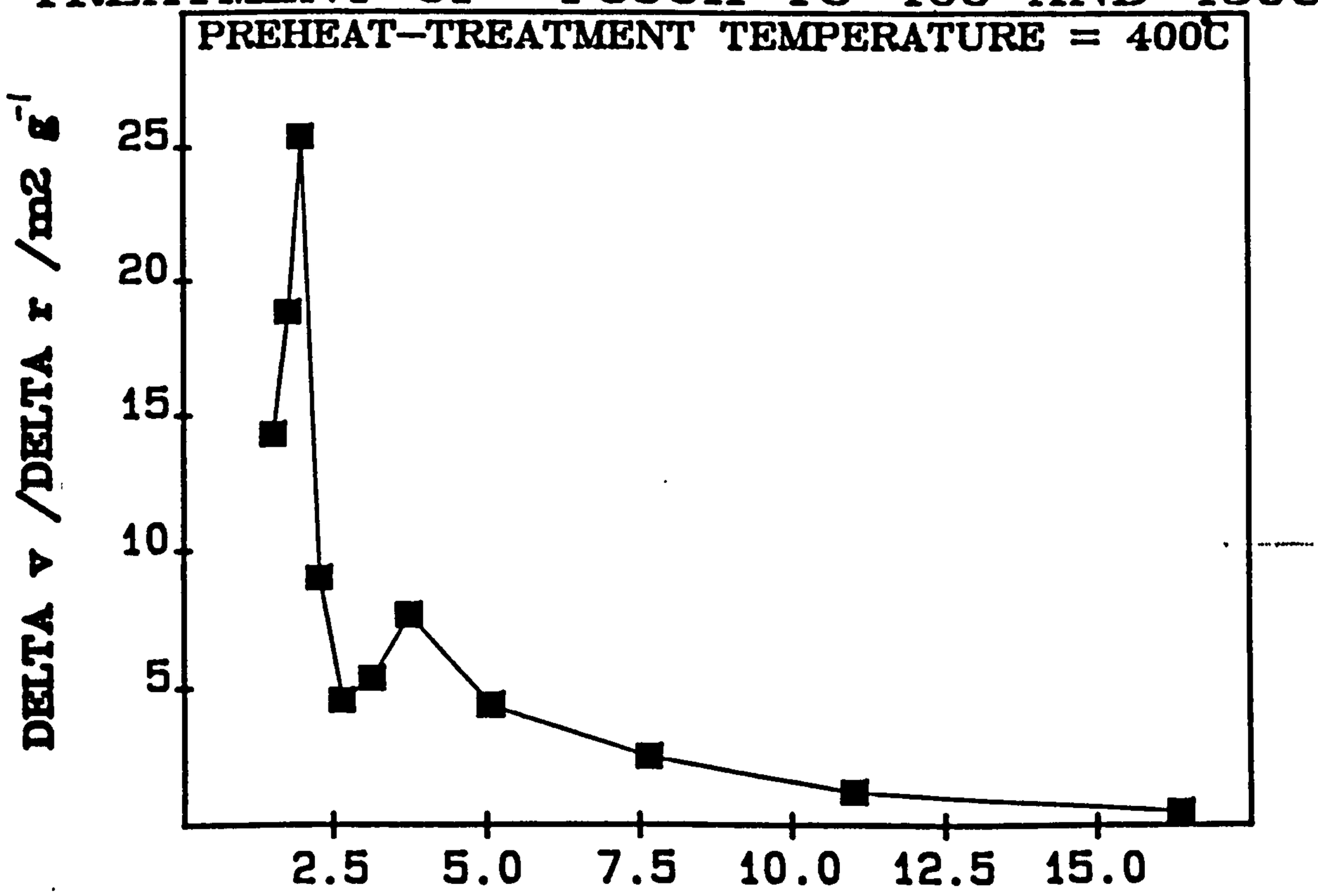

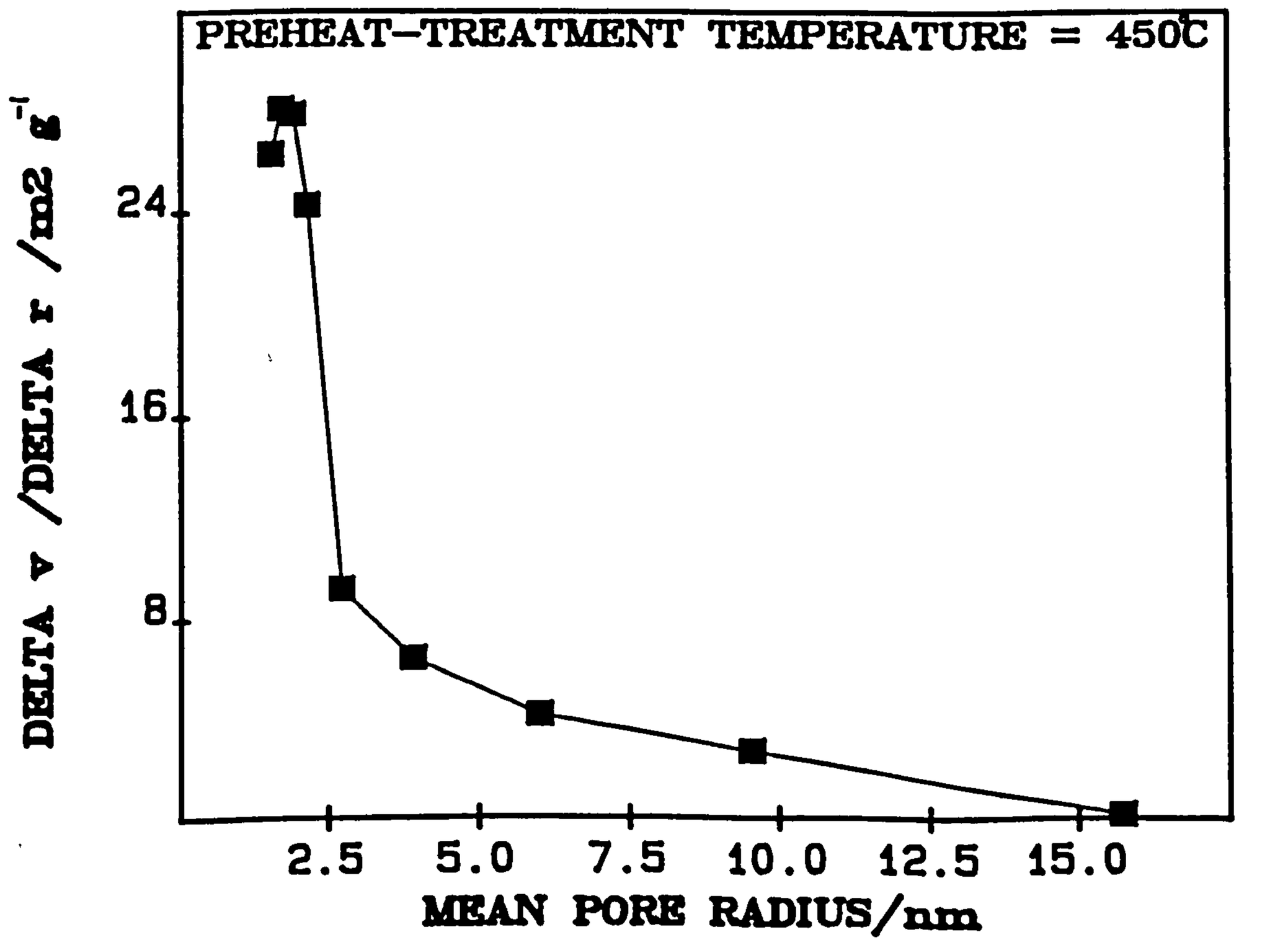

FIGURE A3.27

PORE SIZE DISTRIBUTIONS OF THE PRODUCTS OF THE THERMAL TREATMENT OF ∝FeOOH TO 500 AND 705°C.

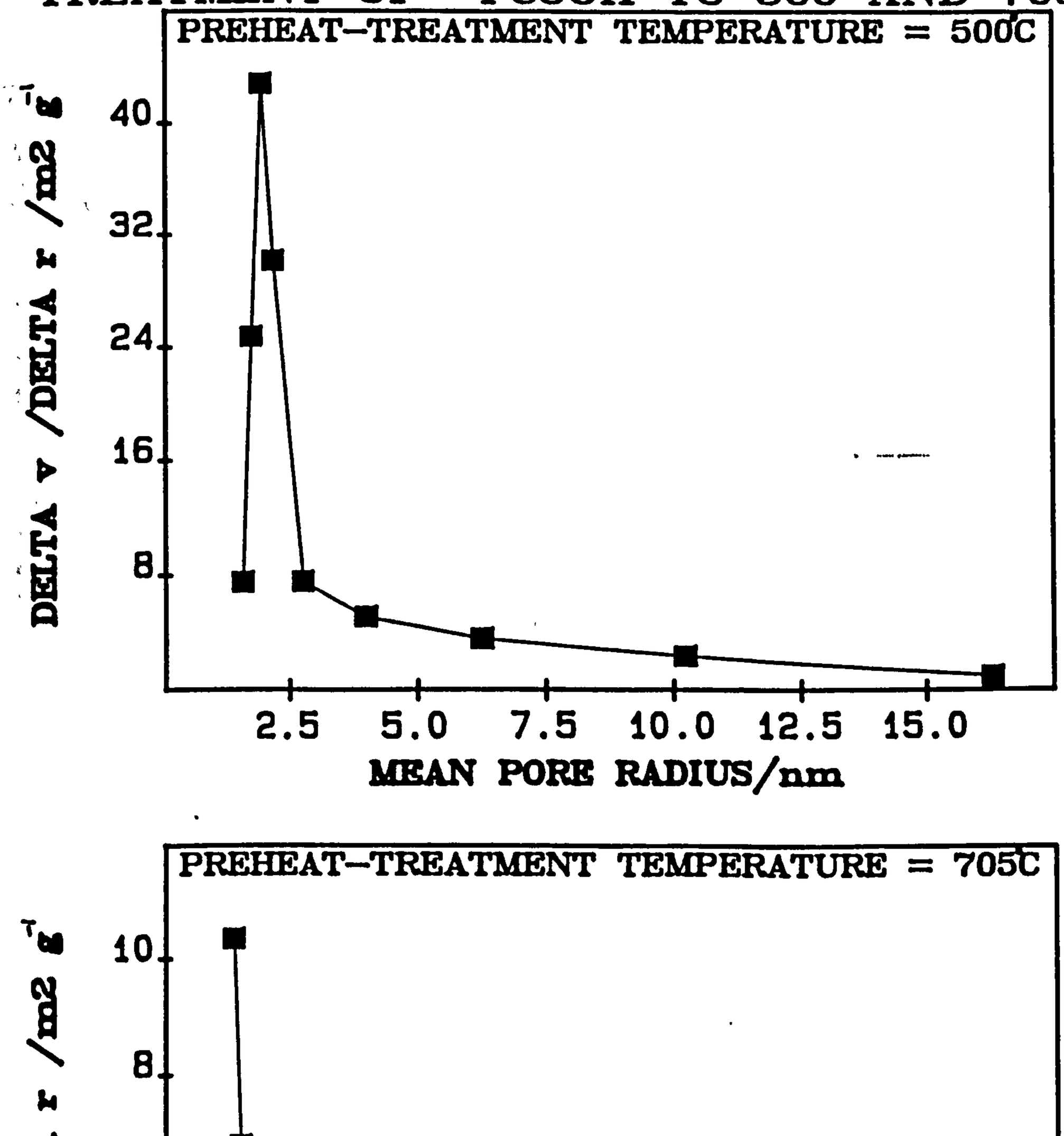

FIGURE A3.28

PORE SIZE DISTRIBUTION OF THE PRODUCT OF THE THERMAL TREATMENT OF αFeOOH TO 850°C.

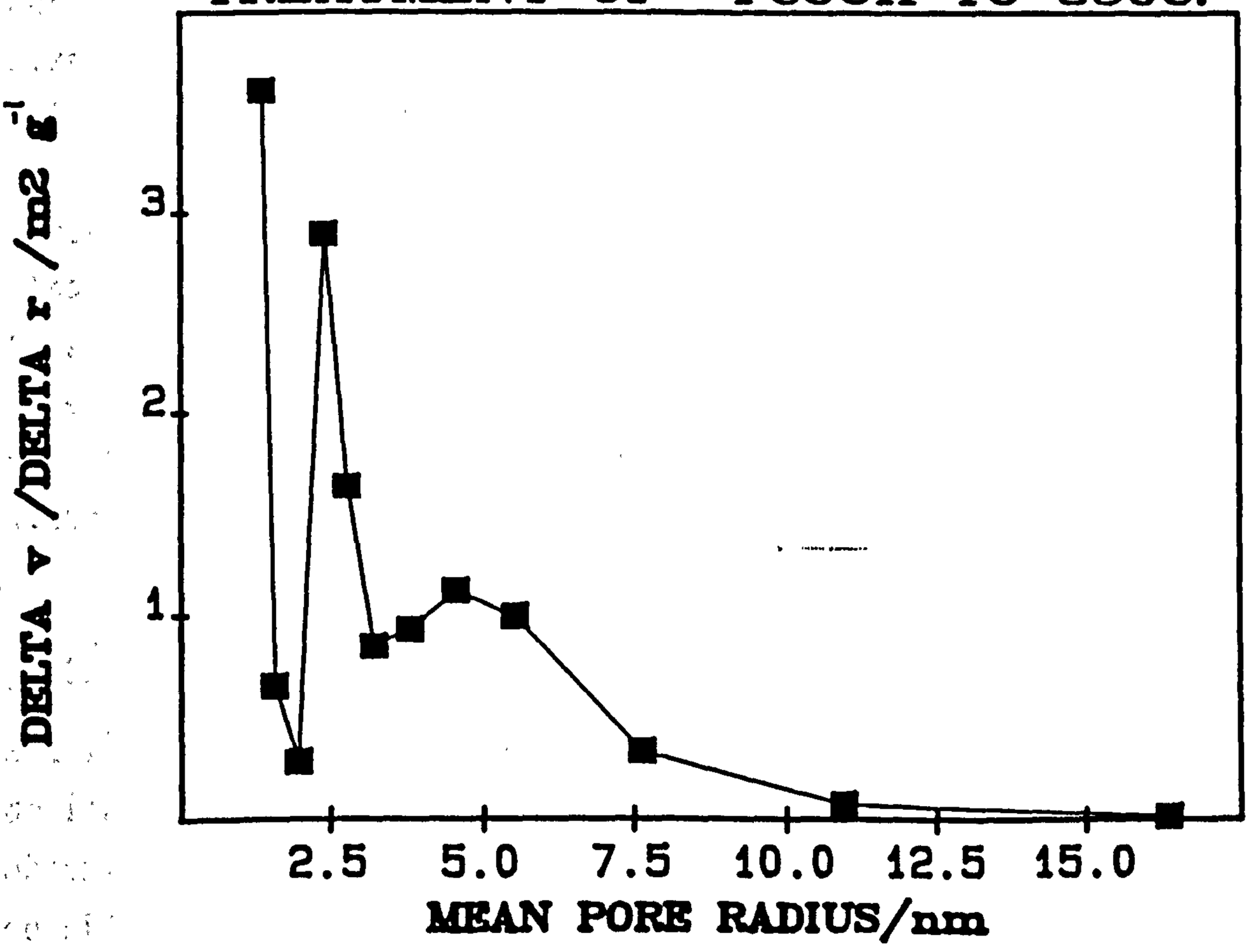

the pore size distribution of a product is (are) given in Table A3.2(a). In the case of amb. G, 250G, 450A and 500A, the $(\bar{r}_p)_{MAX}$ values were in close agreement with twice the corresponding values of t_I, whereas the value of $(\bar{r}_p)_{MAX}$ for 705H was in close agreement with four times the corresponding t_I value. The pore size distributions of 400A and 850H each have two maxima at values of $\bar{r}_p$ that were twice and, approximately, four times the corresponding t_I values. However, the maxima occurring ca. $4t_I$ in the pore size distributions of 400A and 850H are of a relatively low intensity. This evidence suggests that in 705H there were slit-shaped pores (mesopores) that had each been formed by the coalescence of two smaller slit-shaped pores (micropores). Although the pore size distribution evidence would also suggest the possible existence of such mesopores in 400A and 850H, this evidence is not corroborated by t-plot analysis. The results for 500H were also slightly ambiguous in that a suggestion of mesoporosity in the t-plot of this product was not supported by the corresponding pore size distribution.

The deviations of the cumulative measures S_p^{MESO} and V_p^{MESO}, and the sums $S_p^{MESO} + S^{MICR}$ and $V_p^{MESO} + V_t^{MICR}$, from the corresponding total values S_{BET} and V^{TOT} are given in Table A3.2(b) for each product. Noticeably larger deviations of S_p^{MESO} and V_p^{MESO} from the corresponding total values are observed for amb. G, 400A, 705H and 850H reflecting the absence of any consideration of the micropores present in these products, in the present cumulative mesopore analysis. In contrast, the sums $S_p^{MESO} + S^{MICR}$ and $V_p^{MESO} + V_t^{MICR}$ agree particularly well with the corresponding total values for 400A, 450A and 500A.

4.3. IR absorptions.

The IR absorption spectra of the products are shown in Figs. A3.29 to A3.31, and the frequencies of the absorption bands of each product are given in Table A3.3. The characteristic OH bending bands of αFeOOH (at ca. 892 cm^{-1} and 795 cm^{-1}) were only present in the spectra of amb. G, 250G, 300G and 350GA. This suggests that IR detectable quantities of αFeOOH were only present in those products formed at temperatures up to 350°C. The OH bending band at ca. 892 cm^{-1} in the spectra of 250G, 300G and 350GA became progressively sharper with increasing preheat-treatment temperature. However, the 892 cm^{-1} OH bending band in the spectrum of amb. G was significantly sharper than that in the spectrum of 250G. The spectra of

Table A3.2(b)

Areal and volumetric data of a prepared αFeOOH and products formed by preheating this αFeOOH to various temperatures.

preheat-treatment temperature	$\frac{(S_{BET} - S_p^{MESO})100}{S_{BET}}$	$\frac{(V^{TOT} - V_p^{MESO})100}{V^{TOT}}$	$\frac{(S_{BET} - (S_p^{MESO} + S^{MICR}))100}{S_{BET}}$	$\frac{(V^{TOT} - (V_p^{MESO} + V_t^{MICR}))100}{V^{TOT}}$
°C	%	%	%	%
ambient	49.0	23.5	26.7	5.8
250	39.2	16.7	39.2	16.7
300	33.6	13.7	- 2.1	-18.0
350	34.5	15.0	- 1.9	-18.2
400	50.0	28.5	0.6	- 9.9
450	37.9	21.1	0.7	- 8.8
500	29.2	14.2	0.5	- 9.8
705	56.1	24.1	14.6	- 1.5
850	70.6	50.3	-11.4	-31.0

FIGURE A3.29

INFRARED ABSORPTION SPECTRA OF ∝FeOOH AND THE PRODUCTS OF ITS THERMAL TREATMENT TO VARIOUS TEMPERATURES UP TO 350°C.

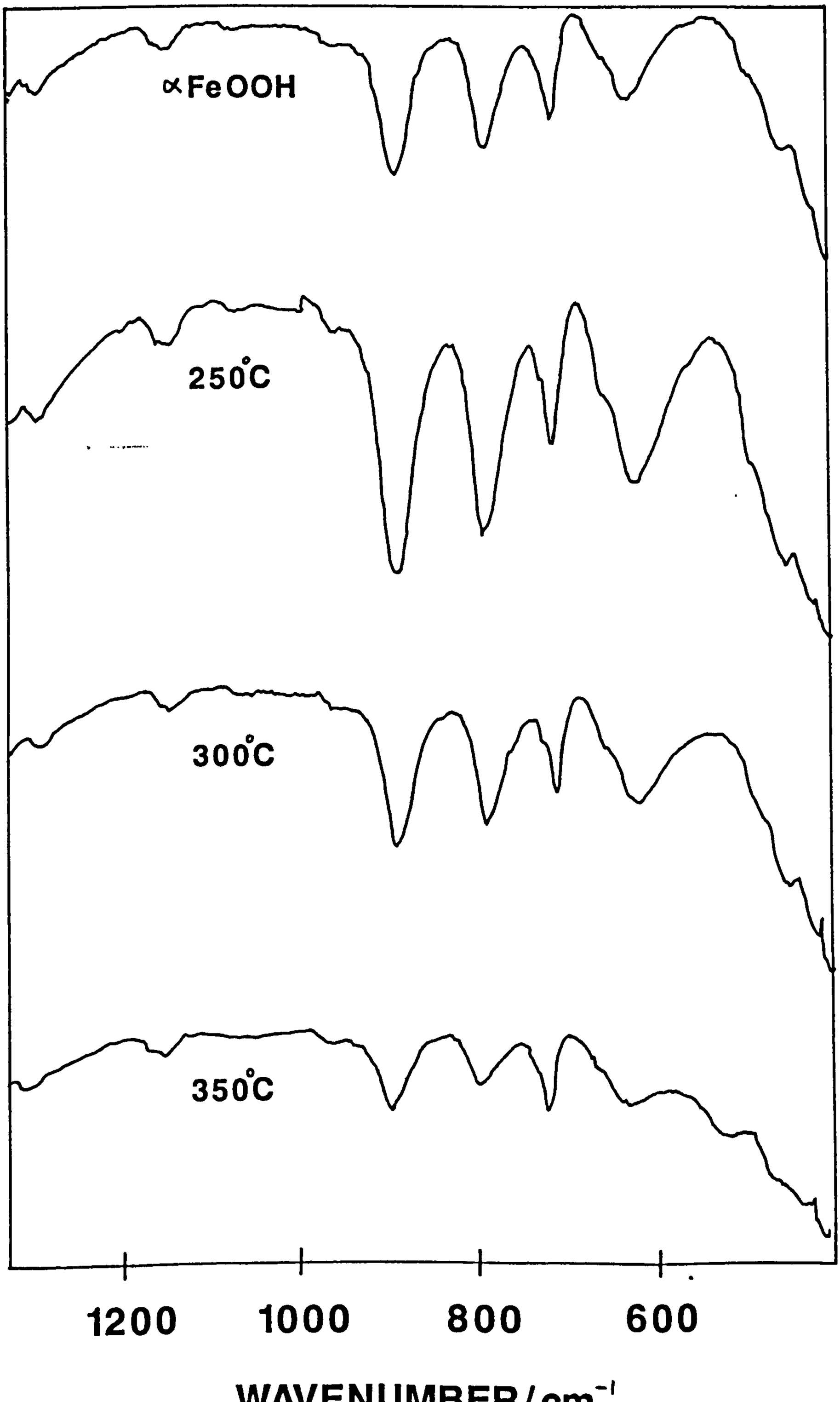

FIGURE A3.30

INFRARED ABSORPTION SPECTRA OF THE PRODUCTS OF THE THERMAL TREATMENT OF αFeOOH TO VARIOUS TEMPERATURES UP TO 450°C.

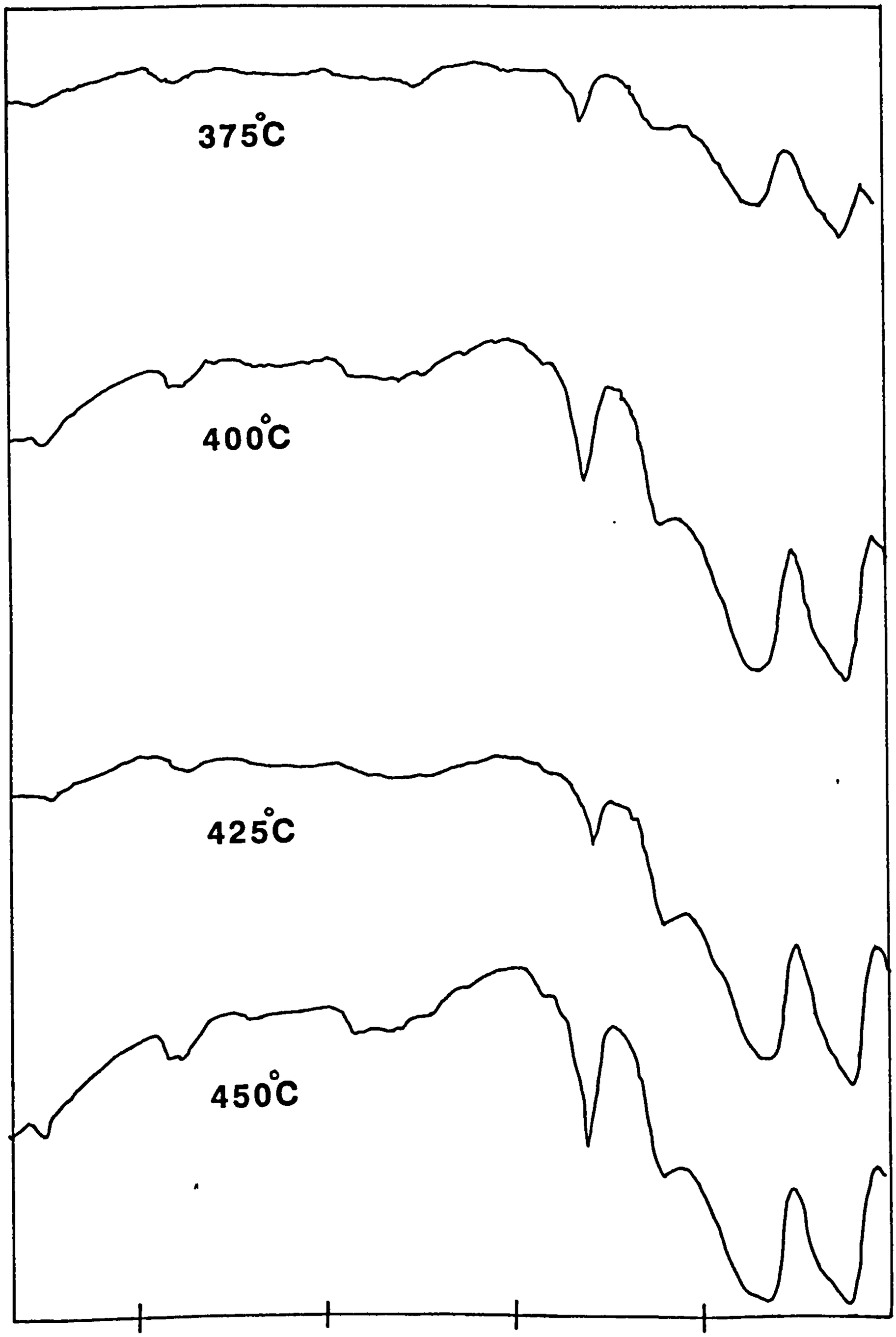

FIGURE A3.31

INFRARED ABSORPTION SPECTRA OF THE PRODUCTS OF THE THERMAL TREATMENT OF αFeOOH TO VARIOUS TEMPERATURES UP TO 850°C.

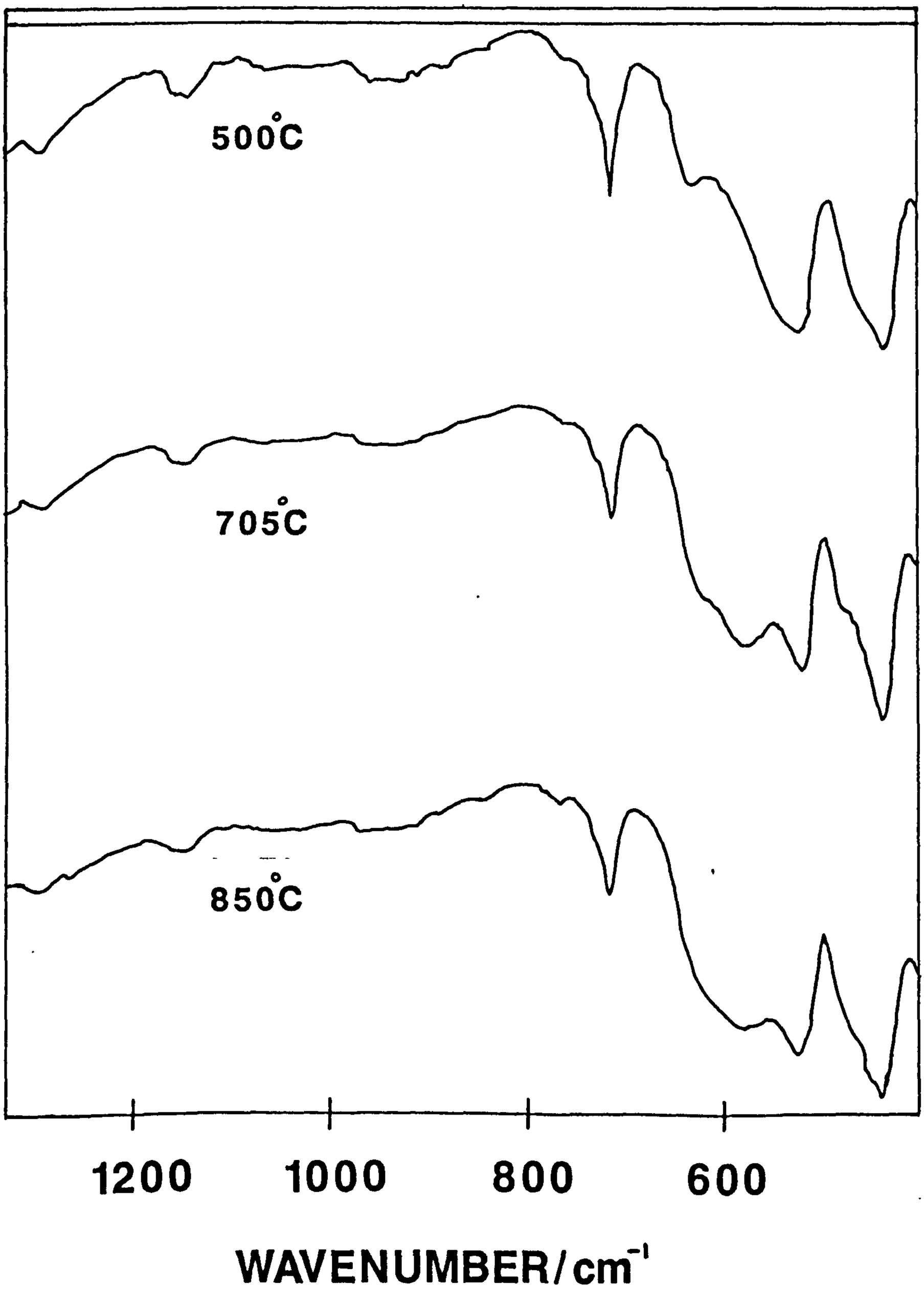

Table A3.3

Infrared absorption bands (in wavenumbers) of αFeOOH
and the products of its thermal treatment to various temperatures.

	Preheat-treatment temperature/°C									
αFeOOH	250	300	350	375	400	425	450	500	705	850
402	402	401	402-405							
	408									
	420-422	420								
	427		426-431							
				439	442	439	438-441	438	439	438
452-454		454								
		458								
			516							
				523-531	527-530	528-532	528	530	522	523
									578	579
			624							
629-633	624-632	623-629	630	618-641	636-638	643	642	640	621	
			636							
791-693	797	794	795							
892	894	892	895							

375A, 400A, 425A, 450A and 500A were very similar. The spectra of 705H and 850H were also similar, but different from those of 500A, 450A etc.. Noticeably, the absorption band at 640 cm^{-1} in the spectrum of 500A was shifted to a lower frequency (621 cm^{-1}) in the spectrum of 705H. Furthermore, the absorption (O^{2-} displacement) at 530 cm^{-1} in the spectrum of 500A was apparently split into two bands (at 522 cm^{-1} and 582 cm^{-1}) in the spectrum of 705H. The frequency of the absorption band (O^{2-} displacement) at ca. 439 cm^{-1} in the spectra of products formed at temperatures above 350°C was apparently independent of preheat-treatment temperature.

4.4. SEM data.

Electron micrographs of 400A are shown in Plate A3.2, and those of 850H are shown in Plate A3.3. These micrographs may be compared with those shown earlier (Chapter A1) for amb. G. The micrographs shown here are not of a particular good standard, due to poor focussing, but some salient features of the particles are distinguishable. In comparison with the particles of amb. G, the particles of 400A have a more irregular size and shape. The surfaces of the particles of 400A appear to be covered with disc-like structures having a diameter of ca. 20 nm; these structures are most apparent in Plate 4. In contrast, the particles of 850H are of a more regular size and shape, with a smooth surface that contains no disc-like structures. The length and width of these smooth particles are ca. 310 nm and 60 nm, respectively. If it is assumed that the geometric shape of these elongated particles is cylindrical with hemi-spherical ends, then it is possible to calculate (by the insertion of the relevant dimensional information into eqn. A1.3) the specific surface area of these particles to be 2.85 $m^2\ g^{-1}$ (based on a density of 5.2749g cm^{-3} (Weast)). This area is very similar to the external area (2.18 $m^2\ g^{-1}$) of these particles, as evaluated by t-plot analysis, and such a similarity indicates a correctness in the assumed particle shape of 850H.

5. CONCLUSIONS.

a) On heating αFeOOH to temperatures up to 850°C the original yellow colour changes to red at ca. 400°C and darker red at higher temperatures. This change in colour corresponds to the transformation of αFeOOH into αFe_2O_3.

PLATE A3.2

The product of the thermal treatment of αFeOOH to 400°C.

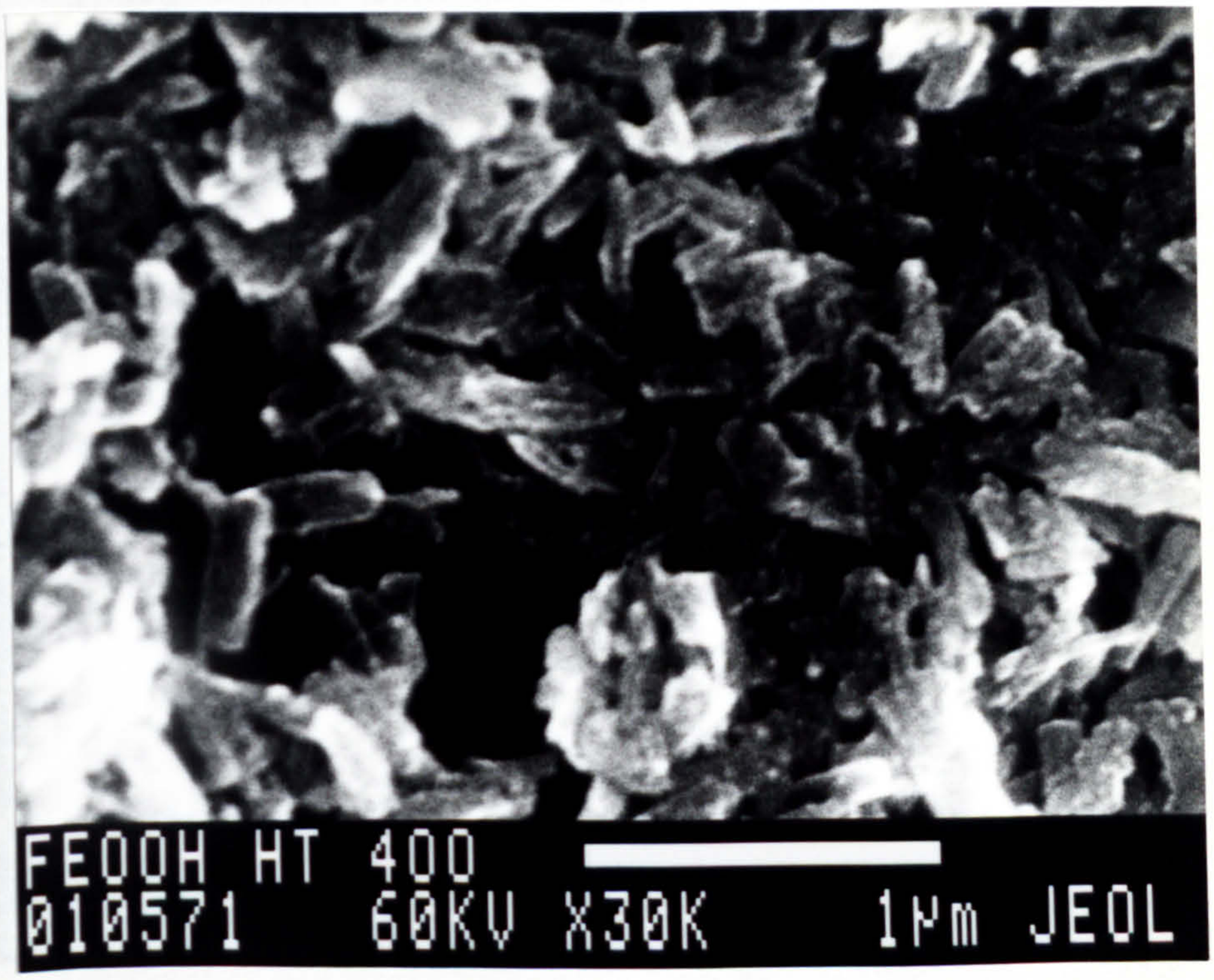

Magnification:- x 30000

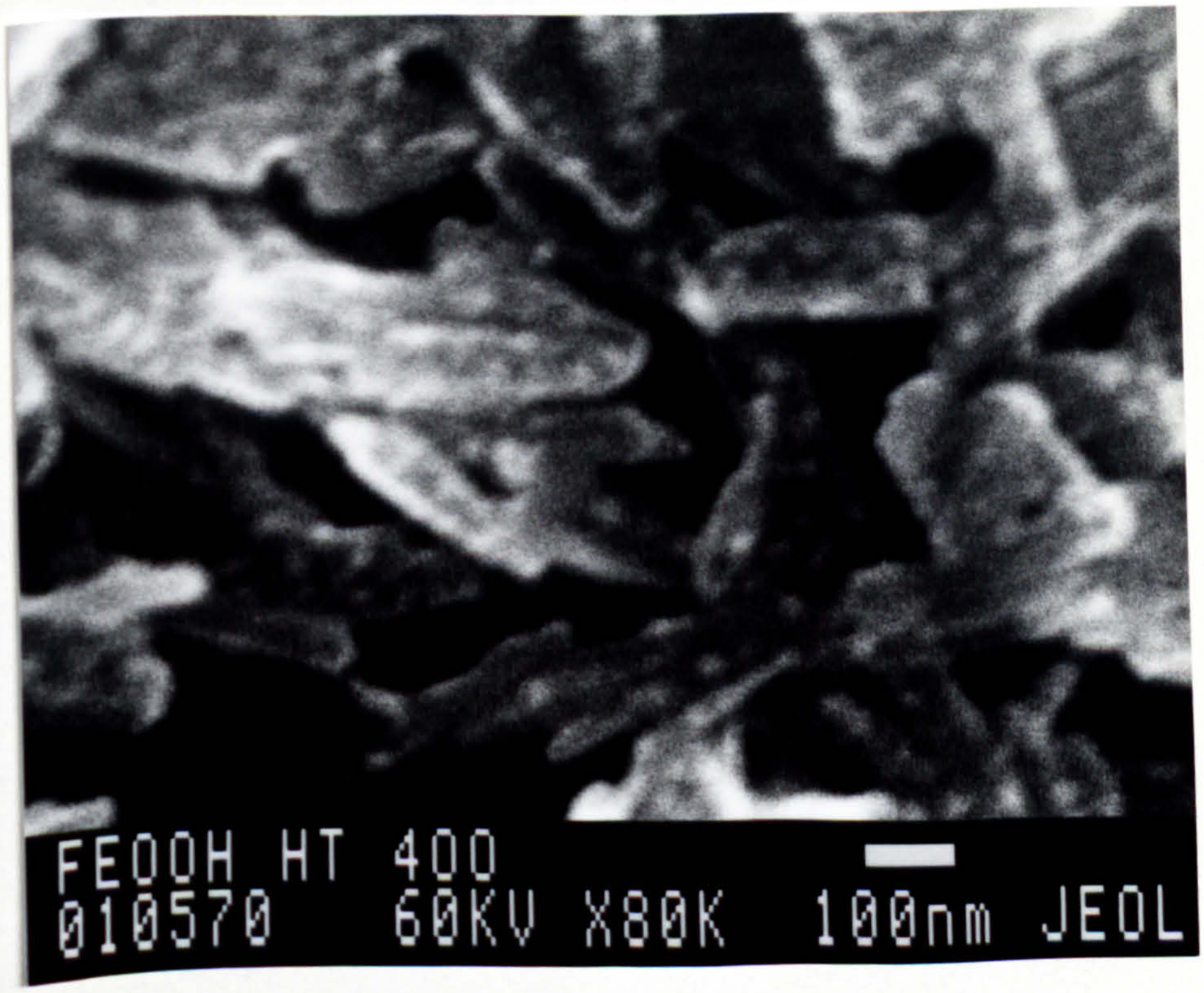

Magnification:- x 80000

PLATE A3.2 (continued)

Magnification:- x 150000

PLATE A3.3

The product of the thermal treatment of αFeOOH to 850°C.

Magnification:- 30000

Magnification:- x 80000

PLATE A3.3 (continued)

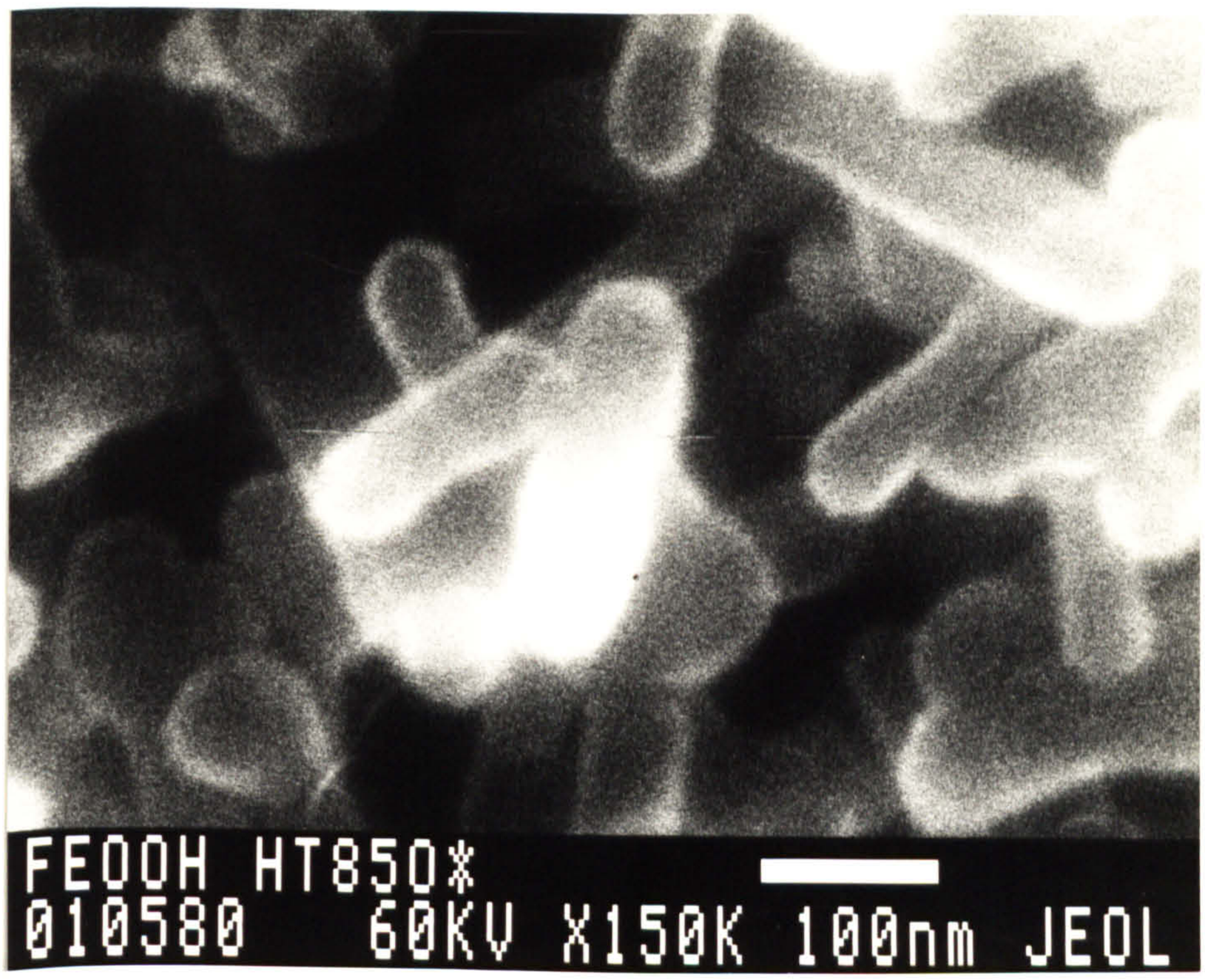

Magnification:- x 150000

b) The αFeOOH crystallinity of products formed by heating αFeOOH to temperatures up to ca. 275°C is improved with increasing preheat-treatment temperature.

c) The decomposition of the αFeOOH crystal structure of a 97.4% pure αFeOOH sample, consisting of particles having a regular size and shape, begins at ca. 275°C and is complete at 400°C, resulting in particles with an irregular surface. For a large proportion of the αFeOOH content of such particles, this decomposition, and subsequent transformation to αFe_2O_3, commences at between 300 and 350°C. In this decomposition over 80% of the αFeOOH is initially transformed into high specific surface area, microporous amorphous material, while the remainder is apparently transformed directly into an unusual αFe_2O_3 phase that gives rise to a non-uniform line-broadened XRD profile and whose crystal structure contains an appreciable degree of microstrain. There is a progressive crystallisation of all this microporous amorphous material into αFe_2O_3, and a coalescence of micropores into larger mesopores, with increasing temperature up to 850°C. In addition, this increasing temperature also causes a growth, and a reduction in the microstrain, of the so formed αFe_2O_3 crystals. The outcome of this crystallisation and subsequent crystal growth is that highly crystalline, almost microstrain-free, low specific surface area αFe_2O_3 is the only phase present in such thermally treated particles at 850°C. Thus, it would appear that the thermal dehydration of αFeOOH occurs by an homogenous mechanism in which water is lost from most parts of the αFeOOH particles resulting in an incomplete arrangement of oxygen and iron III ions throughout the greater extent of such particles.

d) The αFe_2O_3 XRD peak intensities of the initial dehydration products of αFeOOH, formed by heating αFeOOH to temperatures between 300 and 850°C, vary with preheat-treatment temperature. Thus, it may be concluded that the non-uniform line-broadening phenomenon of the XRD profiles of such products is better explained by the incomplete Fe^{3+} ion arrangement theory of Francombe and Rooksby rather than the direct αFe_2O_3 formation theory of Watari et.al..

e) The shapes of product particles formed by heating αFeOOH to temperatures up to 500°C are geometrically very similar. Thus,the observed high specific surface areas of products formed by heating αFeOOH to temperatures up to 500°C can be entirely attributed to the formation of pores within the particles and not to any visible change in particle shape. However, there

is a change in particle shape, and consequent change in specific surface area, when αFeOOH is heated to temperatures above 500°C.

f) Product particles formed by heating αFeOOH to 850°C have a regular size and shape which is best described as cylindrical with hemispherical ends.

g) In a low temperature gas adsorption experiment the thickness of the adsorbed layer of nitrogen present on either a prepared αFeOOH, or a product formed by heating this αFeOOH to temperatures up to 850°C, is better estimated by reference to the desorption data of one of these products (preferably one that is non-porous), such as that formed at 250°C, than by the use of an empirical relation, such as that of Halsey.

h) During the raising of the temperature of a prepared αFeOOH from 400 to 500°C, micropores are transformed into mesopores such that the principal type of porosity of a product formed at 500°C is mesoporosity.

i) The structures of the IR absorbing groups present in a product formed by heating αFeOOH to 375°C are unaffected by further heating of the product up to 500°C. However, the structures of such groups are altered when the product is further heated to 705°C.

j) IR absorption spectroscopy cannot detect the presence of low (XRD-detectable) weight concentrations (ca. 5%) of αFeOOH in products formed by the thermal treatment of αFeOOH.

k) The results of this study suggest that the thermal dehydration of αFeOOH to αFe_2O_3 is not a simple two phase topotactic transformation, as suggested by Bernal, but rather a two stage process involving the initial decomposition of αFeOOH into amorphous material followed by the crystallisation of this material into αFe_2O_3.

6. APPENDIX

The crystal structures of αFeOOH and αFe_2O_3.

The crystal structures of αFeOOH and the eventual product of its dehydration, αFe_2O_3, are based on stacked hexagonally close-packed layers

of hydroxyl and oxygen ions, with the Fe^{3+} ions arranged interstitially between the hydroxyl/oxygen layers in octahedral grouping (Fasiska, Landa and Gast); the octahedral grouping are slightly distorted by the size of the cation (Blyholder and Richardson). The hydroxyl/oxygen layers are stacked in the (001) direction with a stacking sequence which may be represented as (ABABAB). The cations occupy half and two-thirds of the octahedral interstices in αFeOOH and αFe_2O_3, respectively (Lima-de-Faria).

There are two kinds of oxygen atoms in αFeOOH and each Fe^{3+} ion has three of each kind as neighbours (Ewing). The resulting octahedra share edges to form what Ewing described as "double rutile strings" extending in the c-direction. The double strings are further connected to each other by the sharing of corner oxygens to form the stacked arrangement of close-packed hydroxyl/oxygen layers.

The αFeOOH unit cell has orthorhombic symmetry and contains four molecules (Busing and Levy); the accepted space group for the structure is Pnma (No. 62) (Fasiska). Each hydrogen atom in the αFeOOH structure is associated with an oxygen atom and the pair is assumed to be a discrete hydroxyl group as distinct from independent hydrogen and oxygen atoms; this assumption is supported by IR analysis (Wells). The presence of such directed (or localised) hydroxyl bonds endows the αFeOOH structure with a fairly rigidly-bonded atomic arrangement which has led to the classification of αFeOOH as an oxyhydroxide (rather than a hydroxide) (Lima-de-Faira).

The αFe_2O_3 unit cell has hexagonal symmetry and contains six molecules (Lima-de-Faria); the accepted space group for the structure is $R\bar{3}c$ (No.167) (Fasiska).

REFERENCES

Ball, M.C. and Taylor, H.F.W., Miner. Mag., 32, 754 (1961).

Bernal, J.D., Schweiz. Arch. Wiss. Tech., 26, 69 (1960).

Blyholder, G. and Richardson, E.A., J. Phys. Chem., 66, 2597 (1962).

Bogdanovitch, M.P., Vorobev, Yu. P., Men, A.M., Serebryakova, A.V. and Chufarov, G.I., Opt. Spectrosk., 29, 1151 (1970).

Brindley, G.W. and Brown, G., "Crystal Structures of Clay Minerals and their X-ray Identification", Mineralogical Soc. Monograph No. 5, Mineralogical Soc., London, 1980.

Brunauer, S., Emmett, P.H. and Teller, E., J. Amer. Chem. Soc., 60, 309 (1938).

Brunauer, S., Deming, L.S., Deming, W.E. and Teller, E., J. Amer. Chem. Soc., 62, 1723 (1940).

Busing, W.R. and Levy, H.A., Acta Cryst., 11, 798 (1958).

Cohan, L.H., J. Amer, Chem. Soc., 60, 433 (1938).

Dasgupta, D.R., Indian J. Phys., 35, 401 (1961).

Delhez, R., "The PW 1700 Program Package: Line Profile Analysis", Philips S and I, Almelo and Delft University of Technology, Delft, The Netherlands, 1983.

D'eye, R.W.M. and Wait, E., in "X-ray Powder Photography in Inorganic Chemistry", Chap. 4, Butterworths, London, 1960.

Dollimore, D. and Heal, G.R., J. Colloid Interface Sci., 33, 508 (1970).

Dollimore, D. and Heal, G.R., Surface Technology, 6, 231 (1978).

Duvigneaud, P.H. and Derie, R., J. Solid State Chem., 34, 323 (1980).

Estep, P.A., in "Physical Methods in Determinative Mineralogy", Zussman, J.; Editor, Academic Press, 1977.

Everett, D.H., "The Structure and Properties of Porous Materials", Butterworths, London, 1958.

Ewing, F.J., J. Chem. Phys., 3, 203 (1935).

Farmer, V.C., "The Infrared Spectra of Minerals", Mineralogical Soc., London, 1974.

Farmer, V.C. and Russell, J.D., Spectrochim. Acta, 22, 389 (1966).

Fasiska, E.J., Corros. Sci., 7, 833 (1967).

Feitknecht, W., Wittenbach, A. and Buser, W., in "4th Int. Symp. Reactivity of Solids", de Boer, J.H.; Editor, Elsevier, Amsterdam, 1961.

Francombe, M.H. and Rooksby, H.P., Clay Minerals Bull., 21, 1 (1959).

Garcia-Gonzalez, M.L., Grange, P. and Delmon, B., in "8th Int. Symp. Reactivity of Solids", 1977.

Goodman, J.F., Proc. Roy. Soc., London, 247, 346 (1958).

Gregg, S.J. and Sing, K.S.W., "Adsorption, Surface Area and Porosity", Academic Press, London, 1967.

Halsey, G.D., J. Chem. Phys., 16, 931 (1948).

Hirokawa, S., Naito, T. and Yamaguchi, T., J. Colloid Interface Sci., 112, 268 (1985).

Huckel, W., "Adsorption und Kapillar Kondensation", Akademische Verlaggesellschaft, Leipzig, 1928.

Jenkins, R. and de Vries, J.L., "An Introduction to X-ray Powder Diffractometry", 1970.

Landa, E.R. and Gast, R.G., Clays Clay Miner., 21, 121 (1973).

Langford, J.I., J. Appl. Cryst., 11, 10 (1978).

Liese, H.C., Am. Miner., 52, 1198 (1967).

Lima-de-Faria, J., Z. Krist., 119, 176 (1963).

Lippens, B.C., Linsen, B.G. and de Boer, J.H., J. Cat., 3, 32 (1964).

Lippens, B.C. and de Boer, J.H., J. Cat., 4, 319 (1965).

Mackay, A.L., in "4th Int. Symp. Reactivity of Solids", de Boer, J.H.; Editor, Elsevier, Amsterdam, 1961.

McDevitt, N.T. and Baun, W.L., Spectrochim. Acta, 20, 799 (1964).

Morris, M.C., McMurdie, H.F., Evans, E.H., de Groot, J. and Paretzkin, B., "Powder Diffraction Data", 1st Edition, Joint Committee on Powder Diffraction Standards, Pennsylvania, 1976.

Rendon, J.L. and Serna, C.J., Clay Miner., 16, 375 (1981).

Rendon, J.L., Cornejo, J., de Arambarri, P. and Serna, C.J., J. Colloid Interface Sci., 92, 508 (1983).

Ruppin, R. and Englman, R., Rep. Progr. Phys., 33, 149 (1970).

Scherrer, P., Gottinger Nachrichten, 2, 98 (1918).

Schwertmann, U. and Taylor, R.M., "Minerals in Soil Environment", Soil Sci. Soc. Am., Madison, 1977.

Vlasov, A. Ya., Loseva, G.V., Sakash, G.S. and Solntseva, L.A., Z. Prikl. Spektrosk, 12, 846 (1970).

Watari, F., van Landuyt, J., Delavignette, P., Amelinckx, S. and Igata, N., Phys. Status Solidi A, 73, 215 (1982).

Wells, A.F., "Structural Inorganic Chemistry", 2nd Ed., Oxford University Press, 1950.

Wheeler, A., "Catalysis", Vol. 2, Reinhold, New York, 1955.

Wilson, M.J., Russell, J.D., Tait, J.M., Clark, D.R., Fraser, A.R. and Stephen, I., Clay Miner., 16, 261 (1981).

Yariv, Sh. and Mendelovici, E., Appl. Spectrosc., 33, 410 (1979).

PART B

THE SURFACE ELECTROCHEMISTRY

OF A CORROSION PRODUCT (αFeOOH).

ABBREVIATIONS AND SYMBOLS

ABBREVIATIONS

AM	analytical method (mathematical).
edl	electrical double layer.
HPLC	High Performance Liquid Chromatography
IHP	inner Helmholtz plane: A plane passing through the centres of adsorbed species.
Int	intermediate (intermediate κa regime).
ISE	ion selective electrode.
NT	numerical technique (mathematical).
OHP	outer Helmholtz plane (also recognised as the Stern plane) : A plane located at about a hydrated ion radius from the surface.
pzc	point of zero charge : The electrical charge condition of a surface such that the sum of charges from all sources at that surface equals zero. [The pH of a suspension whose solid surface is at its pzc is designated pH_o, i.e., $\psi_S = 0$.]
PB	Poisson-Boltzmann (complete equation).
ST	Stigter.

SYMBOLS

[Unless stated, values given are according to Weast, R.C., "CRC Handbook of Chemistry and Physics", 59th Edition, 1978].

Symbols based on the Roman alphabet.

a	particle radius; m.
a_G	average radius of hydrated electrolyte ions in the edl; 0.25nm (Gorin, M.H., J. Phys. Chem., 45, 371 (1941)).
a_i	activity.
B	Conversion factor from mol dm^{-3} to Cm^{-2}.
Cl^-_{ADS}	quantity of Cl^- ion adsorbed per unit mass of $\alpha FeOOH$; mol g^{-1}.
c	mole per cubic metre concentration; mol m^{-3}.
$(c_{MAX})_{Cl^-}$	theoretical, maximum mole per cubic metre concentration of Cl^- ions in bulk solution; mol m^{-3}.
D	dielectric constant (also termed relative permittivity); $D = D_W + 2\lambda[NaCl]$ (for NaCl aq. solution).
D_W	static dielectric constant of water at 25°C; 78.36.
$\bar{D}$	mean of reciprocal of dielectric constants.
E_{Cl^-}	the Cl^- ion potential response of a chloride ISE; V.

e elementary charge; $1.6021892 \times 10^{-19}$ C.

F Faraday constant; 96484.56 C mol^{-1}.

f molar activity coefficient as given by the Davis Equation; $\log(f) = -\Omega_D (TD)^{-\frac{3}{2}} [I^{\frac{1}{2}}/(1 + I^{\frac{1}{2}})) - 0.2I]$, where $\Omega_D = e^3 (2 \times 10^3 \pi N_A)^{\frac{1}{2}} (4\pi\varepsilon_{VAC} k)^{-\frac{3}{2}}/\ln(10)$ (Davis, C.W., J. Chem. Soc., 2093 (1938)).

I molar ionic strength; $I = \frac{1}{2} \sum_i [i] z_i^2$ mol dm^{-3}.

K_a^{int} intrinsic equilibrium constant for ionisation reaction (also termed amphoteric reaction); mol dm^{-3}.

K_{ClOH} OH^- ion/Cl^- ion chloride ISE selectivity constant.

$K_{Cl^-}^{int}$ intrinsic equilibrium constant for binding of Cl^- ions; $(mol\ dm^{-3})^{-1}$.

$*K_{Cl^-}^{int}$ intrinsic equilibrium constant for complexation of Cl^- ions; $(mol\ dm^{-3})^2$.

$K_{Na^+}^{int}$ intrinsic equilibrium constant for binding of Na^+ ions; $(mol\ dm^{-3})^{-1}$.

$*K_{Na^+}^{int}$ intrinsic equilibrium constant for complexation of Na^+ ions; $(mol\ dm^{-3})^2$.

K_W ionisation constant (also termed the ionic product) of water; 13.9965 (25°C), 13.3960 (45°), 12.908 (65°C).

K^{CAP} integral capacity; F m^{-2}.

^oK zero order modified Bessel function of the second kind.

^1K first order modified Bessel function of the second kind.

k Boltzmann constant; 1.380662×10^{-23} J K^{-1}.

l_c inter-electrode (platinum wires) distance; m.

l_g length of one division of the eyepiece graticule; 27.6 μm (Shaw, D.J., Liverpool Polytechnic, 1983).

N_A Avogadro constant; 6.022045×10^{23} mol^{-1}.

N_S surface density of exchangeable proton containing sites; 16.8 sites nm^{-2} (Yates, D.E. and Healy, T.W., Proc. Int. Conf. Colloid Surf. Sci., 1975, 1, 7).

N_S^σ surface charge density arising from the charging of every exchangeable proton containing site; $N_S^\sigma = N_S e$ Cm^{-2}.

n number concentration; m^{-3}.

p hydrostatic pressure; N m^{-2}.

pQ_a acidity quotient; $pQ_{a\pm S} = pH \pm \log \frac{\alpha_{\pm S}}{(1-\alpha_{\pm S})}$.

Q charge on the surface of a particle; C particle $^{-1}$.

R molar gas constant; 8.31441 J mol^{-1} K^{-1}.

r distance normal to particle surface; m.

r_{IHP} distance normal to particle surface from IHP; m.

r_{OHP} distance normal to particle surface from OHP; m.

r_{Cl^-} ionic radius of Cl^- ion; 0.181 nm.

S surface.

S_{BET} specific surface area (BET, N_2 at 77K); m^2 g^{-1}.

T absolute temperature; K.

u electrophoretic mobility; m^2 s^{-1} V^{-1}.

u_{ION} local ion mobility; $u_{ION} = \frac{v_{ION}}{X}$ m^2 s^{-1} V^{-1}.

$Vol_{aq.}$ volume of aqueous solution; cm^3.

v velocity; m s^{-1}.

W_{ADS} work of adsorption (from interior of bulk solution to the IHP); J.

X strength of applied electric field; V m^{-1}.

z valence.

Symbols based on Greek alphabet.

α fraction of charged surface sites; $\alpha = \frac{|\sigma_s|}{N_s}$.

β Stigter correction factor (Stigter, D., J. Colloid Interface Sci., 53, 296 (1975)).

Γ adsorption density; mol m^{-2}.

Γ_{MAX} theoretical, maximum adsorption density; mol m^{-2}.

(Γ_{IHP}) adsorption density at the IHP; mol m^{-2}.

$(\Gamma_{IHP+OHP})_{Cl^-}$ sum of the IHP and OHP Cl^- ion adsorption densities; $(\Gamma_{IHP+OHP})_{Cl^-} = \frac{Cl^-_{ADS}}{S_{BET}}$ mol m^{-2}.

δ^{-1} fraction of surface sites in unbound condition.

ΔG^* difference in the standard differential free energies of transfer of H^+ and OH^- ions from bulk solution to the interfacial region at the pzc; J mol^{-1}.

ΔH enthalpy change of equilibrium reaction; J mol^{-1}.

ΔH^* difference in the standard differential heats of transfer of H^+ and OH^- ion from bulk solution to the interfacial region at the pzc; J mol^{-1}.

ΔpH difference in pH from pH_o; $\Delta pH = | pH_o - pH|$.

ΔS entropy change of equilibrium reaction; J mol^{-1} K^{-1}.

ΔS^* difference in the standard ionic entropies of transfer of H^+ and OH^- ions from bulk solution to the interfacial region at the pzc; J mol^{-1} K^{-1}.

ϵ permittivity; $\epsilon = D\epsilon_{VAC}$ Fm^{-1}.

ϵ_{VAC} permittivity of vacuum; $8.85418782 \times 10^{-12}$ Fm^{-1}.

$\bar{\epsilon}$ mean of reciprocals of permittivities; $\bar{\epsilon} = \bar{D}\epsilon_{VAC}$ Fm^{-1}.

ζ zeta potential : Electrical potential at the surface of shear (also termed the electrokinetic potential); V.

η absolute viscosity; kg m^{-1} s^{-1}.

θ intermediate calculation factor; $\theta = BN_s^{\sigma}$ ($[SOH_2^+]$ + $[SO^-]$ + $[SOH_2^+....Cl^-]$ + $[SO^-....Na^+]$).

$\varkappa$ Debye-Huckel reciprocal thickness ($\varkappa^{-1}$ is customarily referred to as the distance over which the potential decreases by an exponential factor and, more simply, the thickness of the edl); $\varkappa = (2x10^3\ e^2\ I\ N_A/\epsilon_{VAC}DkT)^{\frac{1}{2}}$ m^{-1}.

Λ molar limiting ionic conductance at 25°C; 50.11×10^{-4} ohm^{-1} m^2 mol^{-1} (Na^+ ion), 73.52×10^{-4} ohm^{-1} m^2 mol^{-1} (K^+ ion), 76.34×10^{-4} ohm^{-1} m^2 mol^{-1} (Cl^- ion) (Glasstone, S., " Textbook of Physical Chemistry", 2nd Edition, Macmillan, London, 1966).

λ dielectric constant depression factor for NaCl; -5.5 (Hasted, J.B., Ritson, D.M. and Collie, C.H., J. Chem. Phys., 16, 1 (1948)).

μ chemical potential.

ν concentration ratio of a surface species relative to neutral surface hydroxyl groups.

ρ net volume charge density at points in the edl where the potential is ψ; $\rho = \sum_{1}^{i} n_i\ z_i\ e$ C m^{-3}.

σ charge density; C m^{-2}.

σ_E electrokinetic charge density; C m^{-2}.

σ_{IHP} charge density at the IHP; C m^{-2}.

σ_{OHP} charge density at the OHP (also termed the diffuse layer charge); C m^{-2}.

$(\sigma_{IHP+OHP})_{Cl^-}$ the sum of the Cl^- ion charge density at the IHP and OHP; $(\sigma_{IHP+OHP})_{Cl^-} = \dfrac{Cl^-_{ADS} \cdot F}{S_{BET}}$ C m^{-2}

σ_S surface charge density; C m^{-2}.

$(\sigma_S)_{REL}$ relative surface charge density; C m^{-2}.

$\emptyset_{ADS}$ chemical component of work of adsorption (also termed the specific adsorption energy); J.

ψ electrical potential; V.

ψ_{IHP} electrical potential at the IHP; V.

ψ_{OHP} electrical potential at the OHP; V.

ψ_S surface electrical potential; V.

$(\psi_S)_N$ surface electrical potential as given by the Nernst Equation; $\Delta(\psi_S)_N = -kT/e \ . \Delta pH \ \ln (10)$.

Ω constant.

ω number of moles of a species; mol.

ω_{ADD} number of moles of a species added; mol.

ω_S number of moles of a species on the surface of suspended particles; mol.

Other symbols

$\nabla^2\psi$ Laplacian of ψ.

[] molar concentration in aqueous solution; mol dm^{-3}.

$[]_{EQ}$ molar equilibrium concentration in aqueous solution; mol dm^{-3}.

$\sim$ reduced (dimensionless) quantity.

Subscripts

IEP isoelectric point.

i relating to species i.

L relating to linearisation (small $\varkappa a$ regime).

P relating to planar (large $\varkappa a$ regime).

0 relating to the condition at which $\psi = 0$.

1 relating to inner zone of compact region of edl.

2 relating to outer zone of compact region of edl.

+ relating to cation.

+S relating to positive surface.

- relating to anion.

-S relating to negative surface.

// relating to a cylindrical particle with its axis parallel to the applied electric field.

$\perp$ relating to a cylindrical particle with its axis perpendicular to the applied electric field.

Superscript.

j	index for state.
0	relating to standard state.

INTRODUCTION

The electrical double layer (edl) at the αFeOOH-Cl^- aq. interface was conveniently divided into the established regions of diffuse, compact and surface. Each region was investigated, beginning with measurements of the associated charge or potential. These measurements were analysed using double layer, adsorption and thermodynamic theories, resulting in a greater understanding of the interaction between αFeOOH and Cl^- ion, and the αFeOOH-Cl^- aq. edl as a whole. The investigations of the diffuse, compact and surface regions of the edl at the αFeOOH-Cl^- aq. interface are given in chapters B1, B2 and B3, respectively.

Origin of the edl.

When two phases, I and II, are placed in contact there develops a non-uniform distribution of charge at the interface leading to an electrical potential difference between the two phases. The non-uniform distribution of charge in the region between two adjoining phases will take the form of an excess of charge of one sign near-to or on the surface of phase I and the distribution of the balancing charge throughout the surface region of phase II. This non-uniform distribution of charge in an interfacial region is termed the edl. The electrokinetic phenomena electrophoresis and electroosmosis, and many other phenomena such as adsorption, electrode kinetics, electrocatalysis, corrosion, crystal growth, colloid stability and flow behaviour, cannot be treated properly without a knowledge of the nature of the edl involved.

For the case of a solid phase I dispersed in an aqueous phase II, containing electrolyte, the excess charge of one sign on the solid surface is termed the surface charge and the balancing charge distributed throughout the aqueous phase will be those electrolyte ions, termed counterions, attracted from the bulk solution towards the surface. [Those electrolyte ions that are repelled by the surface charge are termed coions.] The sign and magnitude of the charge and potential difference at such an interface will depend upon the nature of the aqueous medium and the type of reaction(s) occurring at the surface of the solid; typical reactions occurring at the surface of a solid in contact with a polar medium are ionisation, ion adsorption and ion dissolution.

An insoluble oxyhydroxide, such as αFeOOH, will develop surface electrical charge by the interaction of its surface hydroxyl groups with H^+ and OH^- ions of the aqueous phase. A positive surface charge is generated by the addition of H^+ ions to the neutral surface hydroxyl groups:

$$SOH_2^+ = SOH + H_S^+$$

(where S denotes the surface).

The generation of a negative surface charge occurs by the dissociation of surface hydroxyl groups:

$$SOH = SO^- + H_S^+$$

The generation of a negative surface by the addition of OH^- ions, in a similar way to the generation of a positive surface by the addition of H^+ ions, is not likely to occur in the case αFeOOH since this would involve the unfavourable increase of the Fe^{3+} coordination number to seven (Parks, G.A., and de Bruyn, P.L., J. Phys. Chem., 66, 967 (1962)). In any event experimental adsorption measurements cannot distinguish between the adsorption of OH^- ions or the desorption of H^+ ions. The surface charging mechanism given above explains why the metal ion Fe^{3+} plays no active role in the development of αFeOOH surface charge, since it is buried under the surface.

Ions which can bestow their charge on a surface and are components of the solid phase or the solvent (for example, H^+ or OH^- ions) are known as potential determining ions. Thus, H^+ and OH^- ions are the potential determining ions for αFeOOH and the surface potential depends on the pH of the αFeOOH aqueous suspension.

SUMMARY

The development of electrophoretic and electical double layer theories from their beginnings to present day treatments are discussed. The electrophoretic mobility of positively charged, acicular αFeOOH particles dispersed in dilute aqueous NaCl solutions was measured, at 25° C, as a function of ionic strength and pH. For αFeOOH particles immersed in a dilute 1:1 electrolyte solution, the ratio of their radius of curvature to the effective thickness of the attendant electrical double layer, $\varkappa a$, was in the intermediate regime $3.2 \leqslant \varkappa a \leqslant 45.9$, while their zeta potential rose to values well above 25mV. Furthermore, such a colloidal system has a geometry which is most simply described as cylindrical . Consequently, the classical planar and linearisation electrophoretic equations cannot be used in the calculation of shear surface quantities. Instead, recourse was made to advanced treatments, in cylindrical geometry, having a range of validity in the intermediate $\varkappa a$ regime and in which allowance was made for the relaxation effect. The mobility data was processed through a number of selected relationships that represent various stages of understanding of electrophoretic theory, culminating in the determination of values of the electrokinetic charge and zeta potential of the colloid αFeOOH/ NaCl aq. that were considered to best represent the real situation.

It was possible to measure the uptake of Cl^- ions by αFeOOH dispersed in aqueous NaCl solution, up to a concentration of 10 mmol dm^{-3}, using Ion Chromatography. Cl^- ion adsorption as a percentage of available Cl^- ion had a maximum value of about 20%. Physically realistic charge density and potential values for the αFeOOH-NaCl aq. interface were obtained by the coupling together of electrophoresis and ion chromatography data, over a wide range of NaCl concentration ([NaCl]). Relatively small surface charge density and αFeOOH surface Cl^- ion coverage values were determined suggesting that not all the BET surface area was either active towards, or accessible to, Cl^- ions. A specificity of Cl^- ions for the αFeOOH surface was exhibited by a) a residual adsorption at the point of zero charge, b) the good correlation observed when the adsorption data was fitted to empirical and theoretical adsorption equations, and c) a significant chemical component of the total work of adsorption. The integral capacity (K_1^{CAP}) of the inner zone of the compact layer of the αFeOOH-NaCl aq. interface attained values in excess of 1 F m^{-2}, at high [NaCl] indicating a close association of the planes passing through the

surface and adsorbed charge centres. An increase in the separation between these planes, with diminishing [NaCl], was indicated by a reducing K_1^{CAP} and in increasing Cl^- ion binding constant. The values for the amphoteric and complexation constants determined in this work reflected a smaller degree of protonation of surface hydroxyls, and a less intense interaction between αFeOOH and Cl^- ions, than was suggested by the values of the corresponding constants determined by other workers (Davis, J.A. PhD. Thesis, Stanford University, 1977, Hingston, F.J. et.al., Adv. Chem. Ser., 79, 82 (1968) and Yates, D.E., Ph.D. Thesis, University of Melbourne, 1975) from H^+/OH^- ion potentiometric titration data. Apparently, that proportion of the αFeOOH surface accessible to Cl^- ions was less than that accessible to H^+ and OH^- ions.

The αFeOOH-NaCl aq. interface was studied at 25°C and at higher temperatures through measurement of surface charge density (σ_s) and point of zero charge (pzc) by means of, respectively, rapid potentiometric titrations and salt titrations. The σ_s results were interpreted in terms of the triple layer, surface ionisation and complexation model of Davis et.al. (J. Colloid Interface Sci., 63, 480 (1978)), such that the measured σ_s was evaluated as the net number of protons released or consumed by all surface reactions. The intrinsic equilibrium constants of surface ionisation and complexation equilibria were determined by the Davis et.al., James et.al. (J. Colloid Interface Sci., 65, 331 (1978)) double and single graphical extrapolation techniques, respectively. The description of the interface given in terms of the Davis et.al. model was elaborated to yield quantitative information concerning interfacial parameters. Thus, the interface was described by a set of simultaneous and associated equations identified in the work of Yates et.al. (J. Chem. Soc. Faraday Trans. I, 70, 1807 (1974)). Solutions to these equations were found by an iterative procedure, and, in this way, σ_s/pH data were translated into values of the interfacial parameters. At 25°C, σ_s was dependent on [NaCl] indicating that both Cl^- and Na^+ ions contribute to σ_s thereby giving support to the use of a complexation model. The maximum measured σ_s was 5.6% of that theoretically possible on the basis of crystallographic data, while the corresponding calculated Cl^- ion surface density was 11.5% of that expected for a hydrated Cl^- ion monolayer in a close packing arrangement However, the measured σ_s was an order of magnitude larger (and more symmetrical about the pzc) than that measured for a relatively simpler

colloid such as AgI/aqueous electrolyte. Interestingly, when allowance was made for the contribution of surface complexation to σ_S, the potential determining ion/surface interaction was similar for both the αFeOOH-NaCl aq. and the classical AgI-aqueous electrolyte interfaces. Negligible ion-pair formation was found at [NaCl] = 1 mmol dm^{-3} while the concentration 50 mmol dm^{-3} was observed to be a cross-over point between the charging and ion-pair formation behaviour of the interface, with ion-pair formation evident at, and above, this concentration. A disagreement between theory and experiment was observed at low σ_S such that the tendency towards ion-pair formation was found to be dependent on the density of ion-pairs already formed, and increased with diminishing [NaCl]. This dependence was substantiated by the attainment of physically realistic interfacial potentials at all concentrations using values for the complexation constants evaluated at each [NaCl]. A possible explanation for this dependence was developed in terms of the active site theory of catalysis. Thus, at high [NaCl] active sites were occupied and, possibly coulombic hindrance prevented the formation of a complete monolayer, while at low [NaCl] active sites not coulombically hindered were not occupied. A predominance of surface complexation reactions over surface ionisation reactions was indicated by the significant calculated values of the Cl^- ion and Na^+ ion binding constants. The magnitudes of such values were exhibited as a lack of any great disparity between σ_S and calculated $|\sigma_{IHP}|$ values, and relatively low calculated $|\sigma_{OHP}|$ values. The order of magnitude of these binding constants was indicative of a relatively strong ion-pair bond, while their near equality, and the observed symmetry of σ_S about the pzc, suggested that ion-pair formation occurred to similar extents on both positive and negative surfaces. An observed dependence of ψ_S on [NaCl] indicated that Cl^- and Na^+ ions could modify this potential. Calculated K_1^{CAP} data indicated that the distance of counterion approach towards the surface became smaller with increasing [NaCl], leading to a very close association of surface and counterions at high [NaCl]. At low [NaCl], calculated K_1^{CAP} data indicated that counterions were further from the αFeOOH surface than the adjacent structured water layer. Such data also indicated a closer approach towards the structured water layer, at the surface, of the structure promoting Na^+ ions than the structure breaking Cl^- ions, and that Na^+ ions were crowded out of this region (preferentially occupied by H^+ and OH^- ions) and Cl^- ions progressively approached the surface with increasing σ_S away from zero.

Indeed, the observed dramatic changes in $(K_1^{CAP})_{-S}$ in the vicinity of pzc, at high [NaCl], suggested penetration of the surface region by Na^+ ions. The relative affinity of H^+ and OH^- ions for the αFeOOH surface was found to be temperature dependent, such that H^+ ions had an increased surface affinity at higher temperatures. The changes in enthalpy (small and positive) and entropy (large and positive) for the transfer of H^+ and OH^- ions from bulk solution to the adsorbed state, suggested that a small amount of energy was expended and an advanced degree of desolvation took place in this process. The density ratio of positively charged surface sites to neutral surface sites was found to be independent of temperature over the range 25° C to 65° C, whereas those ion-pairs involving a positively charged surface site and a Cl^- ion were observed to become more abundant at higher temperatures.

The chloride potential response (E_{Cl}) of a chloride ion selective electrode (ISE) became increasingly susceptible to OH^- interferance at high OH^- ion concentration ($[OH^-]$) and low Cl^- ion concentration ($[Cl^-]$). Indeed, at pH>7 there was detectable OH^- interferance of E_{Cl}- even at the relatively high $[Cl^-]$ of 10 mmol dm^{-3}. Use of the method employed by chloride ISE manufacturers for determining the OH^- chloride ISE selectivity constant, K_{ClOH}, (involving unrealistically high $[Cl^-]$ and $[OH^-]$ values) yielded an apparently favourable value for K_{ClOH} (i.e., $K_{ClOH} \ll 1$). However, when K_{ClOH} was evaluated within the allowed experimental working conditions of a chloride ISE ($1 < pH < 10$) K_{ClOH} values were obtained that obviously declared the significant interferance of OH^- ions on the E_{Cl}- of a chloride ISE.

CHAPTER B1

ELECTRICAL CHARGE AND POTENTIAL AT THE PLANE OF SHEAR IN THE COLLOID αFeOOH/NaCl aq. : MICROELECTROPHORESIS MEASUREMENTS.

1. INTRODUCTION

In the development of colloid science electrophoretic experiments have played an important part. There probably is not a single other method of investigation that has been so widely used in pure as well as in applied research of colloids. The determination of the charge on particles (particularly emphasised in this study), the isoelectric point and colloid stability can all be achieved by electrophoretic studies. Although acid/base potentiometric titration methods give a very precise evaluation of the nature of ionogenic groupings for materials in solution, information can also be obtained, often more conveniently, from electrophoretic studies.

In colloidal electrolyte solutions the interpretation of electrical transport experiments is conceptually and mathematically complex, and relies on the use of ionic distributions and continuum hydrodynamics. In view of the mathematical difficulties, the development of electrophoretic theory has seen the appearance of a variety of approximations, modifications and refinements of greater or less validity. The advent of the computer has added a new dimension to theoretical chemistry in recent years such that earlier approximations in mathematical analysis can now be tested and, if desired, be replaced by more exact numerical analysis.

1.1. Electrokinetic phenomena induced by an electric field.

The electrokinetic phenomena electrophoresis and electroosmosis are the induced, tangential movement of one phase past a second contacting phase by the application of an electric field. When one phase consists of a liquid or gas in which the second phase is suspended as particles, then electrophoresis is said to have occurred when the particles are induced to move relative to stationary liquid by an applied electric field.

The necessary first step towards the interpretation of electrophoretic measurements is a quantitative treatment of the electrical charge separation, and potential difference, developed at a solid-liquid interface. Such a quantitative treatment presents an extremely difficult and in many respects, unresolved problem.

1.2. The electrical double layer (edl).

1.2.1. Electrical charge and potential at a point: Poisson's equation.

The electrical potential (ψ) at a point in the edl will be partly determined by the surface charges on the solid and in the aqueous electrolyte but may also be influenced by an externally imposed electric field, as in electrophoresis. The relation between ψ and the density of charges (ρ) at a point is given by Poisson's equation:

$$\nabla^2\psi = -\frac{\rho}{\epsilon_{VAC}D} \qquad \text{B1.1}$$

The electric charges themselves will respond to three sorts of forces:

a) ψ,
b) the diffusion force, tending to smooth out concentration variations,
and c) the bulk movement of charge.

At the same time the aqueous electrolyte itself is subjected at each point to forces caused by pressure gradients in the system and the electrical charges it contains.

1.2.2. Information concerning the edl that is accessible from electrophoretic measurements.

Beginning with Poisson's equation, the solution of the resulting differential equations, which describe the edl and electrophoresis, is only achieved by the adoption of a number of significant simplifications and to use, at least in the first instance, highly idealised models of the real experimental system. Nevertheless, a great deal of interesting and valuable information can be obtained from electrophoretic measurements.

Theoretical treatments generally assume that the aqueous medium is Newtonian and moving sufficiently slowly so that turbulence and other non-linear effects are absent. The most important concept which is introduced is that of the surface of shear, having an electrical potential ζ. Information which is accessible from electrophoresis

studies relates to the properties at this surface. The location of this surface is never precisely known and, in reality, it is a region of rapidly changing viscosity rather than a mathematical plane. In the case of a particle undergoing electrophoresis, the surface forms a sheath which envelops the particle and stationary fluid. All of the material inside the sheath forms the kinetic unit so that the particle moves along with a certain quantity of the surrounding liquid and its contained charge. Measurement of the electrophoretic mobility, therefore, gives a measure of the net charge on the particle.

2. THEORY

2.1. Classical theories of the edl.

2.1.1. The Helmholtz-Perrin theory: The molecular condenser.

The separation of charge that occurs at the interface between two phases is called an edl because it consists, ideally, of two regions of opposite charge. The simplest model of such a system is one in which both layers of charge are fixed in parallel planes to form a molecular condenser. This model was first explicitly referred to by Perrin, although it is usually attributed to Helmholtz. When considering electrokinetic phenomena Helmholtz proceeded from four simplifying assumptions:

(a) The edl may be regarded as a plane-parallel molecular condenser having a thickness which is considerably less that the linear dimensions of the particle.

(b) The layer of liquid molecules immediately adjoining the solid surface remains stationary during electrokinetic phenomena whereas the following layers are mobile; i.e., there is no slipping.

(c) The wall of the solid is an insulator and the liquid possesses the property of electrical conductance.

(d) The externally imposed potential difference is simply imposed on the difference in potential of the double layer itself. This means that the external field does not deform the double layer, and does not disturb its equilibrium structure.

Although this theory does provide the basis for an important relationship of electrophoresis (discussed later) it has long been recognised as an

inadequate representation of the real situation.

2.1.2. The Gouy-Chapman theory: The diffuse edl.

The ideas about the edl applied in the Helmholtz-Perrin theory were of a formal nature. They merely reflected the fact of redistribution of charges between contacting phases and gave no indications as to the spatial distribution of charges in the edl. Gouy and, independently, Chapman formulated the problem as a purely theoretical one, namely, given a surface charge, find the spatial distribution of the counterions. The merit of their approach is that they took into consideration the important role of thermal motion.

In contrast to potential determining ions, a typical feature of which is a strong specific interaction with the surface, the counterions, even on approaching close to the surface, ordinarily interact with it only electrostatically. Inasmuch as counterions are usually solvated, at their closest approach to the surface they remain a quite considerable distance from it, so that the energy of their electrostatic interaction with the surface cannot substantially exceed the thermal motion energy kT (Dukhin). This consideration indicates the invalidity of the Helmholtz-Perrin molecular condenser theory. If the energy of ions in the field of attraction of the surface charge is of the order of kT then thermal motion should make this layer diffuse. Thus, the spatial distribution of the counterions is determined by the fact that they are in a state of thermal motion and, simultaneously, attracted to the surface charge, as a result of which they form a diffuse atmosphere of definite length.

The electric field strength in the double layer should decrease monotonically with increase in distance from the charged surface since its charge is screened by the charge of the counterions located in the layer between the given point and the surface, this screening being more complete the further the distance from the given point to the surface. At the outer boundary of the double layer the electric field should be reduced to zero, otherwise there would be a continuous flow of ions from the bulk into the double layer; i.e., there would be no equilibrium between the double layer and the bulk.

Quantitative laws of the spatial distributions of ϕ and the ionic concentrations within the edl may be established on the basis of consideration of the equilibrium conditions within the double layer and the laws of electrostatics. A condition of equilibrium within the double layer is the absence of ion streams within it. Such absence is attained through the compensation of the electromigration by diffusion streams. The conditions for compensation of electromigration and diffusion can be mathematically represented as (Hunter)

$$\text{grad } \mu_i = -z_i \, e \, \text{grad } \phi \qquad \text{B1.2}$$

2.2. The complete Poisson-Boltzmann (PB) equation.

Since there is equilibrium in the edl, the distribution of ions across this region will be according to Boltzmann. Therefore, using the definition of the chemical potential (per ion) in the form

$$\mu_i = \mu_i^{\circ} + kT \ln n_i \qquad \text{B1.3}$$

Then, from eqn. B1.2,

$$n_i = (N_o)_i \exp(-z\tilde{\psi}) \qquad \text{B1.4}$$

$$\text{where } \tilde{\psi} = \frac{e\psi}{kT}$$

The net volume charge density at points in the edl where the potential is ψ, becomes

$$\rho = e \sum_i z_i n_i \qquad \text{B1.5}$$

Substituting eqn. B1.5 in B1.I gives the complete PB equation

$$\nabla^2 \psi = -\frac{e}{\epsilon_{VAC} D} \sum_i (n_o)_i z_i \exp(-z_i \tilde{\psi}) \qquad \text{B1.6}$$

2.3. Solutions to the PB equation.

Solutions to the PB equation provide suitable relationships between

charge and potential that are necessary for the reconciliation of theory and experiment in aqueous colloid science. The appropriate equation is obtained from the boundary conditions.

$$\psi|_{surface} = \psi_s \qquad \text{B1.7}$$

$$\text{and } (\nabla\psi)\, r\,|_{surface} = \frac{\sigma_s}{\epsilon_{VAC}D} \qquad \text{B1.8}$$

The colloidal system being studied here consists of aqueous suspensions of rectangular particles (see Chapter A1). However, the attendant edl of these particles will naturally possess more curvature that a rectangular geometry and have a shape which is most simply described as cylindrical. Thus, solutions of charge/potential relationships in cylindrical geometry are of particular relevance to this work.

2.3.1. Limiting solutions to the PB equation.

The derivation of a charge/potential relationship, employing the boundary conditions given by eqns. B1.7 and B1.8, is a straightforward procedure when the size of the particle is such that

$$\kappa a >> 1 \qquad \text{B1.9}$$

$$\text{or} \quad \kappa a << 1 \qquad \text{B1.10}$$

The parameter κ (Kappa) is mainly dependent on electrolyte concentration and is very important in colloid science. κ has units of reciprocal length and it is customary to refer to $1/\kappa$ as the effective "thickness" of the edl, being the distance over which ψ decreases by an exponential factor ($\frac{1}{exp}$) at low potentials. For curved surfaces the dimensionless quantity "κa", being the ratio of particle radius of curvature to edl thickness, describes the shape of the double layer.

2.3.1.1. Solution of the PB equation in planar geometry; large κa regime.

In the κa regime described by eqn. B1.9 the particle is large compared to the edl thickness, which can be regarded as a thin region around the particle surface. In this case, the curvature of the particle surface can be ignored, i.e., the edl is treated as being flat, and the PB equation can be solved in planar geometry:

$$\nabla^2\psi \rightarrow \frac{d^2}{dr^2} \qquad \text{B1.11}$$

Eqn. B1.6 becomes, therefore,

$$\frac{d^2\psi}{dr^2} = \frac{-\rho}{\epsilon_{VAC}D} = \frac{-e}{\epsilon_{VAC}D} \cdot \sum_i (n_o)_i z_i \exp(-z_i \tilde{\psi}) \qquad B1.12$$

A solution of eqn. B1.12 is given by Gouy and, independently, Chapman as the charge/potential relationship for planar geometry:

$$(\sigma_s)_p = (8n_o kT\epsilon_{VAC}D)^{\frac{1}{2}} \sinh \left(\frac{z\tilde{\psi}_s}{2}\right) \qquad B1.13$$

where $n_o = (n_o)_+ = (n_o)_-$, and $z = z_+ = z_-$

When allowance is made for the conversion from number concentration in bulk solution (n_o) to molar concentration of symmetrical electrolyte i in bulk solution ([i]) a more convenient expression is obtained:

$$(\sigma_s)_p = (8\times10^3.[i]kT\epsilon_{VAC}DN_A)^{\frac{1}{2}} \sinh \left(\frac{z\tilde{\psi}_s}{2}\right) \qquad B1.14$$

In the derivation of eqn. B1.14 the integration process can be taken from the bulk solution up to any plane parallel to the surface. When such an integration is done, the accumulated space charge per unit area up to that plane is obtained, and this charge is balanced by the charge between the chosen plane and the particle surface. If, in particular, the integration is stopped at the shear plane then the net charge per unit area over the shear plane, i.e., the electrokinetic charge density (σ_E) is obtained:

$$(\sigma_E)_p = (8\times10^3.[i]kT\epsilon_{VAC}DN_A)^{\frac{1}{2}} \sinh \left(\frac{z\tilde{\zeta}_p}{2}\right) \qquad B1.15$$

2.3.1.2. Solution of the PB equation by linearisation; small κa regime.

In the κa regime described by eqn. B1.10 the particle appears "point-like" in comparison to the extent of the edl and a linearisation of the differential eqn. B1.6 is a good approximation if ψ is small everywhere in the edl; i.e., if $z_i e\psi \ll kT$ [meaning $\psi \ll 25mV$ (at 25°C for a monovalent electrolyte)] then the exponential in eqn. B1.6 can be expanded using $e^{-x} \rightarrow 1-X$ for small X. Hence,

$$\nabla^2\psi = -\frac{1}{\epsilon_{VAC}D}\cdot\left[\sum_i z_i e(n_o)_i - \frac{\sum_i z_i^2 e^2 (n_o)_i \psi)}{kT}\right] \qquad \text{Bl.16}$$

The first summation term in the parenthesis must be zero in order to preserve electroneutrality in the bulk electrolyte so eqn. Bl.16 becomes

$$\nabla^2\psi = \frac{e^2}{\epsilon_{VAC}DkT}\cdot\psi\cdot\sum_i (n_o)_i z_i^2 \qquad \text{Bl.17}$$

or, more simply,

$$\nabla^2\psi = \varkappa^2\psi \qquad \text{Bl.18}$$

The simplification of taking ψ as small in magnitude is referred to as the Debye-Huckel approximation.

The particular form of the charge/potential relationship derived from eqn. Bl.18 will depend upon the geometry of the edl involved. Gorin, in Abramson et. al., employed the charge potential relationship for an edl having cylindrical geometry:

$$(\sigma_S)_L = \psi_S\,\epsilon_{VAC}D\varkappa\cdot\frac{{}^1K(\varkappa a)}{{}^\circ K(\varkappa a)} \qquad \text{Bl.19}$$

The corresponding relation for σ_E being

$$(\sigma_E)_L = \frac{\zeta_L\,\epsilon_{VAC}D}{a}\left[\frac{{}^\circ K(\varkappa a + \varkappa a_G)}{(\varkappa a + \varkappa a_G)\,{}^1K(\varkappa a + \varkappa a_G)} + \ell n\left[\frac{(a + a_G)}{a}\right]\right]^{-1} \qquad \text{Bl.20}$$

Terms involving a_G appearing in eqn. Bl.20 are a speculative correction factor introduced by Gorin to account for the fact that the distance of closest approach to a particle surface, by electrolyte ions, is the hydrated radius of these ions; a more detailed criticism of the inclusion of such a correction was given by Overbeek 1950.

For the majority of colloidal systems both $\varkappa a$ and ζ are such that the PB equation cannot be well approximated either by assuming planar geometry or by linearising i.e., for the majority of colloidal systems

$$1 < \varkappa a < 100 \qquad \text{Bl.21}$$

$$\text{and} \quad 0 \leqslant \zeta < 150\ \text{mV} \qquad \text{Bl.22}$$

Thus, true σ_E for the majority of colloidal systems would be expected to have a magnitude, under the same conditions of electrolyte concentration and pH, that is intermediate between that predicted by the limiting solutions of the PB equation outlined above. As the colloidal system being studied here has a geometry which is most simply described as cylindrical the solution of the PB equation in this geometry, and especially within the $\varkappa a$ and ζ regimes given by, respectively, B1.21 and B1.22, assumes a special importance.

2.3.2. Solution of the PB equation in cylindrical geometry; intermediate $\varkappa a$ and high ψ values.

The PB equation in cylindrical geometry is

$$\frac{d^2\tilde{\psi}}{d(\varkappa r)^2} + \frac{1}{\varkappa r} \cdot \frac{d\tilde{\psi}}{d(\varkappa r)} = \sinh \tilde{\psi} \qquad \text{B1.23}$$

Analytical solutions of eqn. B1.23 are not available and, in general, numerical techniques or approximate analytical methods must be employed.

2.3.2.1. Solution of the PB equation in cylindrical geometry by a numerical technique (NT)

Recently, Stigter 1975 has used a NT to extend the range of validity of the analytical Debye-Huckel-Gorin expression (eqn. B1.20). His results for the case of $z = 1$ are presented in the form of a correction factor (β) which plays the role of converting the results for the Debye-Huckel edl into the correct value for the PB distribution:

$$(\sigma_E)_{Int.NT} = \beta.\frac{\tilde{\zeta}\epsilon_{VAC}DkT}{ae}\left[\frac{^{\circ}K(\varkappa a + \varkappa a_G)}{(\varkappa a + \varkappa a_G)^1K(\varkappa a + \varkappa a_G)} + \ell n\left[\frac{(a + a_G)}{a}\right]\right]^{-1} \qquad \text{B1.24}$$

In general, β depends on $\varkappa$ and ψ. Stigter 1975 determined β for a number of $\varkappa a$ and $\tilde{\psi}$ values by a Runge-Kutta numerical integration method. β is always $\geqslant 1$, which means that the linearised Debye-Huckel-Gorin equation (eqn. B1.20) always underestimates the charge corresponding to a given ζ of the cylinder. For a given $\varkappa a$ value, σ_E approaches that given by the Debye-Huckel approximation as ψ diminishes.

2.3.2.2. Solution of the PB equation in cylindrical geometry by an approximate analytical method (AM) (White).

A number of approximate analytic techniques have been applied to the solution of the PB equation. The earliest and most obvious approach is to attempt a perturbation solution of the linearised PB equation, using as a zero'th approximation the solution

$$\psi_L(r) = \psi_S \, \varkappa a \, e^{\varkappa a} \cdot \frac{e^{-r}}{\varkappa r} \qquad \text{Bl.25}$$

An alternative approach is via the analogous planar PB equation, which has a solution $\psi_p(r)$ satisfying the boundary conditions at the particle surface given by

$$\psi_p(r) = \frac{2kT}{ze} \cdot \ln \left[\frac{1 + e^{-\varkappa z} \cdot \tanh\left(\frac{z\tilde{\psi}_S}{4}\right)}{1 - e^{-\varkappa z} \cdot \tanh \frac{z\tilde{\psi}_S}{4}} \right] \qquad \text{Bl.26}$$

As a general rule, approximate theories which start with the linearised solution are limited to the small $\varkappa a$ regime. The solution in the large $\varkappa a$ regime would require high order perturbation theory for accurate results. However, methods which start with the planar result are restricted to the large $\varkappa a$ regime and furthermore deny the fact that, asymptotically, the form of the linearised solution must hold, i.e., at large r. The matching of this true long-range form with the short-range planar solution is mathematically difficult. Ohshima et. al., have recently derived a surprisingly accurate analytical charge/potential relationship for a cylindrical colloidal particle. This derivation utilises the fact that sufficiently near to the surface of a cylinder of any radius the potential must look like the planar solution, but must go over, at large r, to the asymptotic result. In their paper Ohshima et.al., approximate the cylindrical PB equation by another readily soluble differential equation, yielding an analytical charge/potential expression of remarkable accuracy. At the shear plane this expression reads

$$(\sigma_E)_{Int.AM} = \frac{\varepsilon_{VAC} D \varkappa kT}{e} \cdot 2 \sinh\left(\frac{\tilde{\zeta}}{2}\right) \left[1 + \frac{\left[\frac{{}^{0}K(\varkappa a)}{{}^{1}K(\varkappa a)}\right]^{-2} - 1}{\cosh^2\left(\frac{\tilde{\zeta}}{4}\right)} \right]^{\frac{1}{2}} \qquad \text{Bl.27}$$

2.4. Calculation of zeta potential

Electrophoresis experiments are frequently carried out with the purpose of measuring electrophoretic velocity. The velocity per unit strength of the applied electric field is called the electrophoretic mobility (u) and is a characteristic property of the colloidal system being studied. In this section, u will be considered as a given quantity, and the discussion will be limited to the theoretical interpretation of this electrokinetically determined quantity and its relation to ζ. In this interpretation, the concept of the edl plays a central part.

2.4.1. General considerations (Overbeek 1967).

Shortly after an electric field is applied to a colloidal system the system reaches a stationary state in which the velocity of the particles in the direction of the field is constant in time. There are four different forces acting on a particle that is in electrophoretic motion:

a) the force, k_I, exerted by the electric field on the charge of the particle,

b) the Stokes frictional resistance, k_{II},

c) the electric field exerts a force on the ions in the edl. This force is transferred to the molecules of the solvent. The resulting flow of the liquid causes a retarding force, k_{III}, termed "electrophoretic retardation" on the colloidal particle, and

d) in the stationary state which is present shortly after the application of the electric field, the centre of the ionic atmosphere lags behind the centre of the particle. The coulombic forces between the charge on the particle and the ions tend to rebuild this atmosphere in its "proper" place. However, this takes a finite time called the relaxation time. This causes an electrical force k_{IV} on the charge of the particle; the electrical force k_{IV} is, in most cases, also a retarding force (relaxation effect). In the stationary state, the sum of all forces acting on the particle is zero;

$$k_I + k_{II} + k_{III} + k_{IV} = 0 \qquad \text{B1.28}$$

Generally, the forces k_{III} (retardation effect) and k_{IV} (relaxation effect) are complicated functions of several parameters of the colloid system. In a number of limiting cases one or both of these forces are ignored and rather simple expressions for the relation between u and ζ are obtained.

2.4.2. Limiting u/ζ relationships.

2.4.2.1. Helmholtz-Smoluchowski equation; large κa regime.

Proceeding in the main from the same premises as Helmholtz, Smoluchowski derived a formula for u of a particle of arbitrary shape. Smoluchowski's analysis was, in the first instance, directed upon electroosmosis and he derived his electrophoresis equation by simply remarking that electrophoresis is the reverse phenomenon from electroosmosis, so that, for the relative motion of liquid and solid the same equation applies to both phenomena. Smoluchowski's derivation began as follows: If the particle is a nonconductor of electricity then the applied field has only a component parallel to the surface. In addition, if the edl surrounding the particle is thin compared to the particle's radius of curvature, then the particle surface may be considered as essentially flat with the motion of liquid in the adjacent diffuse part of the edl being parallel to the particle surface. Thus, a volume element of liquid in the edl is subjected to two forces of opposite directions both parallel to the particle surface, one due to the applied electric field working on the charge of the edl, the other due to viscous friction. The volume element of liquid will rapidly attain a uniform velocity parallel to the surface with electrical and viscous forces balanced. By equating these forces, inserting Poisson's equation, and assuming constant relative permittivity and viscosity, Smoluchowski obtained

$$\zeta_p = \frac{u\eta}{\epsilon_{VAC}D} \qquad \text{B1.29}$$

2.4.2.2. Huckel equation; small κa regime.

Debye and Huckel also applied to colloidal particles the method of calculation used in the theory of strong electrolytes. In 1924 Huckel

published a detailed calculation of the electrophoretic retardation force (k_{III}) acting on a spherical particle. His result was

$$k_{III} = (4\pi\epsilon_{VAC}D\zeta_L a - Q)X \qquad \text{Bl.30}$$

Combining this result with eqn. Bl.28 gives

$$QX - 6\pi\eta av + (4\pi\epsilon_{VAC}D\zeta_L a - Q)X + k_{IV} = 0 \qquad \text{Bl.31}$$

Neglecting k_{IV}, gives

$$4\pi\epsilon_{VAC}D\zeta_L aX = 6\pi\eta av \qquad \text{Bl.32}$$

Finally,

$$\zeta_L = \frac{3u\eta}{2\epsilon_{VAC}D} \qquad \text{Bl.33}$$

2.4.2.3. Henry solution of the contradiction between Smoluchowski and Huckel theories.

The apparent contradiction between eqns. Bl.29 and Bl.33 was resolved by Henry, who gave a critical analysis of the assumptions underlying these equations. Henry ascertained that the difference between the concepts of Smoluchowski and Huckel was to be found in the geometry of of the applied field. Whereas Smoluchowski considers the particle as an insulator and takes the deformation of the applied field by the particle explicity into account, Huckel simply assumed that the magnitude and the direction of the electric field have the same value throughout the whole system, i.e., Huckel did not consider deformation of the applied field. These assumptions of Smoluchowski and Huckel are justifiable in the extreme situations of $\varkappa a \gg 1$ and $\varkappa a \ll 1$, respectively. The assumption of Huckel is quite justifiable in the case of electrolyte solutions, because there the extension of the double layer is so much larger than the dimensions of the ions that the deformation of the field is practically without influence. In colloidal systems, however, which of the two concepts must be applied depends wholly upon the ratio of the extension of the double layer and the dimensions of the particles. If the particle is very large then the

deformation of the lines of force must be taken into account and the assumption of Smoluchowski is justified.

2.4.3. Recent theories of electrophoresis; intermediate $\varkappa a$ and high ψ values.

A great deal of work has been done on the theory of electrophoresis to improve upon the models of Smoluchowski and Huckel. These early treatments, and the treatment by Henry of the cylinder, neglected the relaxation of the ionic atmosphere of the colloid and, hence, are valid mainly for low potentials. Relaxation can be safely neglected when $\varkappa a$ is very small or very large, but it is significant for intermediate values of $\varkappa a$ (say, $0.2 < \varkappa a < 50$), especially at high potentials. This was found by Overbeek 1943 and, independently, by Booth, who derived equations for spherical particles which allow for retardation (k_{III}), relaxation (k_{IV}) and surface conductance in the mobile part of the edl. Owing to mathematical difficulties, these equations were only solved for a restricted number of terms and quantitative validity could only be claimed for $\zeta < 25$ mV. The treatments of Overbeek and Booth have now been superseded both in range of validity and convenience by that of Wiersma et.al., Loeb et.al., for spherical particles, and by that of Stigter 1978a, 1978b for cylindrical particles.

2.4.3.1. The treatment of the electrophoresis of a highly charged cylindrical particle in a uni-valent salt solution by Stigter 1978a, 1978b.

The theory of cylinders differs from that of spheres in that there is an orientation problem. For cylindrical particles in an applied electric field the experimental values of u are average results of the randomly orientated particles; there are two principal orientations of cylinders, perpendicular to, and parallel with, the applied electric field. The average mobility of cylinders in random orientation is $(u_{/\!/} + 2u_{\perp})/3$. However, despite this orientation problem, the general approach and fundamental equations for the electrophoresis of the sphere and the cylinder are rather similar. The treatment is for a long, insulating cylinder with a radius a, finite length l, positive charge ze (and capped with hemispherical ends of radius a), in an aqueous univalent salt solution.

2.4.3.1.1. Mobility in tangential field, $u_{//}$.

In the electrophoresis of the cylinder orientated parallel to the applied field the perturbations of the ionic atmosphere at the ends of the cylinder (relaxation effect or end effects, in this case) requires discussion. The mobility of charged particles of arbitrary shape is given by the equation of Smoluchowski as long as $\kappa a >> 1$; thus, eqn. B1.29 holds for the cylinder when $\kappa a >> 1$. For $\kappa a < 1$ the external field and the liquid flow in the double layer are no longer parallel to the charged surface and eqn. B1.29 has to be corrected for relaxation effects. Since the radius a is of the same order as $\frac{1}{\kappa}$ or smaller, a correction is required near the ends of the cylinder. It follows that, as long as flow and field perturbations are localised near the ends, eqn. B1.29 is still a good approximation for long cylinders in a parallel field. The crucial question is: Do these field perturbations vanish over a short distance, or are there long-range effects that may change the applied field in the double layer along the entire cylinder? Fortunately, in his treatment Stigter 1978a, 1978b showed, at least qualitatively, that the end effects were <u>not</u> long range and diminished within a few times $\frac{1}{\kappa}$ along the straight part of the cylinder. Consequently, even if there is a relaxation effect, the end effects are expected to be localised, thus validating eqn. B1.29 for long cylinders in tangential field.

2.4.3.1.2. Mobility in transverse field, $u_{\perp}$.

In the electrophoresis of the cylinder orientated perpendicular to the applied field, end effects are neglected. u of the cylinder follows from the solution of the Navier-Stokes equation which represents the local force balance in the liquid (Hunter):

$$-\eta \text{ curl curl } v + \text{grad } p + \rho \text{ grad } \psi = 0 \qquad \text{B1.34}$$

The viscosity η is assumed to be uniform throughout the solution surrounding the cylinder. For convenience, the cylinder is considered to be at rest while the solution at large distance flows back with the uniform velocity -v. It is assumed that there is no slip at the surface of the cylinder. The ionic space charge neutralises the surface charge of the cylinder. It is assumed that the surface charge has cylindrical symmetry and is fixed to the cylinder, i.e., no conductance or charge

polarisation occurs on the surface of the cylinder when the external field is applied. ψ is a solution of Poisson's equation, and D is considered as uniform throughout the solution. Under electrophoretic conditions, the ionic atmosphere is continually destroyed behind the migrating cylinder and rebuilt in front of it. Because the mobility of the small ions is finite, the reformation of the ionic atmosphere lags behind. Due to this relaxation effect, the steady state ion concentrations n_+ and n_- are not cylindrically symmetric. The asymmetry depends on the local (reduced) mobilities ($\tilde{u}_{ION}$) of the cations (coions) and anions (counterions), given by

$$(\tilde{u}_{ION})_{\pm} = \frac{2}{3} \cdot \frac{\epsilon_{VAC} DkTF}{ne} \cdot \frac{1}{\Lambda} \qquad \text{Bl.35}$$

[For $\Lambda = 70 \times 10^{-4}$ ohm^{-1} m^2 mol^{-1}, $(\tilde{u}_{ION})_{\pm} = 0.1840$ (at 25°C).] The numerical solution of the PB equation for cylindrical geometry employed in the treatment, is that achieved by Stigter 1975 using a numerical technique.

2.4.3.1.3. Numerical results for the randomly orientated cylindrical particle.

In his treatment, Stigter 1978a, 1978b arrived at a set of interdependent, integral relations from which, by a series of successive approximations, he obtained numerical results for the randomly orientated cylindrical particle. [Throughout this treatment the value of 0.184 was used for the local, reduced mobilities of the cations and the anions]. Stigter 1978a, 1978b presented his results as a table of the electrophoretic mobility factor $u_{ST}(\varkappa a, \tilde{\zeta})$, such that

$$\tilde{\zeta} = \frac{\tilde{U}}{u_{ST}} \qquad \text{Bl.36}$$

$$\text{where } \tilde{U} = \frac{3une}{2\epsilon_{VAC} DkT}$$

2.5. Complete expressions for σ_E.

2.5.1. Large $\varkappa a$ regime.

Combining eqns. B1.15 and B1.29, for the large $\varkappa a$ regime, gives the complete expression for σ_E as a function of u:

$$(\sigma_E)_p = (8\times10^3.[i]kT\epsilon_{VAC}DN_A)^{\frac{1}{2}} \sinh\left(\frac{z\tilde{u}}{3}\right) \qquad \text{B1.37}$$

2.5.2. Small $\varkappa a$ and ζ regime, in cylindrical geometry.

Combining eqns. B1.20 and B1.33, for the small $\varkappa a$ and ζ regime, gives the complete expression for σ_E as a function of u (in cylindrical geometry):

$$(\sigma_E)_L = \frac{3un}{2a}\left[\frac{^{\circ}K(\varkappa a + \varkappa a_G)}{(\varkappa a + \varkappa a_G)^{1}K(\varkappa a + \varkappa a_G)} + \ell n\left[\frac{(a + a_G)}{a}\right]\right]^{-1} \qquad \text{B1.38}$$

2.5.3. Intermediate $\varkappa a$ regime, in cylindrical geometry.

Inserting the Stigter function $\tilde{\zeta}_{ST}(\varkappa a, \tilde{u})$ in eqns. B1.24 and B1.27 ($\tilde{\zeta} \rightarrow \tilde{\zeta}_{ST}$) for the intermediate $\varkappa a$ regime, gives two complete expressions for σ_E as a function of u (in cylindrical geometry):
From Debye-Huckel-Gorin-Stigter

$$(\sigma_E)_{Int.NT} = \beta.\frac{\epsilon_{VAC}DkT}{ea}.\tilde{\zeta}_{ST}\left[\frac{^{\circ}K(\varkappa a + \varkappa a_G)}{(\varkappa a + \varkappa a_G)^{1}K(\varkappa a + \varkappa a_G)} + \ell n\left[\frac{(a + a_G)}{a}\right]\right]^{-1} \qquad \text{B1.39}$$

and from Ohshima-Healy-White

$$(\sigma_E)_{Int.AM} = \frac{\epsilon_{VAC}D\varkappa kT}{e}.2\sinh\left(\frac{\tilde{\zeta}_{ST}}{2}\right).\left[1 + \frac{\left[\frac{^{\circ}K(\varkappa a)}{^{1}K(\varkappa a)}\right]^{-2} - 1}{\cosh^2\left(\frac{\tilde{\zeta}_{ST}}{4}\right)}\right]^{\frac{1}{2}} \qquad \text{B1.40}$$

3. METHOD

The velocity of αFeOOH particles dispersed in NaCl aq. solutions, under the influence of an applied electric field, was measured within the concentrations and pH ranges 0.5mmol $dm^{-3} \leqslant$ [NaCl] $\leqslant$ 0.1 mol dm^{-3} and $3.90 \leqslant pH \leqslant 7.70$, respectively.

A dispersion container, containing a teflon coated magnetic flea, was placed on the magnetic stirrer. 200 cm^3 of a NaCl solution was pipetted into the container and the solution stirred. Nitrogen gas was bubbled into the solution, via a pasteur pipette, until the pH of the solution, continuously monitored by the pH electrode system, was 7.00. The pH electrode system and the pasteur pipette were removed from the container and 0.4000 g $\pm$ 0.0005 g of αFeOOH was added to the NaCl solution. The dispersion was stirred for 10-15 minutes and finally left unstirred for 7 days. The dispersion was stirred for several minutes and then allowed to settle. The top of the container was removed and the pH electrode system inserted into the dispersion. By means of the addition of known volumes of dilute HCl aq. and dilute NaOH aq. the pH of the dispersion was adjusted to the desired pH. The dispersion was stirred for several minutes and then allowed to settle in order to facilitate the sedimentation of aggregates of particles. The previously cleaned and dryed cylindrical glass cell, containing an atmosphere of nitrogen, was flushed with two $4cm^3$ portions of the dispersion and finally completely filled with a third $4cm^3$ portion. [It is to be noted that the above procedure of allowing the dispersion to settle before sampling it into the glass cell does not make any significant selection of smaller particles into the cell, since an αFeOOH particle of radius 50nm would, according to Stokes Law, take 2 weeks to fall through 1 cm of aqueous solution.] The cylindrical glass cell was carefully positioned in the auxilliary water bath of the microelectrophoresis apparatus. The platinum metal electrodes were inserted into the cell and the digital voltmeter was connected across the platinum wires of the cell. The quartz iodine illuminator was turned on and the microscope was focussed on the top inside surface of the cell; the micrometer reading, d_1, was recorded. The microscope was then focussed on the upper stationary level of the cell by movement of the micrometer to a reading d_2 given by

$$d_2 = d_1 - d^1 \qquad \text{Bl.41}$$

The voltage across the platinum electrodes was switched on and its value adjusted such that the time for an observed particle to move across one division of the eyepiece graticule was an easily measurable time period, for example two seconds. The voltage was switched off. The particle velocity measurements were then conducted as follows:- The voltage

across the platinum electrodes was switched on in a particular sense, say $\rightarrow$, and the time, $t_{\rightarrow}$, for an observed particle to traverse one division of the eyepiece graticule recorded; the voltage, $V_{\rightarrow}$, across the platinum wires within the cell was also recorded. The voltage across the platinum electrodes was then switched on in the reverse sense, i.e., $\leftarrow$ and once again the time, $t_{\leftarrow}$, for an observed particle to traverse one division of the eyepiece graticule, and the voltage, $V_{\leftarrow}$, across the platinum wires were recorded. This procedure was repeated twenty times giving twenty $t_{\rightarrow}$, $V_{\rightarrow}$, $t_{\leftarrow}$ and $V_{\leftarrow}$ values.

4. RESULTS.

For each pH value to which a particular αFeOOH/NaCl aq. suspension was adjusted, u was calculated using the expressions

$$u = \frac{u_{\rightarrow} + u_{\leftarrow}}{2} \qquad \text{Bl.42}$$

$$\text{where} \quad u_{\rightarrow} = \overline{t_{\rightarrow}^{-1}} \cdot \frac{\ell_g \ \ell_c}{\bar{V}_{\rightarrow}} \qquad \text{Bl.43}$$

$$\text{and} \quad u_{\leftarrow} = \overline{t_{\leftarrow}^{-1}} \cdot \frac{\ell_g \ \ell_c}{\bar{V}_{\leftarrow}} \qquad \text{Bl.44}$$

From a knowledge of the volumes of the different dilute acid and base solutions added to attain a particular series of pH values of an αFeOOH/NaCl aq. suspension, the $[Cl^-]$ and I of the suspension, at each particular pH, was calculated. Using the data of Stigter 1975, and values interpolated from this data, a 2nd order two-dimensional polynomial of $\beta(\varkappa a, \tilde{\psi})$ was obtained in order to facilitate interpolation of β from $\varkappa a$ and $\tilde{\zeta}$ values. Using eqn. Bl.37 and the data of Stigter 1978a, 1979, and further data interpolated from this original Stigter 1978a, 1979 data, the function $\tilde{\zeta}_{ST}(\varkappa a\ \tilde{u})$ was obtained. In order to interpolate this function, for given values of $\varkappa a$ and u, a surface fitting polynomial was calculated. In order to facilitate good surface fitting, the data of the function were divided into the following three $\varkappa a$ ranges

$$\text{range 1} \quad 2 \leqslant \varkappa a \leqslant 5$$

range 2 $5 \leqslant \varkappa a \leqslant 20$

range 3 $20 \leqslant \varkappa a \leqslant 50$

and a second-order two-dimensional polynomial fitted to each $\varkappa a$ range of data. From the experimental data, viz., pH, $[Cl^-]$, I and u, and the polynomials of the functions $\beta(\varkappa a, \tilde{\psi})$ and $\tilde{\zeta}_{ST}(\varkappa a, \tilde{u})$, the various zeta potentials, charges and ancillary functions, viz., ζ_p, ζ_L, ζ_{ST}, $(\sigma_E)_p$, $(\sigma_E)_L$, $(\sigma_E)_{Int.NT}$, $(\sigma_E)_{Int.AM}$, $\varkappa$ and $\varkappa a$ were calculated (using eqns. Bl.29, Bl.33, Bl.37, Bl.38, Bl.39 and Bl.40). The variation of ζ_{ST} and $(\sigma_E)_{Int.AM}$ with I, and pH, is shown in Figs. Bl.1 and Bl.2, respectively. For comparison, the variation with I and pH, of ζ_p and $(\sigma_E)_p$ is shown in Figs. Bl.3 and Bl.4, respectively. In order to show the clear departure of the values of the shear surface quantities evaluated by the planar and linearisation equations from the more representative values evaluated by the treatments of Stigter, Ohshima et. al., the differences $(\zeta_{ST} - \zeta_p)$, $(\zeta_{ST} - \zeta_L)$, $((\sigma_E)_{Int.AM}-(\sigma_E)_p)$ and $((\sigma_E)_{Int.AM}-(\sigma_E)_L)$ are plotted as a function of I, and pH, in Figs. Bl.5 to Bl.8, respectively. [In all calculations the value used for particle radius (a) was that determined from scanning electron microscopy (Chapter Al), namely, 43.8nm.]

5. CONCLUSIONS.

a) For αFeOOH particles immersed in dilute 1:1 electrolyte solutions, the ratio of their radius of curvature to the effective thickness of the attendant edl ($\varkappa a$) is in the intermediate regime $3.2 \leqslant \varkappa a \leqslant 45.9$; in addition, their ζ rises to values well above 25 mV. Consequently, the limiting theoretical treatments of Helmholtz-Smoluchowski, Gouy-Chapman, Huckel, Gorin cannot be used in the calculation of the shear surface quantities of such particles. Instead, recourse must be made to an advanced treatment of electrophoretic theory, directly applicable to cylindrically shaped particles, having a range of validity in the intermediate $\varkappa a$ regime and in which allowance is made for the relaxation effect. Such a treatment is given by Stigter, Ohshima et.al.

b) The values of the shear surface quantities, ζ and σ_E, which best represent the real situation at the αFeOOH-NaCl aq. interface are those evaluated by means of the electrophoretic theories developed by Stigter,

FIGURE B1.1

STIGTER ZETA POTENTIAL OF ∝FeOOH DISPERSION AS A FUNCTION OF pH AT VARIOUS CONCENTRATIONS OF NaCl AND AT 25°C.

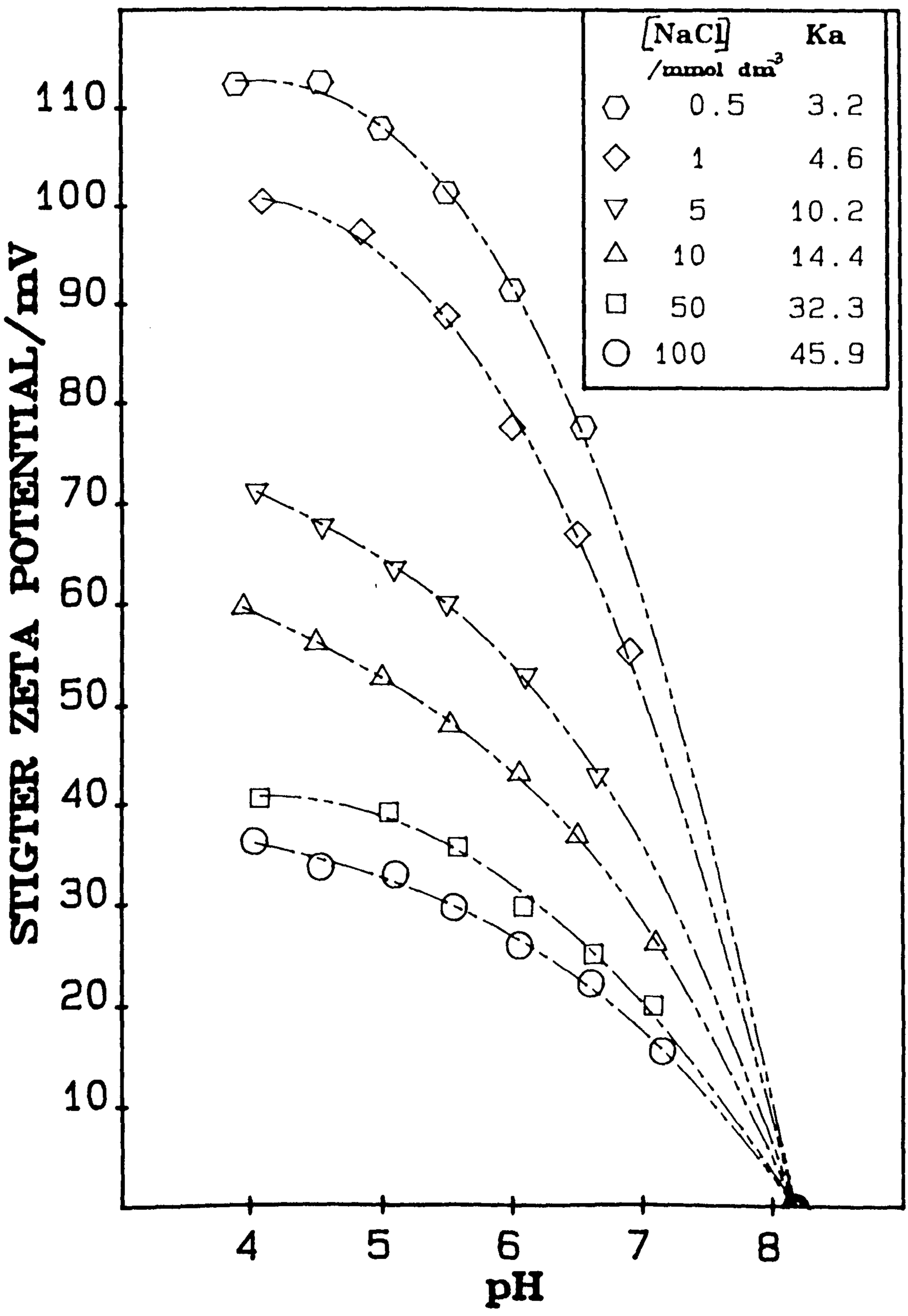

FIGURE B1.2

OHSHIMA–HEALY–WHITE ELECTROKINETIC CHARGE DENSITY OF αFeOOH DISPERSION AS A FUNCTION OF pH AT VARIOUS CONCENTRATIONS OF NaCl AND AT 25°C.

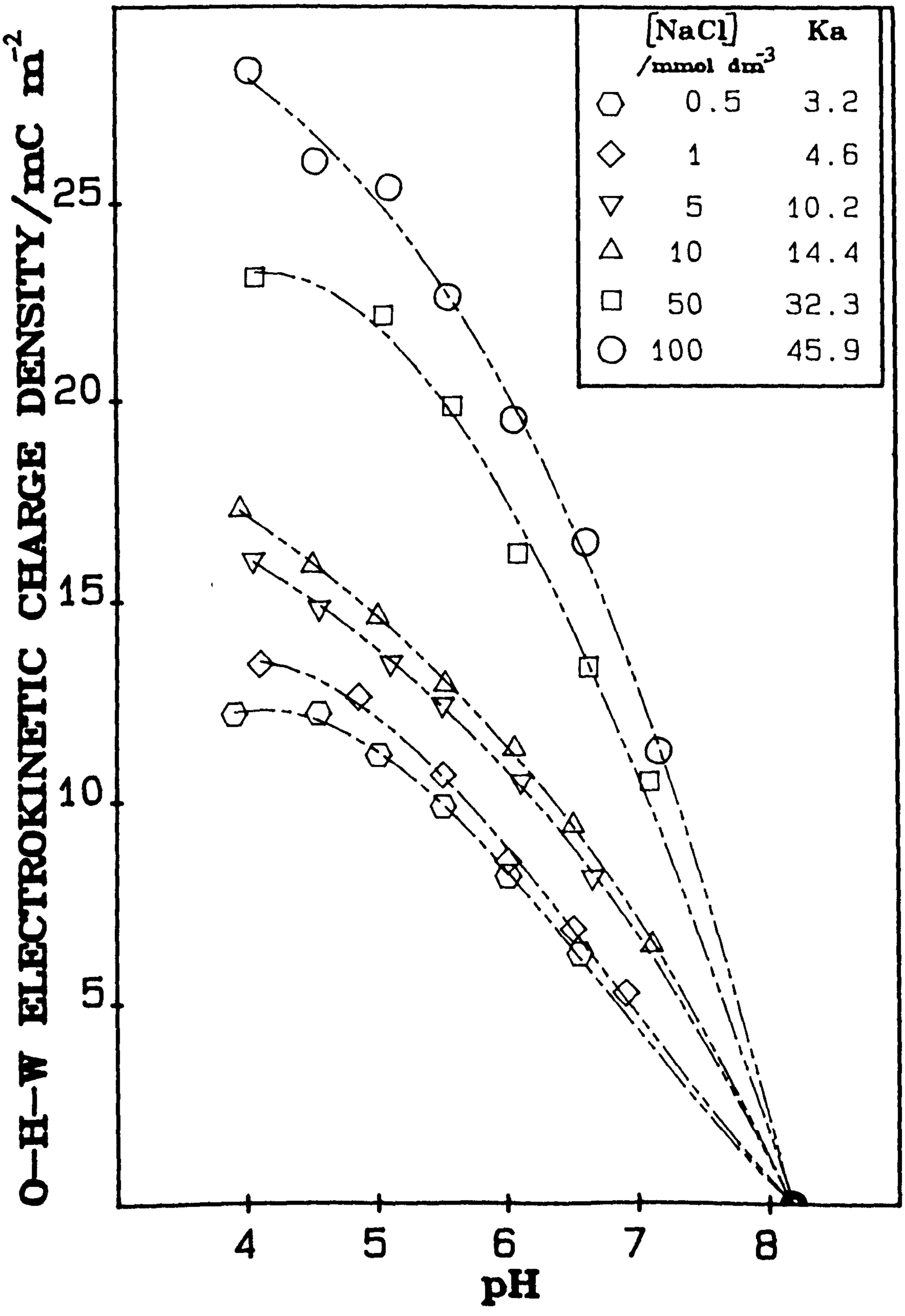

FIGURE B1.3

CLASSICAL 'PLANAR' ZETA POTENTIAL OF αFeOOH DISPERSION AS A FUNCTION OF pH AT VARIOUS CONCENTRATIONS OF NaCl AND AT 25°C.

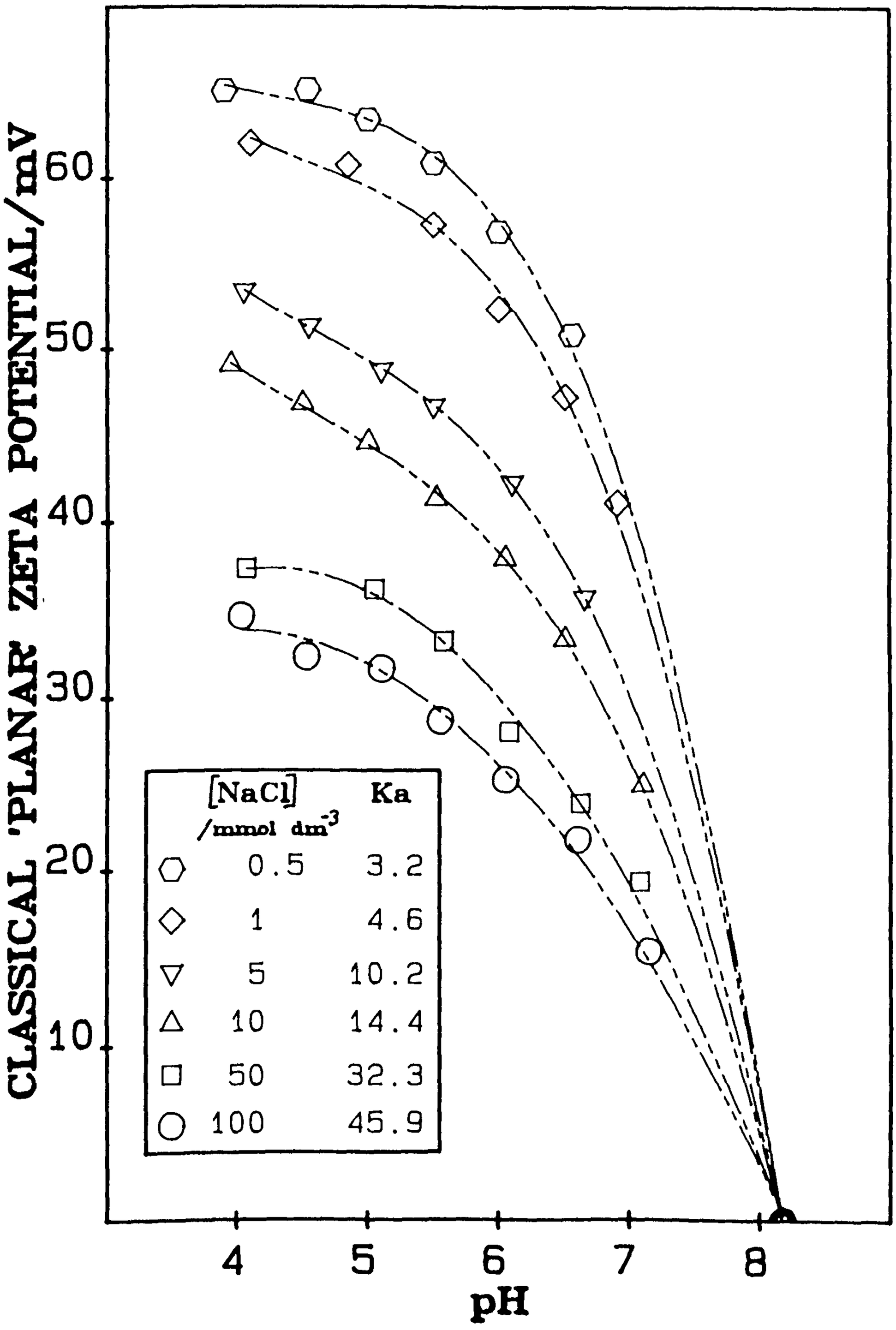

FIGURE B1.4

CLASSICAL 'PLANAR' ELECTROKINETIC CHARGE DENSITY OF ∝FeOOH DISPERSION AS A FUNCTION OF pH AT VARIOUS CONCENTRATIONS OF NaCl AND AT 25°C.

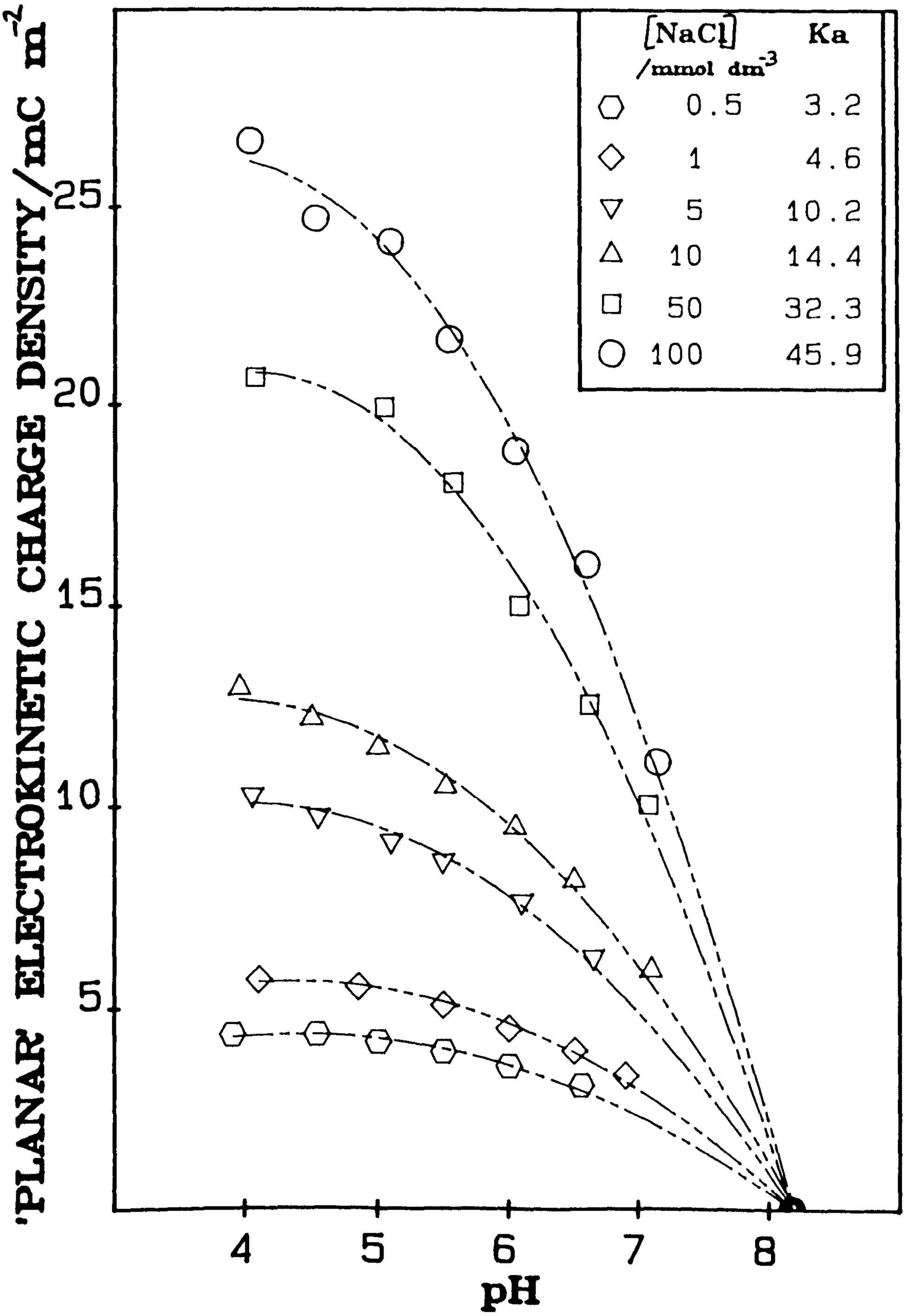

FIGURE B1.5

DEVIATION IN ZETA POTENTIAL OF 'PLANAR' THEORY FROM THAT DUE TO THE TREATMENT OF STIGTER AS A FUNCTION OF pH AT VARIOUS CONCENTRATIONS OF NaCl AND AT 25°C.

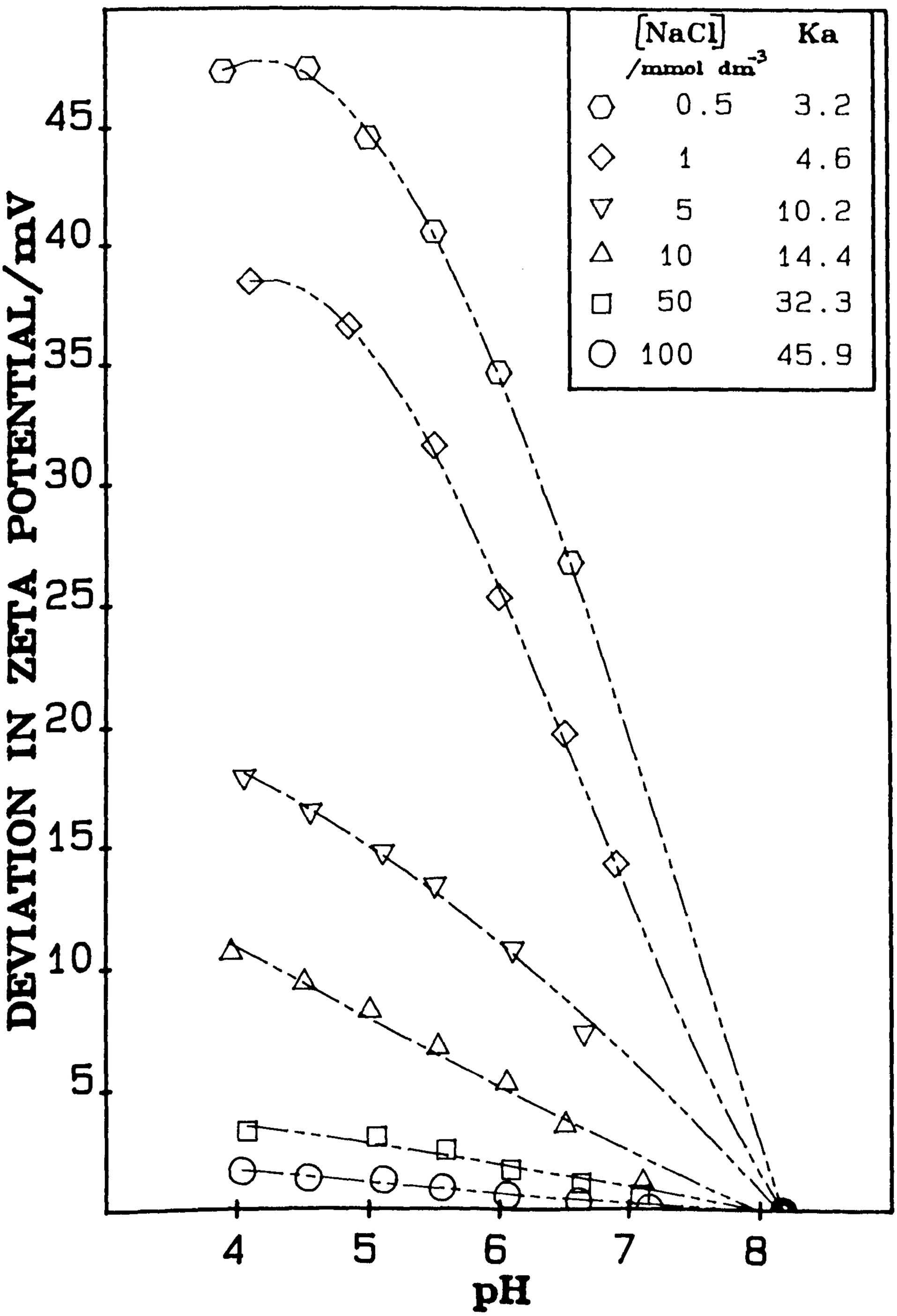

FIGURE B1.6

DEVIATION IN ZETA POTENTIAL OF 'LINEAR' THEORY FROM THAT DUE TO THE TREATMENT OF STIGTER AS A FUNCTION OF pH AT VARIOUS CONCENTRATIONS OF NaCl AND AT 25°C.

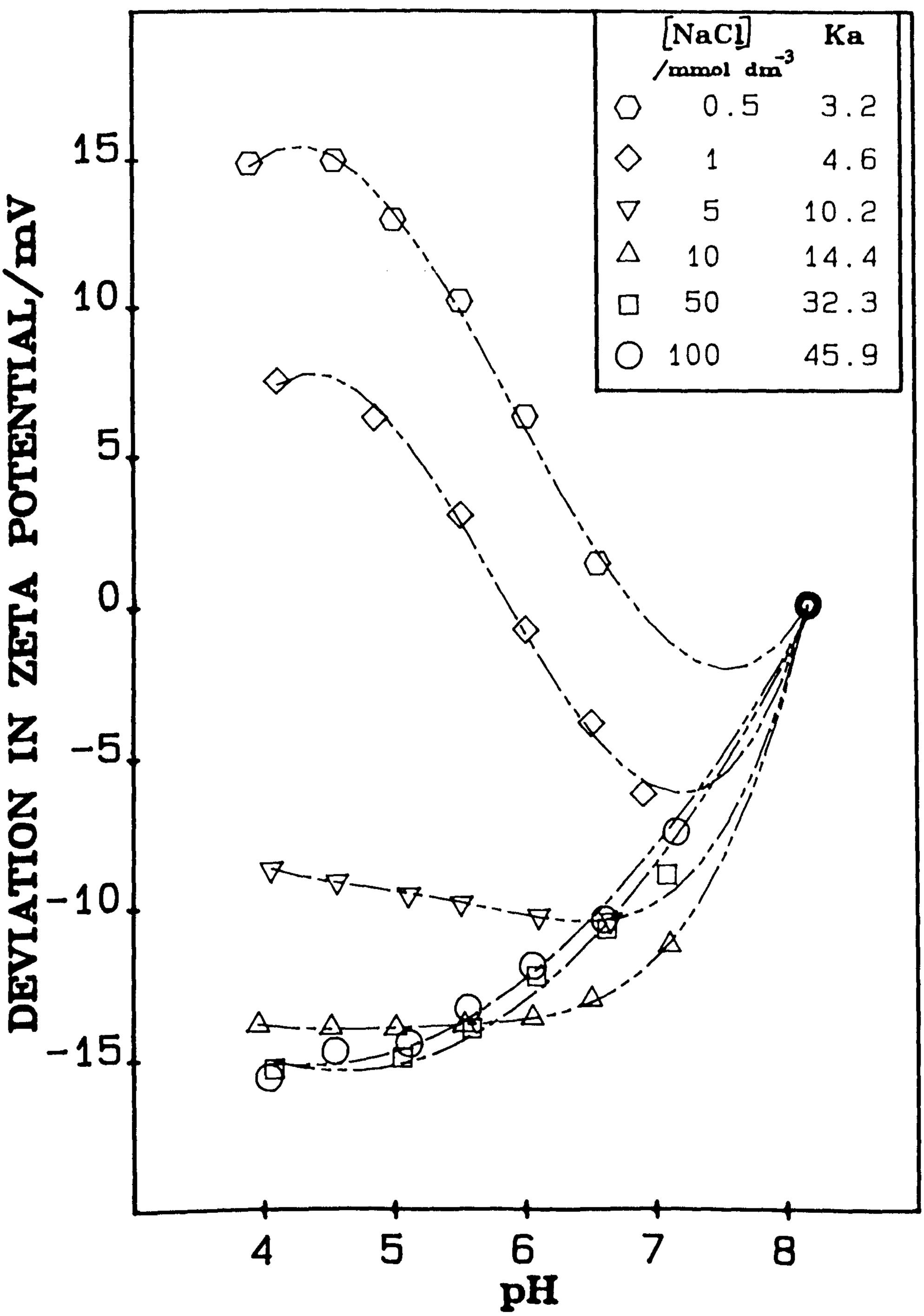

FIGURE B1.7

DEVIATION IN ELECTROKINETIC CHARGE DENSITY OF 'PLANAR' THEORY FROM THAT DUE TO THE TREATMENT OF OHSHIMA et.al. AS A FUNCTION OF pH AT VARIOUS CONCENTRATIONS OF NaCl AND AT 25°C.

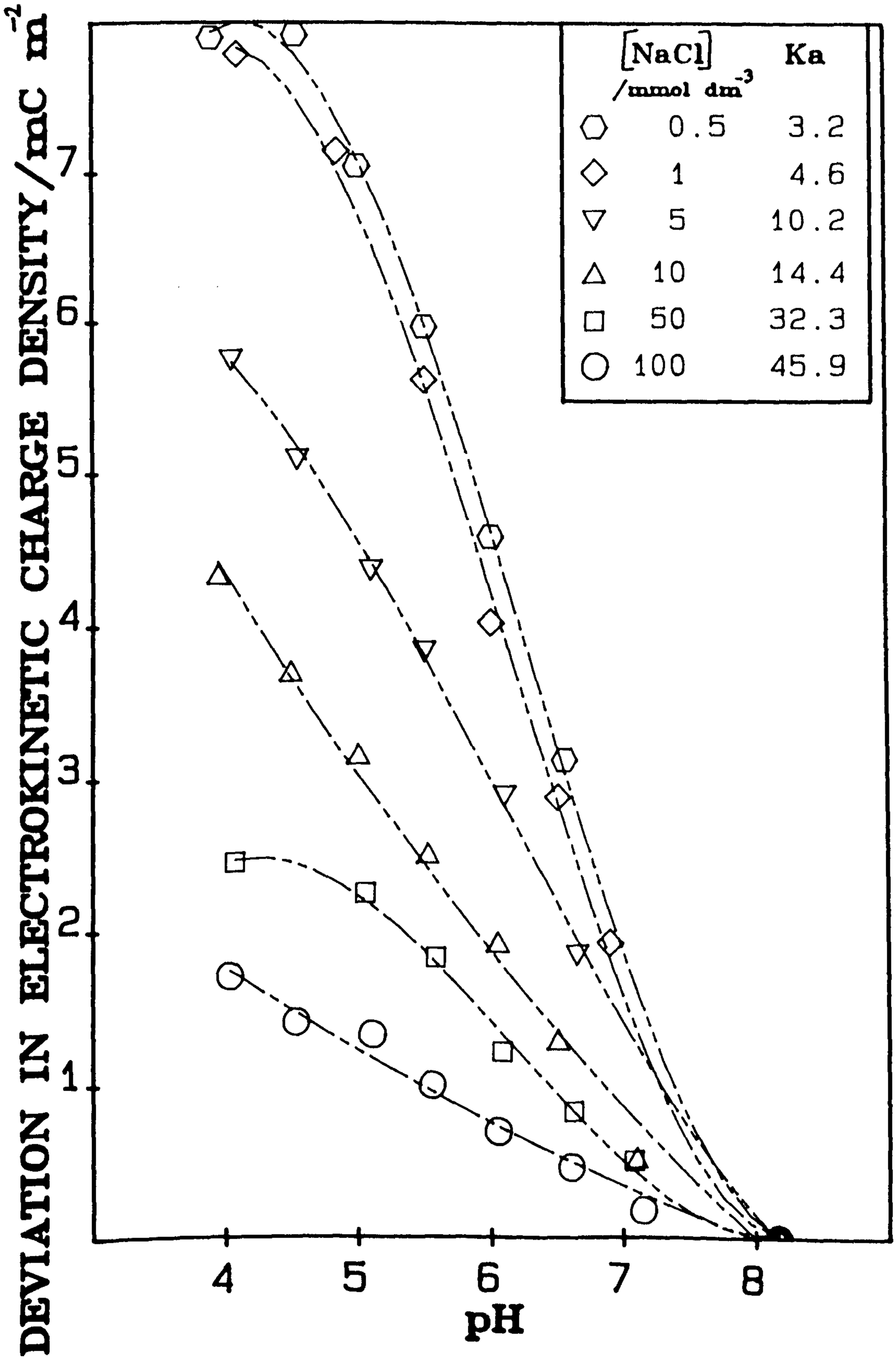

FIGURE B1.8

DEVIATION IN ELECTROKINETIC CHARGE DENSITY OF 'LINEAR' THEORY FROM THAT DUE TO THE TREATMENT OF OHSHIMA et.al. AS A FUNCTION OF pH AT VARIOUS CONCENTRATIONS OF NaCl AND AT 25°C.

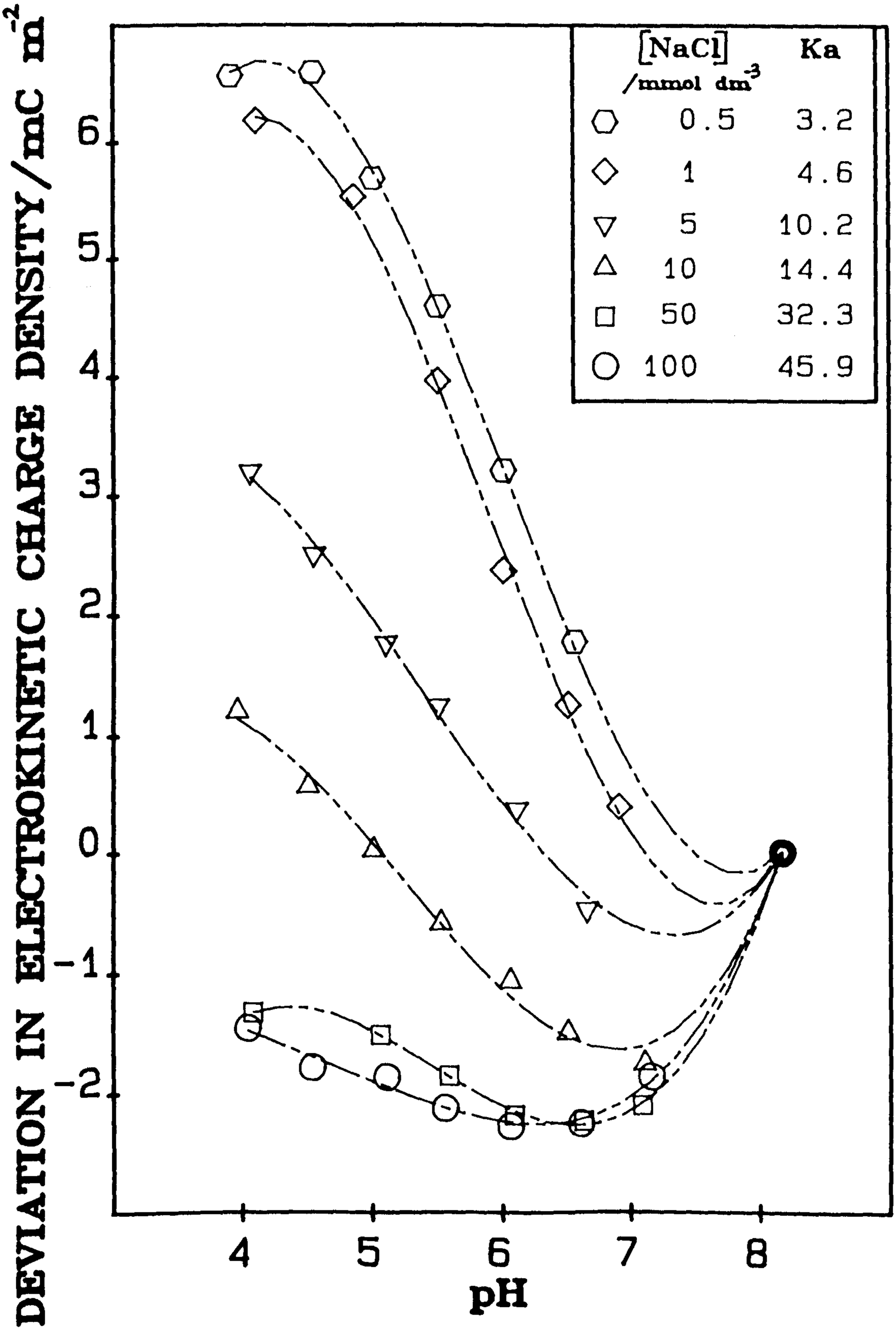

Ohshima et. al..

c) In general, the values of ζ and σ_E evaluated by the treatment of Stigter, Ohshima et al., differ significantly from those determined by the limiting planar and linearisation equations of Helmholtz-Smoluchowski, Gouy-Chapman, Huckel, Gorin; the difference increasing, as expected, with diminshing κa and, in most cases, increasing ψ. It is to be noted that at sufficiently high κa values this difference becomes independent of ψ. More specifically, for the range of [NaCl] employed in this study, ζ and σ_E are always underestimated by the planar equations and overestimated, at low ψ, by the linearisation equations; at high ψ, ζ and σ_E are either underestimated or overestimated by the linearisation equations depending on whether κa is small or large, respectively.

REFERENCES

Abramson, H. A., Moyer, L. S. and Gorin, M. H., "Electrophoresis of Proteins", Chap. 5, Rheinhold, New York, 1942.

Booth, F., Proc. Roy. Soc., A203, 514 (1950).

Chapman, D. L., Philos. Mag., 25, (6), 475 (1913).

Debye and Huckel, Physik. Z., 24, 305 (1923).

Dukhin, S. S., in "Surface and Colloid Science", Matijevic, E.; Editor, Vol. 7, Chap. 1, Wiley, New York, 1974.

Gouy, G., J. Phys. Radium, 9, 457 (1910).

Helmholtz, H., Wied. Ann., 7, 337 (1879).

Henry, D. C., Proc. Roy. Soc., A133, 106 (1931).

Huckel, E., Physik. Z., 25, 204 (1924).

Hunter, R. J., "Zeta Potential in Colloid Science", Academic Press, London, 1981.

Loeb, A. L., Overbeek, J.Th.G. and Wiersma, P. H., "The Electrical Double Layer Around a Spherical Colloid Particle", MIT Press, Cambridge, Mass, 1961.

Ohshima, H., Healy, T. W. and White, L. R., J. Colloid Interface Sci., 90, 17 (1982).

Overbeek, J.Th.G., Kolloidchem. Beih., 54, 287 (1943).

Overbeek, J.Th.G., Adv. Colloid Sci., 3, 97 (1950).

Overbeek, J.Th.G., in "Electrophoresis", Bier, M.; Editor, Volume II, Chap. 1., Academic Press, New York, 1967.

Perrin, J. J. Chim. Phys., 2, 607 (1904).

Smoluchowski, M., in "Handbuch der Electrizitat und des Magnetismus", Graetz, W.; Editor, Vol. 2, Barth, Leipzig, 1921.

Stigter, D., J. Colloid Interface Sci., 53, 296 (1975).

Stigter, D., J. Phys. Chem., 82, 1417 (1978).

Stigter, D., J. Phys. Chem., 82, 1424 (1978).

Stigter, D., J. Phys. Chem., 83, 1663 (1979).

White, L. R., J. Chem. Soc. Faraday Trans. 2, 73, 577 (1977).

Wiersma, P. H., Loeb, A. L. and Overbeek, J.Th.G., J. Colloid Sci., 22, 78 (1966).

CHAPTER B2

ELECTRIC CHARGE AND POTENTIAL AT THE SURFACE AND IHP IN THE COLLOID αFeOOH/NaCl aq.: CHLORIDE ION ADSORPTION MEASUREMENTS.

1. INTRODUCTION.

The continuous measurement of electrolyte adsorption from solution onto a solid phase, over a range of pH, presents an analytical problem, especially if the adsorbate/adsorbent interaction is not very strong. Without introducing any 'tracer' chemical into the solution (which may lock-up adsorbent surface or adsorbate), and avoiding the problems associated with electrolyte selective electrodes at variable pH (see Addendum) and radioactive isotopes in the presence of an iron compound (Kovacina and Venezky), sampling of the solution phase is required. Such sampling must unavoidably alter the quantities of available adsorbate, adsorbent and solvent, leading to a perturbation of the adsorbate/adsorbent equilibrium at the solid/solution interface. Thus, the quantity being measured is being altered by the act of measurement leading to erroneous results. However, perturbation of the adsorbate/adsorbent equilibrium can be greatly reduced, or even negated, if sampling involves the removal of only a relatively small volume of solution. The problem then becomes the reproducible analysis of the electrolyte contained in a relatively small volume of solution. This problem is surmounted by the quantitative analysis of very small amounts of sample using the recently developed High Performance Liquid Chromatography (HPLC) technique of Ion Chromatography. (Wittner et.al., Waters Associates, Knox and Laird, Knox and Jurand, Sood et.al., Bidlingmeyer et.al). By means of this technique for example, the Cl^- ion concentration of a colloid dispersion of total volume, say, 200 cm^3 can be ascertained by the sampling of a 200 mm^3 aliquot of the colloid dispersion. In this example, the sample volume is one thousand times smaller than the dispersion under study and can, therefore, be considered as causing negligible perturbation of the adsorbate/adsorbent equilibrium.

This study describes the use of Ion Chromatography to measure Cl^- ion adsorption at the αFeOOH-NaCl aq. interface, and, in conjunction with electrophoresis data (Chapter B1.), presents a thorough analysis of the adsorption data obtained in terms of both electrical double layer(edl) and electrolyte adsorption theories.

2. THEORY

2.1. The compact region of the edl (Shaw, Hunter).

The simplest quantitative treatment of the edl is that due to Gouy, Chapman. This treatment is based on the assumptions i) that the electrolyte ions can be regarded as point charges and ii) that the solvent can be treated as a structureless dielectric of constant permittivity. The finite size of the ions (whether hydrated or not) will, however, limit their maximum concentration at the wall and their distance of closest approach to it, while the high electric fields near the wall (10^6 to 10^8 V m^{-1}) must produce some ordering of solvent molecules, especially for water. Thus, the Gouy-Chapman diffuse edl has an inner limiting boundary. Stern recognised this problem and proposed a model in which the space charge in the electrolyte solution is divided into two regions separated by a plane, the Stern Plane (also recognised as the Outer Helmholtz Plane (OHP)), located at about a hydrated ion radius from the wall. The region between the wall and the OHP is called the Stern Layer (also known as the compact region) in which the charge and potential distribution are determined chiefly by the geometrical restrictions of ion and molecule size and the short range interactions between ions, the wall and the adjoining dipoles. The region beyond the OHP is a Gouy-Chapman-like diffuse region where the Poisson-Boltzmann equation may be expected to give a reasonable representation of the potential distribution. In the modern version of Stern's theory due to Parsons the OHP is at a distance r_{OHP} from the wall and for $r > r_{OHP}$ specific interaction forces are negligible. The distance of closest approach to the wall is r_{IHP}, (the distance from the wall to the (IHP) Inner Helmholtz Plane); the region $o \leqslant r \leqslant r_{IHP}$ is free of charge.

In addition to ions in the compact region, a certain amount of solvent will probably be bound to the charged surface and form part of the electrokinetic unit. It is, therefore, reasonable to expect that the Shear Plane is located at a small distance further out from the wall than the OHP, and that the electrokinetic potential (ζ) is, in general, marginally smaller in magnitude than the electrical potential at the OHP (Ψ_{OHP}). However, the bulk of experimental evidence suggests that the errors introduced by assuming the identities

$$\psi_{OHP} = \zeta \qquad \text{B2.1}$$

$$\text{and} \qquad \sigma_{OHP} = \sigma_E \qquad \text{B2.2}$$

are generally small.

In the most elementary models of the compact region a single value is assigned to the permittivity, corresponding to 10 < dielectric constant (D) < 50. In slightly more elaborate models such as those of Grahame, Bockris et.al., the compact region is divided into two zones of differing permittivities, one zone between the wall and the IHP (the inner zone) and the other between the IHP and the OHP (the outer zone). For water, the limiting value of $D \simeq 6$, corresponding to zero orientation polarisation, is often used for the inner zone, and a somewhat lower level of water organisation corresponding to $20 < D < 40$ is commonly assumed for the outer zone. Attempts have been made to overcome the limitations of even these elaborate models and to avoid the discontinuities in the permittivity which they entail. However, even in cases where the permittivity is allowed to vary over the compact region, it is still possible to define integral capacities for the two zones (Levine).

The surface charge density (σ_S) must balance that charge density in the adjacent edl:

$$\sigma_S = -\int_o^\infty \rho dr \qquad \text{B2.3}$$

Substituting for ρ from

$$\frac{d^2\psi}{dr^2} = \frac{\rho}{\varepsilon_{VAC} D} \qquad \text{B2.4}$$

gives

$$(\sigma_S)_P = -\varepsilon \left(\frac{d\psi}{dr}\right)_{r=0} \qquad \text{B2.5}$$

In terms of the elementary model of the compact region, integration of eqn. B2.5 over the appropriate limits leads to the expressions

$$\frac{\varepsilon_1}{r_{IHP}} = \frac{\sigma_S}{(\phi_S - \psi_{IHP})} \qquad \text{B2.6}$$

and $$\frac{\epsilon_2}{(r_{OHP} - r_{IHP})} = \frac{\sigma_E}{(\psi_{IHP} - \zeta)} \qquad B2.7$$

(assuming the identities given by eqns. B2.1 and B2.2). In terms of the more advanced model of the compact region, where the permittivity is allowed to vary with distance, integration of eqn. B2.5 leads to the expressions

$$\frac{\bar{\epsilon}_1}{r} = \left[\int_{\circ}^{r_{IHP}} \frac{dr}{\epsilon_1(r)}\right]^{-1} = \frac{\sigma_S}{(\psi_S - \psi_{IHP})} = K_1^{CAP} \qquad B2.8$$

and

$$\frac{\bar{\epsilon}_2}{(r_{OHP} - r_{IHP})} = \left[\int_{r_{IHP}}^{r_{OHP}} \frac{dr}{\epsilon_2(r)}\right]^{-1} = \frac{\sigma_E}{(\psi_{IHP} - \zeta)} = K_2^{CAP} \qquad B2.9$$

Thus, in the simple model of the compact region the charge per potential drop across the inner and outer zones is equal to $\frac{D_1 \epsilon_{VAC}}{r_{IHP}}$ and $\frac{D_2 \epsilon_{VAC}}{(r_{OHP} - r_{IHP})}$, respectively. In the more advanced model of the compact region, the charge per potential drop across the inner and outer zones is equal to the integral capacities K_1^{CAP}, and K_2^{CAP}, respectively, while the integral capacity of the whole of the compact region per unit area, K_C^{CAP} is given by

$$\frac{1}{K_C^{CAP}} = \frac{1}{K_1^{CAP}} + \frac{1}{K_2^{CAP}} \qquad B2.10$$

An estimation, D_1^*, of the order of magnitude of a single value for the dielectric constant of the inner zone can be made from K_1^{CAP}, by making the assumption

$$\frac{D_1^* \epsilon_{VAC}}{r_{IHP}} = K_1^{CAP} \qquad B2.11$$

2.2. Interpretation of Cl^- ion adsorption measurements: Surface complexation.

Measurements of the adsorption of a species from the liquid phase onto

a solid phase are usually expressed as the quantity of adsorbate per unit mass of adsorbent, which in the present context is the quantity of Cl^- ion adsorbed per unit mass of $\alpha FeOOH$ (Cl^-_{ADS}). Such measurements can also be expressed as Cl^- ion adsorption density (Γ_{Cl^-}) or Cl^- ion charge density (σ_{Cl^-}).

In terms of the acid-base site binding model of Yates et.al., and its development by Davis et.al., (Chapter B3), σ_S, σ_{IHP} and σ_{OHP} are expressed as the concentrations of various surface (S) species:

$$\sigma_S = B([SOH_2^+] + [SOH_2^+....Cl^-] - [SO^-] - [SO^-....Na^+]) \quad B2.12$$

$$\sigma_{IHP} = B([SO^-....Na^+] - [SOH_2^+....Cl^-]) \quad B2.13$$

$$\sigma_{OHP} = - B([SOH_2^+] - [SO^-]) \quad B2.14$$

Electrophoretic and potentiometric evidence given in chapters B1 and B3, respectively, would suggest that at pH < pH of point of zero charge (pH_0) it is reasonable to assume the concentrations $[SO^-....Na^+]$ and $[SO^-]$ are negligible. Consequently, at pH < pH_0 we obtain

$$\sigma_S = B([SOH_2^+] + [SOH_2^+....Cl^-]) \quad B2.15$$

$$\sigma_{IHP} = - B([SOH_2^+....Cl^-]) \quad B2.16$$

and

$$\sigma_{OHP} = - B([SOH_2^+] \quad B2.17$$

In terms of the edl theory described, adsorbed Cl^- ions are distributed <u>mostly</u> in the compact region in association with SOH_2^+ surface species and <u>partly</u> as a countercharge in the diffuse region. It can be recognised, therefore, that the concentration of those Cl^- ions in the compact region is $[SOH_2^+....Cl^-]$, while the concentration of those Cl^- ions constituting a countercharge in the diffuse region is $[SOH_2^+]$. Hence, σ_{Cl^-} is equal in magnitude to the sum of two charge densities, one at the IHP and the other at the OHP:

$$\sigma_{Cl^-} = | \ (\sigma_{IHP})_{Cl^-} + (\sigma_{OHP})_{Cl^-} \ | = (\sigma_{IHP + OHP})_{Cl^-} \quad B2.18$$

Similarly,

$$\Gamma_{Cl^-} = (\Gamma_{IHP})_{Cl^-} + (\Gamma_{OHP})_{Cl^-} = (\Gamma_{IHP\ +\ OHP})_{Cl^-} \qquad B2.19$$

Furthermore, by the electroneutrality condition

$$\sigma_S + \sigma_{IHP} + \sigma_{OHP} = 0 \qquad B2.20$$

$(\sigma_{IHP\ +\ OHP})_{Cl^-}$ is equal in magnitude to σ_S.

2.3. The calculation of charge densities, potentials, integral capacities (compact layer) and positive surface amphoteric and complexation constants of the edl at the αFeOOH-NaCl aq. interface.

The identification of the IHP component of σ_S can be achieved by recourse to σ_E data assuming the identity given by eqn. B2.2. ψ_S and ψ_{IHP} can be calculated from their corresponding charge densities by means of an iteration procedure involving, as a first approximation, the Gouy-Chapman 'planar' charge/potential relationship in cylindrical geometry (White):

$$\psi_p = \frac{2kT}{e} \cdot \sinh^{-1}\left[\frac{\sigma_p {}^{\circ}K\ (\varkappa a)}{{}^{1}K\ (\varkappa a)} \cdot \frac{e}{2\varepsilon_{VAC} D \varkappa\ kT}\right] \qquad B2.21$$

[using $\sinh^{-1} x = \ln [(x + (x^2 + 1)^{\frac{1}{2}})]$ and the more exacting charge/potential relationship of Ohshima et.al.:

$$\sigma_{Int.AM} = \frac{2\varepsilon_{VAC} D \varkappa kT}{e} \cdot \sinh\left(\frac{\tilde{\psi} Int}{2}\right) \cdot \left[1 + \frac{\left[\frac{{}^{\circ}K(\varkappa a)}{{}^{1}K(\varkappa a)}\right]^{-2} - 1}{\cosh^2\left(\frac{\tilde{\psi}_{Int}}{4}\right)}\right]^{\frac{1}{2}} \qquad B2.22$$

Thus, beginning with σ_S, σ_E and ζ, the remaining charge density and potentials, viz., σ_{IHP}, ψ_S and ψ_{IHP}, and the integral capacities, viz., K_1^{CAP}, K_2^{CAP} and K_c^{CAP}, of the edl at the αFeOOH-NaCl aq. interface can be calculated. [It must be noted that for the correct calculation of these remaining edl quantities the values of σ_S, σ_E and ζ must be evaluated from experimental measurements made under identical conditions of temperature, pH and $\varkappa a$.]

According to Davis et.al. James et.al., the intrinsic equilibrium constants for the simple amphoteric ionisation and complexation reactions

$$SOH_2^+ \overset{K_{a+s}^{int}}{\rightleftharpoons} SOH + H_S^+ \qquad \text{B2.23}$$

$$\text{and} \quad SOH_2^+ + Cl_S^- \overset{K_{Cl^-}^{int}}{\rightleftharpoons} SOH_2^+....Cl^- \qquad \text{B2.24}$$

can be evaluated by, respectively, a double and a single graphical extrapolation procedure. However, the evaluation of $K_{Cl^-}^{int}$ requires extrapolation of σ_S/pH functions calculated from data obtained at a much higher concentration, usually $\geqslant$ 0.1mol dm^{-3}, than is reached in this study. Instead, $K_{Cl^-}^{int}$ can be evaluated from the chemical component of the work of adsorption of the Cl^- ion $(\emptyset_{ADS})_{Cl^-}$ by means of their thermodynamic relationship:

$$K_{Cl^-}^{int} = \exp\left(-\frac{(\emptyset_{ADS})_{Cl^-}}{kT}\right) \qquad \text{B2.25}$$

2.4. Adsorption equations.

It is often possible to express the equilibrium distribution of adsorbate i between the interface and the bulk liquid phase by one of the following mathematical relationships

$$\Gamma_i = \frac{(\Gamma_{MAX})_i \, \Omega_I \, [i]_{EQ}}{(1 + \Omega_I \, [i]_{EQ})} \qquad \text{B2.26}$$

$$\Gamma_i = \Omega_{II} + \Omega_{III} \log [i]_{EQ} \qquad \text{B2.27}$$

$$\log \Gamma_i = \log \Omega_{IV} + \left(\frac{\log [i]_{EQ}}{\Omega_V}\right) \qquad \text{B2.28}$$

Eqn. B2.26 is the familiar Langmuir Adsorption Equation. This equation does not consider the electrical effects produced at an interface by the adsorption of charged adsorbates and, therefore, cannot be applied to electrolyte systems involving adsorption of ions. Both eqns. B2.27 and

B2.28 are empirical relationships that were determined experimentally, and are characteristic of the adsorption of electrolytes from solution. The adsorption behaviour of certain specific electrolytes is described approximately by eqn. B2.27 at low concentration (Kellerman and Lange, Kruyt and Van der Willigen). Such an electrolyte has, as one of its constituent ions, an ion which is common to both the liquid and solid phase and is generally known as a potentially determining ion. Eqn. B2.28 is the familiar Freundlich Adsorption Equation. This empirical relationship has been found to be characteristic of the adsorption of surface-active non-potential determining electrolytes.

Stern derived an adsorption equation, analogous to that derived by Langmuir, for those ions coming closer to the interface than the OHP, i.e., those ions entering the compact region of the edl. In the present context of Cl^- ion adsorption, this Stern-Langmuir Adsorption Equation can be expressed as

$$\frac{(\Gamma_{IHP})_{Cl^-}}{[(\Gamma_{MAX})_{Cl^-} - (\Gamma_{IHP})_{Cl^-}]} = \frac{c_{Cl^-}}{[(c_{MAX})_{Cl^-} - c_{Cl^-}]} \cdot \exp\left(-\frac{(W_{ADS})_{Cl^-}}{kT}\right) \qquad \text{B2.29}$$

where

$$(W_{ADS})_{Cl^-} = z_{Cl^-} e \psi_{IHP} + (\phi_{ADS})_{Cl^-} \qquad \text{B2.30}$$

Grahame in his treatment of the compact region of the edl, based upon Stern's original concept, derived a more useful expression for the adsorption density of counterions in the Stern layer. For Cl^- ion adsorption this expression is

$$(\Gamma_{IHP})_{Cl^-} = \frac{(\Gamma_{MAX})_{Cl^-}}{(c_{MAX})_{Cl^-}} \cdot c_{Cl^-} \cdot \exp\left(-\frac{(W_{ADS})_{Cl^-}}{kT}\right) \qquad \text{B2.31}$$

Furthermore, since the ratio of the thickness of the region in question to the thickness of a cubic metre corresponds to the ratio of the diameter of the adsorbed ion to 1 (in the context of the edl theory described, the diameter of the adsorbed ion equals $2r_{IHP}$), i.e.,

$$\frac{(\Gamma_{MAX})_{Cl^-}}{(c_{MAX})_{Cl^-}} = 2r_{IHP} \qquad \text{B2.32}$$

then

$$(\Gamma_{IHP})_{Cl^-} = 2r_{IHP}\, c_{Cl^-} \exp\left(\frac{-(W_{ADS})_{Cl^-}}{kT}\right) \qquad \text{B2.33}$$

Assuming the identity

$$r_{IHP} = r_{Cl^-} \qquad \text{B2.34}$$

then

$$(\Gamma_{IHP})_{Cl^-} = 2r_{Cl^-}\, c_{Cl^-} \exp\left(\frac{-(W_{ADS})_{Cl^-}}{kT}\right) \qquad \text{B2.35}$$

The validity of the condition

$$\frac{(\Gamma_{MAX})_{Cl^-}}{(c_{MAX})_{Cl^-}} = 2r_{Cl^-} \qquad \text{B2.36}$$

may be tested by assuming a closest packing arrangement of Cl^- ions in the evaluation of $(\Gamma_{MAX})_{Cl^-}$ and $(c_{MAX})_{Cl^-}$, and by making the further assumption that the Cl^- ions are dehydrated at the surface and hydrated in bulk solution: In the closest packing arrangement of equal spheres of radius r, the volume occupied per sphere equals $5.66r^3$ (Wells). On the basis of this arrangement, and using a value of $(r_{Cl^-} + 0.010nm)$ for the hydrated Cl^- ion radius as suggested by Latimer et.al., gives the estimated value, viz., $((c_{MAX})_{Cl^-})_{Est.} = 42106$ mol m^{-3} (cf. molarity of water = 55509 mol m^{-3}). In the closest packing arrangement of equal spheres of radius r on a flat surface, the area occupied per sphere is $\left(\frac{5.66r^3 \cdot 3\pi^{\frac{1}{2}}}{4}\right)^{\frac{2}{3}}$. Then, using the dehydrated Cl^- ion radius (r_{Cl^-}) gives the estimated value, viz., $((\Gamma_{MAX})_{Cl^-})_{Est.} = 13.201$ μmol m^{-2}. Thus, $((\Gamma_{MAX})_{Cl^-})_E / ((c_{MAX})_{Cl^-})_E = 0.314$ nm, similar to $2r_{Cl^-}$ (= 0.362 nm).

3. METHOD

The quantitative adsorption of Cl^- ions from aqueous NaCl solution onto dispersed αFeOOH particles was measured at 25°C, within the concentration and pH ranges of 0.5mmol dm^{-3} $\leqslant$ [NaCl] $\leqslant$ 100mmol dm^{-3} and $3.8 \leqslant pH \leqslant 8.5$, respectively, by sampling the bulk aqueous phase and analysing by ion chromatography.

The pump was primed and the mobile phase pumped through the chromatograph for at least 3 hours before the commencement of an analysis.

An analysis was conducted as follows:

200.00 cm^3 $\pm$ 0.05 cm^3 of a NaCl solution was pipetted into the reaction vessel and its pH brought to the value of 7.00. A calibration curve was obtained and its regression coefficients recorded. 2.0000g $\pm$ 0.0005 of αFeOOH was added to the NaCl solution contained in the reaction vessel. After at least 2 hours after the addition, the pH of the αFeOOH/NaCl aq. suspension was adjusted, by the addition of a known volume of NaOH aq. (0.1mol dm^{-3}), to approximately 8.4, i.e., a $pH > pH_o$. The suspension was allowed to attain equilibrium. [The suspension was adjudged to have attained equilibrium when the rate of change of its continuously monitored pH was < 0.01 pH unit min^{-1} (Yates and Healy)].

Two integrated areas were recorded of acceptable 'chloride' peaks generated by injection of two filtered samples of the αFeOOH/NaCl aq. suspension. The pH of the suspension was lowered approximately one pH unit, by the addition of a known volume of HNO_3aq.(0.1mol dm^{-3}), and the suspension allowed to attain equilibrium. This procedure of sampling followed by pH adjustment was repeated four times; normally, in total, five pairs of integrated areas were obtained. From a knowledge of the volumes of acid and base added to, and the total volume previously withdrawn from, the αFeOOH/NaCl aq. suspension, the volume of aqueous solution present in the reaction vessel ($Vol_{aq.}$) immediately prior to each withdrawal of sample was calculated.

4. RESULTS

For each analysis, the integrated areas, corresponding to filtered samples of the αFeOOH/NaCl aq. suspension, were converted to bulk equilibrium Cl^- ion concentrations, $[Cl^-]^*_{EQ}$, by means of a calibration curve, and thence to corrected equilibrium Cl^- ion concentrations ($[Cl^-]_{EQ}$) by subtraction of the appropriate 'filter-chloride' value (see Table AA.1). The variation of Cl^-_{ADS} with pH, at the four lowest NaCl concentrations, viz., 0.5, 1.0, 5.0 and 10.0 mmol dm^{-3}, is shown in Fig. B2.1. At the higher concentrations, viz., 25.0, 50.0 and 100.0 mmol dm^{-3}, much of the adsorption data obtained was inconsistent and was, accordingly, disregarded. Cl^-_{ADS} did not diminish to zero, but rather a residual value, at pH_o; this residual adsorption increased with increasing [NaCl]. Percentage Cl^- ion adsorption, calculated on the basis of total available Cl^- ion originally present in solution, had a maximum value of about 20% at [NaCl] = 0.5mmol dm^{-3} and pH 4 (Fig. B2.2).

For each of the four average κa (ratio of particle radius of curvature to edl thickness) values ($\bar{\kappa}a$) at which electrophoretic (Chapter B1) and Cl^- ion adsorption measurements have been made (14.5, 10.3, 4.8 and 3.5) a polynomial curve was fitted to the variation with pH of each of the following edl quantities :- Cl^-_{ADS}, σ_E and ζ. Then, by means of the coefficients of each polynomial, values of Cl^-_{ADS}, σ_E and ζ were calculated at the arbitrary set of pH values 4.0, 4.5, 5.0, 5.5, 6.0, 6.5, 7.0, 7.5, 8.0 and 8.17. Using these interpolated values and, respectively, eqns. B2.20, B2.21, B2.22, B2.8, B2.9 and B2.10, the remaining edl quantities, viz., σ_{IHP}, ψ_S, ψ_{IHP}, K_1^{CAP}, K_2^{CAP} and K_C^{CAP} were calculated. The variation of the charges and potentials, viz., σ_S, σ_{IHP}, σ_E, ψ_S, ψ_{IHP} and ζ, with pH, for each $\bar{\kappa}a$ value, is shown in Figs. B2.3 to B2.6. σ_S attained a maximum value of about 80mC m^{-2} at [NaCl] = 10mmol dm^{-3} and pH4, this being 3.0% of the charge density that would be generated by the protonation of every available αFeOOH surface hydroxyl group. Correspondingly, the calculated value of σ_{IHP} at this concentration and pH was about -60mC m^{-2}, this being 4.7% of the theoretical charge density of a complete surface monolayer of dehydrated Cl^- ions of radius 0.181nm in a close packing arrangement. The double extrapolation of James et.al., gave the value of 1.769×10^{-4}mol dm^{-3} for K^{int}_{a+s} (Fig. B2.7). The integral capacities, viz., K_1^{CAP}, K_2^{CAP} and K_C^{CAP}, are shown as functions of pH for each $\bar{\kappa}a$ value in Figs. B2.8 to B2.11. At high [NaCl] and low pH,

FIGURE B2.1

CHLORIDE ION ADSORPTION OF αFeOOH DISPERSION AS A FUNCTION OF pH AT VARIOUS CONCENTRATIONS OF NaCl AND AT 25°C.

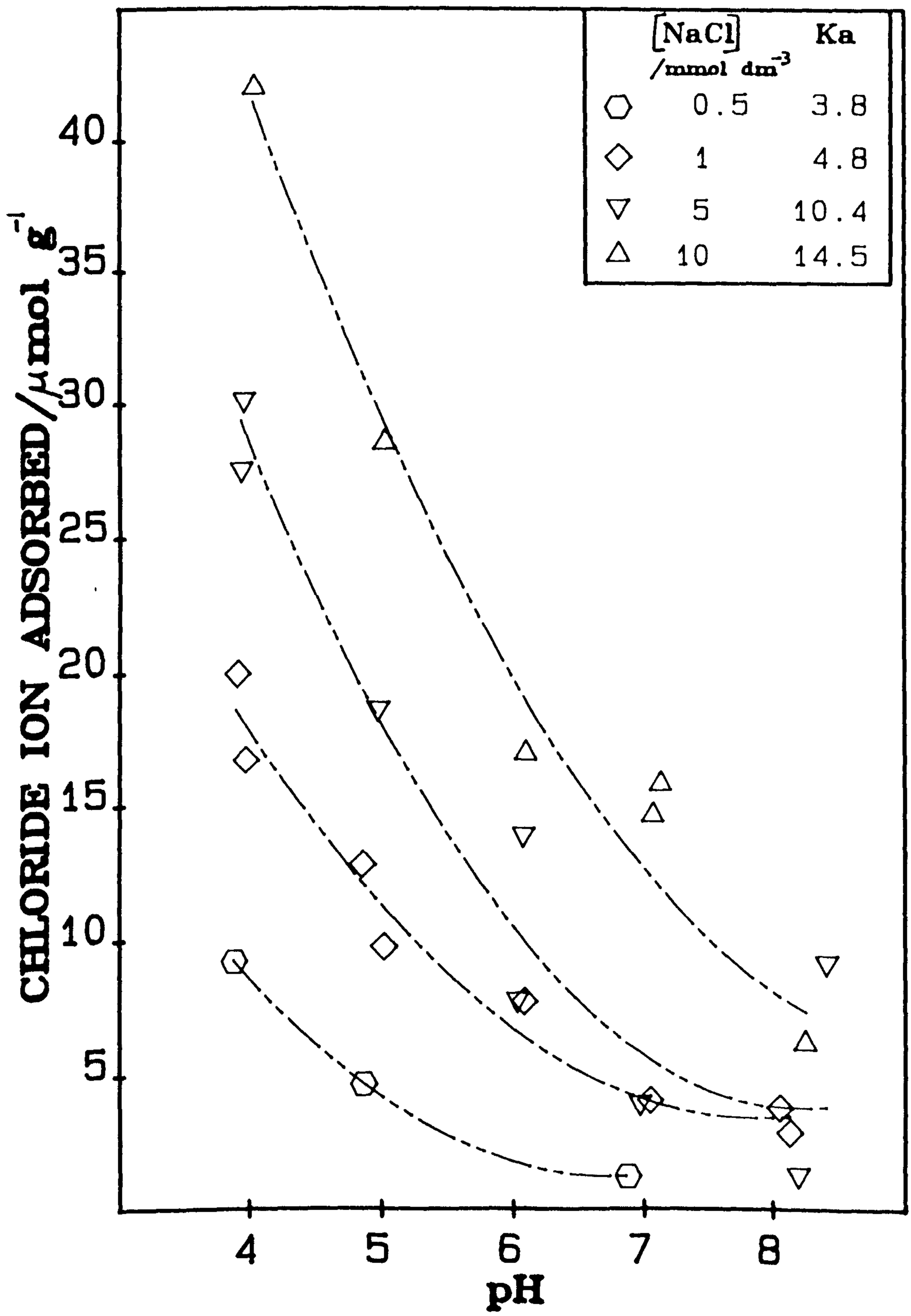

FIGURE B2.2

PERCENTAGE CHLORIDE ION ADSORBED AS A FUNCTION OF NaCl CONCENTRATION AT 25°C AND OVER THE pH RANGE 4 TO 8.

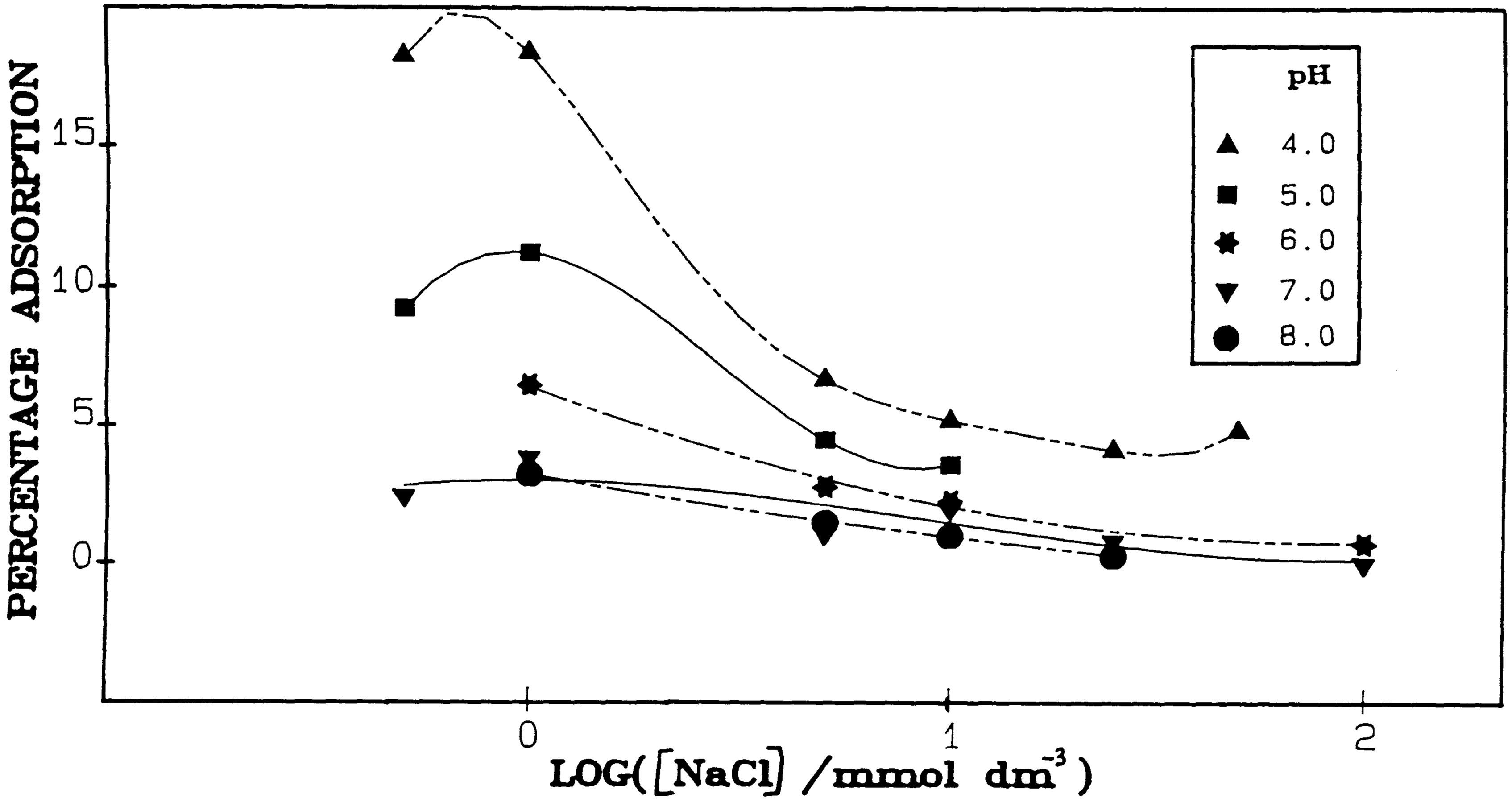

FIGURE B2.3

CHARGE DENSITY OF ∝FeOOH/NaCl aq. INTERFACE AS A FUNCTION OF pH AT 25°C.

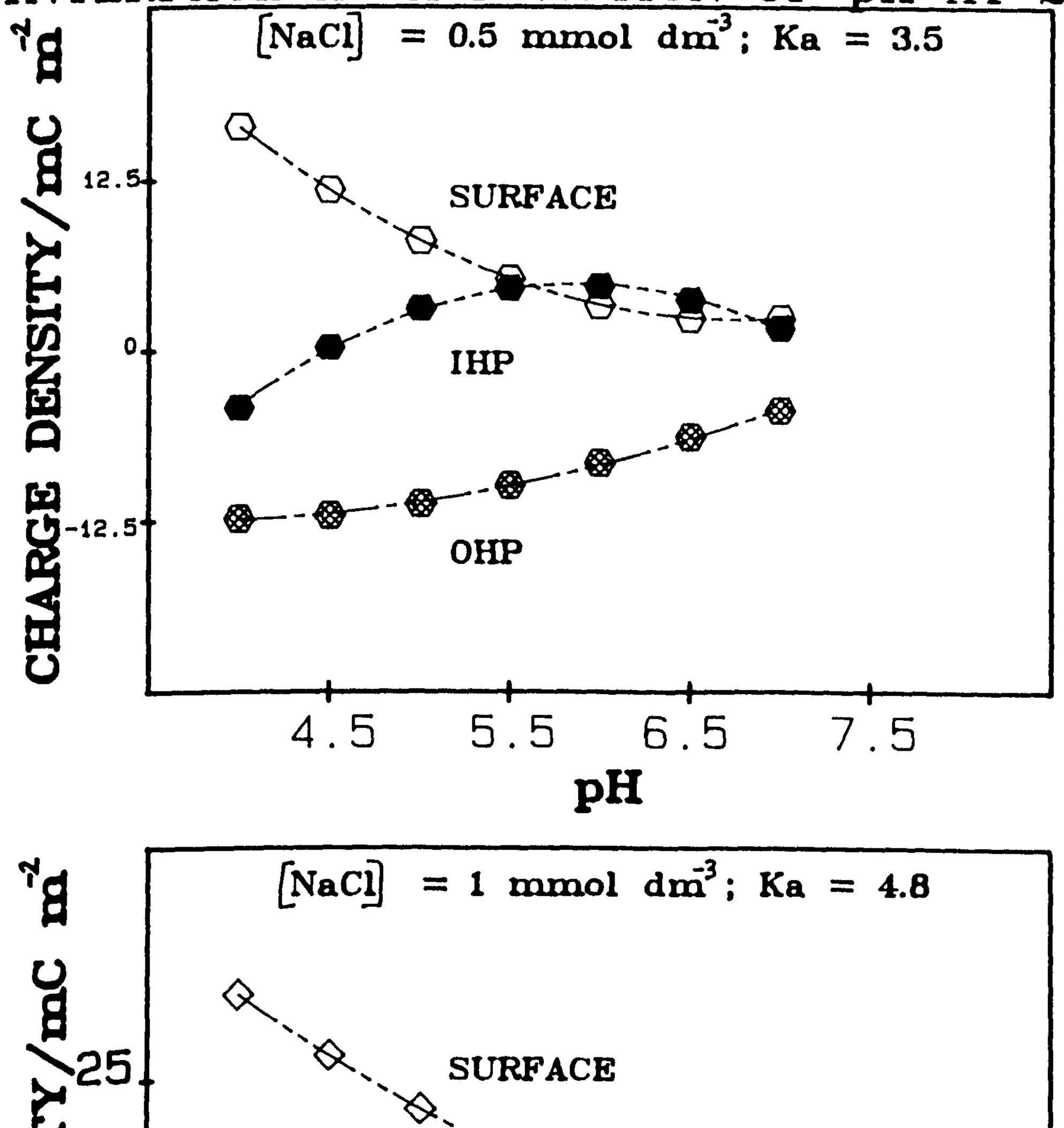

FIGURE B2.4

CHARGE DENSITY OF αFeOOH/NaCl aq. INTERFACE AS A FUNCTION OF pH AT 25°C.

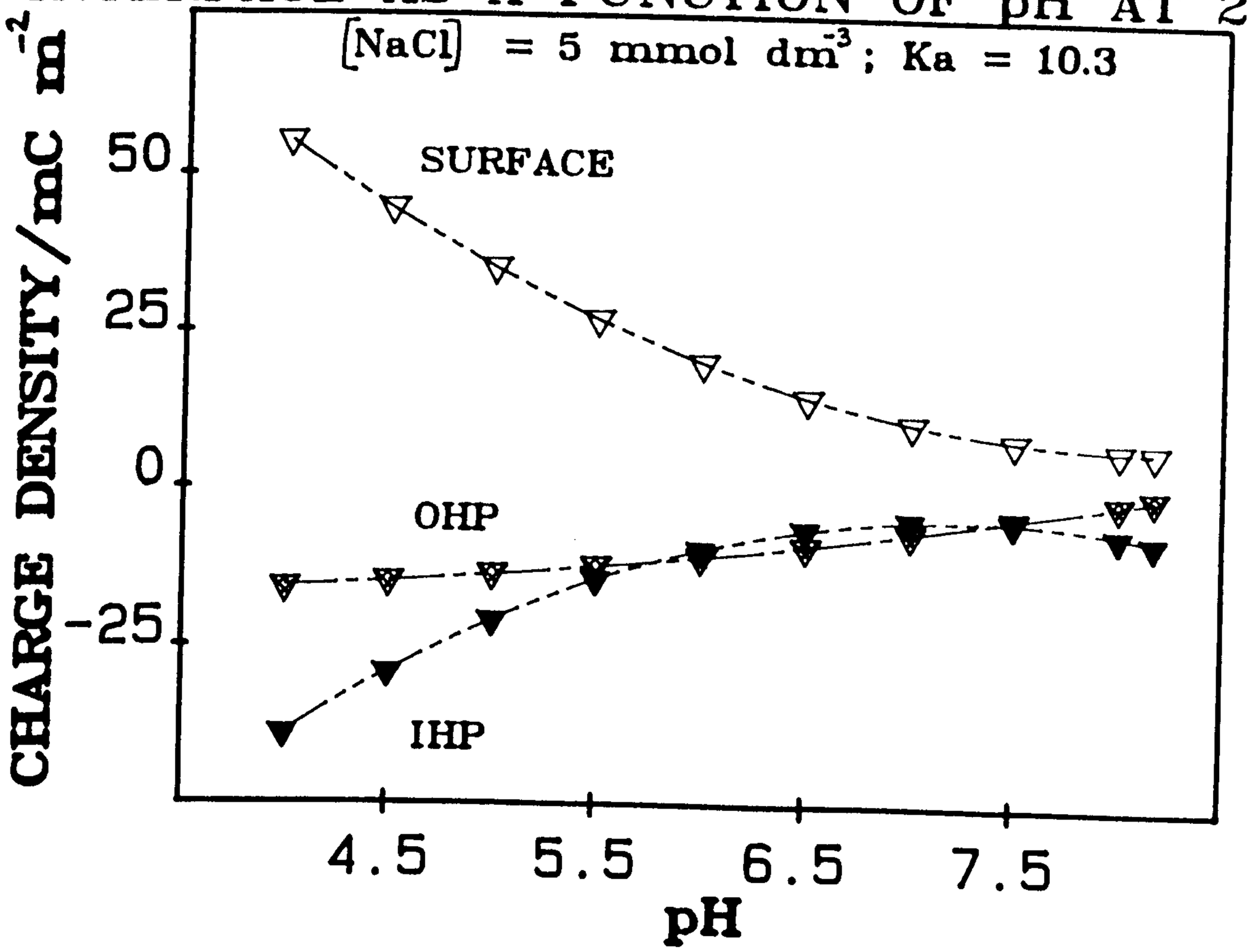

FIGURE B2.5

POTENTIAL OF ∝FeOOH/NaCl aq. INTERFACE AS A FUNCTION OF pH AT 25°C.

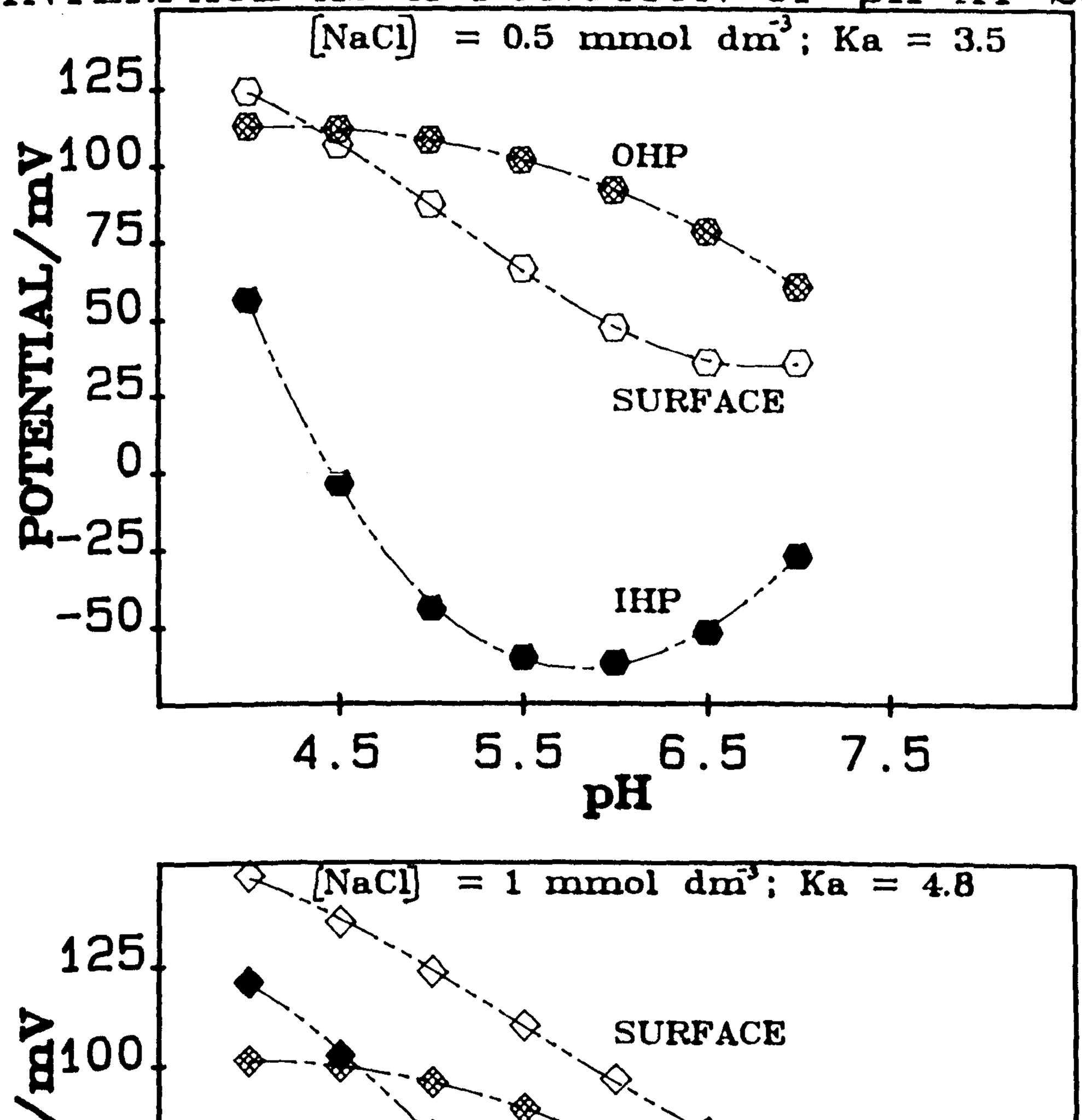

FIGURE B2.6

POTENTIAL OF ∝FeOOH/NaCl aq. INTERFACE AS A FUNCTION OF pH AT 25°C.

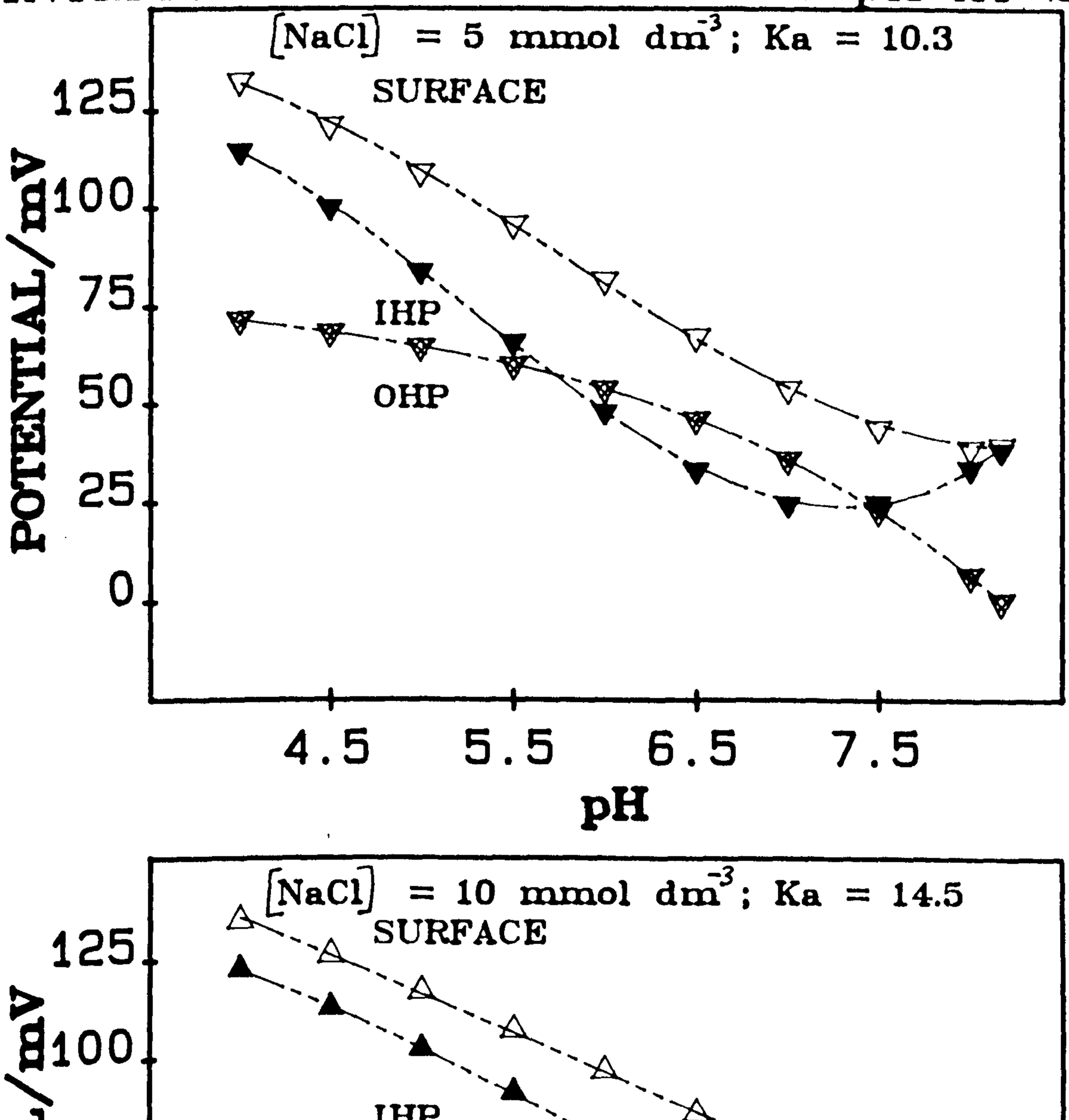

FIGURE B2.7

DAVIS et. al. SINGLE EXTRAPOLATION PLOT FOR THE DETERMINATION OF ∝FeOOH/aq. AMPHOTERIC CONSTANT (K^{int}_{a+s}).

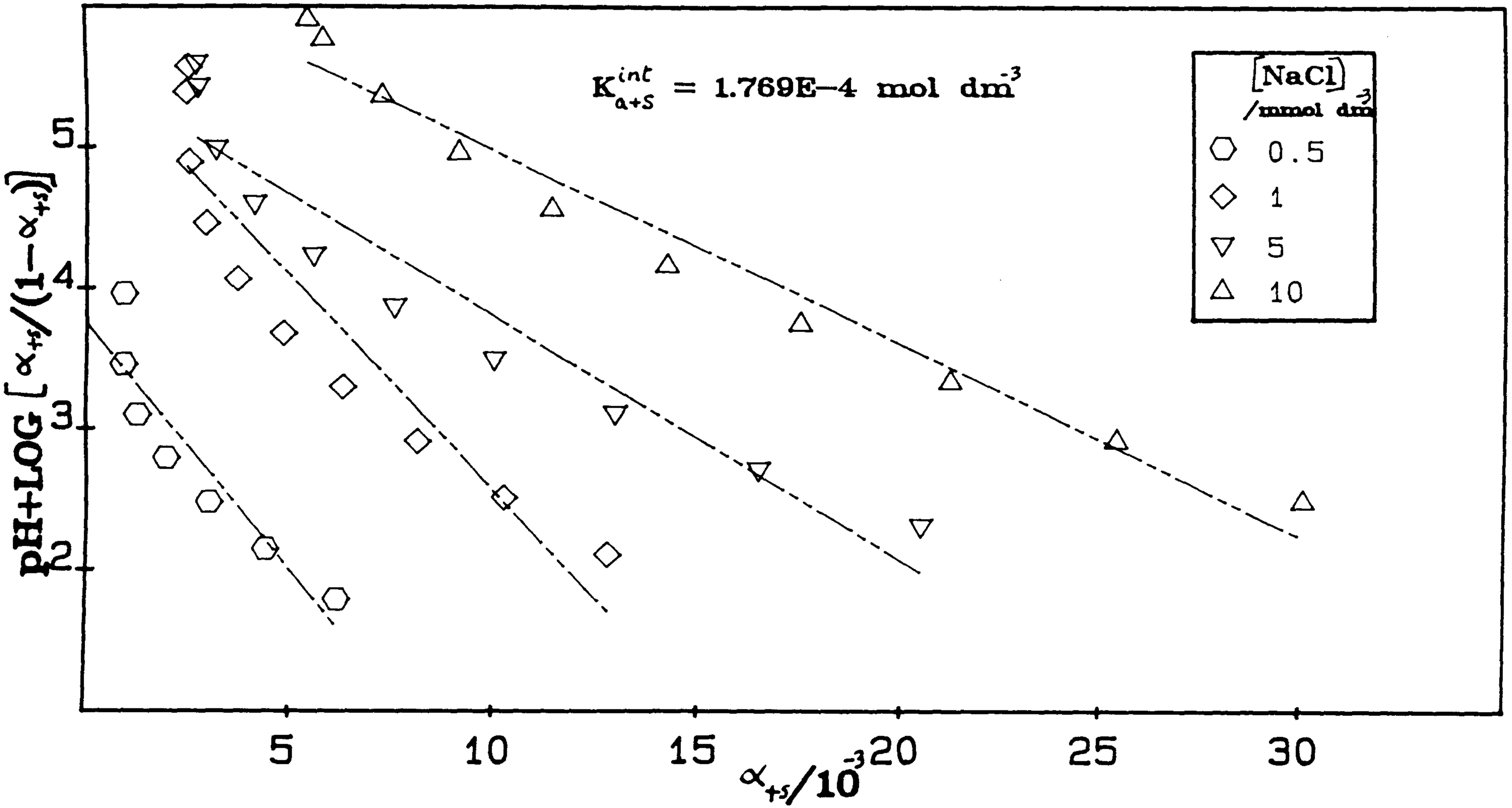

FIGURE B2.8

INTEGRAL CAPACITIES OF COMPACT REGION OF ∝FeOOH/NaCl aq. INTERFACE AS A FUNCTION OF pH AT 25°C; [NaCl] = 0.5 mmol dm^{-3} Ka = 3.5

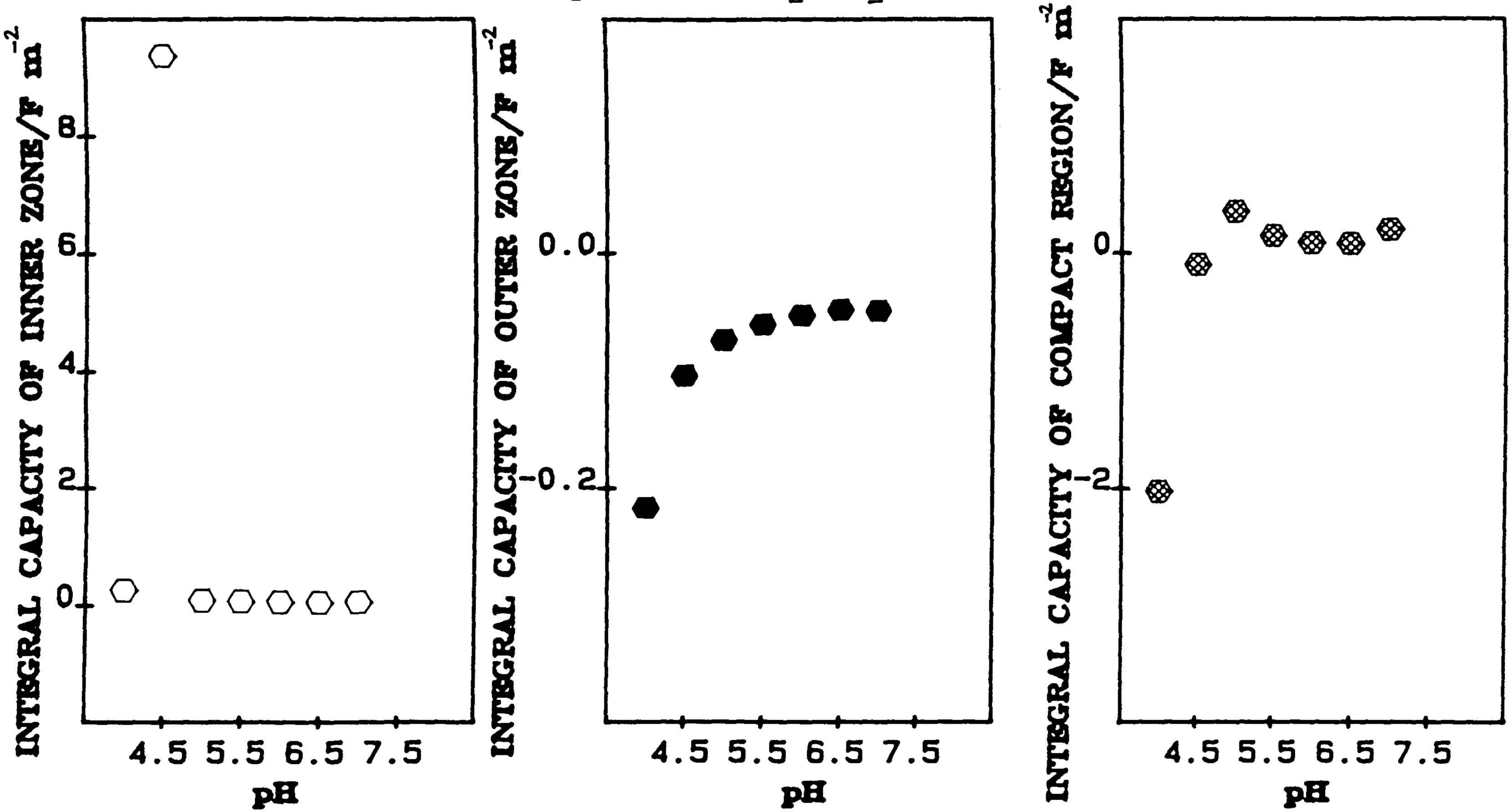

FIGURE B2.9

INTEGRAL CAPACITIES OF COMPACT REGION OF ∝FeOOH/NaCl aq. INTERFACE AS A FUNCTION OF pH AT 25°C; [NaCl] = 1 mmol dm^{-3} Ka = 4.8

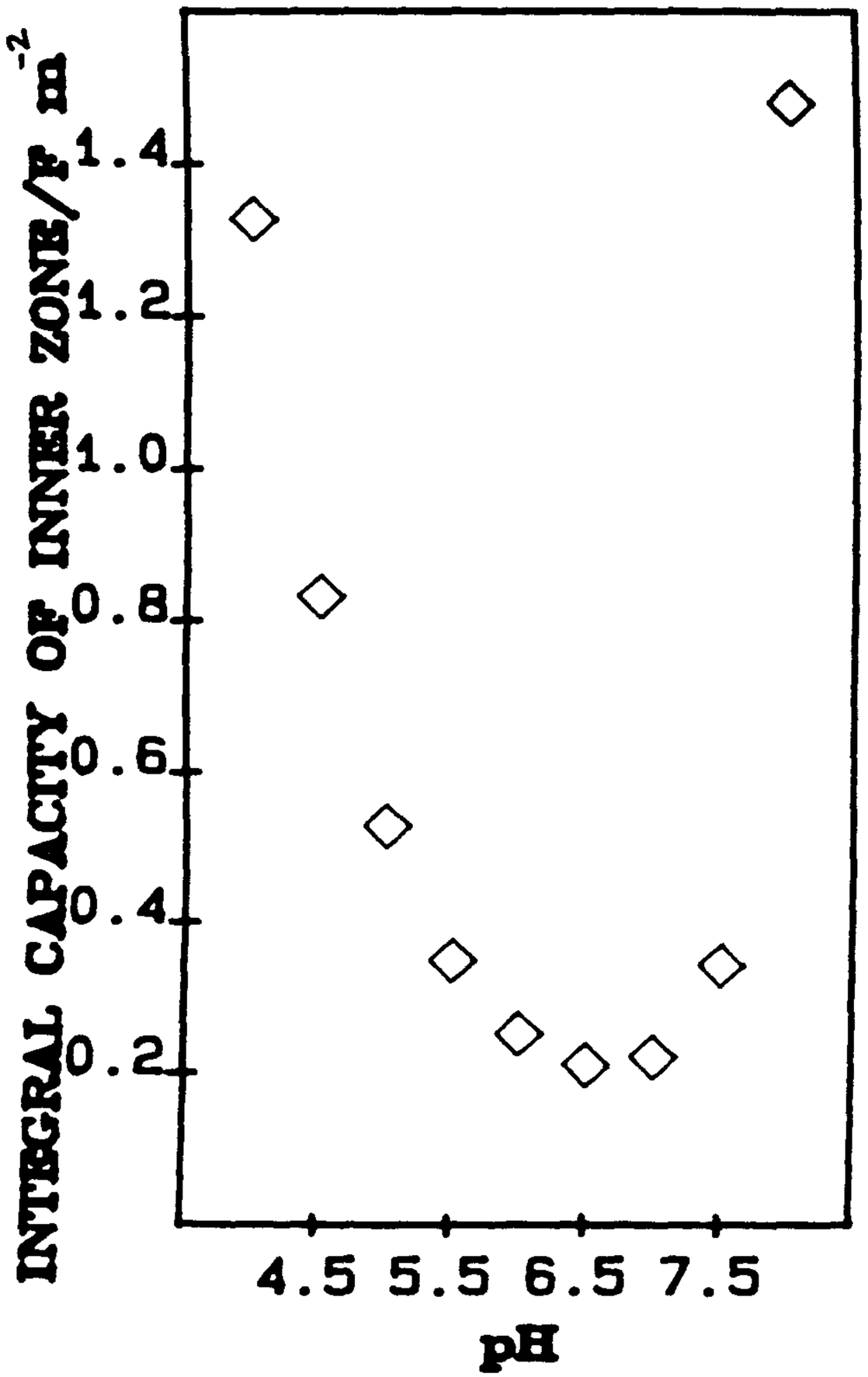

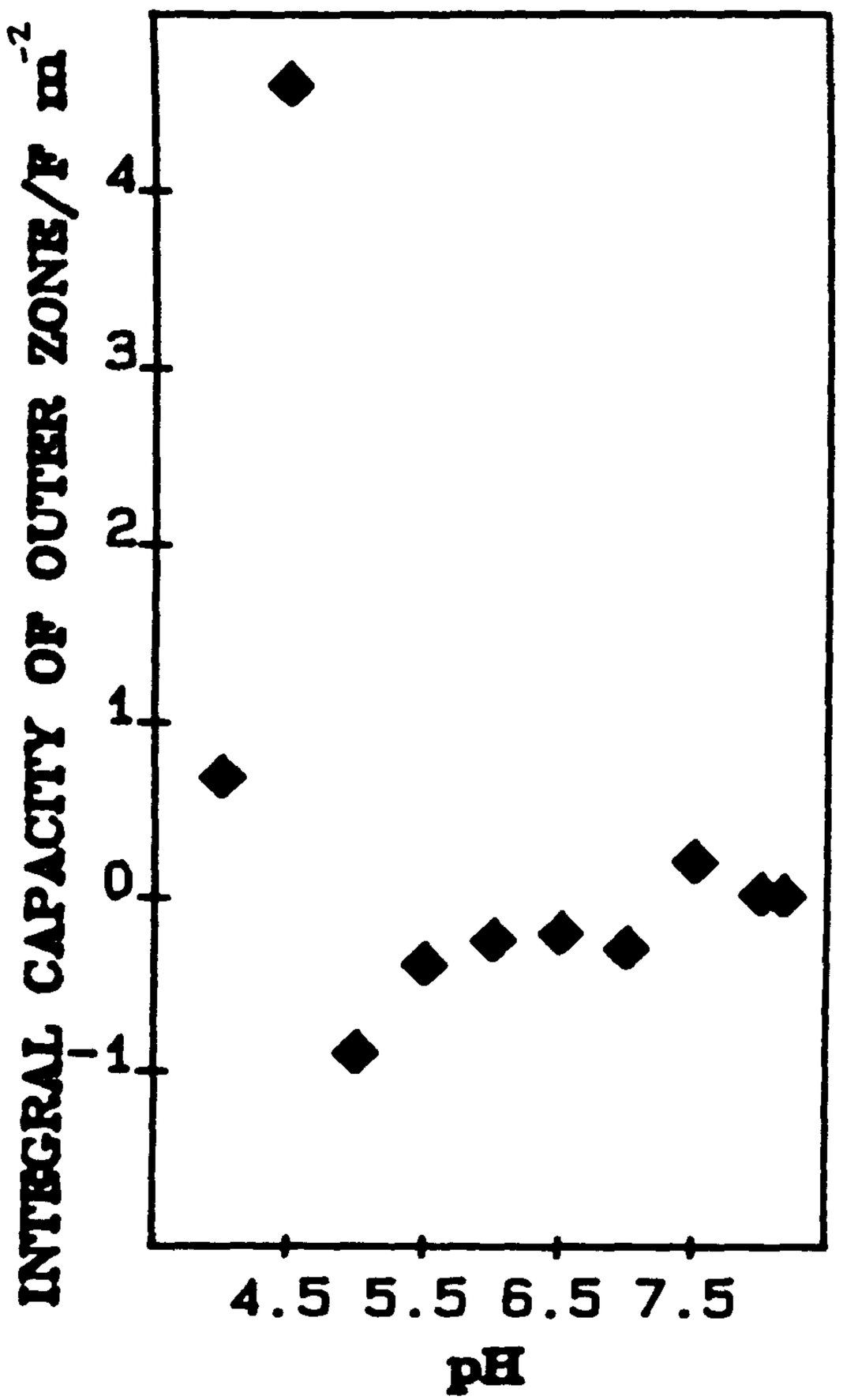

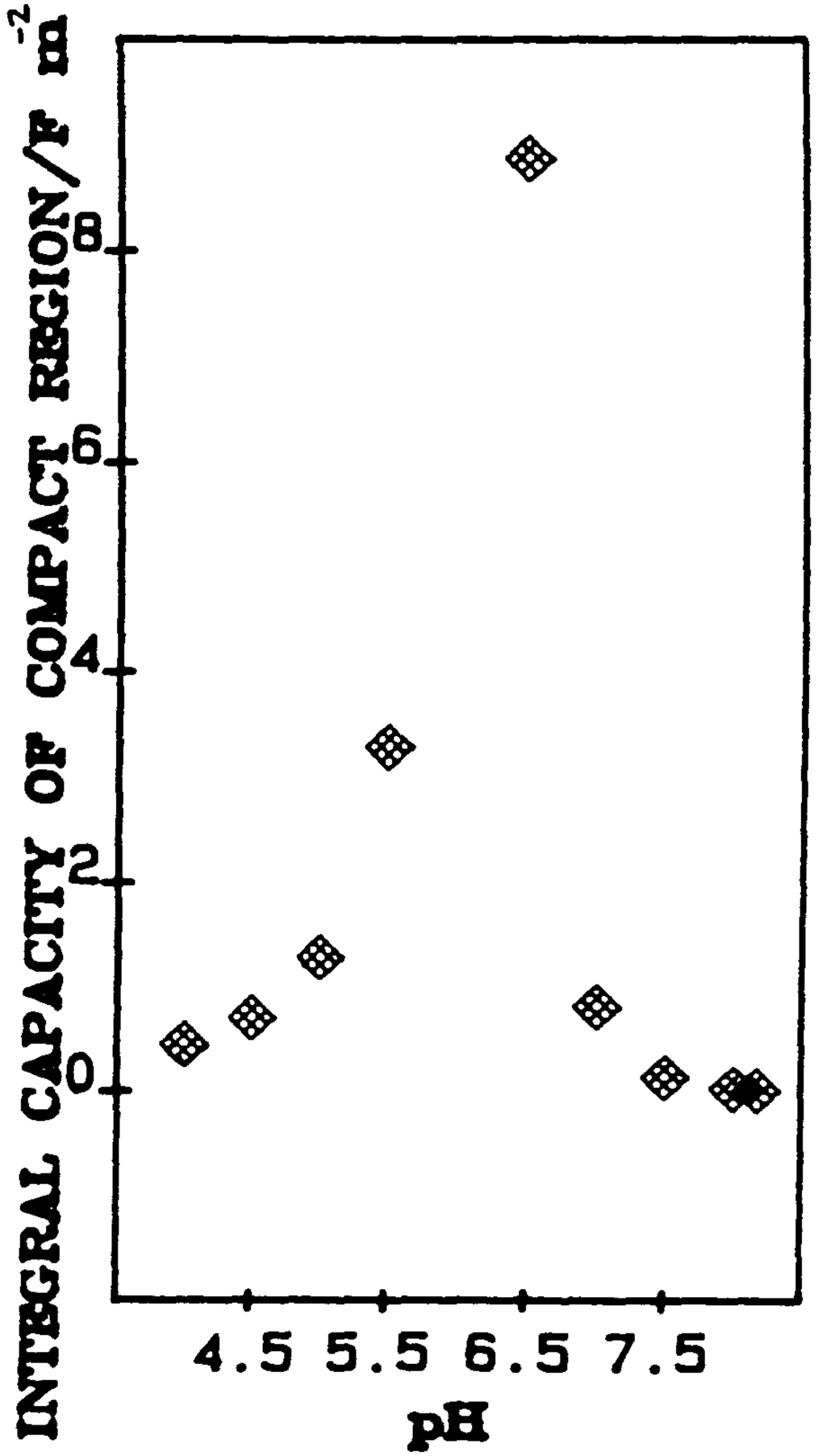

FIGURE B2.10

INTEGRAL CAPACITIES OF COMPACT REGION OF ∝FeOOH/NaCl aq. INTERFACE AS A FUNCTION OF pH AT 25°C; [NaCl] = 5 mmol dm^{-3} Ka = 10.3

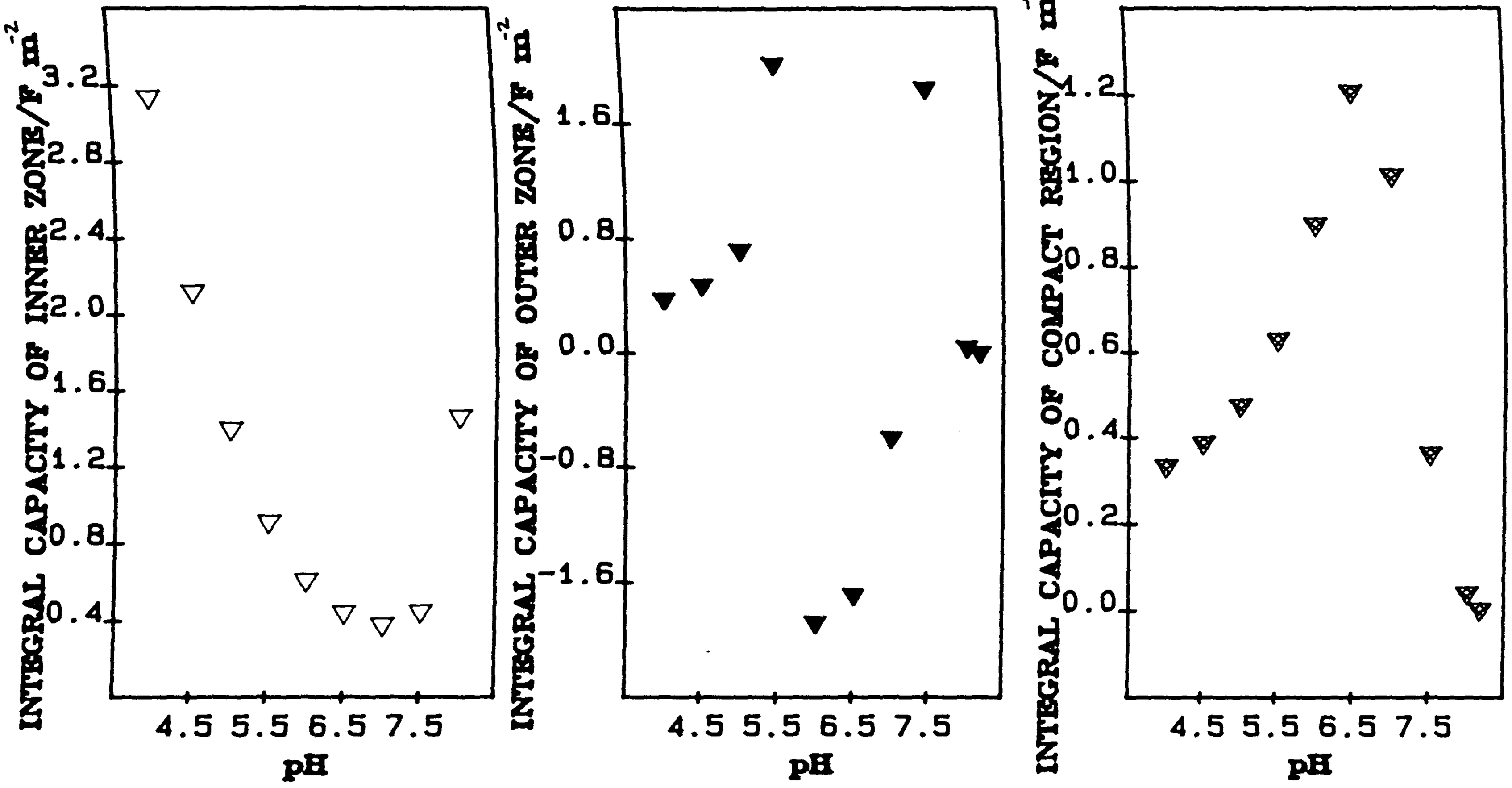

FIGURE B2.11

INTEGRAL CAPACITIES OF COMPACT REGION OF ∝FeOOH/NaCl aq. INTERFACE AS A FUNCTION OF pH AT 25°C; [NaCl] = 10 mmol dm^{-3} Ka = 14.5

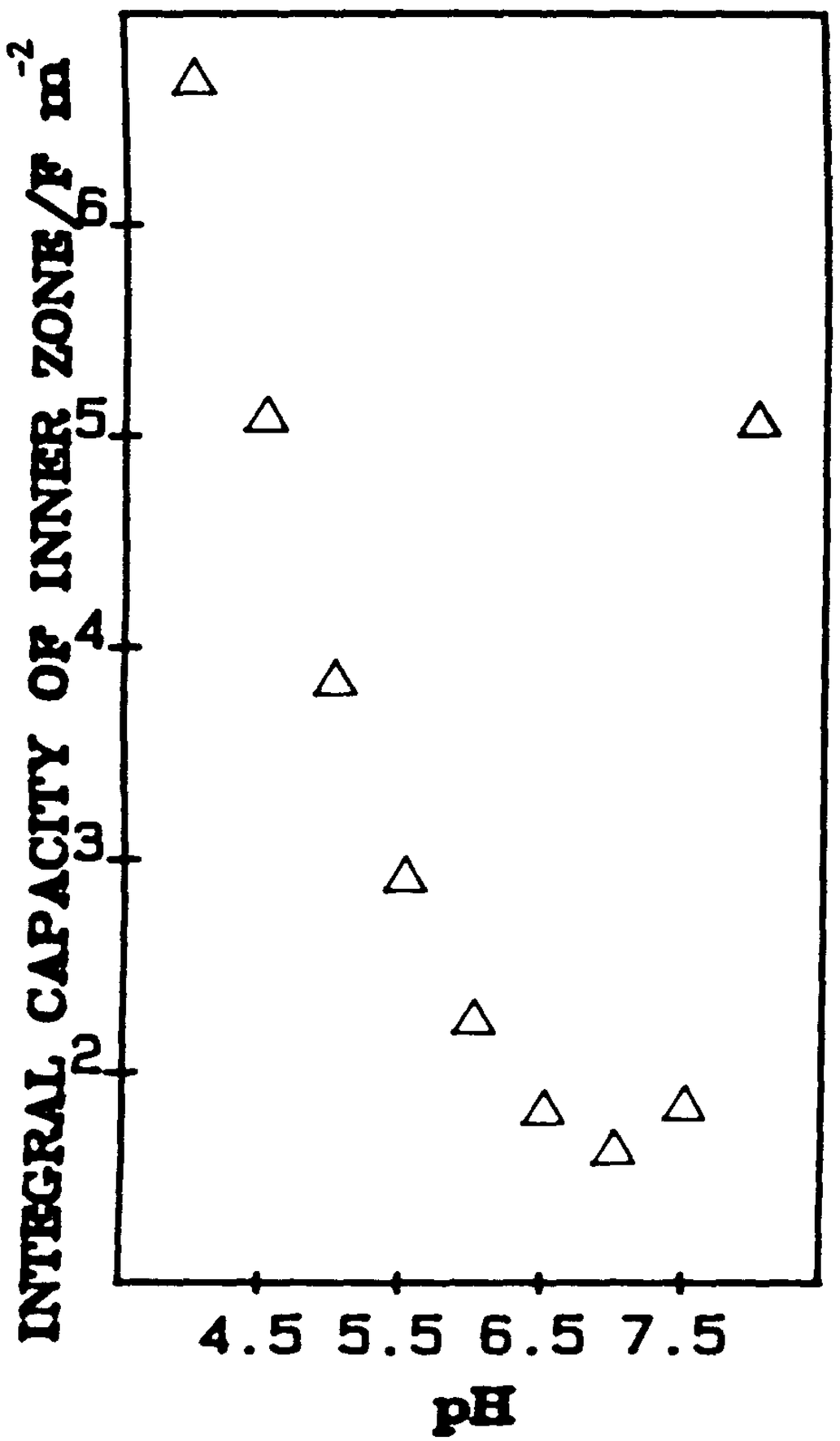

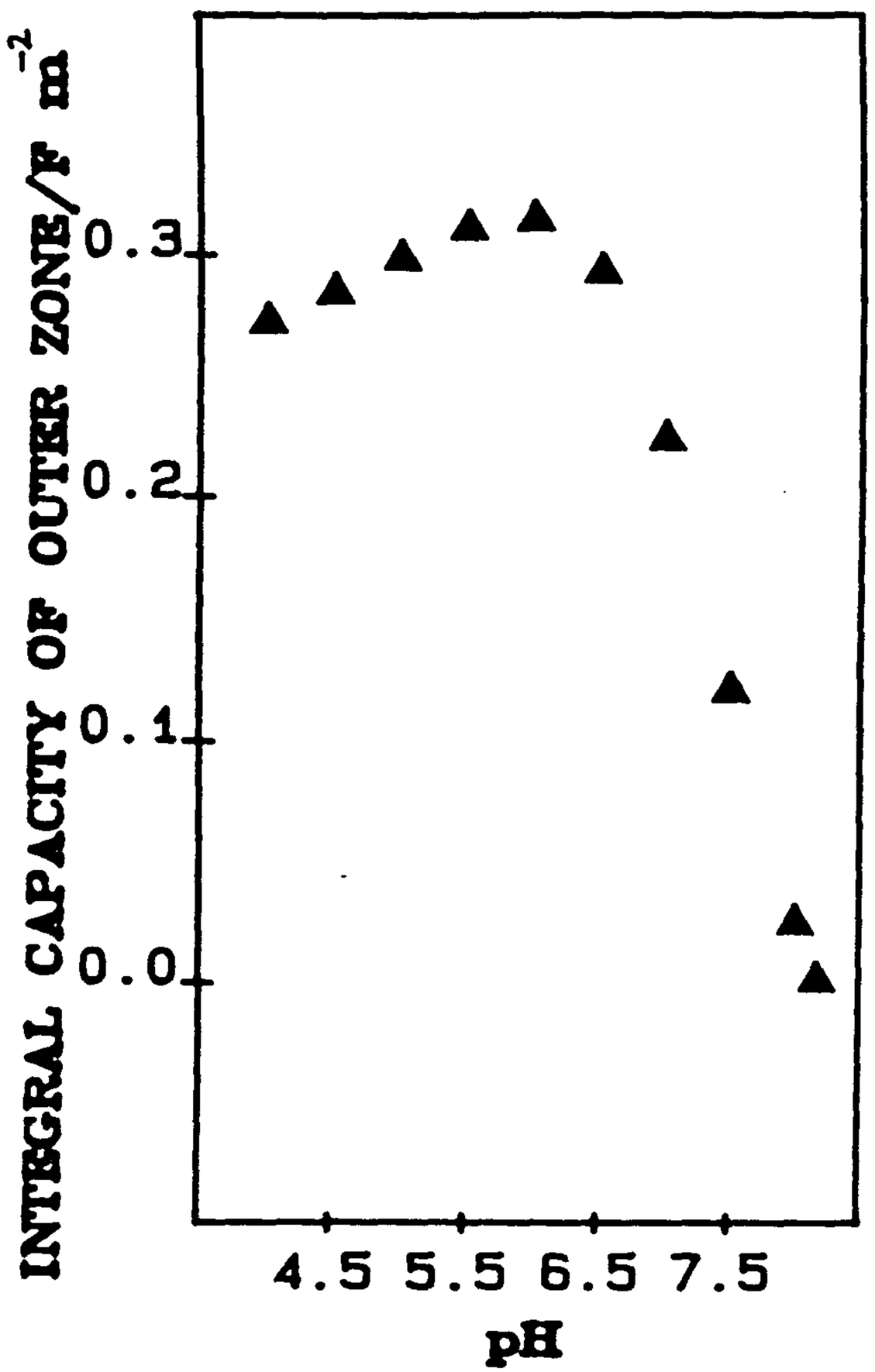

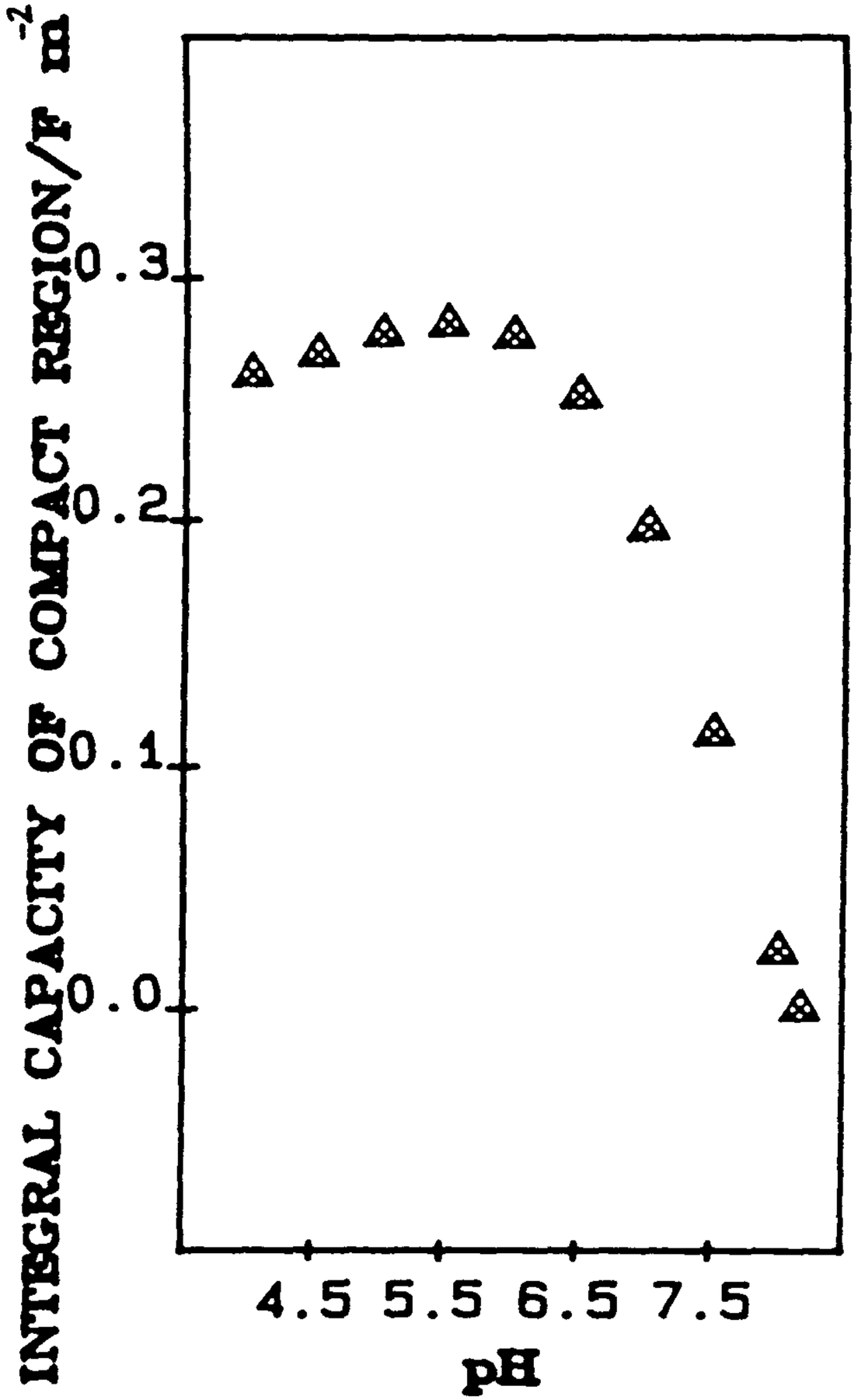

K_2^{CAP} and K_C^{CAP} were fairly constant at about $0.3Fm^{-2}$. At [NaCl] = 10, 5 and 1mmol dm^{-3} K_1^{CAP} had fairly steady values across the middle pH range of 2, 1 and $0.5Fm^{-2}$, respectively.

For each $\bar{\varkappa}a$ value, a polynomial curve was fitted to the variation of $[Cl^-]_{EQ}$ with pH. Then, by means of the coefficients of each polynomial, values of $[Cl^-]_{EQ}$ were calculated at the arbitrary set of pH values. In the present context of Cl^- ion adsorption, eqns. B2.27 and B2.28 become, respectively,

$$\Gamma_{Cl^-} = \Omega_{II} + \Omega_{III} \log [Cl^-]_{EQ} \qquad \text{B2.27A}$$

and

$$\log \Gamma_{Cl^-} = \log \Omega_{IV} + \frac{\log [Cl^-]_{EQ}}{\Omega_V} \qquad \text{B2.28A}$$

The Cl^- ion adsorption of αFeOOH dispersion is expressed graphically as each one of these adsorption equations, and the Stern-Grahame Adsorption Equation (eqn. B2.35), in Figs. B2.12 to B2.14. For each adsorption equation plot (at an arbitrary pH value) the slope, intercept and correlation coefficient are given in Tables B2.1 to B2.3. In the case of the Stern-Grahame Adsorption Equation plots, the quantity W_{Cl^-}/kT was evaluated from the slope for each arbitrary pH value. From a knowledge of $z_{Cl^-}e\psi_{IHP}/kT$ at each arbitrary pH value (and a particular $\varkappa a$ value) $(\phi_{ADS})_{Cl^-}/kT$ was calculated by eqn. B2.30. The variation of $(W_{ADS})_{Cl^-}/kT$, $z_{Cl^-}e\psi_{IHP}/kT$ and ϕ/kT with pH, for each $\varkappa a$ value is shown in Figs. B2.15 and B2.16. $(W_{ADS})_{Cl^-}$ attained a maximum value of about -5kT at pH4. In general, and for a given pH, $z_{Cl^-}e\psi_{IHP}/kT$ diminished, i.e., became less negative, with reducing [NaCl], while $(\phi_{ADS})_{Cl^-}/kT$ increased, i.e., became more negative, with reducing [NaCl]. $K_{Cl^-}^{int}$ calculated from $(\phi_{ADS})_{Cl^-}$ had a value of about 4 at [NaCl] = 10mmol dm^{-3}, and a value of about 16 over the concentration range 5mmol $dm^{-3} \geqslant$ [NaCl] $\geqslant$ 1.0mmol dm^{-3}; a very large value of $K_{Cl^-}^{int}$ was calculated at [NaCl] = 0.5mol dm^{-3}. It is noteworthy that the use of a larger value than r_{Cl^-} for r_{IHP}, in the calculation of $(\phi_{ADS})_{Cl^-}$ (eqns. B2.30 and B2.33), does lead to a smaller $K_{Cl^-}^{int}$ value (eqn. B2.25).

FIGURE B2.12

CHLORIDE ION ADSORPTION OF ∝FeOOH DISPERSION EXPRESSED AS THE ADSORPTION EQUATION:-

$$\Gamma_{\alpha^-} = \Omega_{II} + \Omega_{III} \mathrm{LOG}([Cl^-]_{EQ})$$

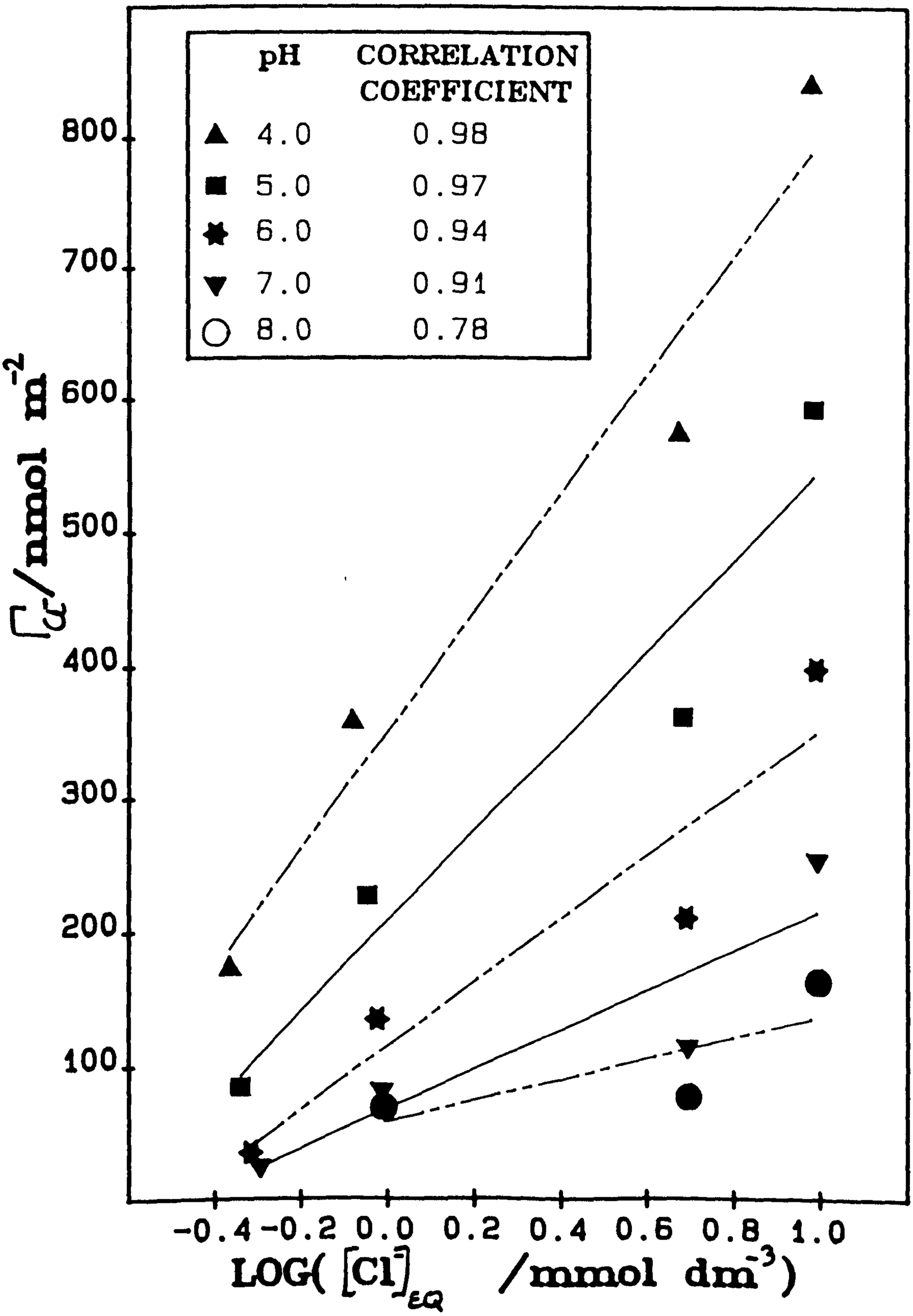

FIGURE B2.13

CHLORIDE ION ADSORPTION OF ∝FeOOH DISPERSION EXPRESSED AS THE FREUNDLICH ADSORPTION EQUATION.

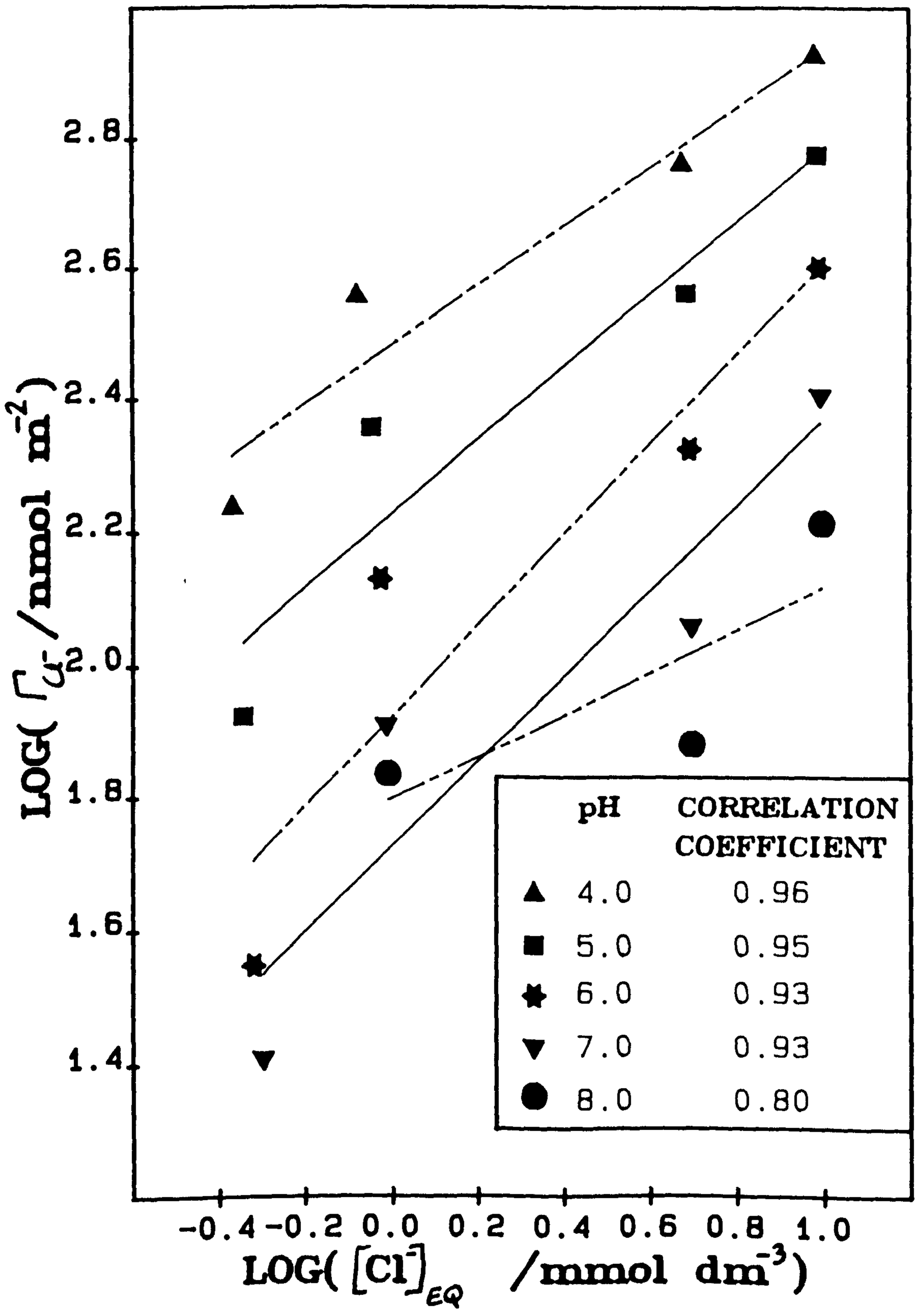

FIGURE B2.14

CHLORIDE ION ADSORPTION OF ∝FeOOH DISPERSION EXPRESSED AS THE STERN–GRAHAME ADSORPTION EQUATION.

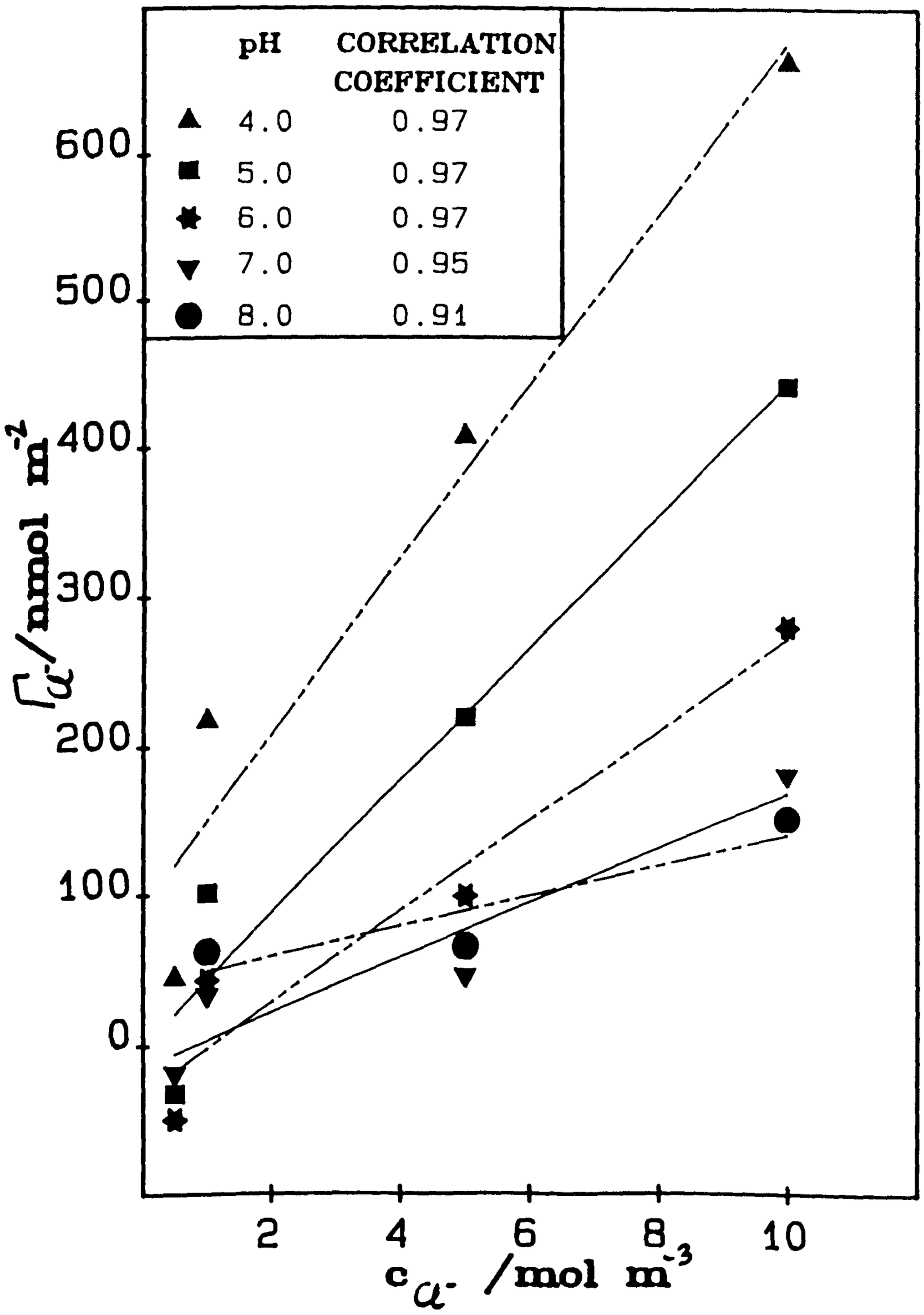

Table B2.1

Adsorption equation:- $\Gamma_{Cl^-} = \Omega_{II} + \Omega_{III} \log \left(\frac{[Cl^-]_{EQ}}{(\text{mmol dm}^{-3})}\right)$

pH	Ω_{II} / nmol m^{-2}	Ω_{III} / nmol m^{-2}	Correlation coefficient
4.0	350.7	445.9	0.978
4.5	273.1	390.5	0.972
5.0	208.1	337.1	0.965
5.5	155.4	285.8	0.956
6.0	114.7	236.8	0.944
6.5	85.6	190.3	0.929
7.0	68.1	146.5	0.909
7.5	57.1	111.5	0.810
8.0	58.1	78.3	0.779
8.17	60.8	67.9	0.768

Table B2.2

Adsorption equation:- $\log \frac{\Gamma_{Cl^-}}{\text{nmol m}^{-2}} = \log \Omega_{IV} + \frac{1}{\Omega_V} \log \left[\frac{[Cl^-]_{EQ}}{\text{mmol dm}^{-3}}\right]$

pH	$\frac{\Omega_{IV}}{\text{nmol}^{(1-\Omega_V)}\text{m}^{(3\Omega_V-2)}}$	Ω_V	Correlation coefficient
4.0	281.9	2.200	0.963
4.5	228.6	1.997	0.958
5.0	167.6	1.799	0.950
5.5	119.0	1.615	0.940
6.0	83.3	1.469	0.931
6.5	61.3	1.417	0.926
7.0	53.0	1.562	0.931
7.5	64.1	2.503	0.855
8.0	62.5	3.147	0.803
8.17	64.4	3.545	0.786

Table B2.3

Adsorption equation:- $-(\Gamma_{IHP})_{Cl^-} = 0.362 \times 10^{-9} \cdot c_{Cl^-} \cdot \exp^{\frac{(-w_{ADS})_{Cl^-}}{kT}}$

pH	$\frac{(w_{ADS})_{Cl^-}}{kT}$	Intercept ≠ o / nmol m^{-2}	Correlation coefficient
4.0	-5.0858	90.33	0.973
4.5	-4.9590	36.26	0.974
5.0	-4.8098	- 1.44	0.974
5.5	-4.6349	-24.09	0.973
6.0	-4.4313	-33.04	0.968
6.5	-4.1945	-29.62	0.961
7.0	-3.9221	-15.20	0.948
7.5	-3.5775	12.90	0.905
8.0	-3.3295	38.19	0.909
8.17	-3.2552	48.79	0.922

FIGURE B2.15

WORK OF ADSORPTION OF CHLORIDE ION AT THE ∝FeOOH/NaCl aq. INTERFACE AS A FUNCTION OF pH AT 25°C.

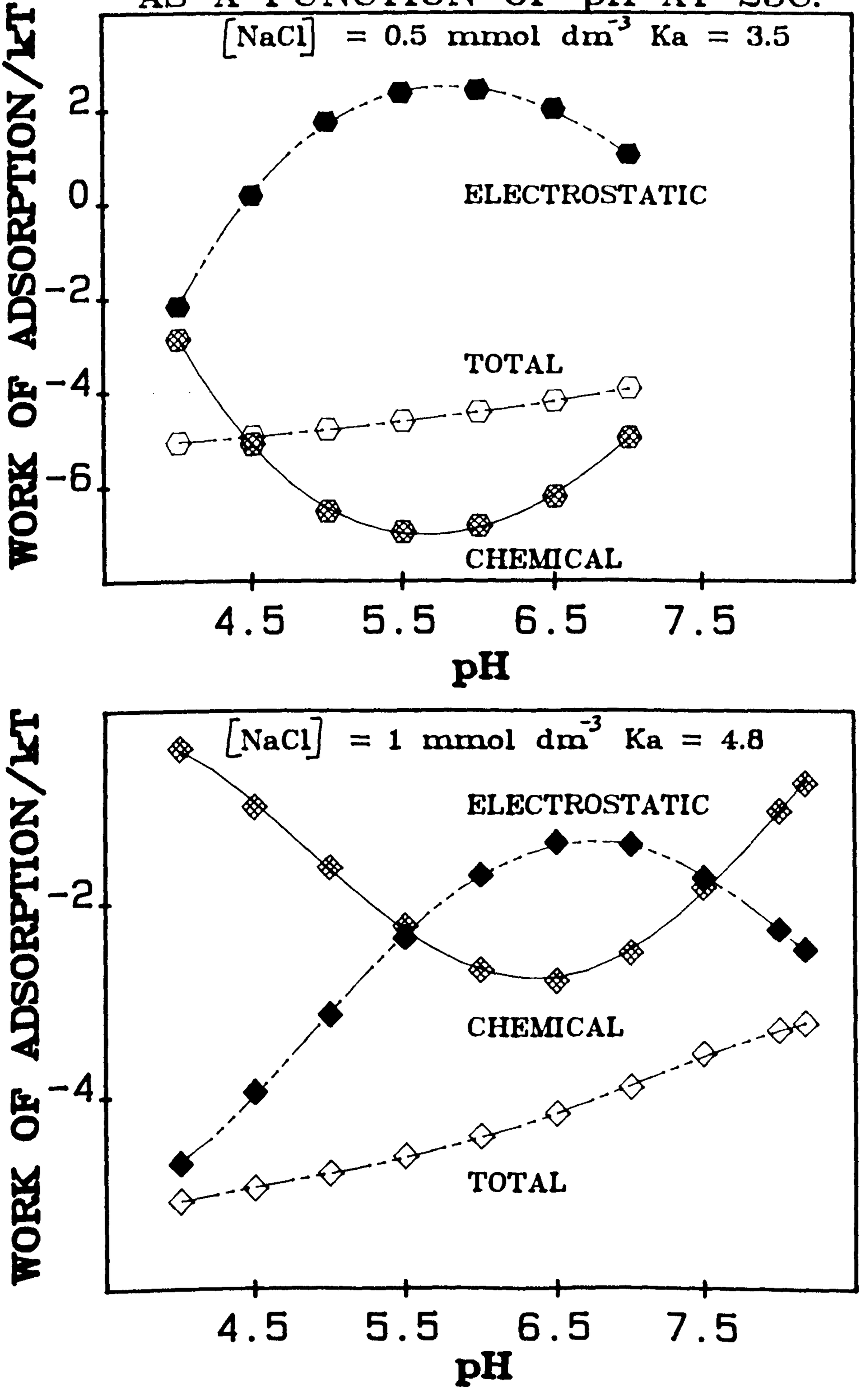

FIGURE B2.16

WORK OF ADSORPTION OF CHLORIDE ION AT THE ∝FeOOH/NaCl aq. INTERFACE AS A FUNCTION OF pH AT 25°C.

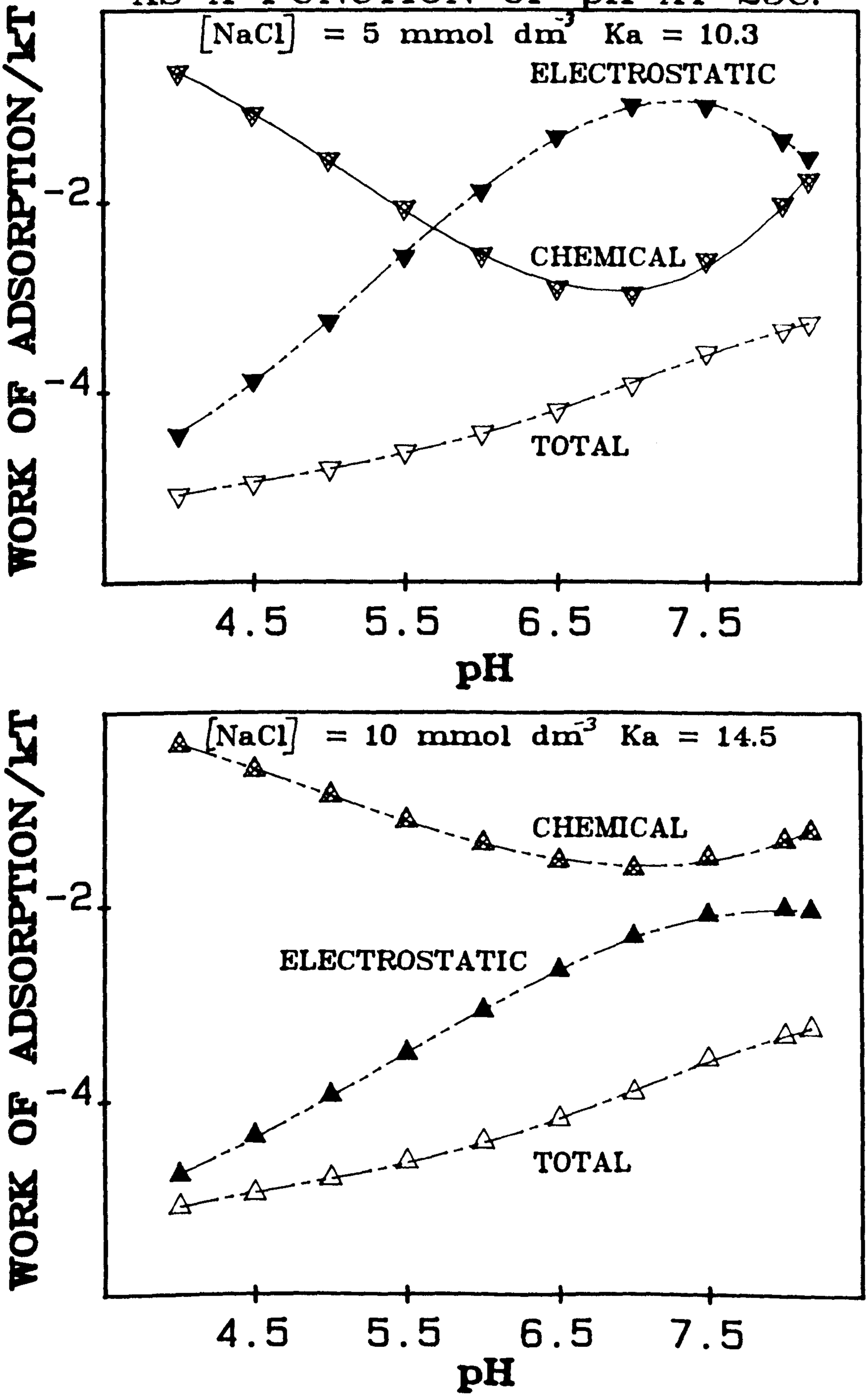

5. CONCLUSIONS

a) It is possible to measure the uptake of Cl^- ions, at 25°C by 2g of αFeOOH dispersed in 200 cm^3 of NaCl solution within the concentration and pH ranges of 0.5 mmol $dm^{-3} \leqslant$ [NaCl] $<$ 10 mmol dm^{-3} and $3.8 \leqslant pH \leqslant 8.5$, respectively, using the HPLC technique of Ion Chromatography. However, for such a static experimental set-up the Cl^- ion adsorbed is < 20% of the available Cl^- ion.

b) The observed residual Cl^- adsorption at pH_o indicates a specificity of Cl^- ions for the αFeOOH surface.

c) Physically realistic σ and ψ values for the αFeOOH-NaCl aq. interface can be obtained by the coupling together of electrophoresis (σ_E, ζ) and ion chromatography data (σ_S). Thus, for a given pH and [NaCl], $\sigma_S \geqslant |\sigma_E|$ (within experimental error) and $\psi_S > \zeta$ (except at low [NaCl]), while, at a given pH, σ_{IHP} and ψ_{IHP} diminish with reducing [NaCl]. However, at very low [NaCl] such data-coupling results in potentials that are meaningless in the present context of Cl^- ion adsorption measurements. Apparently, ψ is a steep function of σ at low [NaCl] and small inconsistencies between σ_S and σ_E data, at this low concentration, lead to gross discrepancies between the potentials ψ_S, ψ_{IHP} and ζ.

d) The observed relatively small σ_S and αFeOOH Cl^- ion coverage values, even for the low [NaCl] range studied here, could be explained by the assumption that not all of the specific surface area determined by the BET method is, either active towards, or accessible to, Cl^- ions. It may be that only the external specific surface area of an αFeOOH particle, rather than the total (i.e. BET) specific surface area, can freely interact with a Cl^- ion.

e) The observed K_1^{CAP} values in excess of $1 Fm^{-2}$ reflects, even for values of D_1^* approaching $D_w/2$, a very small r_{IHP} value. The implication is that the IHP is closer to the plane of the centres of the surface charge than would be expected on the basis of ionic radii. It must be assumed, then, that at [NaCl] $\geqslant$ 5 mmol dm^{-3} the adsorbed Cl^- ions can penetrate the plane of the surface charge to some extent. The observed reduction in K_1^{CAP} with reducing [NaCl] suggests that r_{IHP} increases with diminishing [NaCl].

f) The expression of Cl^- ion adsorption of αFeOOH dispersion in terms of empirical and theoretical adsorption equations shows the Cl^- ion to exhibit both specific and surface-active behaviour, especially at low pH.

g) In view of the apparent increase in r_{IHP} with diminishing [NaCl], and the knowledge that the use of a larger value than r_{Cl^-} for r_{IHP} in the calculation of $(\emptyset_{ADS})_{Cl^-}$ does lead to a smaller $K^{int}_{Cl^-}$ value, it would seem conceivable that the observed dependence of $K^{int}_{Cl^-}$ on [NaCl] could be eliminated by the acknowledgement of a [NaCl] dependence of r_{IHP} in the calculation of $(\emptyset_{ADS})_{Cl^-}$.

6. COMPARISON WITH OTHER WORK

The σ_S determined in this work is significantly smaller, for a given [NaCl] and pH, than that determined by Yates and Healy, who used potentiometric titration measurements. A comparison between the determined values of K^{int}_{a+s} and $K^{int}_{Cl^-}$, and those values determined by other workers is shown in Table B2.4. Significantly, the value of K^{int}_{a+s} determined in this work indicates a smaller degree of protonation of neutral surface sites than is suggested by the K^{int}_{a+s} values determined by other workers. Furthermore, the anion binding constant (K^{int}_{ANION}) determined from potentiometric titration data by other workers indicatesa greater intensity of interaction between a positive surface and Cl^- ion or NO_3^- ion, than is suggested by the corresponding constant of this work. Apparently, that proportion of the αFeOOH surface accessible to Cl^- ions is less that that accessible to H^+ and OH^- ions.

Table B2.4

Comparison of determined values of positive surface amphoteric and complexation constants with those values determined by other workers.

Reference	K^{int}_{a+s}	K^{int}_{ANION}
system	mmol dm^{-3}	mol^{-1} dm^3
<u>This work</u>		
αFeOOH/NaCl	1.769×10^{-1}	4 (10mmol dm^{-3})
		16 (1 to 5 mmol dm^{-3})
<u>Hingston et.al.</u>		
αFeOOH/NaCl	1.259×10^{-2}	50.1
<u>Yates</u>		
αFeOOH/KNO_3	6.310×10^{-2}	79.4
<u>Davis</u>		
$Fe(OH)_3$/$NaNO_3$	7.943×10^{-3}	50.1

REFERENCES

Bidlingmeyer, B.A., Deming, S.N., Price, W.P., Sachok, B. and Petrusek, M.J., J. Chromatog., 186, 419 (1979).

Bockris, J.O'M., Devantham, M.A.V., and Muller, K., Proc. Roy. Soc. (London), A274, 55 (1963).

Chapman, D.L., Philos. Mag., 25, (6), 475 (1913).

Davis, J.A., Ph.D. Thesis, Stanford University, 1977.

Davis, J.A., James, R.O. and Leckie, J.O., J. Colloid Interface Sci., 63, 480 (1978).

Freundlich, H., "Colloid and Capillary Chemistry", Methuen, London, 1926.

Gouy, G., J. Phys. Radium, 9, 457 (1910).

Grahame, D.C., Chem. Rev., 41, 441 (1947).

Hingston, F.J., Posner, A.M. and Quirk, J.P., Adv. Chem. Ser., 79, 82 (1968).

Hunter, R.J., "Zeta Potential in Colloid Science", Academic Press, London 1981.

James, R.O., Davis, J.A. and Leckie, J.O., J. Colloid Interface Sci., 65, 331 (1978).

Kellerman, A. and Lange, E., Kolloid-Z., 81, 88 (1933).

Knox, J.H., and Laird, G.R., J. Chromatog., 122, 17 (1976).

Knox, J.H. and Jurand, J., J. Chromatog., 125, 89 (1976).

Kovacina, T.A., and Venezky, D.L., "Naval Research Laboratory Report 7264", Washington D.C., 1971.

Kruyt, H.R. and Van Der Willigen, P.C., Z. Physikal Ch. (A) 139, 53 (1928).

Langmuir, I., J. Am. Chem. Soc., 40, 1361 (1918).

Latimer, W.M., Pitzer, K.S. and Slansky, C.M., J. Chem. Phys., 7, 108 (1939).

Levine, S., J. Colloid Interface Sci., 37, 619 (1971).

Ohshima, H., Healy, T.W. and White, L.R., J. Colloid Interface Sci., 90, 17 (1982).

Parsons, R., in "Modern Aspects of Electrochemistry", Bockris, J.O.M. and Conway, B.E.; Editors, Vol. 1, 103, Butterworths, London, 1954.

Stern, O., Z. Electroche., 30, 508 (1924).

Sood, S.P., Sartori, L.E., Wittner, D.P. and Haney, W.G., Anal. Chem., 48, 796 (1976).

Waters Associates, "Paired-Ion Chromatography, An Alternative to Ion Exchange", Milford, Mass., December, 1975.

Wells, A.F., "Structural Inorganic Chemistry", 3rd Edition, Oxford University Press, 1962.

White, L.R., J. Chem. Soc. Faraday Trans. II, 73, 577 (1977).

Wittner, D.P., Nuessle, N.O. and Haney, W.G., Anal. Chem., 47, 1422 (1975).

Yates, D.E., Levine, S. and Healy, T.W., J. Chem. Soc. Faraday Trans. I, 70, 1807 (1974).

Yates, D.E., Ph.D. Thesis, University of Melbourne, 1975.

Yates, D.E. and Healy, T.W., J. Colloid Interface Sci., 52, 222 (1975).

CHAPTER B3

MODELLING AND TEMPERATURE DEPENDENCE OF THE αFeOOH-NaCl aq. INTERFACE: PROTON ADSORPTION AND POINT OF ZERO CHARGE MEASUREMENTS (POTENTIOMETRIC AND SALT TITRATIONS).

INTRODUCTION

1.1. Potentiometric titration of metal oxides.

In contrast to double layer studies with AgI, studies with metals (other than mercury) and metal oxides are much more difficult to perform and analyse (Lyklema 1966). Two major problems arise in double layer studies of metal oxides, for example the oxides of iron. Firstly, most inorganic solids are incapable of being fashioned into electrodes (Healy 1978), and, secondly, since H^+ and OH^- ions may not be components of both bulk phases (in contrast to the potential determining ions Ag^+ and I^- of the AgI/aqueous colloid) there is doubt that H^+ and OH^- ions are potential determining ions for oxides in the same sense that the ions Ag^+ and I^- may be shown to be potential determining ions for a reversible colloid systems such as AgI/aqueous electrolyte (Davis et.al.). The first problem is currently insurmountable. The second problem can be overcome with recourse to the relevant solubility data. For example, in iron (III) oxide the contribution made to the surface charge by transfer of iron hydroxo complex ions across the interface is usually considered to be very small in relation to H^+ and OH^- ion transfer, since solubility data show that either H^+ or OH^- ions always greatly exceed iron (III) hydroxo complex ions in concentration for a pH range 3.5 to 11 (Atkinson et.al.). Thus, H^+ and OH^- ions can be called potential determining ions for oxides only insofar as the common method of definition of surface charge density (σ_s) is through the uptake or release of potential determining ions at the surface. Hence, σ_s determination requires adsorption/desorption measurements for H^+ (see section 7.), and these are readily carried out by the direct method of potentiometric titration of microcrystalline particles of oxide, in dilute aqueous suspension, using various ionic strengths of electrolyte. Bolt, Parks and de Bruyn were among the first to apply potentiometric titration to the study of oxide surface equilibria and confirm the importance of H^+ and OH^- ions in the establishment of the electrical double layer (edl) at the oxide/water interface.

1.2. The slow proton transfer process at the surface of metal oxides.

Potentiometric titration measurements on oxide suspensions usually show a slow drift of pH with time, after an initial fairly rapid change on adding acid or base (Levine and Smith). Berube et.al., were among the first to study this slow proton transfer process. In their study of the αFe_2O_3-

aqueous electrolyte interface Berube et.al. performed potentiometric titrations at three different titration rates; rapid, intermediate and very slow. The proton adsorption densities evaluated from the very slow titrations, conducted at several different ionic strengths, were an order of magnitude larger than the corresponding adsorption densities evaluated from the rapid titrations. In addition, whereas sorption isotherms evaluated from the rapid and very slow titrations exhibited no hysteresis, the sorption isotherms evaluated from intermediate rate titrations displayed a marked hysteresis. Berube et.al. conclude that potentiometric titrations of aqueous oxide suspensions performed at intermediate titration rates that are too slow to exclude the slow proton transfer process, and too fast to assure complete equilibration, yield irreversible displacements of isotherms at fixed ionic strength. Onoda and de Bruyn, Berube et.al. propose that the observed kinetic behaviour of the abstraction of protons from solution (or the release of protons to the fluid phase) in the αFe_2O_3/aqueous electrolyte system, namely a fast step followed by a slow step, may be explained by the rapid adsorption (or desorption) of protons at the hydrated surface of the oxide phase followed, initially, by the slow diffusion of <u>adsorbed</u> protons through a geothite-like interphase; the equilibration process within the hydrated layer takes place much more slowly because of proton diffusion. It is the chemical potential gradient across this layer which constitutes the driving force for this diffusion. Protons diffusing into or out of the geothite-like interphase create proton-excesses or proton-deficites in the lattice and build up a proton-excess or proton-deficit space charge, thereby extending the double layer into the solid. Furthermore, Onoda and de Bruyn suggest that the slow step as a whole includes more than one mechanism, possibly an anion exchange process involving OH^- ions and inorganic anions from the supporting electrolyte, such as Cl^- ions. The importance of the proposed geothite-like layer is seen in that it will act as a source of protons in order to explain the occurrence of the slow step (diffusion of protons into the solution) when the pH of the system is kept above pH_o.

A two step process, similar to that observed for the transfer of protons between suspended oxide and aqueous electrolyte, has also been reported by Wei and Bernstein in a study of the exchange of D_2O vapour with $\alpha AlOOH$, and by Feitknecht et.al. in tritium exchange studies between tritiated $Ni(OH)_2$, and $\alpha FeOOH$, and the fluid phases liquid water and water vapour. Hydrogen exchange was suggested to take place on hydrogen

atoms attached to oxygen atoms which are virtually immobile in the lattice, thus excluding the possibility that they are carried by migrating OH^- or H_2O species. Wyttenbach calculated the number of OH layers involved in the rapid surface exchange at 25°C and 174°C as 1 and 4.5, respectively, assuming isotropic diffusion. However, Gallagher and Phillips in their tritium exchange study between αFeOOH and tritiated water propose a highly anisotropic proton transfer along the αFeOOH tunnels involving the hydrogen bonds $[O_{II}— H \ldots\ldots O_I]^{3-}$. On the basis of this latter model the fast exchange reaction would account for the penetration of H^+ ions to the extent of 40 OH layers into the solid from the ends of the needles instead of the 1 layer overall predicted by Wyttenbach. Gallagher and Phillips noted that after exchanging all the surface OH groups, further penetration (the slow diffusion process) could only take place via the tunnels.

The different coordinations of the three types of hydroxyl groups at the αFeOOH surface (Russell et.al., Parfitt et.al. 1975, Parfitt et.al. 1976) should have different influences upon their acid-base behaviour, in as much as there exists on the surface of αFeOOH adsorption sites with different proton affinities. On the basis of this surface model Madrid and de Arambarri attribute the hysteresis in the proton sorption isotherms of the αFeOOH/aqueous electrolyte system, for example the slowness of the desorption of H^+ ions, to partial alterations of the αFeOOH surface by rearrangement of surface atoms; in particular, the translocation of H^+ ions between sites of different basicity by the rearrangement of surface Fe atoms and OH groups.

Other workers in this field, notably Tadros and Lyklema 1969 (SiO_2/aqueous electrolyte), Trimbos and Stein (ZnO/aqueous electrolyte) have observed that even rapid potentiometric titrations of aqueous suspensions of oxides yield irreversible displacement of isotherms at fixed ionic strength if the pH range covered is appreciably large, or if the magnitude of the titrant volume added between successive measurements is not constant at the same stage in the adsorption and desorption titrations.

Consequently, in a study of surface ionisation and complexation reactions at an oxide-aqueous electrolyte interface employing the potentiometric titration technique, the time between successive additions of titrant and the overall titration regime are important experimental parameters.

Potentiometric titrations of aqueous suspensions performed very rapidly, over a relatively small pH range, will result in σ_s/pH data that have been solely generated by surface ionisation and complexation reactions, whereas σ_s and, consequently, the total integral or differential capacity values obtained from slow potentiometric titrations of aqueous suspensions conducted over a relatively large pH range will be erroneously high due to the contribution to the real surface charges of that charge derived from the slow proton transfer process.

1.3. Point of zero charge (pzc) determination of metal oxides.

The most important parameter which may be used to describe a double layer of free charges is its pzc. In addition to the adsorption method of Parks and de Bruyn, the pzc of metal oxides may also be determined by a great variety of other methods because much of the behaviour of colloidal suspensions depends upon the structure of the edl which is absent or collapsed at the pzc (Parks 1965). Thus, the pzc is inferred from the zero point of any property which depends on the presence of an edl. For example, Yates and Healy 1975b, Davis and Leckie, Tadros and Lyklema 1968 have employed a salt titration method to determine the pzc of aqueous suspensions of α-chromia, amorphous iron oxyhydroxide and SiO_2, respectively. In this method the change in pH is observed upon the addition of salt, say NaCl, to a suspension. At the pH_o there should be no change in pH upon the addition of salt, while the addition of salt to a suspension whose pH is different from its pH_o will cause a shift in pH towards the pH_o by increasing σ_s. The reverse of the salt titration method, namely the addition of adsorbent method, has been used successfully by Regazzoni et.al., Breeuwsma and Lyklema 1971 to determine the pzc of aqueous suspensions of ZrO_2 and Fe_3O_4, and αFe_2O_3 respectively. This method involves the addition of adsorbent, say Fe_3O_4, to a volume of electrolyte at a fixed concentration and a given pH value. As with the salt titration method the addition of adsorbent to an electrolyte solution, whose pH is different from the pH_o of the suspended adsorbent, will result in a shift of the suspension pH towards the pH_o.

Other experimental methods for determining the pzc of a colloidal suspension include the direct analytical determination of counterion adsorption (Tadros and Lyklema 1969, Breeuwsma and Lyklema 1971), the maximum flocculation rate (Parks and de Bruyn), the maximum rate of deposition (Hermansson), the suspension effect (Honig and Hengst), the point of

maximum surface tension (Parks and de Bruyn) and the minimum solubility of the solid constituting the colloid (Parks and de Bruyn). Finally, Yoon et.al. have developed a modified version of an equation originally formulated by Parks that is capable, within limits, of predicting the pzc of oxides from a knowledge of the radius of the particular metal ion within the oxide lattice.

1.4. Models of the oxide-aqueous electrolyte interface.

The role of potential determining ions in defining the surface charge and related magnitudes can be represented by the equations

$$SOH_2^+ = SOH + H_S^+ \qquad B3.1$$

and

$$SOH = SO^- + H_S^+ \qquad B3.2$$

(where S denotes surface)

On the other hand, indifferent ions also contribute to the generation of charge as shown by the changes in the titration curves of oxide suspensions brought about by changes in the ionic strength.

Models formulated to explain the development of charge at the interface between a solid and an aqueous solution have a long history. Most are based on theories summarised by Verwey and Overbeek for describing the charge distribution at the interface between a mercury electrode and an aqueous electrolyte. This theoretical summary has been extended to describe charge development at mineral surfaces (de Bruyn and Agar) and at soil surfaces (Van Raij and Peech). A major advance was made by Levine and Smith when they derived general expressions for the relation between surface charge, surface potential and the activity of those ions in solution that react with the surface.

Models based on the Levine and Smith approach may differ in detail and in complexity, because choices must be made between controversial alternatives and because the level of approach can be different. For example, there are differences in the way the surface reactions are defined. Thus, Levine and Smith, Yates et.al., consider that every neutral M-OH group at a surface may be either protonated or deprotonated. This allows for at least twice as many charging sites as the Bowden et.al., concept, in which a neutral site is defined as $OH\text{-}M\text{-}OH_2$. Another controversial point is

whether electrolytes, such as aqueous NaCl, can be considered as 'indifferent' electrolytes or whether there are reactions between the electrolyte ions and the surface of the metal oxides. Such reactions were included, for example, in the model of Davis et.al. They were excluded in the theoretical development of their model by Bowden et. al., but were in fact used in fitting data to their model. The arrangement of ions near a charged surface is complex (Bowden et.al.). The models attempt to simplify this complexity by defining planes of equal potential near the surface. [However, it must be pointed out that, even from a rudimentary examination of their crystallography, any model involving only a few planes of adsorption at the surface will be an oversimplification of the actual complex surface condition.] Thus, for example, Grahame expanded the two-plane model of Stern to three planes. Bowden et.al., for the sake of simplicity, used only two planes in their interface model while accepting that several planes would be more realistic. In their study of ion adsorption models on variable charge surfaces, Barrow et.al., showed that a three-plane model gave a more realistic description of the charging curves for αFeOOH.

In the past several years there has been a remarkable increase in the number of studies devoted to chemical modelling of the interfacial region between an oxide and an aqueous solution. In large measure, these studies have produced successful quantitative models of both cation and anion adsorption phenomena, principally because of their frequent use of a fertile combination of concepts from coordination chemistry and the theory of the edl. In the most recent, successful, models of the double layer surrounding an oxide particle immersed in water, termed surface complexation models (Sposito 1983), the number of interrelated magnitudes employed to fully characterise the double layer is rather large. Included are the charges and potentials related to three different planes (solid surface, Helmholtz plane (IHP) and outer Helmholtz plane (OHP)), two different capacities and several surface ionisation and complexation constants. These magnitudes are used to describe the interaction of the surface with potential determining ions (H^+ and OH^-) and with swamping electrolyte (Regazzoni et.al.).

2. THEORY

2.1. A comparison between the electrical double layers at the AgI-aqueous electrolyte and metal oxide-aqueous electrolyte interfaces.

It is natural to compare the electrical properties of the oxide-aqueous electrolyte interface with those of the well studied AgI-aqueous electrolyte interface. In order to compare the results obtained from these two quite different interfaces it has been usual to assume the validity of a Nernst equation and write for the change in interfacial (i.e. surface) potential (Levine and Smith)

$$\Delta(\psi_s)_N = -\Delta pH(\frac{kT}{e})\ell n\,10 \qquad B3.3$$

When this assumption is made it is found that the variation of σ_s with ψ_s for oxides is markedly different from that observed with AgI. Specifically, a) σ_s and the derived total differential or integral capacity of the oxide interface can rise to much higher values than for AgI, b) charges and capacities on positively and negatively charged surfaces are more symmetrical than for AgI which has noticeably higher capacities on the positive side, c) the actual values of σ_s for oxides tend to be higher the more porous the surface is (the porosity of the surface even appears to be a more important parameter than its chemical composition), and d) σ_s is, especially with very porous surfaces, higher than the charge that would correspond to full dissociation of all surface hydroxyls. Despite the high σ_s measured on oxides, studies of electrokinetic potential (ζ) and colloid stability indicate that electrokinetic charge density (σ_E) is relatively low, seldom exceeding 20% of σ_s (Breeuwsma and Lyklema, Yates 1975a). This difference in charge must be balanced by adsorption of electrolyte ions within the region inside the hydrodynamic shear plane. Explanations of the striking differences between the double layers on oxides and those on a relatively simple system such as AgI have been postulated by several authors. Confirmation of the strong chemisorption of water at the TiO_2 surface given by Yates, D.J.C., Lewis and Parfitt, Mays and Brady, Jurinak, Day and Parfitt, Dawson, Hollabaugh and Chessick, Wade and Hackerman has led Berube and de Bruyn 1968b to propose that the potential determining ions are situated beyond this contiguous, order imposing, water layer, at some distance away from the solid. Thus, the site of the surface charge is, accordingly, in a region in which the

surrounding water is less influenced by the ordering effect of the chemisorbed surface water, and counterions can, therefore, squeeze closer to the potential determining ions and form water-bridged ion-pairs. This arrangement minimises the effect of the electrostatic repulsion between like charged potential determining ions and hence a much higher σ_s becomes possible. Although αFeOOH has been shown to exhibit no significant porosity to N_2, Ar and Kr (Bye, Aylemore), Tadros and Lyklema 1968 have suggested the existence of a porous or gel-like hydrated oxide surface layer at the aqueous-solid interface, penetrable by both potential determining ions and counterions. Accordingly, the surface charge is not confined to the external surface proper but is distributed within some depth of the surface layer, so that more charge can be accommodated per unit area. The centres of the two classes of ions, potential determining and supporting electrolyte, are located on two planes which are parallel to the interface and lie <u>within</u> the porous layer (Yates et.al.). The counterions compensate the adsorbed potential determining ion charge essentially by forming ion-pairs. Although the extent of porosity is commonly assessed from gaseous adsorption, it is the <u>porosity towards aqueous ions</u> that is important (Breeuwsma and Lyklema 1971). If a solid displays ion porosity, the double layer properties are expected to be due partly to charge and counter-charge build-up inside the solid surface, and partly due to the same within the Stern layers. Levine et.al., in a theoretical study of the electrical properties of the oxide-aqueous electrolyte interface demonstrated that penetration of the oxide surface by potential determining ions, and by supporting electrolyte, can lead to a compensation of the high values of σ_s typical of oxide surfaces sufficient to account for the low values of σ_E. Yates et.al., propose that the "primary" surface charge is distributed as discrete charges over the oxide surface and that the adsorbed supporting electrolyte cations and anions are mainly distributed in two ways, viz., (a) in interfacial ion pairs, (b) in a diffuse layer to balance the remaining unneutralised surface charges. In their analysis Yates et.al., demonstrate that such a discrete acid-base site-binding model, involving ion-pair formation of counterions with surface sites does reproduce the distinctive properties of the oxide-aqueous electrolyte interface. In a later work, Yates and Healy 1975a discovered a close correlation between the experimentally determined surface density of rapidly exchangeable protons on αFeOOH, and the number of such protons predicted on the basis of the known crystal faces and their proportions, present at the αFeOOH surface. Yates and Healy conclude that

the αFeOOH-aqueous electrolyte interface is closely approximated by a plane rather than a penetrable gel, and that the typical high σ_s is a characteristic of this plane.

The discrete acid-base site-binding model of Yates et.al., was developed by Davis et.al. This site-binding model and its development is adopted in this work as a means of characterising the αFeOOH-NaCl aq. interface, using proton adsorption and pzc measurements.

2.2. The triple-layer, surface complexation model of the oxide-aqueous electrolyte interface.

2.2.1. Description (Fig. B3.1)

The principal mechanism of surface charge development is the reaction of major electrolyte ions with ionizable surface sites. The formation of surface complexes occurs in addition to simple ionisation of surface groups by the association/dissociation reactions of H^+ and OH^- ions. These ions form inner-sphere surface complexes whereas all other adsorbed metal cations and inorganic, or organic, anions form outer-sphere complexes (Sposito 1984). Therefore, when such cations and anions are adsorbed, a water molecule is understood to separate them from the surface charge region.

The intrinsic equilibrium constants for the simple amphoteric ionization reactions of surface sites are written as

$$K_{a+s}^{int} = \frac{[SOH][H^+]}{[SOH_2^+]} \cdot \exp(-\tilde{\psi}_s) \qquad B3.4$$

and

$$K_{a-s}^{int} = \frac{[SO^-][H^+]}{[SOH]} \cdot \exp(-\tilde{\psi}_s) \qquad B3.5$$

To account for adsorption of electrolyte ions within the shear plane, Yates et.al., propose the formation of "ion-pairs" at charged surface sites. For an oxide in NaCl solution, for example,

$$SO^- + Na_s^+ \overset{K_{Na^+}^{int}}{\rightleftharpoons} SO^- \ldots Na^+ \qquad B3.6$$

FIGURE B3.1

SCHEMATIC REPRESENTATION OF THE ∝FeOOH/NaCl aq. INTERFACE.

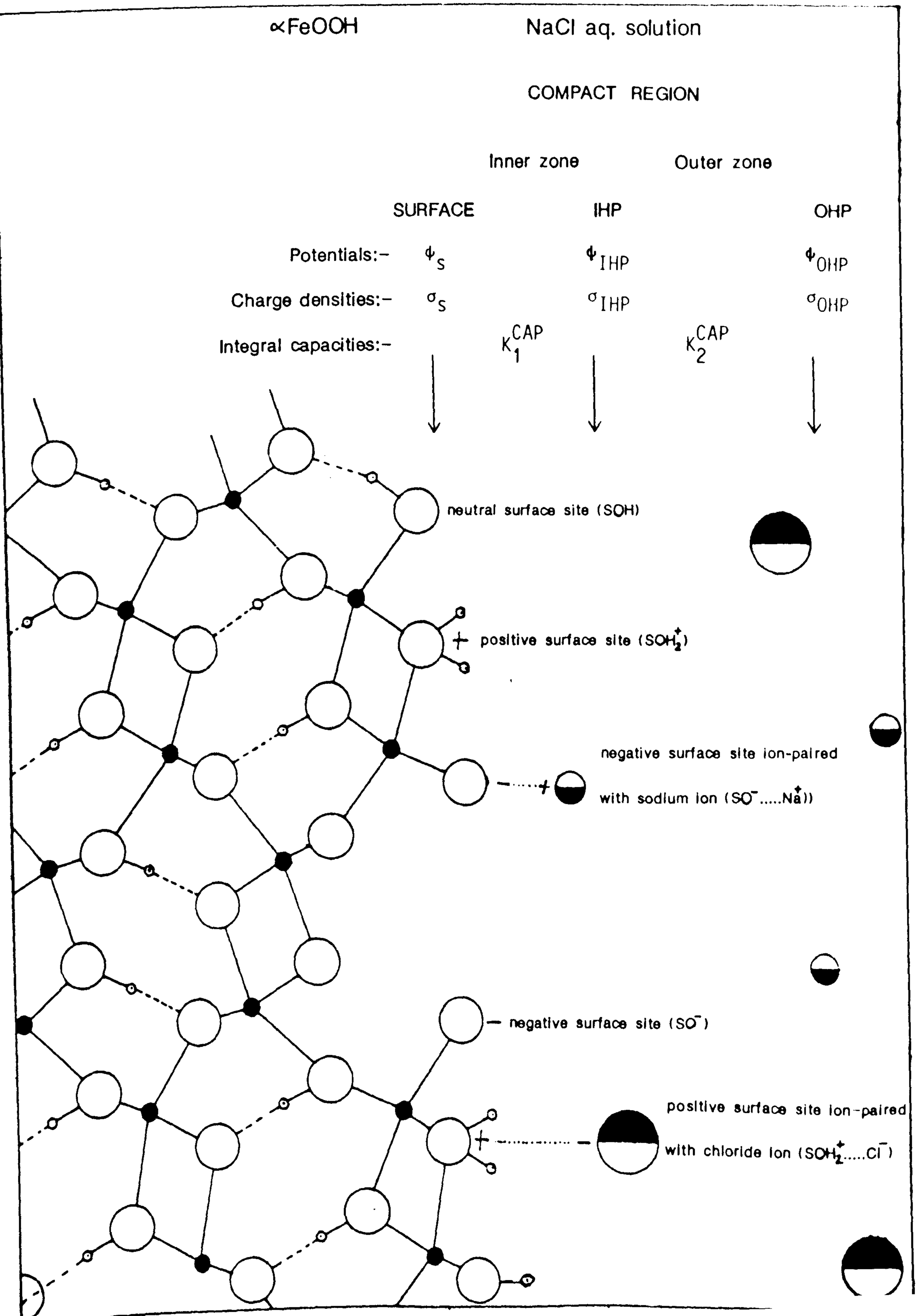

$$\text{and} \quad SOH_2^+ + Cl_s^- \overset{K^{int}_{Cl^-}}{\rightleftharpoons} SOH_2^+ \ldots Cl^- \qquad \text{B3.7}$$

The intrinsic equilibrium constants of these ion-pairs are written, respectively, as

$$K^{int}_{Na^+} = \frac{[SO^- \ldots Na^+]}{[SO^-][Na^+]} \exp(\tilde{\psi}_{IHP}) \qquad \text{B3.8}$$

$$\text{and} \quad K^{int}_{Cl^-} = \frac{[SOH_2^+ \ldots Cl^-]}{[SOH_2^+][Cl^-]} \exp(-\tilde{\psi}_{IHP}) \qquad \text{B3.9}$$

However, it is also instructive to write the reactions as complex ionisation reactions:

$$SOH + Na_s^+ \overset{{}^*K^{int}_{Na^+}}{=} SO^- \ldots Na^+ + H_S^+ \qquad \text{B3.10}$$

$$SOH_2^+ \ldots Cl^- \overset{{}^*K^{int}_{Cl^-}}{=} SOH + H_s^+ + Cl_s^- \qquad \text{B3.11}$$

The intrinsic equilibrium complexation constants of these reactions are written, respectively, as

$${}^*K^{int}_{Na^+} = \frac{[SO^- \ldots Na^+][H^+]}{[SOH][Na^+]} \exp(\tilde{\psi}_{IHP} - \tilde{\psi}_s) \qquad \text{B3.12}$$

$$\text{and} \quad {}^*K^{int}_{Cl^-} = \frac{[SOH][H^+][Cl^-]}{[SOH_2^+ \ldots Cl^-]} \exp(\tilde{\psi}_{IHP} - \tilde{\psi}_s) \qquad \text{B3.13}$$

$$\text{so that} \quad {}^*K^{int}_{Na^+} = K^{int}_{a\text{-}s} \; K^{int}_{Na^+} \qquad \text{B3.14}$$

$$\text{and} \quad {}^*K^{int}_{Cl^-} = K^{int}_{a+s} \; / \; K^{int}_{Cl^-} \qquad \text{B3.15}$$

The formation of surface complexes readjusts the acid/base equilibrium and affects σ_s. σ_s determined from a proton mole balance (see section 7.) represents the net number of protons released or consumed by all surface

reactions and not just the formation of the ionised surface species SO^- and SOH_2^+. Increase in electrolyte concentration causes additional binding of counterions until equilibrium is re-established. In this manner surface complexation provides a mechanism for the development of σ_s in addition to the role of H^+ and OH^- ions. σ_s and the charge densities at the IHP and OHP are, therefore, expressed as, respectively,

$$\sigma_s = B([SOH_2^+] + [SOH_2^+ \ldots\ldots Cl^-] - [SO^-] - [SO^- \ldots\ldots Na^+]) \quad B3.16$$

$$\sigma_{IHP} = B([SO^- \ldots\ldots Na^+] - [SOH_2^+ \ldots\ldots Cl^-]) \quad B3.17$$

and $$\sigma_{OHP} = -B([SOH_2^+] - [SO^-]) \quad B3.18$$

σ_{OHP} is calculated by the Gouy-Chapman equation.

Ionised surface sites are confined to a mean surface plane and adsorbed counterions to the IHP. Constant capacitances (K^{CAP}) are assumed in the regions between the planes (surface, IHP and OHP), and the charge/potential relationships are

$$\psi_s - \psi_{IHP} = \frac{\sigma_s}{K_1^{CAP}} \quad B3.19$$

and $$\psi_{IHP} - \psi_{OHP} = \frac{\sigma_{OHP}}{K_2^{CAP}} \quad B3.20$$

The inner zone integral capacity (K_1^{CAP}) is more sensitive to changes in double layer structure than is any other interfacial property. Consequently, much useful information concerning the $\alpha FeOOH/Cl^-$ aq. edl can be interpreted from K_1^{CAP} data. K_1^{CAP} is inversely proportional to the distance normal to the particle surface (r) the proportionality constant being permittivity (ε), either ε_1 or $\bar{\varepsilon}_1$ depending on which model of the inner zone is used. The surface species are distributed among the total number of sites available (N_s^σ):

$$N_s^\sigma = B([SOH_2^+] + [SOH_2^+ \ldots\ldots Cl^-] + [SOH] + [SO^-] + [SO^- \ldots\ldots Na^+]) \quad B3.21$$

when the limit of negligible surface complexation is enforced the following relationships are obtained

$$\sigma_s = B([SOH_2^+] - [SO^-]) \qquad B3.22$$

$$pK_{a+s}^{int} = pQ_{a+s} + \frac{\tilde{\psi}_s}{\ell n 10} \qquad B3.23$$

and

$$pK_{a-s}^{int} = pQ_{a-s} + \frac{\tilde{\psi}_s}{\ell n 10} \qquad B3.24$$

Conversely when the limit of complete surface complexation is enforced the following relationships describe the interface

$$\sigma_s = B([SOH_2^+ \ldots Cl^-] - [SO^- \ldots Na^+]) \qquad B3.25$$

$$^{*}pK_{Cl^-}^{int} = pQ_{a+s} - \log [Cl^-] + \frac{(\tilde{\psi}_s - \tilde{\psi}_{IHP})}{\ell n 10} \qquad B3.26$$

and

$$^{*}pK_{Na^+}^{int} = pQ_{a-s} + \log [Na^+] + \frac{(\tilde{\psi}_s - \tilde{\psi}_{IHP})}{\ell n 10} \qquad B3.27$$

2.2.2. The evaluation of surface amphoteric and complexation constants.

2.2.2.1. pK_{a+s}^{int} and pK_{a-s}^{int}: The limit of negligible surface complexation.

Either $[SO^-]$, negatively charged surface, or $[SOH_2^+]$, positively charged surface, constitutes a large fraction of σ_s. pK_{a+s}^{int} may be obtained by plotting the acidity quotient for a positive surface (pQ_{a+s}) as a function of the fraction of positively charged sites (α_{+s}) and extrapolating to $\alpha_{+s} = 0$ (i.e., $\sigma_s = \psi_s = 0$ in the absence of net specific adsorption) at the lowest electrolyte concentration. An analogous procedure in the alkaline branch yields pK_{a-s}^{int}. In order to check the value of pK_{a+s}^{int} obtained by the single extrapolation described, pQ_{a+s} is plotted as a function of $\alpha_{+s} + \sqrt{[NaCl]}$ and doubly extrapolated to $\alpha_{+s} = 0$ and $[NaCl] = 0$ (James et.al.). The value of pK_{a-s}^{int} obtained by single extrapolation may also be checked by an analogous double extrapolation.

2.2.2.2. $^{\star}pK^{int}_{Cl^-}$ and $^{\star}pK^{int}_{Na^+}$: The limit of σ_s being solely generated by surface complexation.

Either [SO^- .... Na^+], negatively charged surface, or [SOH_2^+ .... Cl^-], positively charged surface, constitutes a large fraction of σ_s. $^{\star}pK^{int}_{Cl^-}$ may be obtained by plotting pQ_{a+s} - log [Cl^-] as a function of α_{+s} and extrapolating to $\alpha_{+s} = 0$ at the highest electrolyte concentration. An analogous procedure in the alkaline branch yields $^{\star}pK^{int}_{Na^+}$.

2.2.3. The modelling of interfacial charges and potentials, K_1^{CAP} and surface charge densities.

The surface and interfacial quantities can be modelled by the mathematical solution of a set of equations, using an iteration procedure. The set of equations, which describe the charging and ion-pair formation behaviour of the oxide-aqueous electrolyte interface, include the Gouy-Chapman charge/potential relationship, the defining charge/potential relation for the integral capacity of the outer zone (K_2^{CAP}), and several equations formulated by Yates et.al., they are

$$\sinh\left(\frac{z\tilde{\psi}_{OHP}}{2}\right) = -\frac{\sigma_{OHP}}{(8\times10^3[NaCl]\,\epsilon_o D\,RT)^{\frac{1}{2}}} \qquad B3.28$$

$$\left[\text{using } \sinh^{-1}(x) = \ell n\,(x + (x^2+1)^{\frac{1}{2}})\right]$$

$$\psi_{IHP} = \psi_{OHP} - \frac{\sigma_{OHP}}{K_2^{CAP}} \qquad B3.29$$

$$\delta_{+s} = 1 + K^{int}_{Cl^-}\,[Cl^-].\ \exp(\tilde{\psi}_{IHP}) \qquad B3.30$$

$$\delta_{-s} = 1 + K^{int}_{Na^+}\,[Na^+].\ \exp(-\tilde{\psi}_{IHP}) \qquad B3.31$$

$$\theta = \gamma^{-1}\left[1 - [(1-\gamma)(1-\gamma\alpha^2)]^{\frac{1}{2}}\right] \qquad B3.32$$

where $$\gamma = 1 - \frac{K^{int}_{a+s}}{4\,K^{int}_{a-s}\,\delta_{+s}\,\delta_{-s}} \qquad B3.33$$

$$\text{and} \quad -\sigma_{OHP} = \frac{N_S^{\sigma}}{2}\left[\alpha\left(\frac{1}{\delta_{+S}} + \frac{1}{\delta_{-S}}\right) + \theta\left(\frac{1}{\delta_{+S}} - \frac{1}{\delta_{-S}}\right)\right] \qquad B3.34$$

The terms of these equations may be categorised as follows

a) independent variable which can be changed by the experimenter ([NaCl]),
b) dependent variables which change as a result of changes in the independent variable (σ_{OHP}, ψ_{IHP}, ψ_{OHP}),
c) parameters determined by separate experiments (N_S^{σ}, K_{a+s}^{int}, K_{a-s}^{int}, $K_{Cl^-}^{int}$, $K_{Na^+}^{int}$, K_2^{CAP}),
d) constants (e, k, T, ε).

The iteration procedure adopted was first to assign an estimated value to one of the dependent variables (ψ_{IHP}) and then to follow the sequence

a) calculate δ_{+S} and δ_{-S} from eqns. B3.30 and B3.31,
b) calculate γ from eqn. B3.33,
c) calculate θ from eqn. B3.32,
d) calculate σ_{OHP} from eqn. B3.34,
e) calculate $\sinh\left(\frac{z\psi_{OHP}}{2}\right)$, $\frac{z\psi_{OHP}}{2}$, and thence ψ_{OHP}, from eqn. B3.28,
f) calculate ψ_{IHP} from eqn. B3.29,
g) compare the calculated value of ψ_{IHP} with the assigned estimated value and, if they do not agree, change the value of ψ_{IHP}, repeat the procedure using successively smaller adjustments of ψ_{IHP} until the assigned and calculated values of ψ_{IHP} agree within a chosen tolerance.

Solution of the set of equations, using the iteration procedure, leads to values for the dependent variables σ_{OHP}, ψ_{IHP} and ψ_{OHP}. σ_s and ψ_{IHP} can be evaluated from, respectively, the modified Nernst equation given by Yates et.al.

$$\tilde{\psi}_s = -\Delta pH \ell n\ 10 - \tfrac{1}{2}\ \ell n\left[\frac{(\theta + \alpha)\delta_{-S}}{(\theta - \alpha)\delta_{+S}}\right] \qquad B3.35$$

and the electroneutrality condition

$$\sigma_s + \sigma_{IHP} + \sigma_{OHP} = 0 \qquad \text{B3.36}$$

K_1^{CAP} can be evaluated from eqn. B3.19.

Rearranging eqns. B3.4, B3.5, B3.12 and B3.13 gives, respectively,

$$\frac{[SOH_2^+]}{[SOH]} = \frac{[H^+]}{K_{a+s}^{int}} \cdot \exp(-\tilde{\psi}_s) = \nu_{SOH_2^+} \qquad \text{B3.37}$$

$$\frac{[SO^-]}{[SOH]} = \frac{K_{a-s}^{int}}{[H^+]} \cdot \exp(\tilde{\psi}_s) = \nu_{SO^-} \qquad \text{B3.38}$$

$$\frac{[SOH_2^+ \ldots Cl^-]}{[SOH]} = \frac{[H^+][Cl^-]}{{}^*K_{Cl^-}^{int}} \cdot \exp(\tilde{\psi}_{IHP} - \tilde{\psi}_s) = \nu_{SOH_2^+ \ldots Cl^-} \qquad \text{B3.39}$$

and

$$\frac{[SO^- \ldots Na^+]}{[SOH]} = \frac{{}^*K_{Na^+}^{int}[Na^+]}{[H^+]} \cdot \exp(\tilde{\psi}_{IHP} - \tilde{\psi}_s) = \nu_{SO^- \ldots Na^+} \qquad \text{B3.40}$$

Thus,

$$N_s^{\sigma} = B[SOH](1 + \nu_{SOH_2^+} + \nu_{SO^-} + \nu_{SOH_2^+ \ldots Cl^-} + \nu_{SO^- \ldots Na^+}) \qquad \text{B3.41}$$

i.e.,

$$(\sigma_s)_{SOH} = B[SOH] = N_s^{\sigma}(1 + \nu_{SOH_2^+} + \nu_{SO^-} + \nu_{SOH_2^+ \ldots Cl^-} + \nu_{SO^- \ldots Na^+})^{-1} \qquad \text{B3.42}$$

Finally,

$$(\sigma_s)_{SOH_2^+} = (\sigma_s)_{SOH}\ \nu_{SOH_2^+} \qquad \text{B3.43}$$

$$(\sigma_s)_{SO^-} = (\sigma_s)_{SOH}\ \nu_{SO^-} \qquad \text{B3.44}$$

$$(\sigma_s)_{SOH_2^+ \ldots Cl^-} = (\sigma_s)_{SOH}\ \nu_{SOH_2^+ \ldots Cl^-} \qquad \text{B3.45}$$

$$(\sigma_s)_{SO^-} \ldots Na^+ = (\sigma_s)_{SOH} \ {}^{\nu}{}_{SO^-} \ldots Na^+ \qquad B3.46$$

2.3. Influence of temperature on the αFeOOH-Cl^- aq. interface.

If the relative affinity of H^+ and OH^- ions (i.e., the surface charge density of H^+ and OH^- ions) for an oxyhydroxide surface is independent of temperature, a constant ratio of the concentration of these ions in the solution phase will be observed at the pzc of the oxyhydroxide. For such a temperature independent condition, the pzc of the oxyhydroxide will shift with temperature in the same direction, and in the same relative proportion, as the change in the neutral point of water ($\frac{1}{2}pK_W$). Conversely, if the relative affinity of H^+ and OH^- ions for an oxyhydroxide surface is changing with temperature then a difference will be apparent between the magnitudes of the change in pzc and the change in $\frac{1}{2}pK_W$ with change in temperature.

At equilibrium the electrochemical potentials of H^+ and OH^- ions must be constant throughout the system. Thus, the difference in standard free energy of transferring H^+ and OH^- ions from bulk solution to the interface at the pzc is given by

$$\Delta G^* = [\mu^\circ_{H^+} \text{ (surface)} - \mu^\circ_{H^+} \text{ (solution)}] - [\mu^\circ_{OH^-} \text{ (surface)} - \mu^\circ_{OH^-} \text{ (solution)}] \qquad B3.47$$

From this equation Berube and de Bruyn 1968a have derived the following thermodynamic relation which describes how the pzc, measured as pH_o, depends on temperature

$$2R\ (\tfrac{1}{2}pK_W - pH_o)\ \ell n\ 10 = \frac{\Delta H^*}{T} - \Delta S^* \qquad B3.48$$

According to these authors the quantity ($\frac{1}{2}pK_W - pH_o$) should decrease with temperature. ΔH^* and ΔS^* are the enthalpy and entropy changes accompanying the process

$$SO^- + H_2O + H^+ = SOH_2^+ + OH^- \qquad B3.49$$

i.e., the transfer of 1 mole of H^+ ions from bulk solution to interface and, concomittantly, the transfer of 1 mole of OH^- ions from interface to bulk solution.

In a different approach, the enthalpy and entropy changes accompanying the processes given by equations B3.1, B3.2, B3.10 and B3.11 can be determined from the variation with temperature of the corresponding equilibrium constants, viz., K^{int}_{a+s}, K^{int}_{a-s}, $*K^{int}_{Na^+}$ and $*K^{int}_{Cl^-}$, evaluated from σ_s/pH data by means of the Davis et.al., James et.al., extrapolation procedures.

The enthalpy and entropy changes determined from a study of the variation of pzc with temperature, and those changes determined from a study of the variation of intrinsic equilibrium constants with temperature are made compatible in that

$$\Delta H^* = - \Delta H^\circ_{a+s} - \Delta H^\circ_{a-s} + \Delta H^\circ_{w} \qquad \text{B3.50}$$

and

$$\Delta S^* = - \Delta S^\circ_{a+s} - \Delta S^\circ_{a-s} + \Delta S^\circ_{w} \qquad \text{B3.51}$$

Furthermore, the thermodynamic relationship for equilibrium can also be written as (Blesa et.al.)

$$\Delta G^* = RT\ell n \left(\frac{a_{H^+}}{a_{OH^-}}\right)_{pH_o} \qquad \text{B3.52}$$

3. METHOD.

The pzc of αFeOOH was determined by a salt titration with NaCl (added in the form of a concentrated solution) at each of the following temperatures:- 25°C, 45°C and 65°C. The relative surface charge density ($(\sigma_s)_{REL}$) of αFeOOH/NaCl aq. suspensions was determined (see section 7.), at each of the same three temperatures, from proton adsorption measurements made by potentiometric acid/base titrations conducted within the concentration and pH ranges 1.0 mmol $dm^{-3} \leqslant [NaCl] \leqslant 1.0$ mol dm^{-3} and $4.7 \leqslant pH \leqslant 9.5$, respectively. [Two samples of αFeOOH, prepared in exactly the same manner, were used, designated 'MAY 84' and 'JULY 85', differing only in surface area (surface areas:- 45.11 m^2g^{-1} (MAY 84) and 46.47 m^2g^{-1} (JULY 85)). To ensure complete consistency of available solid surface area within each of the two main experiments, viz., a) temperature dependence of pzc and σ_s and b) σ_s determination at 25°C, the same αFeOOH sample was used throughout a main experiment.]

4. RESULTS

4.1. Determined pzc values.

The pzc of αFeOOH was shifted to lower pH with increasing temperature (Fig. B3.2), and occurred at the following pH_o values

$$(pH_o)_{25°C} = 8.17 \pm 0.02$$

$$(pH_o)_{45°C} = 8.00 \pm 0.02$$

$$(pH_o)_{65°C} = 7.87 \pm 0.02$$

[It was confirmed by salt titration that the two αFeOOH samples had the same pzc at 25°C.] The enthalpy and entropy changes accompanying the transfer of 1 mole of H^+ ions from bulk solution to interface and, concomittantly, the transfer of 1 mole of OH^- ions from interface to bulk solution, as given by eqn. B3.49, had the following values (calculated from a plot of $(\frac{1}{2}pK_W - pH_o)$ versus T^{-1} (Fig. B3.3))

$$\Delta H^* = +23.57 \text{ kJ mol}^{-1}$$

FIGURE B3.2

SALT TITRATION OF ∝FeOOH SHOWN AS THE VARIATION OF pH, AFTER EACH SALT ADDITION, WITH THE RESULTING SALT CONCENTRATION.

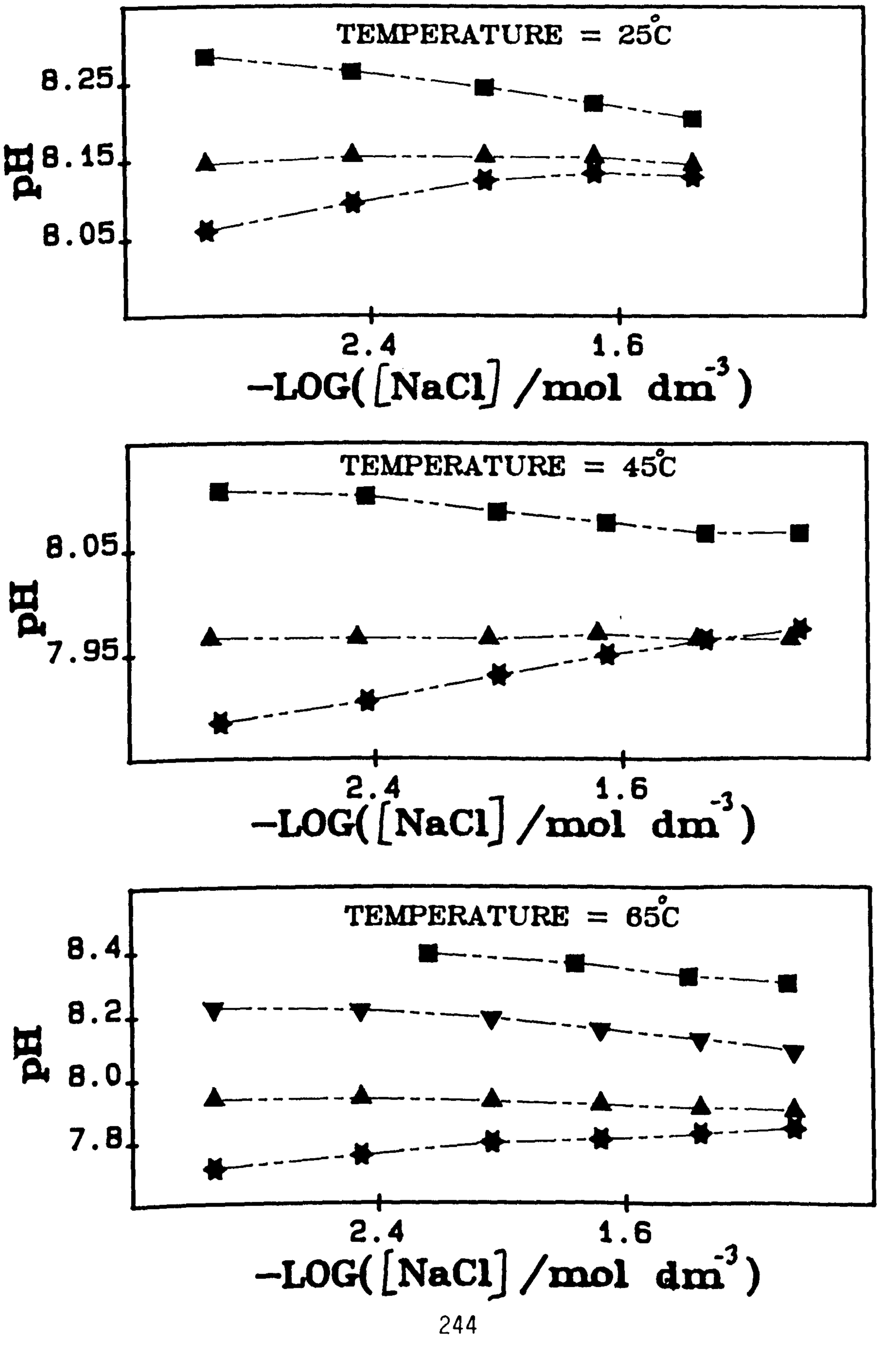

FIGURE B3.3

INFLUENCE OF TEMPERATURE ON THE pH_o OF THE COLLOID $\propto$FeOOH/NaCl aq..

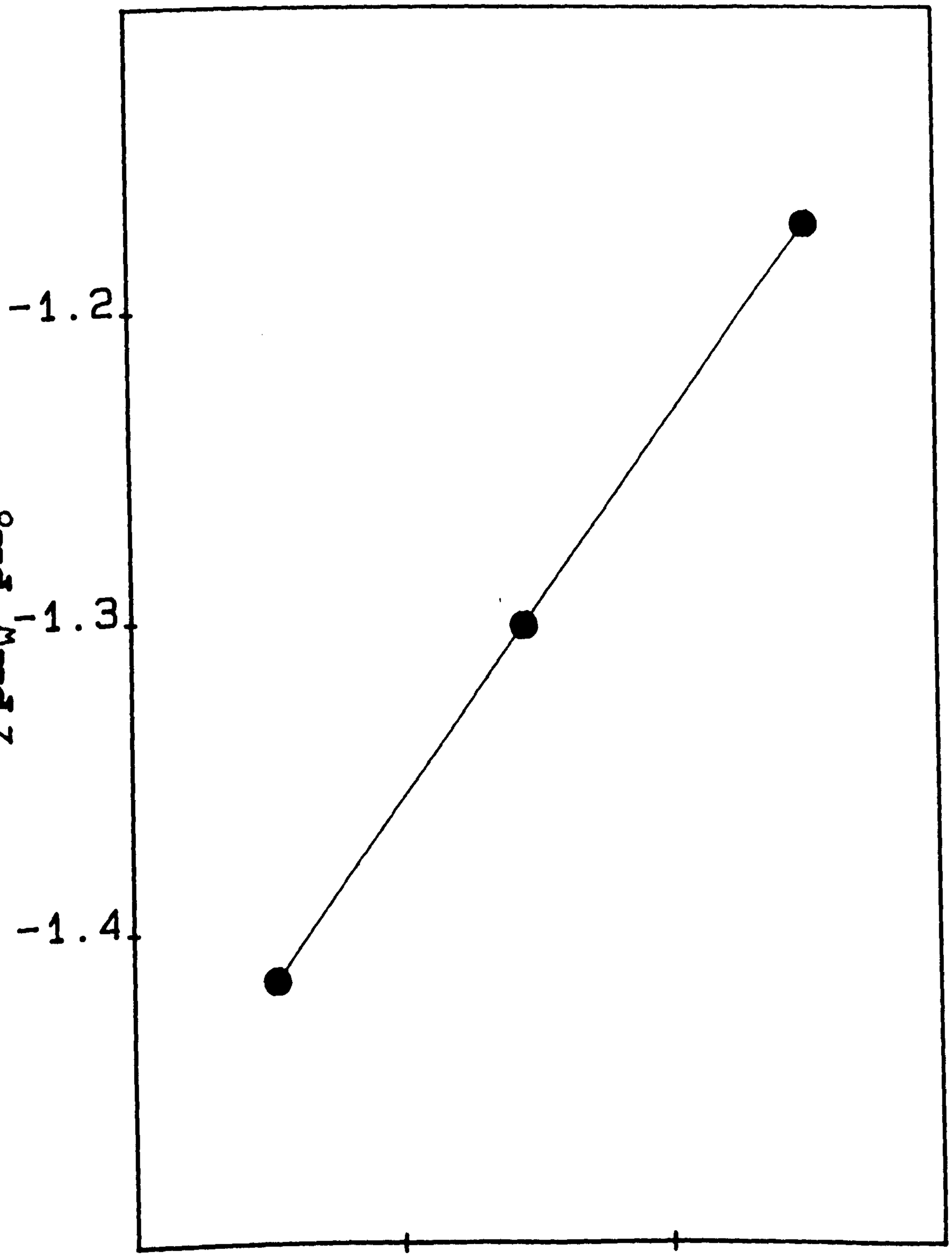

and $\Delta S^* = + 123.93 \text{ J mol}^{-1} \text{ K}^{-1}$

The standard free energy change of the process given by eqn. B3.49 (calculated from $RT \ell n \left(\frac{a_{H^+}}{(a_{OH^-})_{pH_o}}\right)$) became more negative with increasing temperature and diminishing pH_o:

$$(\Delta G^*)_{pH_o} = 8.17(25°C) = -13.38 \text{ kJ mol}^{-1}$$

$$(\Delta G^*)_{pH_o} = 8.00(45°C) = -15.86 \text{ kJ mol}^{-1}$$

$$(\Delta G^*)_{pH_o} = 7.87(65°C) = -18.33 \text{ kJ mol}^{-1}$$

4.2. Determined σ_s values.

All acid/base titrations were reversible, the average deviation between corresponding proton adsorption and desorption pH values being $\pm$ 0.05 pH unit. Noticeably higher deviations, up to $\pm$ 0.08 pH unit, were observed in the experimental domain of high concentration and high temperature. By means of graphical interpolation, all $(\sigma_s)_{REL}$/pH data obtained at a particular temperature (T) was converted to σ_s/pH data (Figs. B3.4 to B3.6) by its normalisation to $\sigma_s = 0$ at $(pH_o)_T$. σ_s at 25°C attained a maximum value of about 150 mC m^{-2} at 1 mol dm^{-3} NaCl aq. and pH 5.

4.3. Evaluated intrinsic equilibrium constants at 25°C; complexation constants evaluated at 1.0 mol dm^{-3} NaCl aq..

Values of the equilibrium and associated constants, viz., pK^{int}_{a+s}, pK^{int}_{a-s}, ΔpK_a, $\overset{\star}{p}K^{int}_{Cl^-}$, $\overset{\star}{p}K^{int}_{Na^+}$, $pK_{complex}$, $K^{int}_{Cl^-}$ and $K^{int}_{Na^+}$, at 25°C (evaluated using the single and double extrapolation procedures (Figs. B3.7 to B3.10)) are given in Table B3.1. The values of pK^{int}_{a+s} and pK^{int}_{a-s} evaluated using the single extrapolation procedure are very similar to the corresponding values evaluated by the double extrapolation procedure. In view of the more exacting nature (i.e., extrapolation to $\alpha_{\pm s} = 0$ and [NaCl] = 0) of the latter procedure it would seem reasonable to suggest that the values of pK^{int}_{a+s} and pK^{int}_{a-s} which best represent the αFeOOH-NaCl aq. interface were those determined by this procedure. The values of $\overset{\star}{p}K^{int}_{Cl^-}$

FIGURE B3.4

SURFACE CHARGE DENSITY OF ∝FeOOH/NaCl aq. INTERFACE AS A FUNCTION OF pH AT VARIOUS CONCENTRATIONS OF NaCl AND AT 25℃.

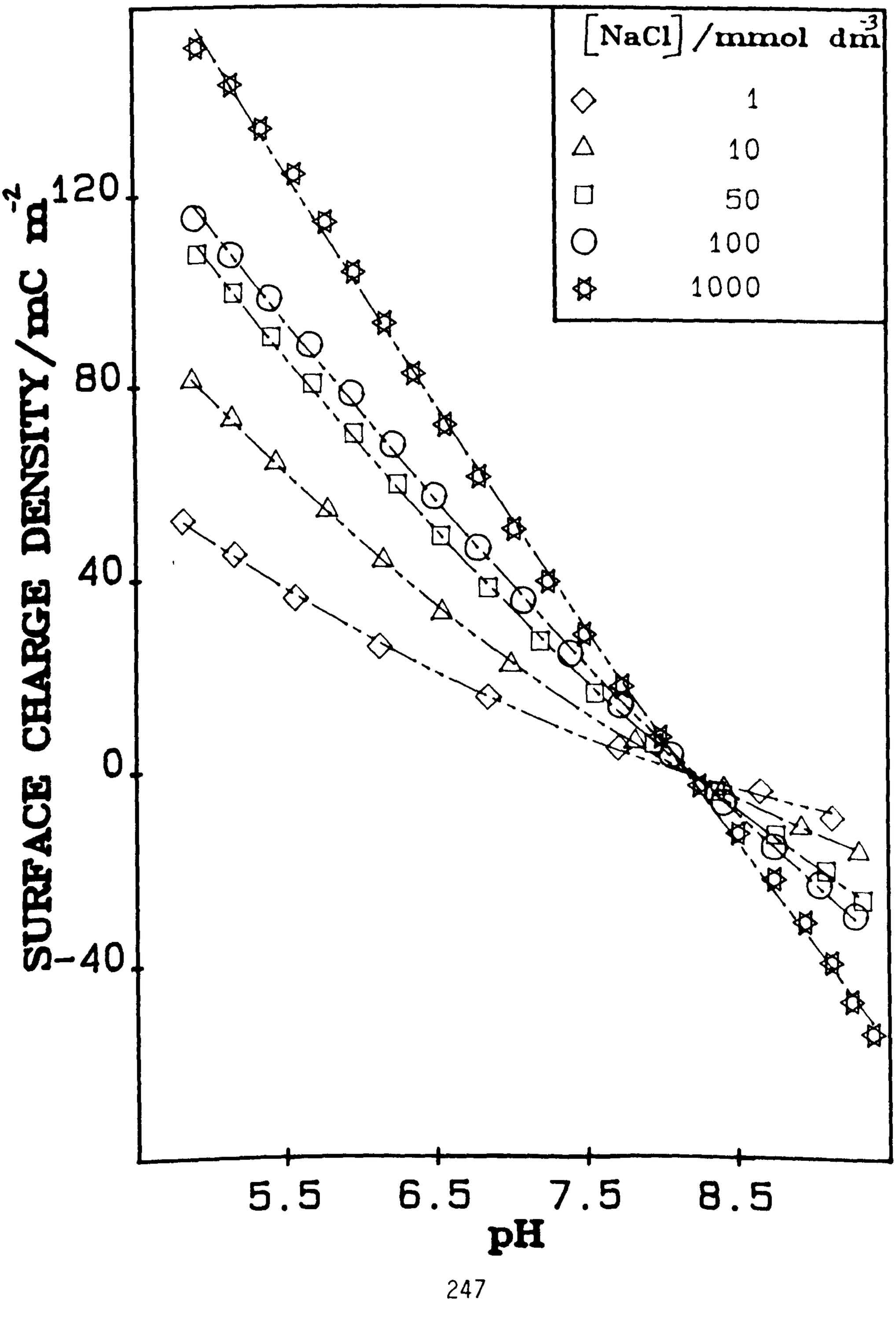

FIGURE B3.5

SURFACE CHARGE DENSITY OF ∝FeOOH/NaCl aq. INTERFACE AS A FUNCTION OF pH AT VARIOUS CONCENTRATIONS OF NaCl AND AT 45°C.

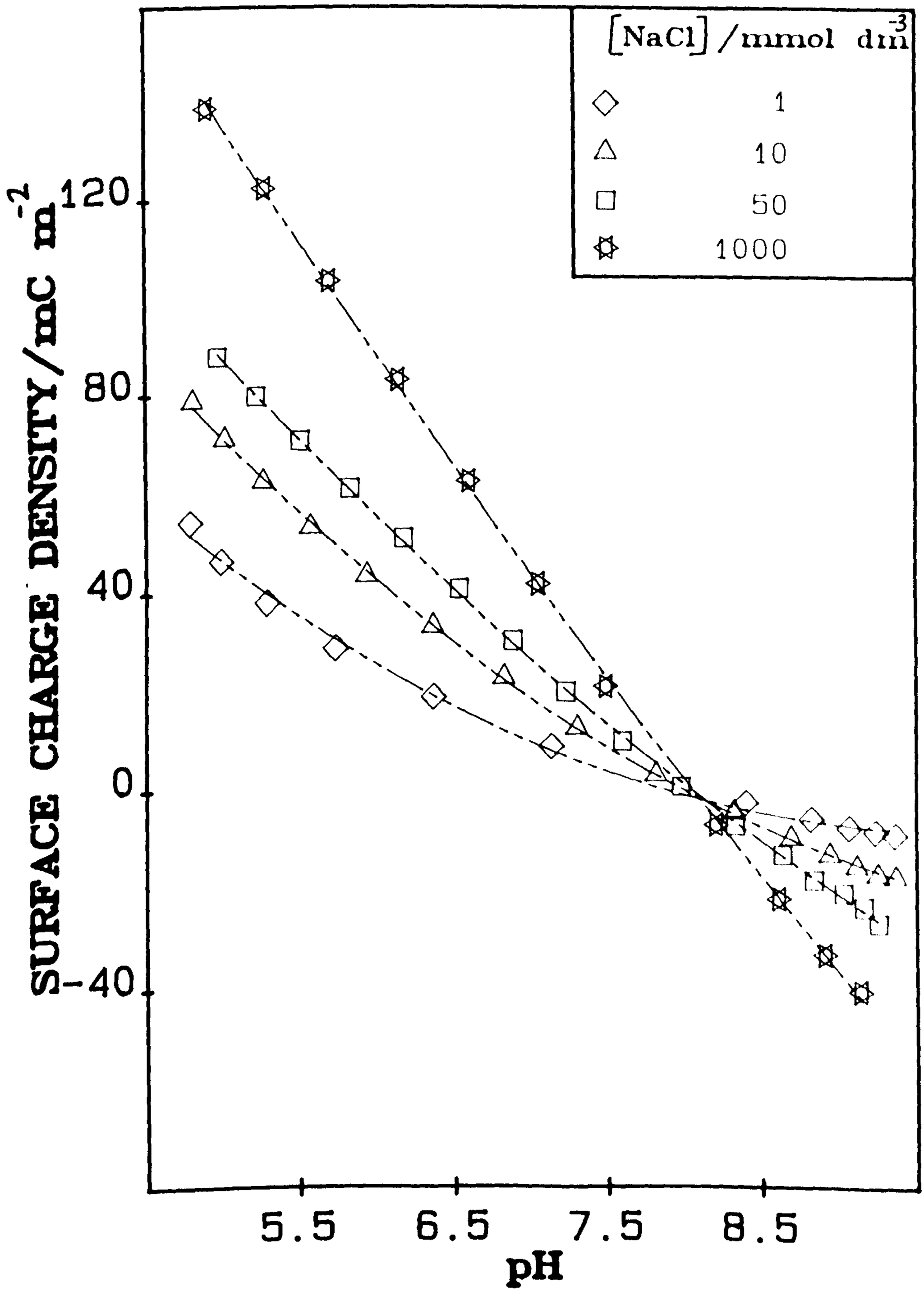

FIGURE B3.6

SURFACE CHARGE DENSITY OF ∝FeOOH/NaCl aq. INTERFACE AS A FUNCTION OF pH AT VARIOUS CONCENTRATIONS OF NaCl AND AT 65°C.

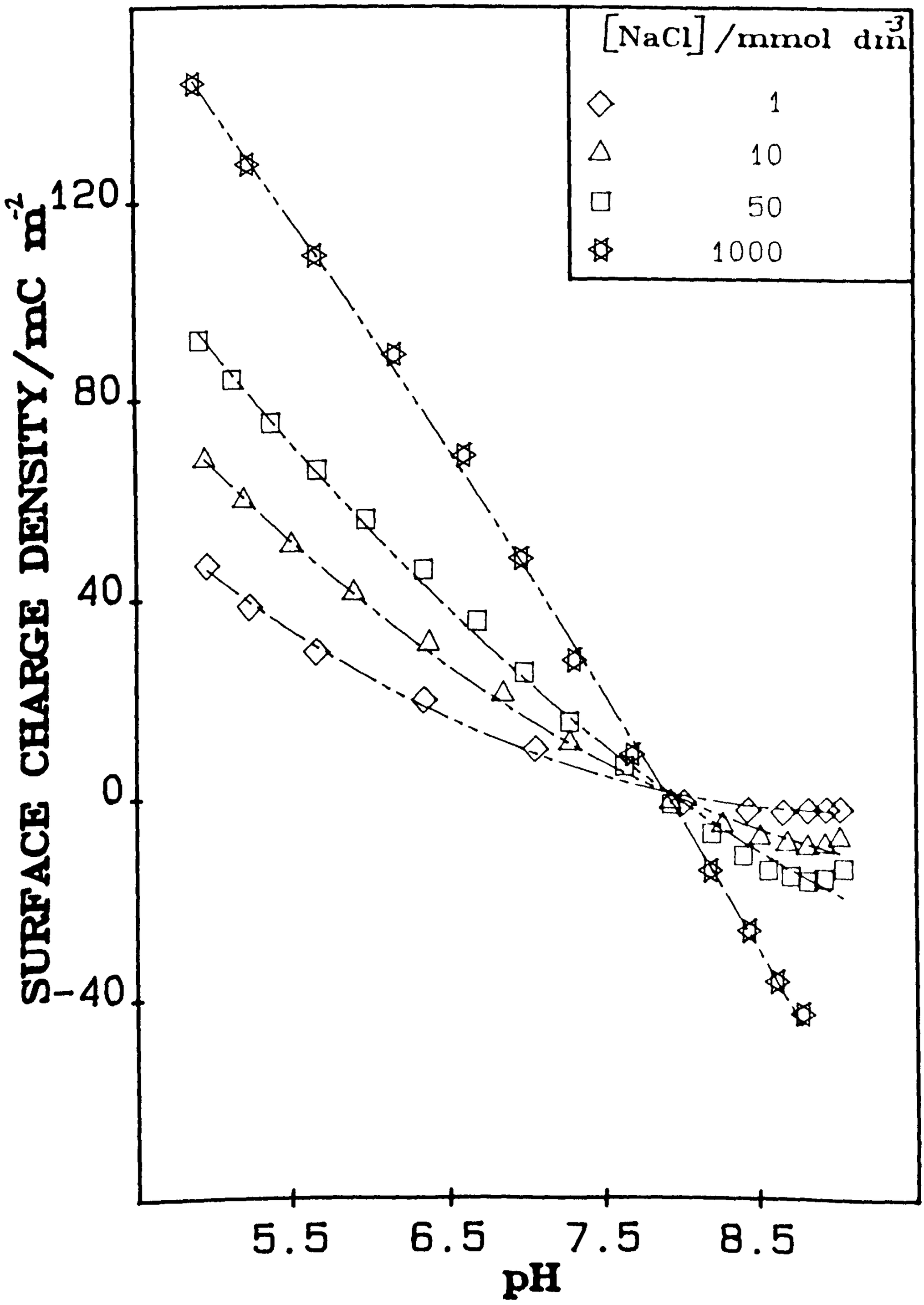

FIGURE B3.7

SINGLE EXTRAPOLATION PLOTS

FOR DETERMINATION OF ∝FeOOH/aq. AMPHOTERIC CONSTANTS.

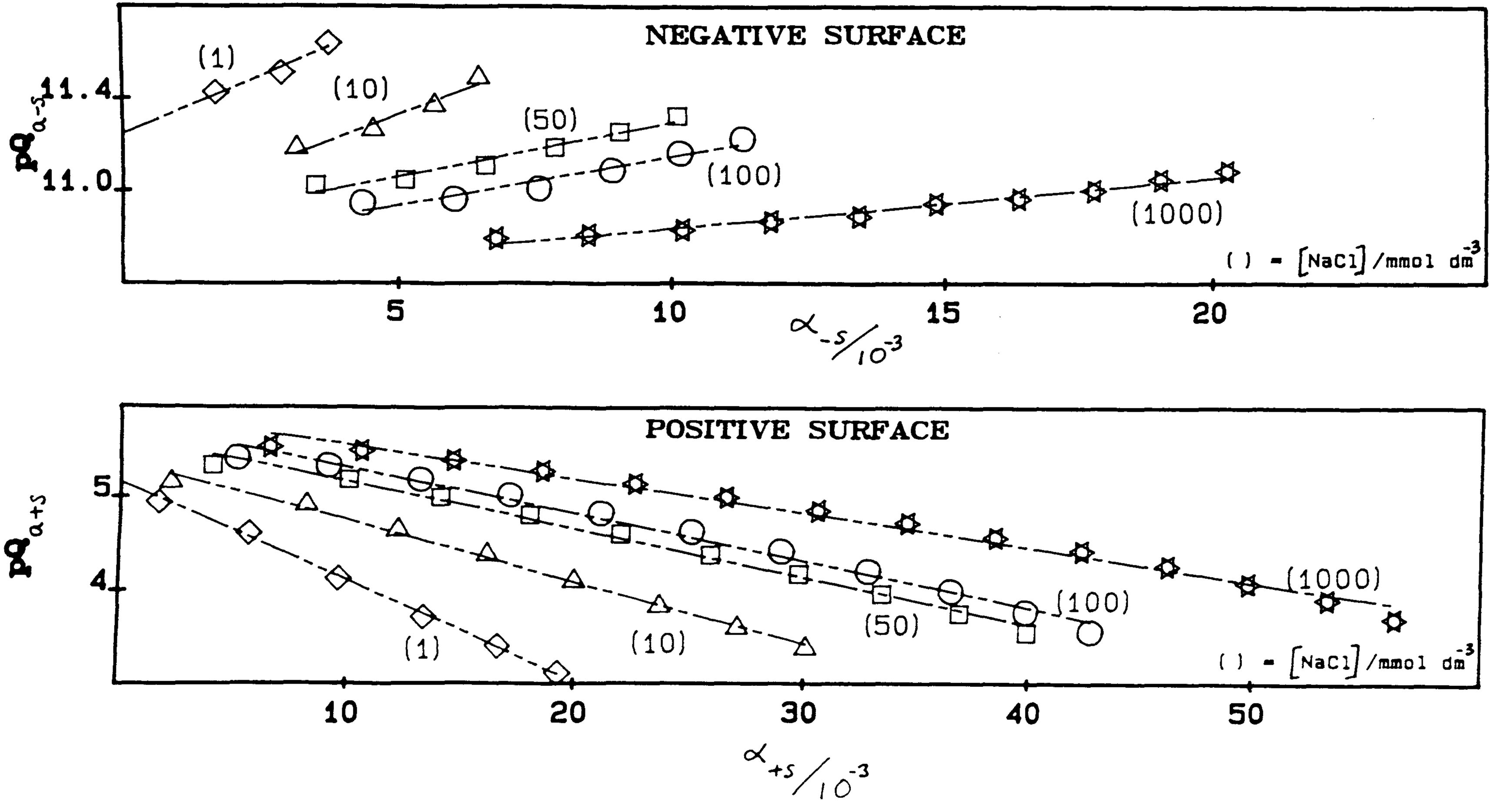

FIGURE B3.8

DOUBLE EXTRAPOLATION PLOTS

FOR DETERMINATION OF ∝FeOOH/aq. AMPHOTERIC CONSTANTS.

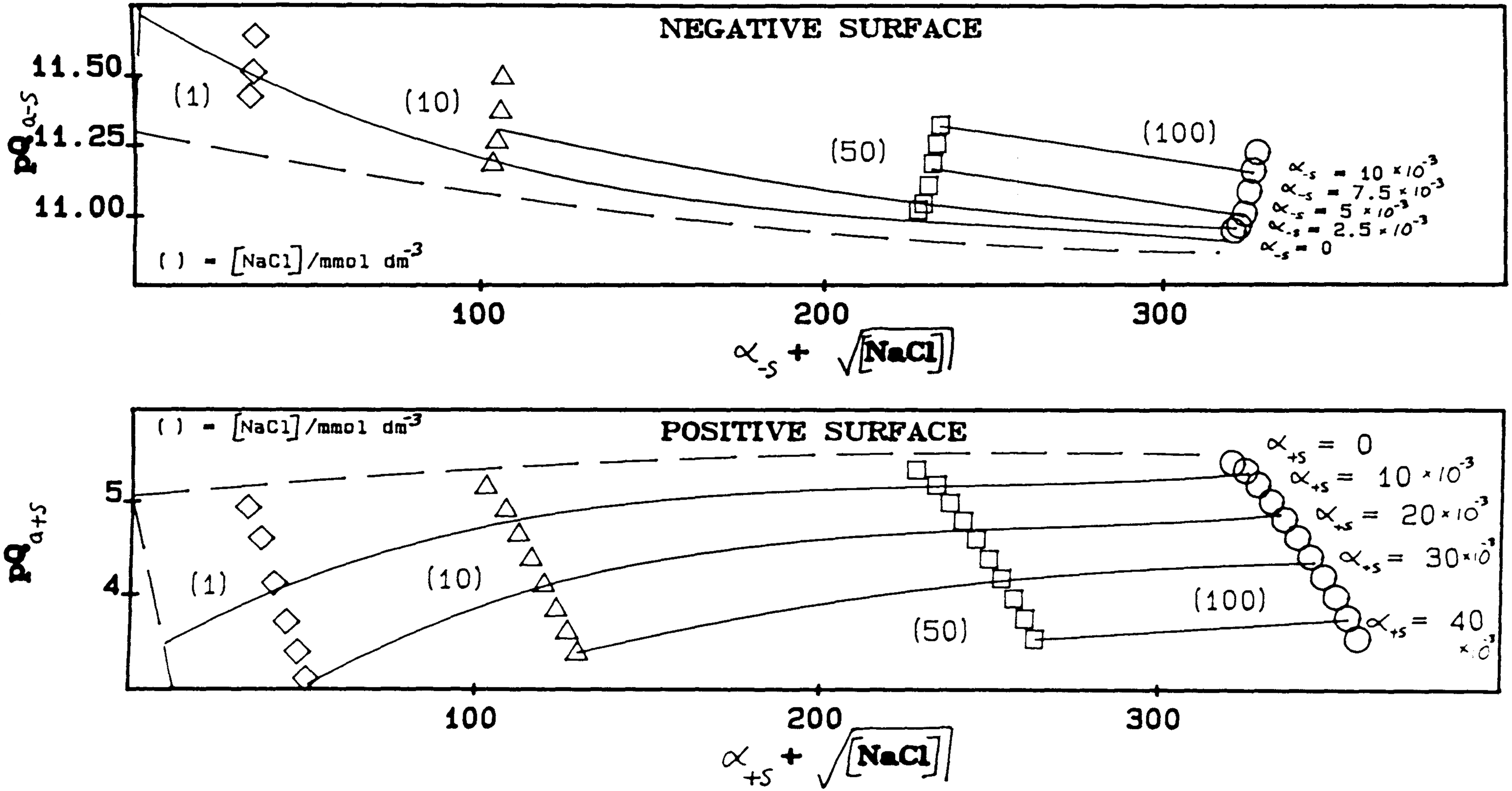

FIGURE B3.9

SINGLE EXTRAPOLATION PLOTS

FOR DETERMINATION OF ∝FeOOH/NaCl aq. COMPLEXATION CONSTANTS.

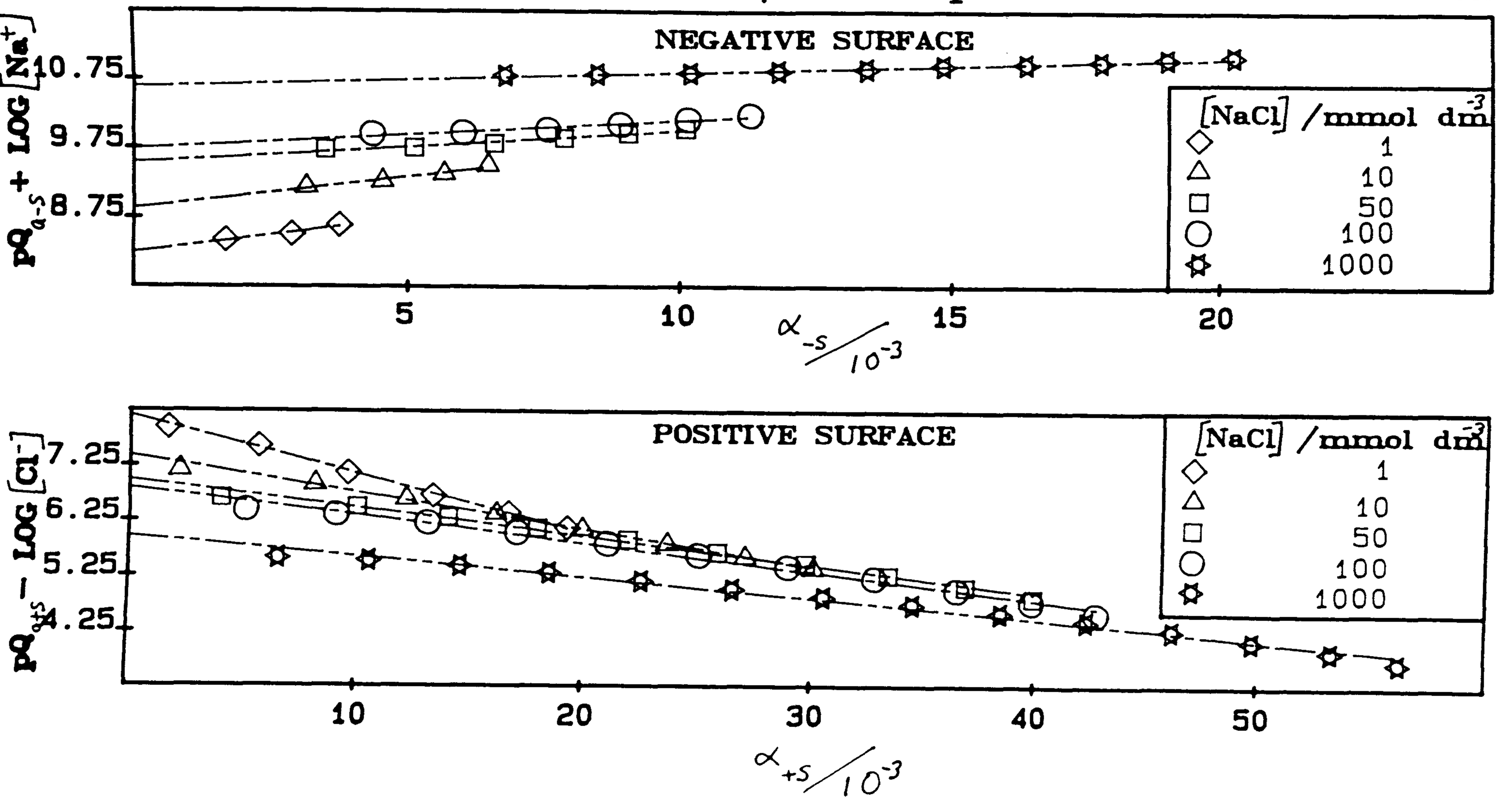

FIGURE B3.10

DOUBLE EXTRAPOLATION PLOTS

FOR DETERMINATION OF ∝FeOOH/NaCl aq. COMPLEXATION CONSTANTS.

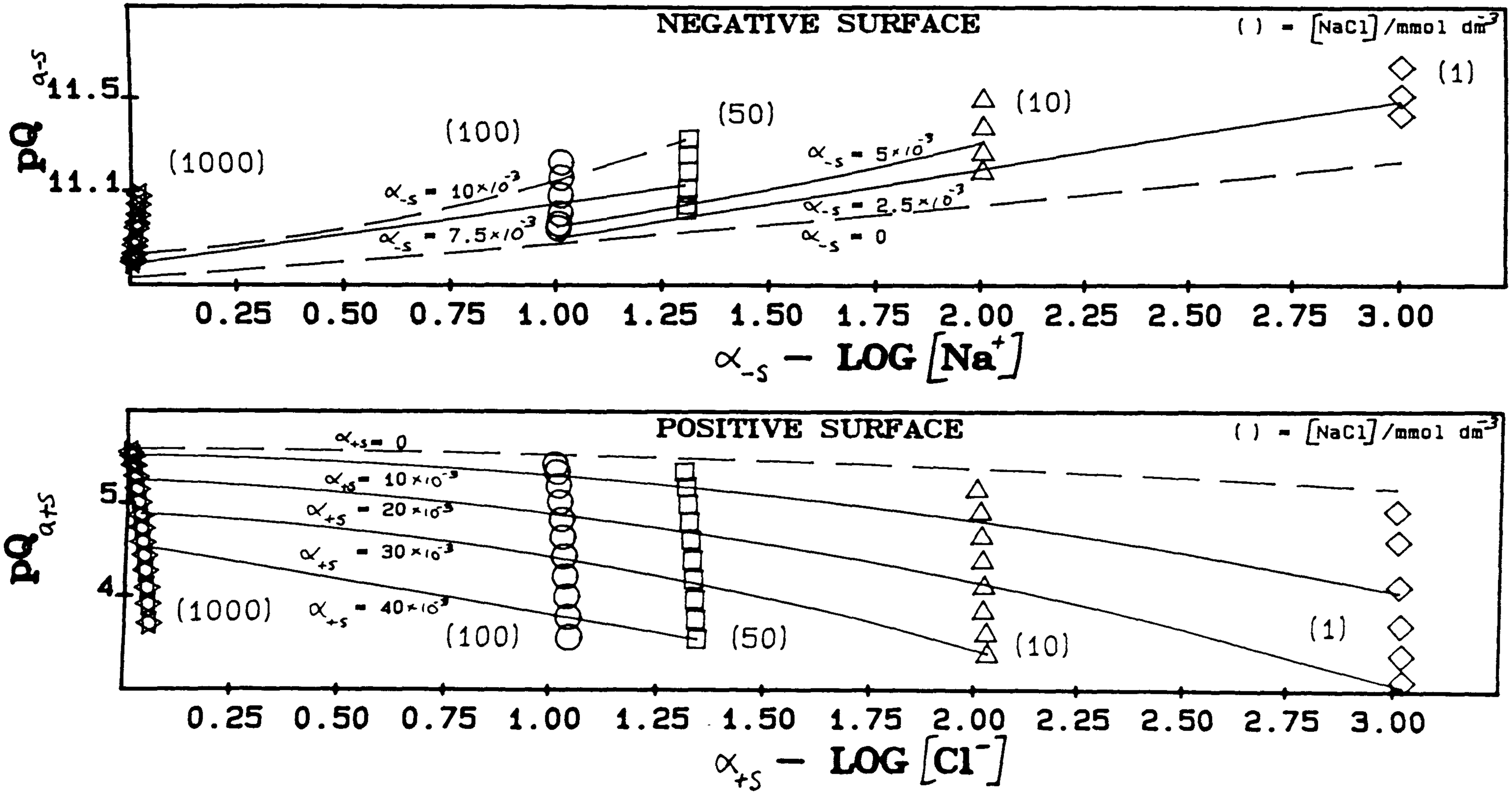

Table B3.1

Intrinsic equilibrium and associated constants at 25°C;
complexation constants evaluated at 1.0 mol dm^{-3} NaCl aq..

Graphical procedure	pK_{a+s}^{int}	pK_{a-s}^{int}	ΔpK_a^{int}	$^{*}pK_{Cl^-}^{int}$	$^{*}pK_{Na^+}^{int}$	$\Delta pK_{COMPLEX}^{int}$	$\frac{K_{Cl^-}^{int}}{mol^{-1}\ dm^3}$	$\frac{K_{Na^+}^{int}}{mol^{-1}\ dm^3}$
single extrapolate	5.155	11.243	6.088	5.954	10.625	4.671	6.295	4.150
double extrapolation	5.040	11.300	6.260	5.600	10.760	5.140	3.631	3.631

(αFeOOH sample:- MAY84)

and $^{*}pK^{int}_{Na^+}$ evaluated using the double extrapolation procedure are significantly different from the corresponding values evaluated by the single extrapolation procedure; the value of $\Delta pK_{complex}$ being (approximately) 5.1 and 4.7 for the double and single extrapolated constants, respectively. In the single extrapolation procedure a straight line was drawn to $\alpha_{\pm s} = 0$ from those data points which covered both the largest $\alpha_{\pm s}$ range and gave rise to the highest correlation coefficient. Such data points usually covered the highest $\alpha_{\pm s}$ range studied, at which ion-pair formation would be expected to be prevelant. Thus, single extrapolation usually gave rise to an equilibrium constant whose value reflected the influence of ion-pair formation on σ_s. Conversely, the double extrapolation procedure emphasised those data points at low $\alpha_{\pm s}$, at which ion-pair formation would be expected to be negligible. Therefore, it would seem reasonable to suggest that the value of $^{*}pK^{int}_{Cl^-}$ and $^{*}pK^{int}_{Na^+}$ which best represent ion-pair formation at the αFeOOH-NaCl aq. interface were those determined by the single extrapolation procedure. The amphoteric and complexation constants (evaluated from 1.0 mol dm^{-3} NaCl aq. σ_s/pH data) which are considered to best represent, respectively, simple ionisation and complexation reactions at the αFeOOH-NaCl aq. interface (designated, best-fit/1.0 mol dm^{-3} constants) are given, with their associated constants, in the first row of Table B3.2.

4.4. Modelled values of the interfacial quantities at 25°C; complexation constants evaluated at 1.0 mol dm^{-3} NaCl aq..

The variation of the interfacial charges, potentials and surface charge densities, viz., σ_{IHP}, σ_{OHP}, ψ_s, ψ_{IHP}, ψ_{OHP}, $(\sigma_s)_{SOH}$, $(\sigma_s)_{SOH_2^+}$, $(\sigma_s)_{SO^-}$, $(\sigma_s)_{SOH_2^+}$ ....Cl^-, $(\sigma_s)_{SO^-}$ .... Na^+, with pH at 25°C (Calculated from the σ_s/pH data and the 'best-fit/1.0 mol dm^{-3}' equilibrium constants, using the set of equations and the iteration procedure) are shown, at five NaCl concentrations, in Figs. B3.11 to B3.19. [In the modelling of interfacial charges, potentials and surface charge densities the value of 0.2 Fm^{-2} was used for K_2^{CAP}, since this is a reasonable value for the compact layer capacitance on Hg and AgI (Lyklema and Overbeek, Stumm et.al. 1970) and provides qualitative agreement between the potential at the OHP (ψ_{OHP}) and measured ζ (Yates et.al.).] The maximum modelled value of σ_{IHP} was about -146mC m^{-2}, at 1 mol dm^{-3} NaCl aq. and pH 5. For a given concentration and pH, the modelled value of $|\sigma_{IHP}|$ was in excess of 90% of σ_s while the modelled value of $|\sigma_{OHP}|$ was less than 10%

FIGURE B3.11

CHARGE DENSITY OF αFeOOH/NaCl aq. INTERFACE AS A FUNCTION OF pH AT 25°C.

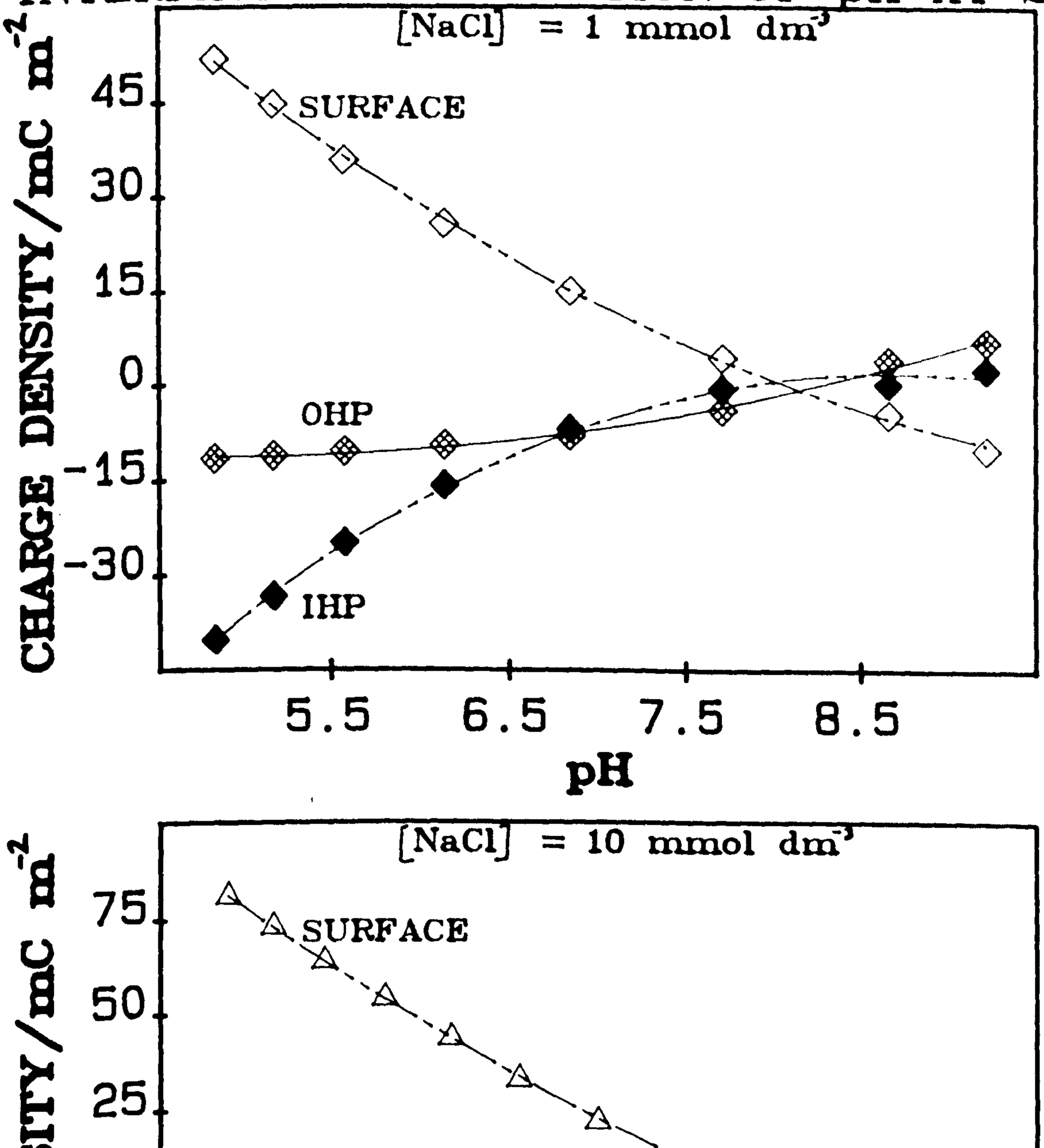

FIGURE B3.12

CHARGE DENSITY OF ∝FeOOH/NaCl aq. INTERFACE AS A FUNCTION OF pH AT 25°C.

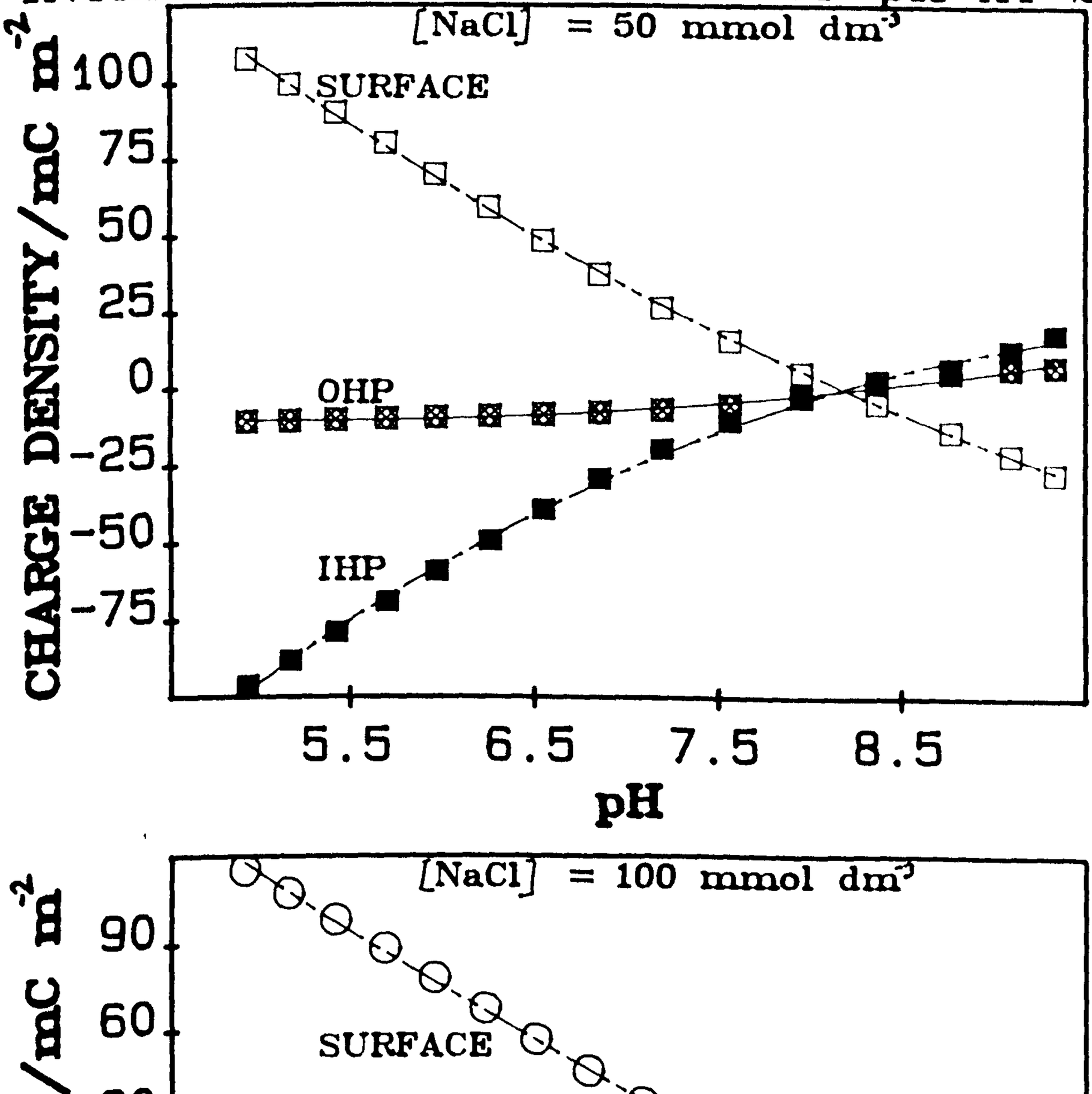

FIGURE B3.13

CHARGE DENSITY OF ∝FeOOH/NaCl aq. INTERFACE AS A FUNCTION OF pH AT 25°C.

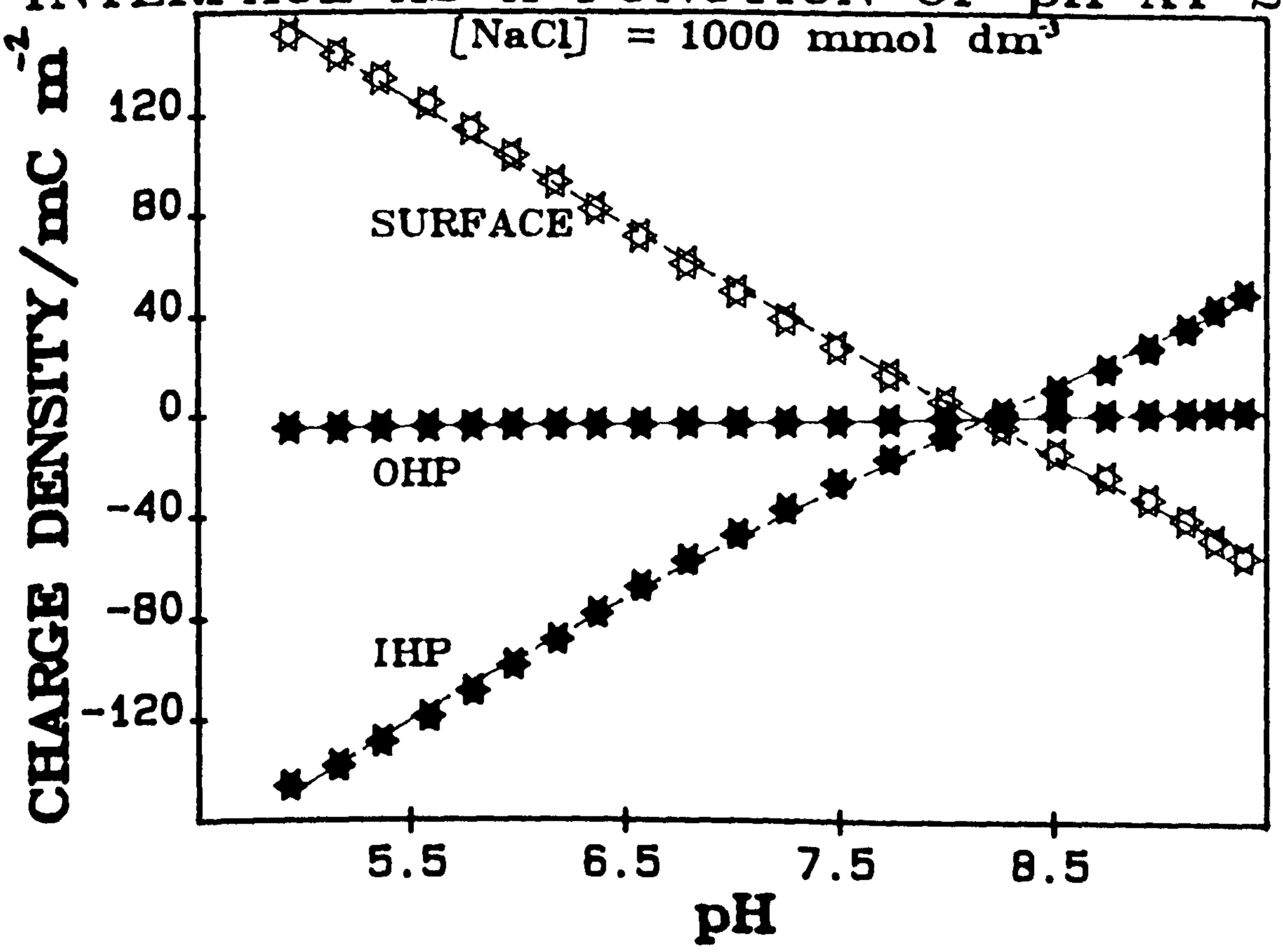

FIGURE B3.14

POTENTIAL OF ∝FeOOH/NaCl aq. INTERFACE AS A FUNCTION OF pH AT 25°C.

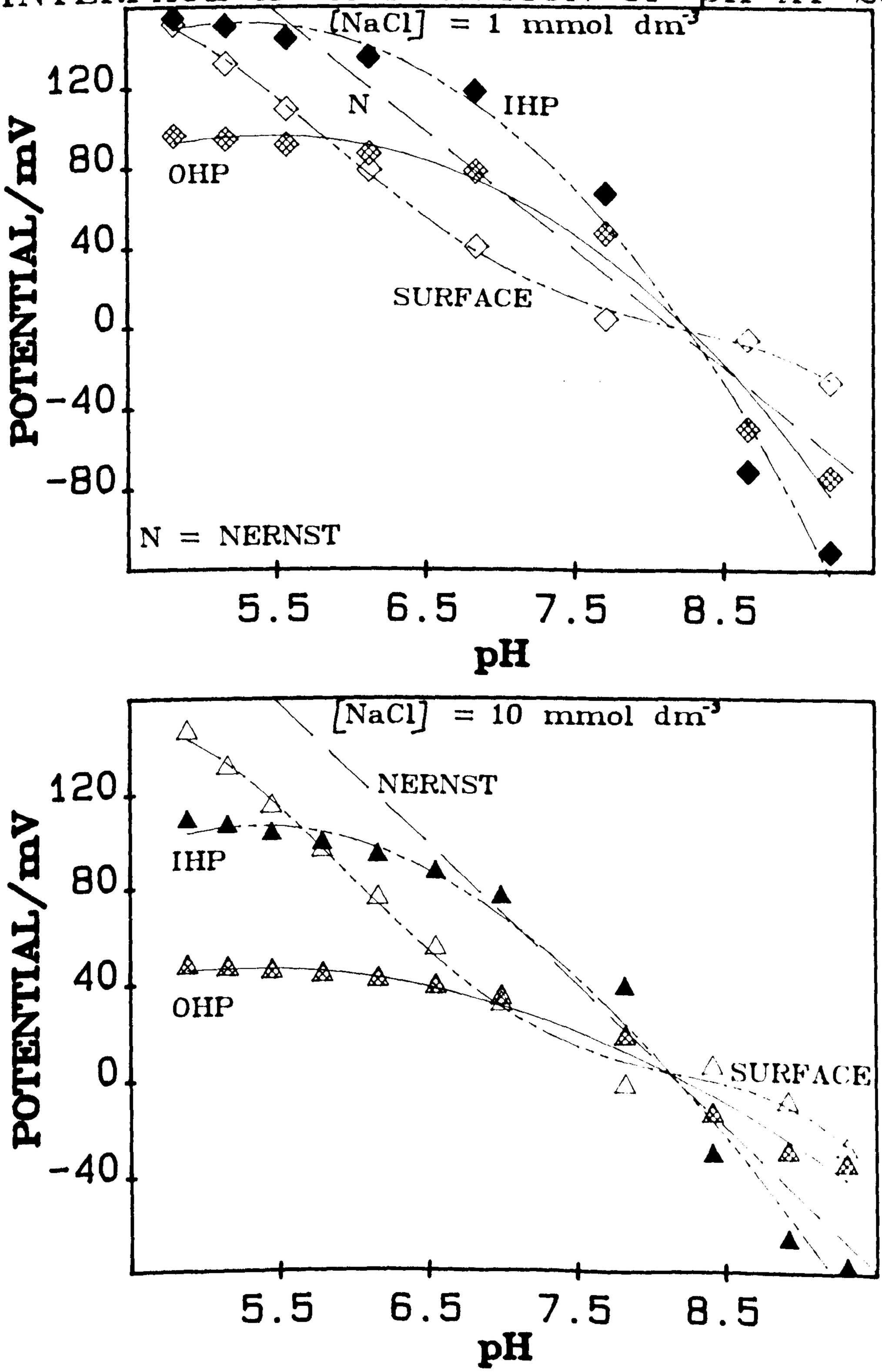

FIGURE B3.15

POTENTIAL OF αFeOOH/NaCl aq. INTERFACE AS A FUNCTION OF pH AT 25°C.

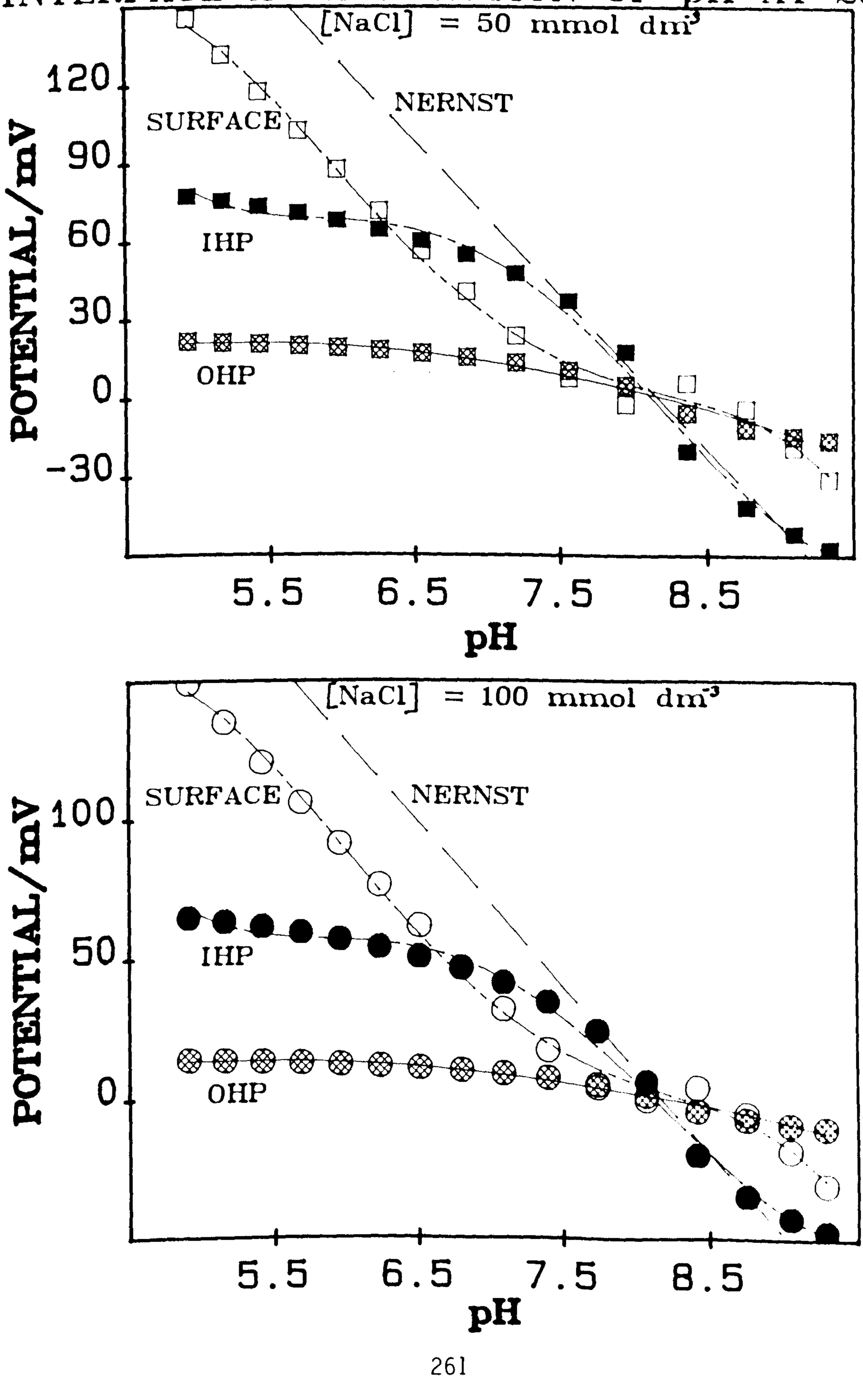

FIGURE B3.16

POTENTIAL OF ∝FeOOH/NaCl aq. INTERFACE AS A FUNCTION OF pH AT 25°C.

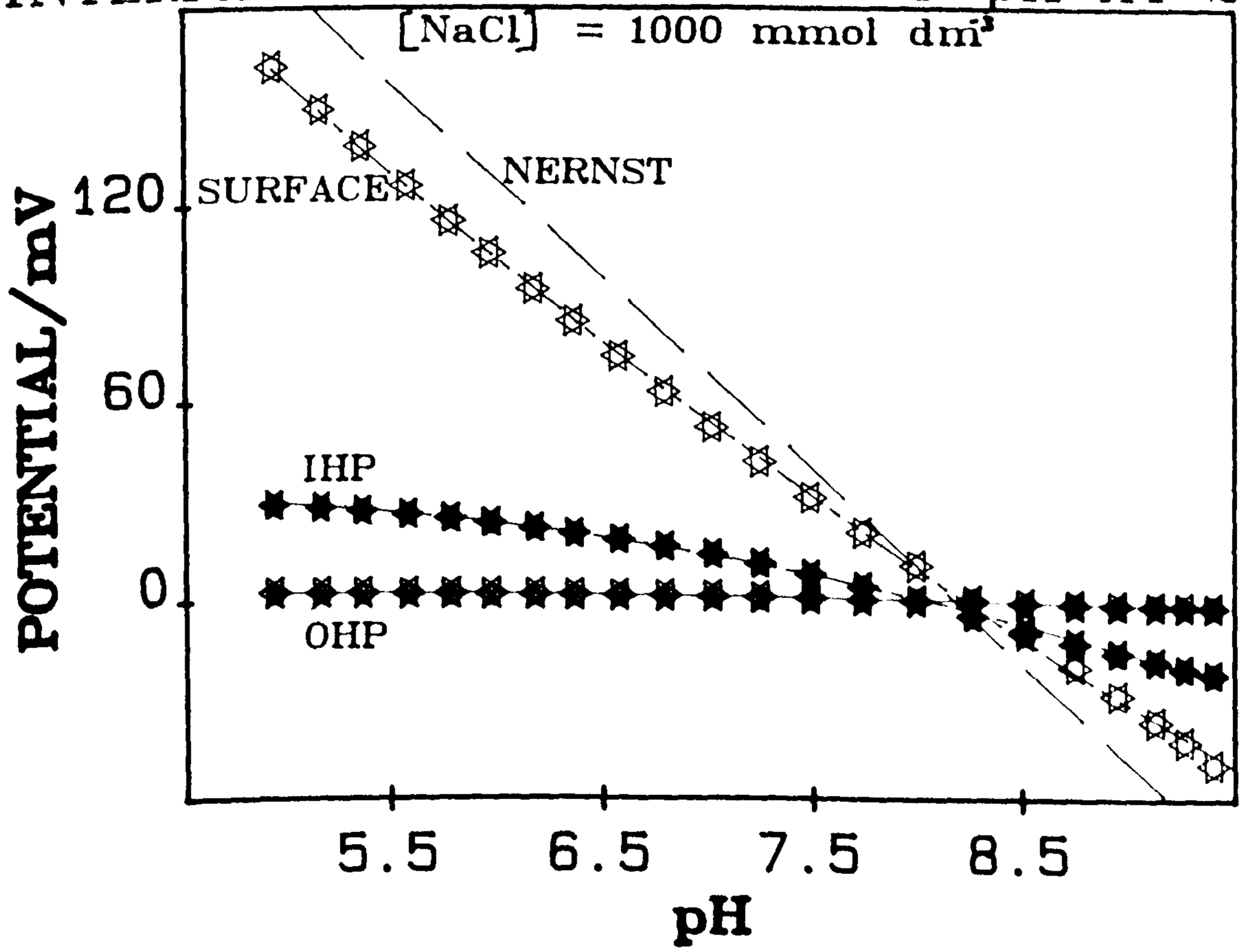

FIGURE B3.17

SURFACE CHARGE DENSITY OF ∝FeOOH/NaCl aq. INTERFACE AS A FUNCTION OF pH AT 25°C.

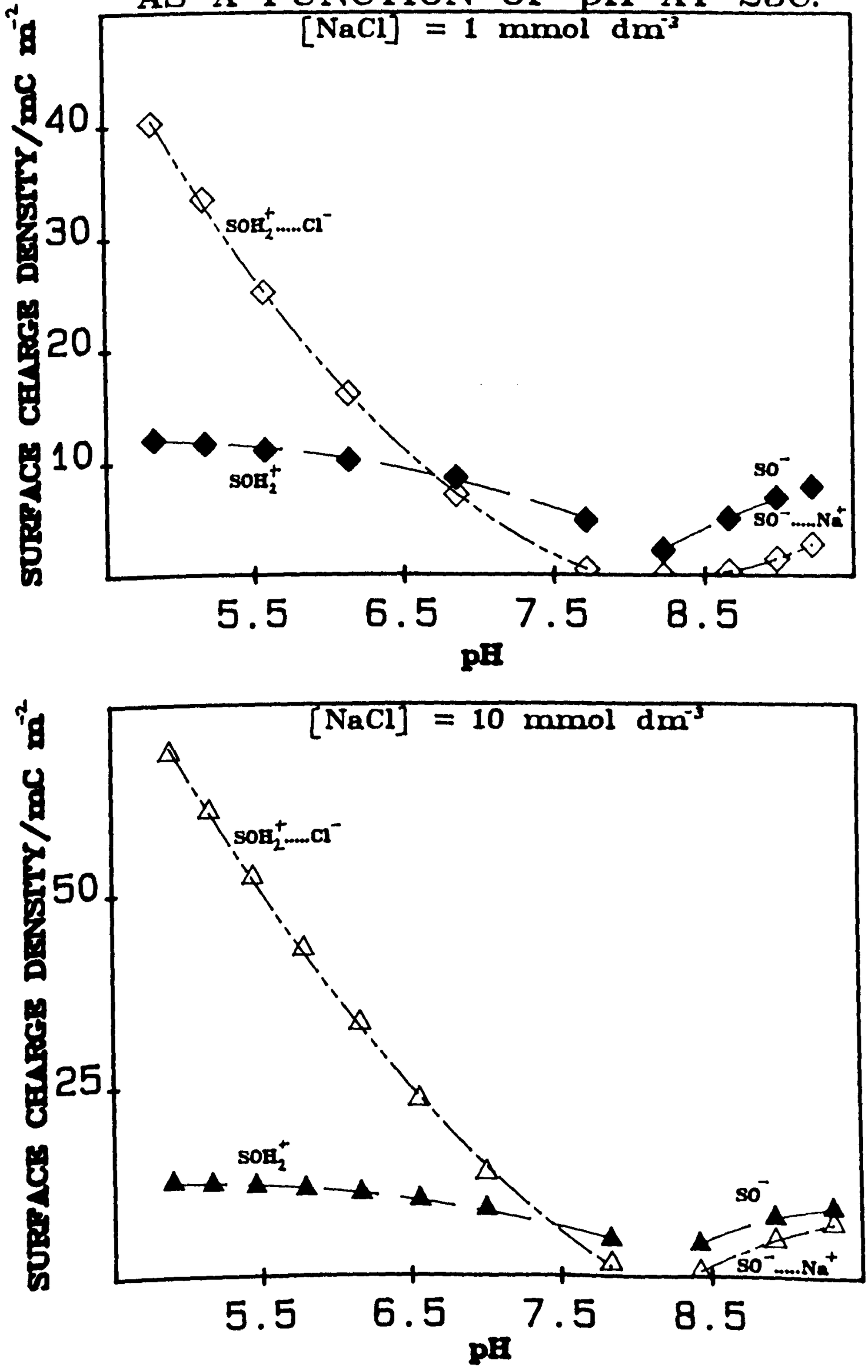

FIGURE B3.18

SURFACE CHARGE DENSITY OF ∝FeOOH/NaCl aq. INTERFACE AS A FUNCTION OF pH AT 25°C.

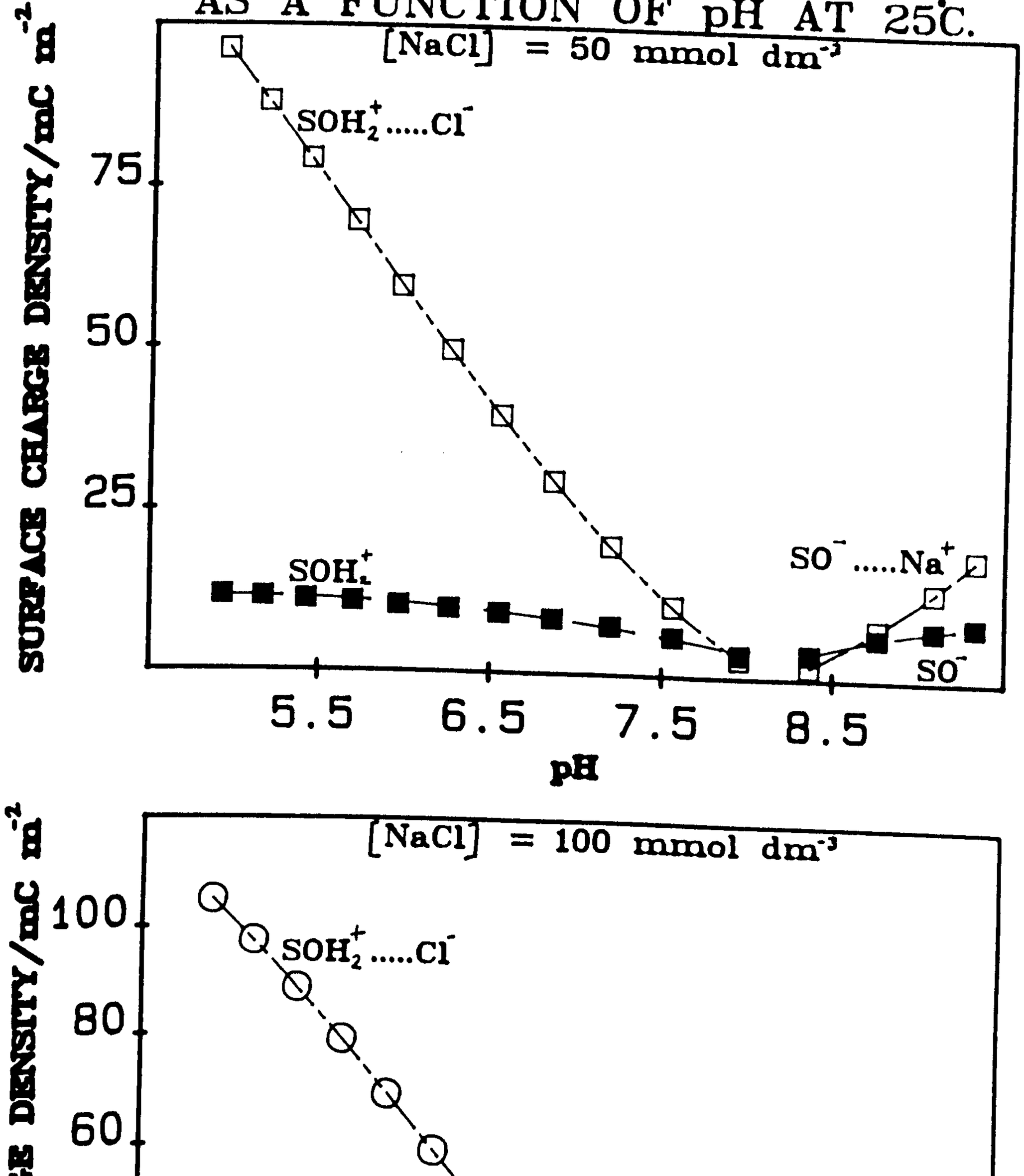

FIGURE B3.19

SURFACE CHARGE DENSITY OF ∝FeOOH/NaCl aq. INTERFACE AS A FUNCTION OF pH AT 25°C.

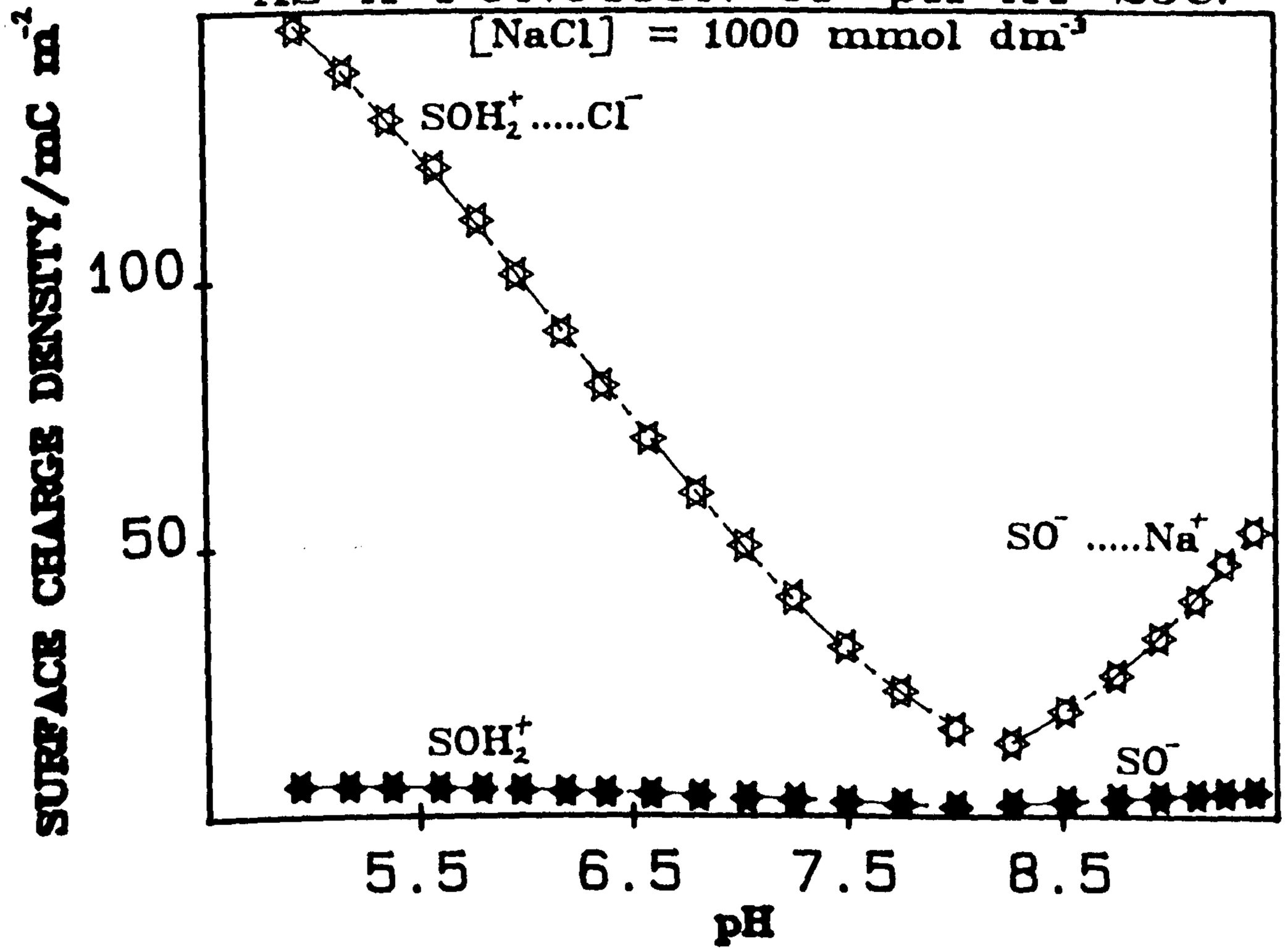

of σ_s. For a given concentration and pH the modelled value of ψ_s was less than $(\psi_s)_N$, and this difference increased with diminishing [NaCl]. Within two pH units of pH_o the values of ψ_{IHP} and ψ_{OHP}, modelled from low concentration σ_s/pH data, were unusually high such that $\psi_{IHP} > \psi_s$ and $\psi_{OHP} > \psi_s$; correspondingly, K_1^{CAP} was negative. This situation is physically unrealistic for ions such as Cl^- and Na^+, and is in contradiction with the determined/modelled, and expected, relative magnitudes of the interfacial charges, these being

$$\sigma_s > |\sigma_{IHP}| > |\sigma_{OHP}|$$

4.5. Evaluated intrinsic equilibrium constants at 25°C; complexation constants evaluated at each [NaCl].

At $\alpha_{\pm s} < 0.05$ the function $pQ_{a\pm s} \mp \log$ [NaCl] was dependent on [NaCl]. Indeed, it was possible to extrapolate (single) a $^{*}pK_{Ion}^{int}$ value for each value of [NaCl] at low $\alpha_{\pm s}$. Values of the complexation constants evaluated from such multi-extrapolation, and the amphoteric and corresponding associated constants, are given in the second and subsequent rows of Table B3.2. The values of the constants appearing in either the second or a subsequent row of this table constitute a group and are designated 'best-fit/[NaCl]'. Values of the intrinsic equilibrium and associated constants determined at 0.1 mol dm^{-3} are compared with the corresponding values obtained by other workers, who determined surface complexation constant values at this concentration, in Table B3.3.

4.6. Modelled values of the interfacial quantities at 25°C; complexation constants evaluated at each [NaCl].

For a given pH, the magnitudes of the interfacial charges, surface charge densities and ψ_s (at a particular [NaCl]) modelled using the appropriate group of 'best-fit/[NaCl]' constants were not significantly different from the corresponding magnitudes modelled using the 'best-fit/1.0 mol dm^{-3}' constants; interestingly, ψ_s modelled using these latter values approached $(\psi_s)_N$ with decreasing [NaCl]. However, for a given pH and [NaCl], the relative magnitudes of the interfacial potentials modelled using the appropriate group of 'best-fit/[NaCl]' constants conformed to physical reality and mirrored the relative magnitudes of the interfacial

Table B3.3

Comparison of the evaluated (at 0.1 mol dm^{-3} NaCl aq.) intrinsic equilibrium and associated constants with those values determined by other workers for the αFeOOH/NaCl aq. interface and similar interfaces.

Interface	Reference	pK^{int}_{a+s}	pK^{int}_{a-s}	ΔpK^{int}_{a}	$^{\star}pK^{int}_{Cl^-}$	$pK^{int}_{Na^+}$	$\Delta pK^{int}_{COMPLEX}$	$\frac{K^{int}_{Cl^-}}{mol^{-1}\ dm^3}$	$\frac{K^{int}_{Na^+}}{mol^{-1}\ dm^3}$
αFeOOH/NaCl aq.	This work	5.04	11.30	6.26	6.84	9.73	2.89	63.4	37.3
αFeOOH/NaCl aq.	Hingston et.al.	4.9	b	-	6.6	b	-	50.1	b
αFeOOH/KNO_3 aq.	Yates D.E.	4.2	10.8	6.6	6.1	8.9	2.8	79.4	79.4
$Fe(OH)_3$/$NaNO_3$ aq.	Davis	5.1	10.7	5.6	6.9	9.0	2.1	50.1	63.1
Fe_3O_4/KNO_3 aq.	Regazzoni et.al.	4.4	9.0	4.6	6.2	7.2	1.0	63.1	63.1

b = not determined

charges, in that

$$\psi_s > \psi_{IHP} > \psi_{OHP}$$

and

$$K_1^{CAP} > 0$$

The variation of the interfacial potentials and K_1^{CAP} (modelled from σ_s/pH data and the appropriate group of 'best-fit/[NaCl]' constants) with pH at 25°C, and at a particular [NaCl], are shown in Figs. B3.16, and B3.20 to B3.22.

4.7. Evaluated positive surface intrinsic equilibrium constants, from 25°C to 65°C, and thermodynamic data.

Values of the positive surface intrinsic equilibrium constants, viz., pK_{a+s}^{int}, $^{*}pK_{Cl^-}^{int}$ and $K_{Cl^-}^{int}$, from 25°C to 65°C (evaluated using the single extrapolation procedure for $^{*}pK_{Cl^-}^{int}$, and double extrapolation procedure for, pK_{a+s}^{int}) are given in Table B3.4. The corresponding enthalpy, entropy and free energy changes (calculated from, respectively, a plot of ℓnK versus T^{-1} (Fig. B3.23), and the relationships $\frac{\Delta H^\circ}{T} + R\ell nK$ and $\Delta H^\circ - T\Delta S^\circ$) are given in Table B3.5. In the experimental domain of low concentration, high temperature and pH > pH_σ, σ_s varied inconsistently with pH.

5. CONCLUSIONS

5.1. σ_s at 25°C.

a) The observed increase of σ_s with increasing [NaCl] indicates that both Na^+ and Cl^- ions are, in addition to the potential determining ions, contributing to σ_s.

b) The observed steady increase of σ_s over the entire pH range studied, even at the highest [NaCl], would indicate that the situation in which all available surface hydroxyl groups are charged is not attained at the pH extrememma. Indeed, the maximum determined value of σ_s was only 5.6% of that theoretically possible, i.e., the σ_s that would be generated by the protonation of every available surface hydroxyl group, while the

FIGURE B3.20

POTENTIAL OF ∝FeOOH/NaCl aq. INTERFACE AS A FUNCTION OF pH AT 25°C.

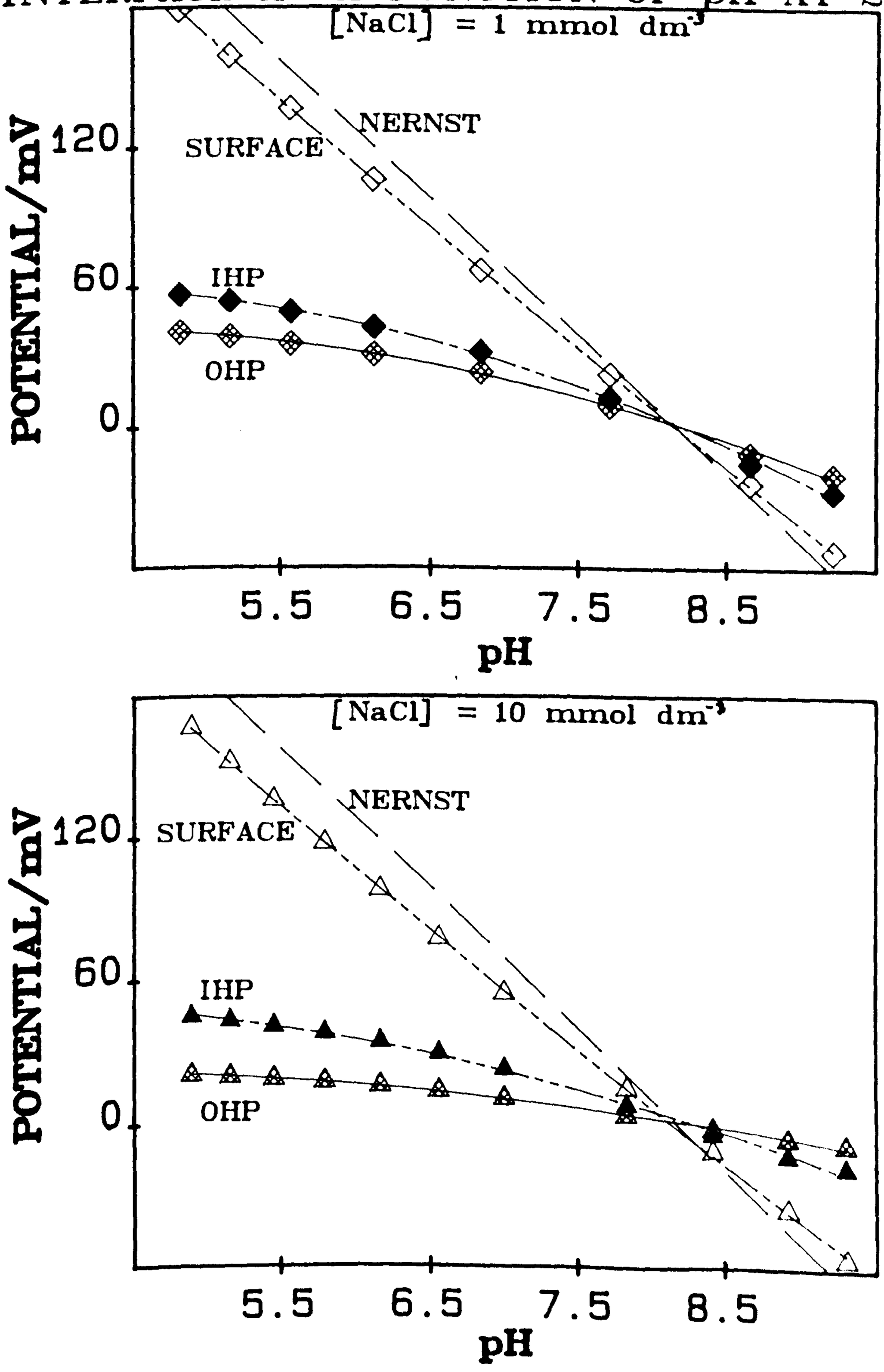

FIGURE B3.21

POTENTIAL OF ∝FeOOH/NaCl aq. INTERFACE AS A FUNCTION OF pH AT 25°C.

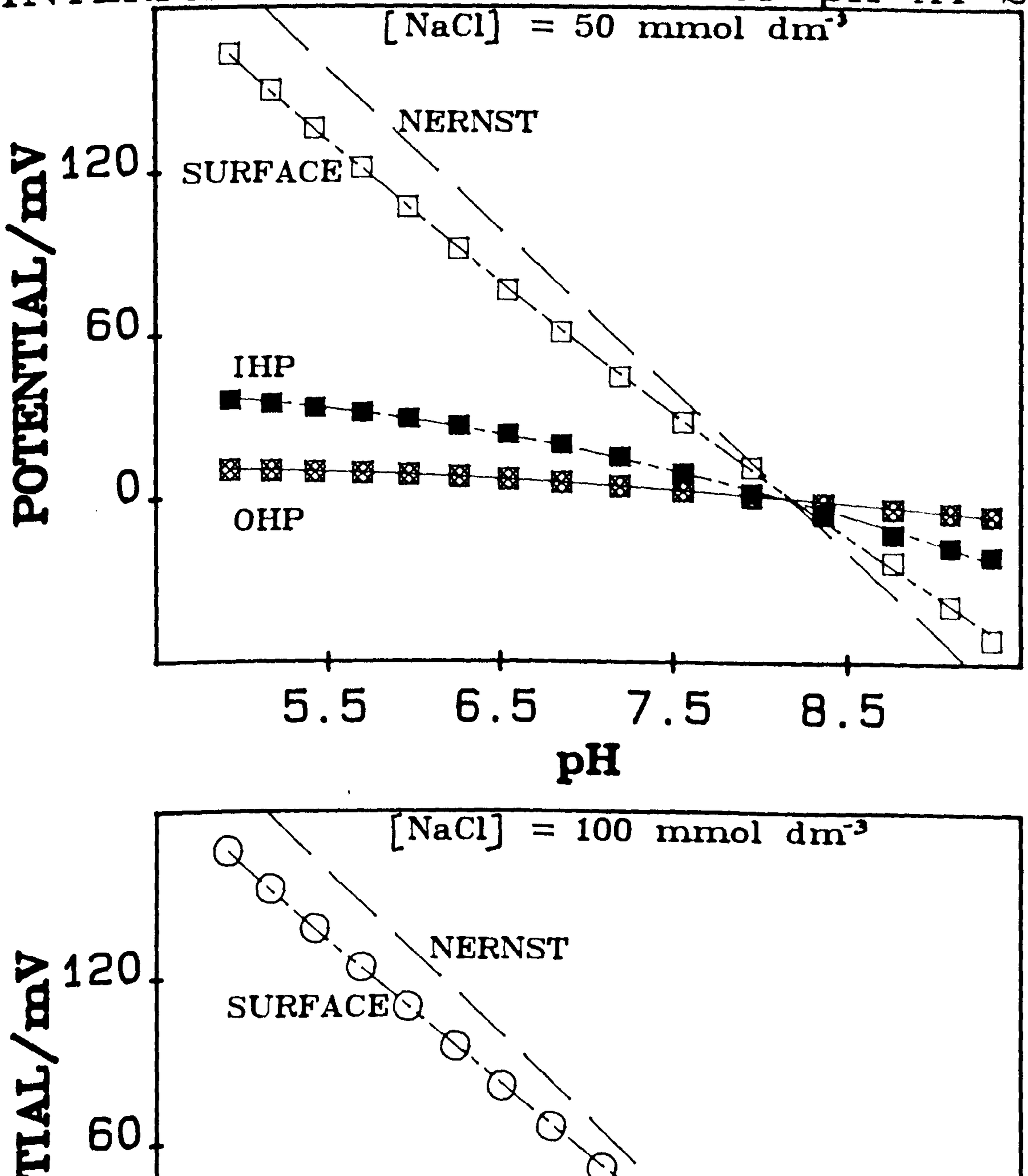

FIGURE B3.22

INTEGRAL CAPACITY OF INNER ZONE OF COMPACT REGION OF ∝FeOOH/NaCl aq. INTERFACE AS A FUNCTION OF pH AT VARIOUS CONCENTRATIONS OF NaCl AND AT 25°C.

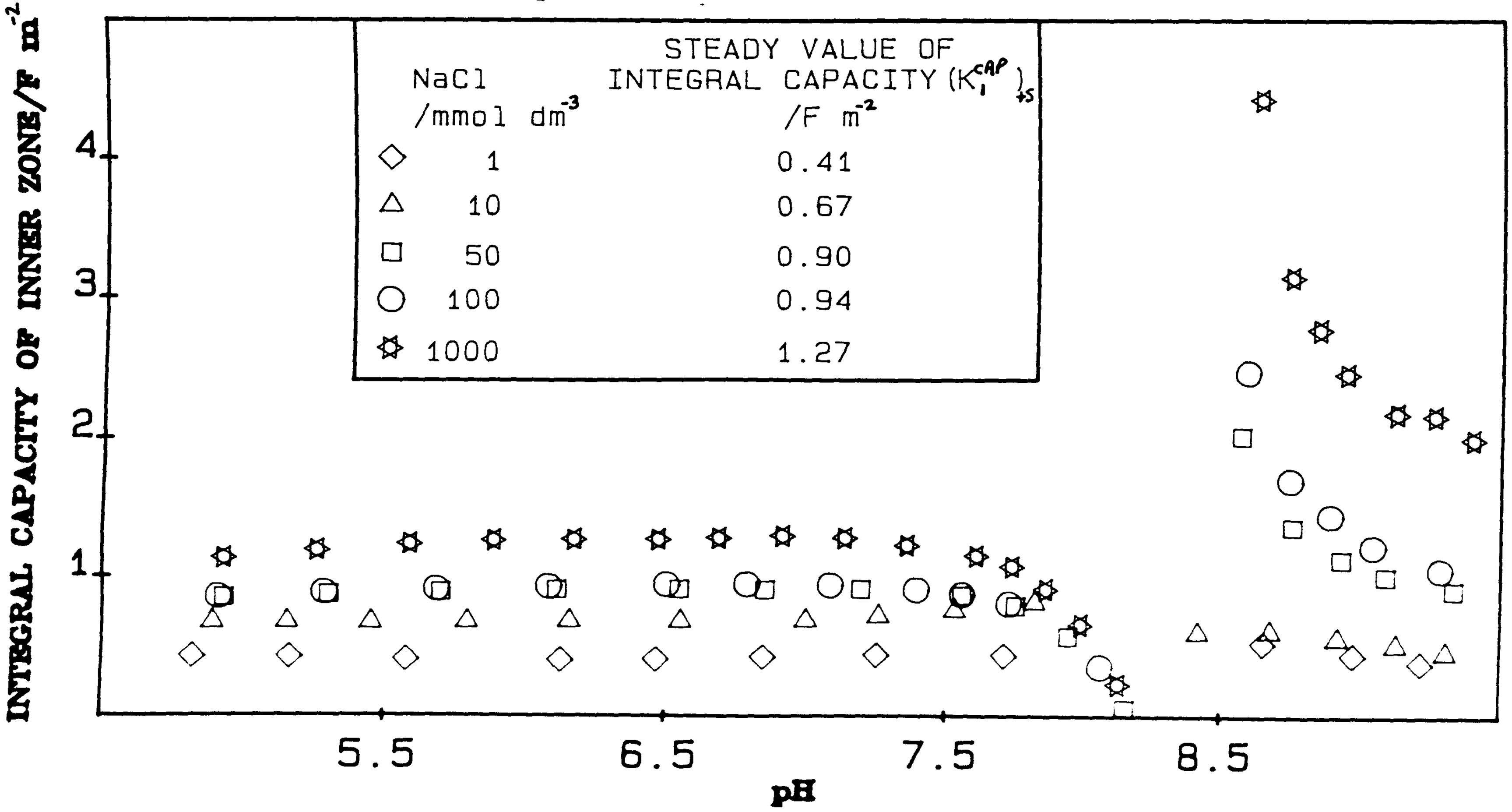

Table B3.4

Positive surface intrinsic equilibrium constants from 25°C to 65°C.

Temperature / K	pK_{a+s}^{int}	$^{*}pK_{Cl^-}^{int}$	$K_{Cl^-}^{int}$ / $mol^{-1}\ dm^3$
298.15	4.686	5.861	14.96
318.15	4.735	6.047	20.51
338.15	4.683	6.335	44.87

pK_{a+s}^{int} and $^{*}pK_{Cl^-}^{int}$ values evaluated by, respectively, double and single extrapolation.

(αFeOOH sample:- JULY85)

FIGURE B3.23

INFLUENCE OF TEMPERATURE ON THE POSITIVE ∝FeOOH SURFACE INTRINSIC EQUILIBRIUM CONSTANTS.

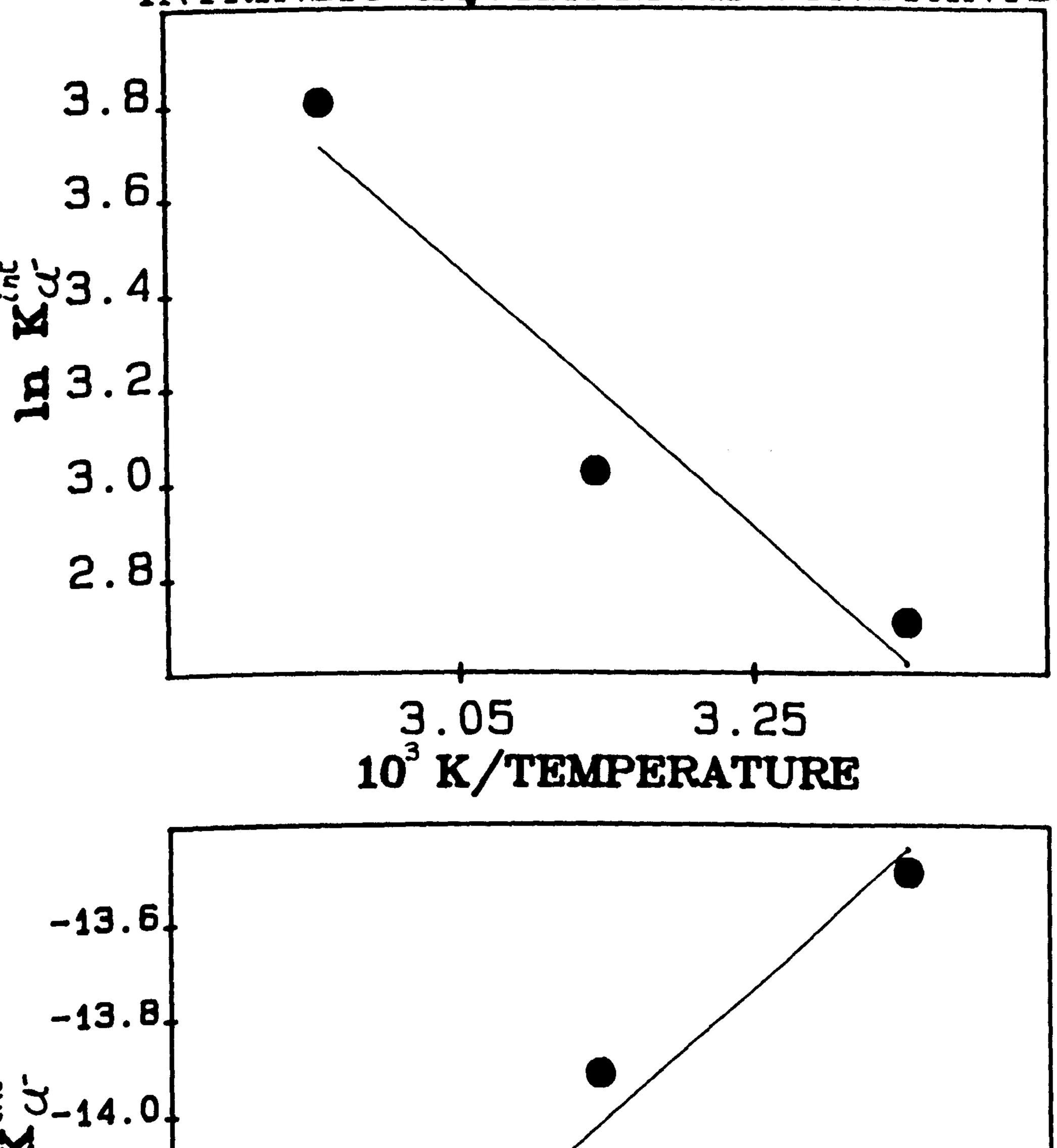

Table B3.5

Thermodynamic parameters of surface reactions (25°C).

Surface reaction	Eqn. No.	ΔH° / kJ mol^{-1}	ΔS° / J mol^{-1} K^{-1}	ΔG° / kJ mol^{-1}
$SOH_2^+ = SOH = H_s^+$	B3.1	0	-89.71	+26.75
$SOH_2^+ \cdots Cl^- = SOH + H_s^+ + Cl_s^-$	B3.11	-22.97	-189.25	+33.45
$SOH_2^+ + Cl_s^- = SOH_2^+ \cdots Cl^-$	B3.7	+23.05	+99.81	-6.71

corresponding modelled Cl^- ion coverage was 11.5% of that expected for a dehydrated Cl^- ion monolayer in a close packing arrangement.

c) The observed surface charge density arising from the amphoteric surface reactions was of the same order of magnitude as that due to the interaction of Ag^+ and I^- ions with the AgI surface (Lyklema 1963). Thus, when allowance is made for the contribution of surface complexation reactions to σ_s, the potential determining ion/surface interaction is the same for both the αFeOOH/NaCl aq. and the AgI/aqueous electrolyte colloids.

d) All $\alpha_{\pm s}$ contours on double extrapolation plots exhibited a change in behaviour at about 50 mmol dm^{-3} NaCl aq.. It would appear that this concentration is a crossover point between two different descriptions of the charging characteristics, and ion-pair formation behaviour of the αFeOOH-NaCl aq. interface.

5.2. A comparison between singly and doubly extrapolated constant values, evaluated from 25°C data.

a) The close similarity between singly extrapolated values of pK^{int}_{a+s} and pK^{int}_{a-s} (extrapolation of 1 mmol dm^{-3} NaCl aq. data to $\alpha_{\pm s} = 0$) and the corresponding doubly extrapolated values, implies that there is negligible ion-pair formation at 1 mmol dm^{-3} NaCl aq..

b) The smaller $pK_{complex}$ value calculated from singly extrapolated constants, compared to that calculated from doubly extrapolated constants, indicates both a greater pH dependence of σ_s and a greater ionisation tendency of SOH groups, than would be expected from doubly extrapolated constants. The root of this problem is, as yet, unknown. It may lie in inadequacies of the triple layer model or, more likely, it may arise in neglect of the ion-porosity of the αFeOOH surface.

5.3. Concentration dependence of intrinsic equilibrium, complexation constants, at 25°C.

The observed dependence of the function ($pQ_{\alpha \pm s} \mp \log$ [NaCl]) on [NaCl] at $\alpha_{\pm s} < 0.05$ indicates a disagreement between theory and experiment. Apparently, at low surface charge the tendency towards ion-pair formation, i.e., K^{int}_{Ion}, dependent on the quantity of ion-pairs already formed and increases with diminishing [NaCl]. This dependence was substantiated by the attainment of physically realistic interfacial potentials which

mirrored the relative magnitudes of the interfacial charges, using K^{int}_{ION} and $^{*}K^{int}_{ION}$ values evaluated at each NaCl concentration. A possible explanation of this dependence can be developed in terms of the active site theory of catalysis. Thus, at high concentration active sites that are available to engage in ion-pair formation become occupied and, possibly, coulombic hindrance prevents the formation of a complete monolayer; such hindrance being exhibited as a relatively reduced tendency towards ion-pair formation. At low concentration, active sites that are available to engage in ion-pair formation, and not coulombically hindered, are not occupied; such non-occupancy being exhibited as a relatively increased tendency towards ion-pair formation.

5.4. The relative importance and intensity of surface complexation reactions, at 25°C.

The relative importance of surface complexation reactions over surface ionisation reactions in an oxide/aqueous electrolyte colloid system is determined by the magnitude of the differences

$$^{*}pK^{int}_{ANION} - pK^{int}_{a+s} = \log K^{int}_{ANION} \qquad B3.53$$

and

$$pK^{int}_{a-s} - {}^{*}pK^{int}_{CATION} = \log K^{int}_{CATION} \qquad B3.54$$

For the αFeOOH/NaCl aq. colloid these differences were significant. Thus, for this colloid, surface complexation reactions are considerably more important than surface ionisation reactions; i.e., Na^+ and Cl^- ions are the principal charge determining ions. The observed order of magnitude of the binding constants $K^{int}_{Cl^-}$ and $K^{int}_{Na^+}$ corresponded to a specific adsorption energy $(\emptyset_{ADS})_{ION}$ of ca.-5kT, a value that is indicative of a relatively strong ion-pair bond (the bond energy of -5kT is of the same order of magnitude as that for a hydrogen bond). The observed near equality of the two binding constants, and the symmetry of σ_s about the pzc, suggests that ion-pair formation occurs to a similar extent on both positive and negative αFeOOH surfaces. [Authors often refer to simple colloid systems in which pH_o equals pH_{IEP} as being "in the absence of specific adsorption". However, such a condition is also satisfied by symmetrical specific adsorption of electrolyte anion and cation, as observed in this study.] The value of $(\emptyset_{ADS})_{ION}$ derived

from the binding constants is more favourable by several kT than that used to describe analogous adsorption at the AgI-aq. interface. With the triple layer model, as used in this work, this stronger binding seems reasonable since the adsorption energy includes ion -ion interaction between an adsorbed counterion and a discrete charge site on the αFeOOH surface. In contrast, in the theory of ion adsorption on AgI the surface charge is regarded as continuously distributed.

5.5. edl structure-sensitive properties modelled at 25°C.

a) The lack of any great disparity between determined σ_s and modelled $|\sigma_{IHP}|$ values, and the small modelled $|\sigma_{OHP}|$ values relative to σ_s, suggests a considerable extent of ion-pair formation.

b) For a given pH, ψ_s decreased with decreasing [NaCl]. This concentration dependence suggests that, while H^+ and OH^- ions are the principal potential determining ions for the αFeOOH/NaCl aq. colloid, electrolyte ions can modify the value of ψ_s.

c) The observed reduction in K_1^{CAP} with decreasing [NaCl] indicates that the distance of counterion approach towards the surface increases with diminishing concentration.

d) The observed high K_1^{CAP} values at high concentration ($\geqslant$ 50mmol dm^{-3} NaCl aq.) implies a close association (< 0.15nm) of counterions with charged surface sites. Because of the structure promoting ability of the oxyhydroxide surface to generate an adjacent highly structured chemisorbed water layer, it can be conjectured that an approaching counterion could have a chemisorbed water molecule as part of its hydration shell thereby facilitating a close approach. In terms of the ion-pair model, this close association of surface and countercharge would mean that the dipoles are orientated almost parallel to the surface plane. A possible explanation of the observed high K_1^{CAP} values, together with the low K_2^{CAP} value used in the computations, is that the surface plane and IHP are embedded in an ion-porous hydrated oxide layer at the interface; depending on the thickness of such a layer, a wide separation between the IHP and the OHP is possible. However, such an ion-porous layer at the surface of αFeOOH is in contradiction with the findings of Yates and Healy 1975a.

e) At very high concentration ($\geqslant$ 0.1 mol dm^{-3} NaCl aq.) $(K_1^{CAP})_{-s}$ was

observed to be greater than $(K_1^{CAP})_{+s}$, indicating a closer approach to the solid surface for Na^+ ions than for Cl^- ions. This difference in adsorption can be interpreted in terms of the structured water layer close to the solid surface being more conducive to structure promoting ions such as hydrated Na^+ ions, than structure breaking ions such as weakly hydrated Cl^- ions. At low concentration ($\leqslant$ 10 mmol dm^{-3} NaCl aq.) the observed near equality of corresponding $(K_1^{CAP})_{+s}$ and $(K_1^{CAP})_{-s}$ values indicates that Na^+ and Cl^- ions have about the same distance of approach to oppositely charged surfaces, and suggests that this distance is further from the solid surface than the structured water layer.

f) At high concentration the observed infinite values of $(K_1^{CAP})_{-s}$ at pH_o suggests that Na^+ ions penetrate the surface charge region.

g) For a given high [NaCl], and increasing σ_s from zero, the observed dramatic increase in $(K_1^{CAP})_{+s}$ can be interpreted as a progressive approach of Cl^- ions towards the αFeOOH surface, while the observed corresponding dramatic decrease in $(K_1^{CAP})_{-s}$ can be interpreted as a crowding-out of Na^+ ions from the structured water region preferentially occupied by H^+ and OH^- ions.

5.6. Temperature dependence.

a) For a given increase in temperature the variation of $\frac{1}{2}$ pK_w was not fully accounted for by the magnitude of the shift in the pzc of αFeOOH. Therefore, the relative affinity of H^+ and OH^- ions for the αFeOOH surface, i.e., the charge density of H^+ and OH^- ions on the oxyhydroxide surface, is dependent on temperature. It would appear that H^+ has an increased affinity, relative to that for OH^-, for the αFeOOH surface at higher temperatures.

b) The observed small and large positive values of, respectively, ΔH^* and ΔS^* indicate that in the transfer of H^+ and OH^- ions from bulk solution to the adsorbed state a small amount of energy is expended, and a large increase in the randomness of the system takes place (such as the occurrence of an advanced degree of desolvation).

c) The ratio $\frac{[SOH_2^+]}{[SOH]}$ is not influenced by temperature over the range 25°C to 65°C.

d) The ion-pair $SOH_2^+ \ldots Cl^-$ becomes increasingly more abundant as temperature

is increased due to the, observed, positive enthalpy change accompanying its formation.

e) Since SOH_2^+ .... Cl^- ion-pairs become increasingly more abundant at elevated temperatures, more SOH_2^+ groups must enter into ion-pair formation at higher temperatures. Therefore, the protonation of an increased number of SOH groups must occur at such temperatures, to maintain constancy of the ratio $\frac{[SOH_2^+]}{[SOH]}$. Hence, there is an increased affinity of H^+ ions (relative to OH^- ions) for the αFeOOH surface at higher temperatures.

6. COMPARISON WITH OTHER WORK.

σ_s determined at 25°C shows excellent agreement with that of Yates and Healy 1975b for corresponding electrolyte concentrations and arbitrary ΔpH values, within the range 1 mmol dm^{-3} to 0.1 mol dm^{-3}. However, the evaluated (at 0.1 mol dm^{-3}) intrinsic equilibrium constants are slightly higher than the corresponding values obtained by these workers (see Table B3.3), reflecting the higher pH_o determined in this study. More importantly, the determined values of the binding constants (at 0.1 mol dm^{-3}) and the observed differences ΔpK_a and $\Delta pK_{complex}$ compare very favourably with the corresponding values of Yates, D.E., Hingston et.al., Davis. A striking confirmation of the determined value (at 0.1 mol dm^{-3}) of the Cl^- ion binding constant has been found in a completely different approach by Sasaki et.al., who studied the kinetics of adsorption of this anion in acidic suspensions.

The description of the interface by a set of equations, and their solution by an iterative procedure leading to values of the interfacial parameters, constitutes a significant improvement of the model presented by Yates et.al., who assume a constant K_1^{CAP} value of 1.4Fm^{-2} for all oxides and electrolytes, and in the development of this model by Davis et.al., who treat K_1^{CAP} as an adjustable parameter. In this study K_1^{CAP} was considered to be a dependent variable. At 1.0 mol dm^{-3} the calculated value of K_1^{CAP} is similar to those values assumed by Yates et.al., and used by Davis et.al., Regazzoni et.al., to obtain simultaneous agreement of calculated σ_s and ψ_{OHP} values with experimental values of σ_s and ζ.

The variability of intrinsic equilibrium constants with concentration, found in this study, has also been observed by other workers. In their study of the interfacial properties of zirconium dioxide and magnetite in water, Regazzoni et.al., observed a disagreement between the Davis et.al. model and experimental data. Thus, the addition of the term $\mp \log [KNO_3]$ to each $pQ_{a\pm s}$ line (of $pQ_{a\pm s}$ versus $\alpha_{\pm s}$ plots) did not bring all the experimental points to a single straight line, resulting in a value of $^{*}pK^{int}_{ION}$ at each concentration. Using an empirical relationship to account for the variation of surface ionisation constants with surface charge, Schindler and Kamber, Schindler and Gamsjäger, Stumm et.al. 1970 derived operational surface ionisation constants and observed that these constants varied smoothly with surface charge. By extrapolating to $\sigma_s = 0$, these workers obtained an intrinsic ionisation constant. This apparent intrinsic ionisation constant was later found to be sensitive to ionic strength. In many of their calculations for oxides, Chan et.al. 1975, Chan et.al. 1976, Healy et.al., have used ionisation constants as variable parameters, while James and Parks have suggested there is good reason to suspect "that ionisation constants are in fact ionisation quotients that show significant variance with concentration". It can be expected that variability of ionisation constants, as described above, would be manifested as a variability of anion and cation binding constants.

In this study a different value of K_1^{CAP} was obtained, from the iterative solution of the equations describing the interface, for each value of [NaCl] and sign of σ_s. Interestingly, several groups of workers have found it necessary to use different values of K_1^{CAP}, at different concentrations and different signs of σ_s, to fully describe the charging and ion-pair formation behaviour of interfaces. For example, Stumm et.al. 1976, Sigg and Stumm in their description of the edl at the Fe_3O_4-aqueous electrolyte interface used i) for a given concentration, different values of K_1^{CAP} for each σ_s branch, ii) for a given σ_s branch, values of K_1^{CAP} that increased with increasing concentration, and iii) for a given high concentration, values of K_1^{CAP} such that $(K_1^{CAP})_{-s} > (K_1^{CAP})_{+s}$. Regazzoni et.al., observed an assymmetry in their titration curves which "cannot be accounted for unless different capacity values are assumed for each branch".

The results concerning the influence of temperature on the αFeOOH-NaCl aq. interface are the first to be reported. However, in their study of the

temperature dependence of the pzc of alumina, and cobalt and nickel oxides and hydroxides, Tewari and McLean, Tewari and Campbell observed large positive changes in entropy in the transfer of H^+ and OH^- ions from bulk solution to the adsorbed state, while Berube and de Bruyn 1968a observed a small positive change in enthalpy for this process at the TiO_2-aqueous electrolyte interface.

7. Appendix: Derivation of a mole balance equation for the calculation of σ_s from proton adsorption data.

When unit mass of a water insoluble particulate solid is suspended in an aqueous solution of its potential determining ions, H^+ and OH^-, the suspension can be considered to be at an unperturbed state I such that the numbers of moles of H^+ and OH^- ions in solution are $\omega^I_{H^+}$ and $\omega^I_{OH^-}$, respectively, and the numbers of moles of H^+ and OH^- ions present on the surface of the suspended particles are $(\omega_s)^I_{H^+}$ and $(\omega_s)^I_{OH^-}$, respectively. When one type of potential determining ion, say H^+, is added to the aqueous suspension, such a perturbation to the colloid system will alter the distribution of H^+ and OH^- ions on the solid surface and in solution, and will thereby generate state II; the numbers of moles of H^+ and OH^- ions present in solution being $\omega^{II}_{H^+}$ and $\omega^{II}_{OH^-}$, respectively, and the numbers of moles of H^+ and OH^- ions present on the surface of the suspending particles being $(\omega_s)^{II}_{H^+}$ and $(\omega_s)^{II}_{OH^-}$, respectively. If $(\omega_{Add})^{II}_{H^+}$ is the number of moles of the potential determining ion H^+ added, resulting in the generation of state II, the mole balance equation can be formulated as

$$(\omega_{Add})^{II}_{H^+} = (\omega^{II}_{H^+} - \omega^{I}_{H^+}) + (\omega^{I}_{OH^-} - \omega^{II}_{OH^-})$$

$$+ ((\omega_s)^{II}_{H^+} - (\omega_s)^{I}_{H^+}) + ((\omega_s)^{I}_{OH^-} - (\omega_s)^{II}_{OH^-}) \qquad \text{B3.55}$$

Rearranging, gives

$$((\omega_{Add})^{II}_{H^+} + \omega^{I}_{H^+} - \omega^{II}_{H^+}) - (\omega^{I}_{OH^-} - \omega^{II}_{OH^-})$$

$$= ((\omega_s)^{II}_{H^+} - (\omega_s)^{II}_{OH^-}) + ((\omega_s)^{I}_{OH^-} - (\omega_s)^{I}_{H^+}) \qquad \text{B3.56}$$

Finally, the addition of the other potential determining ion, OH^-, to the aqueous suspension will also alter the distribution of H^+ and OH^- ions on the solid surface and in solution, and generate a new state, <u>state III</u>; the numbers of moles of H^+ and OH^- ions present in solution being $\omega_{H^+}^{III}$ and $\omega_{OH^-}^{III}$, respectively, and the numbers of H^+ and OH^- ions present on the surface of the suspended particles being $(\omega_s)_{H^+}^{III}$ and $(\omega_s)_{OH^-}^{III}$, respectively. If $(\omega_{Add})_{OH^-}^{III}$ is the number of moles of the potential determining ion OH^- added resulting in the generation of state III, then the mole balance equation becomes

$$((\omega_{Add})_{H^+}^{II} + \omega_{H^+}^{I} - \omega_{H^+}^{III}) - ((\omega_{Add})_{OH^-}^{III} + \omega_{OH^-}^{I}$$

$$- \omega_{OH^-}^{III} = ((\omega_s)_{H^+}^{III} - (\omega_s)_{OH^-}^{III}) + ((\omega_s)_{OH^-}^{I}$$

$$- (\omega_s)_{H^+}^{I}) \qquad \text{B3.57}$$

The mole balance equations for subsequent, successive additions of H^+ and OH^- ions to the aqueous suspension, resulting in the generation of <u>state j</u>, will have the form of eqn. B3.57 which can be expressed more generally as

$$((\omega_{Add})_{H^+}^{j} + \omega_{H^+}^{I} + (\omega_{Add})_{H^+}^{Tot} - \omega_{H^+}^{j})$$

$$- ((\omega_{Add})_{OH^-}^{j} + \omega_{OH^-}^{I} + (\omega_{Add})_{OH^-}^{Tot} - \omega_{OH^-}^{j})$$

$$= ((\omega_s)_{H^+}^{j} - (\omega_s)_{OH^-}^{j}) - ((\omega_s)_{H^+}^{I} - (\omega_s)_{OH^-}^{I}) \qquad \text{B3.58}$$

with $(\omega_{Add})_{H^+}^{j}$ or $(\omega_{Add})_{OH^-}^{j}$ equal to zero depending on whether OH^- ions or H^+ ions are being added resulting in the generation of <u>state j</u>, and $(\omega_{Add})_{H^+}^{Tot}$ and $(\omega_{Add})_{OH^-}^{Tot}$ are the total numbers of H^+ and OH^- ions added in all previous H^+ and OH^- additions.

The right hand side of eqn. B3.58 is the excess positive charge on the surface of the suspended particles relative to that surface charge present at the very outset of the potentiometric experiment. If, however, <u>state I</u> describes the pzc of the suspended solid then $(\omega_s)_{H^+}^{I} = (\omega_s)_{OH^-}^{I}$, and the right hand side of eqn. B3.58 is the absolute excess positive charge on the solid surface, at <u>state j</u>. Conversion of relative or

absolute excess positive charge at state j to, respectively, $(\sigma_s)^j_{REL}$ or $\sigma_s{}^j$ is achieved by the factor F/S_{BET}. For example, absolute excess positive charge is expressed as

$$\sigma_s{}^j = \frac{F}{S_{BET}} \left[\left((\omega_{Add})^j_{H^+} + \omega^I_{H^+} + (\omega_{Add})^{Tot}_{H^+} - \omega^j_{H^+} \right) \right.$$

$$\left. - \left((\omega_{Add})^j_{OH^-} + \omega^I_{OH^-} + (\omega_{Add})^{Tot}_{OH^-} - \omega^j_{OH^-} \right) \right]$$

$$\text{for} \quad (\omega_s)^I_{H^+} = (\omega_s)^I_{OH^-} \qquad \text{B3.59}$$

From a continuous monitoring of total quantities of acid and base added, pH, solution volume at state j (Vol^j) and ionic strength at state j (I^j), $(\sigma_s)^j_{REL}$ (and $\sigma_s{}^j$) can be computed using relationships such as

$$\omega^j_{H^+} = \frac{10^{-pH^j}}{f} \cdot \frac{Vol^j}{10^3} \qquad \text{B3.60}$$

$$\text{and} \quad \omega^j_{OH^-} = \frac{10^{(pH^j - K_w)}}{f} \cdot \frac{Vol^j}{10^3} \qquad \text{B3.61}$$

Hence, the potentiometric titration/σ_s experiment involves the successive additions of known amounts of an ion to an aqueous suspension of a water insoluble particulate solid upon the surface of which the ion can bestow charge and, therefore, potential. After each addition, the charge residing on the surface of the suspended solid relative to the surface charge present at the outset of the experiment can be evaluated from a knowledge of the amounts of the potential determining ion, and its conjugate ion, added in previous titrations and currently present in solution. The determination of the pzc of the aqueous suspension, by a separate experiment, will enable the conversion of relative charge to absolute charge.

It is noteworthy that in the work of Davis et.al., Davis and Leckie, James et.al., σ_s is calculated from an expression similar to eqn. B3.59:

$$\sigma_s = \frac{F}{S_{BET}} \left[[Acid] - [Base] + [OH^-] - [H^+] \right] \qquad \text{B3.62}$$

[Acid] and [Base] are defined as the concentrations of acid and base, respectively, after addition, and are analogous to the terms $((\omega_{Add})^{j}_{H^+} + (\omega_{Add})^{Tot}_{H^+})$ and $((\omega_{Add})^{j}_{OH^-} + (\omega_{Add})^{Tot}_{OH^-})$, respectively, of eqn. B3.59. Similarly, $[OH^-]$ and $[H^+]$ are analogous to the terms $\omega^{j}_{OH^-}$ and $\omega^{j}_{H^+}$, respectively, of eqn. B3.59. However, the terms $\omega^{I}_{H^+}$ and $\omega^{I}_{OH^-}$ of eqn. B3.59 find no counterparts in eqn. B3.62. This discrepancy by the authors of this equation will only lead to a significant difference between the σ_s calculated using eqn. B3.59 and that calculated using B3.62 if the pH at the very outset of the potentiometric titration is significantly different from $\frac{1}{2}$ pK_w. In this study use is made of eqn. B3.59.

REFERENCES

Atkinson, R.J., Posner, A.M., and Quirk, J.P., J. Phys. Chem., 71, 550 (1967).

Aylemore, L.A.G., Clays and Clay Minerals, 22, 175 (1974).

Barrow, N.J., Bowden, J.W., Posner, A.M., and Quirk, J.P., Aust. J. Soil Res., 18, 37 (1980).

Berube, Y.G., Onoda, G.Y., and de Bruyn, P.L., Surface Sci., 8, 448 (1967).

Berube, Y.G., and de Bruyn, P.L., J. Colloid Interface Sci., 27, 305 (1968).

Berube, Y.G., and de Bruyn, P.L., J. Colloid Interface Sci., 28, 92 (1968).

Blesa, M.A., Figliolia, N.M., Maroto, A.J.G., and Regazzoni, A.E., J. Colloid Interface Sci., 101, 410 (1984).

Bolt, G.H., J. Phys. Chem., 61, 1166 (1957).

Bowden, J.W., Posner, A.M., and Quirk, J.P., Aust. J. Soil Res., 15, 121 (1977).

Breeuwsma, A., and Lyklema, J., Discuss Faraday Soc., 52, 324 (1971).

Breeuwsma, A., and Lyklema, J., J. Colloid Interface Sci., 43, 437 (1973).

Bye, G.C., and Howard, C.R., J. Appl. Chem. Biotechnol., 21, 324 (1971).

Chan, D., Perram, J.W., White, L.R., and Healy, T.W., J. Chem. Soc., Faraday Trans. I, 71, 1046 (1975).

Chan, D., Healy, T.W., and White, L.R., J. Chem. Soc., Faraday Trans. I, 72, 2844 (1976).

Davis, J.A., Ph.D. Thesis, Stanford University, 1977.

Davis, J.A., James, R.O., and Leckie, J.O., J. Colloid Interface Sci., 63, 480 (1978).

Davis, J.A., and Leckie, J.O., J. Colloid Interface Sci., 67, 90 (1978).

Dawson, P.T., J. Phys. Chem., 71, 838 (1967).

Day, R.E., and Parfitt, G.D., Trans. Faraday Soc., 63, 708 (1967).

de Bruyn, P.L., and Agar, G.E., in "Froth Flotation", Fuerstenau, D.W.; Editor, 50th Anniversary Vol., Am. Inst. Min. Metall. Pet. Eng., New York, 1962.

Feitknecht, W., Wyttenback, A., and Buser, W., in "4th Int. Symp. Reactivity of Solids", de Boer, J.H; Editor, Elsevier Publ. Co., Amsterdam, 1961.

Gallagher, K.J., and Phillips, D.N., Trans. Faraday Soc., 64, 785 (1968).

Grahame, D.C., Chem. Rev., 41, 441 (1947).

Healy, T.W., Yates, D.E., White, L.R., and Chan, D., J. Electroanal. Chem., 80, 57 (1977).

Healy, T.W., in "Proceedings of the conference on Adsorption from Aqueous Solutions [held by the Royal Australian Chemical Institute, Division of Colloid and Surface Chemistry at the University of Melbourne, March 3rd, 1978]", Yates, D.E.,; Editor.

Hermansson, H.P., Chemica Scripta, 12, 102 (1977).

Hingston, F.J., Posner, A.M., and Quirk, J.P., Adv. Chem. Ser., 79, 82 (1968).

Hollabaugh, C.M., and Chessick, J.J., J. Phys. Chem., 65, 109 (1961).

Honig, E.P., and Hengst, J.H. Th., J. Colloid Interface Sci., 29, 510 (1969).

James, R.O., Davis, J.A., and Leckie, J.O., J. Colloid Interface Sci., 65, 331 (1978).

James, R.O., and Parks, G.A., in "Surface and Colloid Science", Matijevic, E.,; Editor, Vol. 12, Chap. 2, Plenum Press, New York, 1982.

Jurinak, J.J., J. Colloid Sci., 19, 477 (1964).

Levine, S., and Smith, A.L., Discuss. Faraday Soc., 52, 290 (1971).

Levine, S., Smith, A.L., and Brett, A.C., Chem., Phys. Chem. Anwendungstech. Grenzflaechenakten Stoffe, Ber. Int. Kongr. 6th, 1972.

Lewis, K.E., and Parfitt, G.D., Trans. Faraday Soc., 62, 204 (1966).

Lyklema, J., and Overbeek, J.Th.G., J. Colloid Sci., 16, 595 (1961).

Lyklema, J., Trans. Faraday Soc., 59, 418 (1963).

Lyklema, J., J. Discuss. Faraday Soc. 42, 81 (1966).

Lyklema, J., J. Electroanal. Chem. Interfacial Electrochem., 18, 341 (1968).

Lyklema, J., and Healy, T.W., Discuss. Faraday Soc., 52, 318 (1971).

Madrid, L., and de Arambarri, P., Geoderma, 21, 199 (1978).

Mays, J.M., and Brady, G.W., J. Chem. Phys., 25, 583 (1956).

Onoda, G.Y., and de Bruyn, P.L., Surface Sci., 4, 48 (1966).

Parfitt, R.L., Atkinson, R.J., and Smart, R.S.C., Soil Sci. Soc. Am. Proc., 39, 837 (1975).

Parfitt, R.L., Russell, J.D., and Farmer, V.C., J. Chem. Soc. Faraday I, 72, 1082 (1976).

Parks, G.A., and de Bruyn, P.L., J. Phys. Chem., 66, 967 (1962).

Parks, G.A., Chem. Rev., 65, 177 (1965).

Parks, G.A., in "Equilibrium Concepts in Natural Water Systems", Adv. Chem. Ser. No. 67, Am. Chem. Soc. : Washington D.C. (1967).

Regazzoni, A.E., Blesa, M.A., and Maroto, A.J.G., J. Colloid Interface Sci., 91, 560 (1983).

Russell, J.D., Parfitt, R.L., Fraser, A.R., and Farmer, V.C., Nature, 248, 220 (1974).

Sasaki, M., Morlya, M., and Yasunaga, T., J. Phys. Chem., 87, 1449 (1983).

Schindler, P.W., and Kamber, H.R., Helv. Chim. Acta, 51, 1781 (1968).

Schindler, P.W., and Gamsjager, H., Kolloid Ƶ.Ƶ. Polym. 250, 759 (1972).

Sigg, L., and Stumm, W., Colloids and Surf., 2, 101 (1980).

Sposito, G., J. Colloid Interface Sci., 91, 329 (1983).

Sposito, G., "The Surface Chemistry of Soils", Oxford University Press, Oxford, 1984.

Stern, O., Ƶ, Electrochem., 30, 508 (1924).

Stumm, W., Huang, C.P., and Jenkins, S.R., Croat. Chem. Acta, 42, 225 (1970).

Stumm, W., Hohl, H., and Dalang, F., Croat. Chem. Acta, 48, 491 (1976).

Tadros, Th.F., and Lyklema, J., J. Electroanal. Chem. Interfacial Electrochem., 17, 267 (1968).

Tadros, Th.F., and Lyklema, J., J. Electroanal, Chem. Interfacial Electrochem., 22, 1 (1969).

Tewari, P.H., and McLean, A.W., J. Colloid Interface Sci., 40, 267 (1972).

Tewari, P.H., and Campbell, A.B., J. Colloid Interface Sci., 55, 531 (1976).

Trimbos, H.F.A., and Stein, H.N., J. Colloid Interface Sci., 77, 386 (1980).

Van Raij, B., and Peech, M., Proc. Soil Sci. Am., 36, 587 (1972).

Verwey, E.J.W., and Overbeek, J.T.G., in "Theory of the Stability of Lyophobic Colloids", Elsevier, Amsterdam - New York, 1948.

Wade, W.H., and Hackerman, N., J. Phys. Chem., 65, 2597 (1962).

Wei, Y-K., and Bernstein, R.B., J. Phys. Chem., 63, 738 (1959).

Wyttenback, A., Helv. Chim. Acta, 44, 418 (1961).

Yates, D.E., Levine, S., and Healy, T.W., J. Chem. Soc. Faraday Trans. I., 70, 1807 (1974).

Yates, D.E., Ph.D. Thesis, University of Melbourne, 1975.

Yates, D.E., and Healy, T.W., Proc. Int. Conf. Colloid Surf. Sci., 1975, 1, 7.

Yates, D.E., and Healy, T.W., J. Colloid Interface Sci., 52, 222 (1975).

Yates, D.J.C., J. Phys. Chem., 65, 746 (1961).

Yoon, R.H., Salman, T., and Donnay, G., J. Interface Sci., 70, 483 (1979).

ADDENDUM

THE ADVERSE INTERFERENCE BY HYDROXYL IONS ON THE RESPONSE OF A CHLORIDE ION SELECTIVE ELECTRODE.

1. INTRODUCTION

A chloride Ion Selective Electrode (ISE) was initially used to monitor the Cl^- ion activity of an $\alpha FeOOH/Cl^-$ ion aq. suspension. However, it was observed that the Cl^- ion potential response (E_{Cl}-) of the electrode was adversely affected when the pH of the suspension was altered by the addition of a very small volume of either acid or base. Consequently, the chloride ISE was abandoned as a means of measuring Cl^- ion activity at variable pH. This short study is a quantitative assessment of the adverse interferance by OH^- ions on the E_{Cl}- of a chloride ISE.

2. THEORY

Out of hundreds of possibilities an ISE will respond to only seven or eight individual ion species (Philips). Difficulties may arise if a number of responding species are present at the same time, but discrimination can usually be achieved through the qualitative differences in response. Not only is there a characteristic response for each particular species of ion, but the relationship of one ion to another is readily determined by experiment. The concept of "selectivity constant", $K_{i_1 i_2}$, has been introduced to provide a quantitative index of how effectively an electrode will discriminate between a selected ion i_1 and an interfering ion i_2. The constant is defined as the ratio between the selected ion and the activity of the interfering ion that would give an identical electrode response when present alone (in a solution of its own ions but under otherwise identical conditions).

$$K_{i_1 i_2} = \frac{a_{i_1}}{a^*_{i_2}} \qquad \text{A.1}$$

* activity generates same response.

It must be pointed out, however, that although $K_{i_1 i_2}$ is termed a constant this is rather misleading jargon since there is considerable variation of selectivity with interferant concentration (Moody and Thomas).

A method of determining the OH^- ion chloride ISE selectivity constant (K_{ClOH}) is to obtain the potential difference between two measurements (Eisenman); this method is usually employed by chloride ISE manufacturers to establish their quoted selectivity constants for a number of interfering ions. The first measurement is the potential, $(E_{Cl})_{Cl}$, of the chloride

ISE in an aqueous solution of Cl^- ions, at 0.1 mol dm^{-3} Cl^- aq., without any OH^- ions, i.e., at low pH. The second measurement is the potential, $(E_{Cl})_{OH}$, of the chloride ISE in an aqueous solution of OH^- ions, at 0.1 mol dm^{-3} OH^- aq. (pH 13), without any Cl^- ions. K_{ClOH} is determined from

$$\log K_{ClOH} = \frac{F[(E_{Cl})_{Cl} - (E_{Cl})_{OH}]}{RT \ln 10} \qquad A.2$$

The influence of OH^- ions on the E_{Cl} of a chloride ISE will be indicated by the product of the OH^- ion activity and the OH^- selectivity constant. In particular, the product $a_{OH^-} K_{ClOH}$ will indicate the lowest level of Cl^- ion activity (a_{Cl^-}) that can be measured with confidence (Philips).

3. METHOD

Chloride solutions were prepared having the following molar concentrations :- 0.1, 0.01, 5×10^{-3}, 1×10^{-3}, 5×10^{-4}, 1×10^{-4} and 1×10^{-5} mol dm^{-3} NaCl aq.. The E_{Cl^-} of a chloride solution (100 cm^3) was determined at pH 3 and at a higher pH (pH_B) between pH 6 and pH 12; the alteration of pH was achieved with small volume of acid (HNO_3 aq.) and base (KOH aq.), and E_{Cl^-} at pH 3 and pH_B was designated $(E_{Cl^-})_A$ and $(E_{Cl^-})_B$, respectively. This procedure was repeated using the other six chloride solutions and for water. The entire procedure was repeated several times by the alteration of solution pH to a different pH_B value.

4. RESULTS

The variation of E_{Cl^-} with $[Cl^-]$, for E_{Cl^-} determined at pH 3 and, for example, pH_B = 9.0, is shown in Fig. A.1. $[Cl^-]$ was determined at pH 3 and pH_B from potential/concentration plots like Fig. A.1, for a series of arbitrary E_{Cl^-} values. The apparent percentage decrease in $[Cl^-]$ (% $\Delta[Cl^-]$), caused by the elevation of solution pH from pH 3 to pH_B, was calculated for the series of arbitrary E_{Cl^-} values. The variation of % $\Delta[Cl^-]$ with E_{Cl^-} is shown in Fig. A.2.

A value of K_{ClOH} at each pH_B was calculated (using eqn. A.1) with the aid of plots such as Fig. A.1 and a knowledge of the E_{Cl^-} of water at pH_B.

FIGURE A.1

POTENTIAL RESPONSE OF A Cl– ION SELECTIVE ELECTRODE AS A FUNCTION OF Cl– CONCENTRATION AND pH.

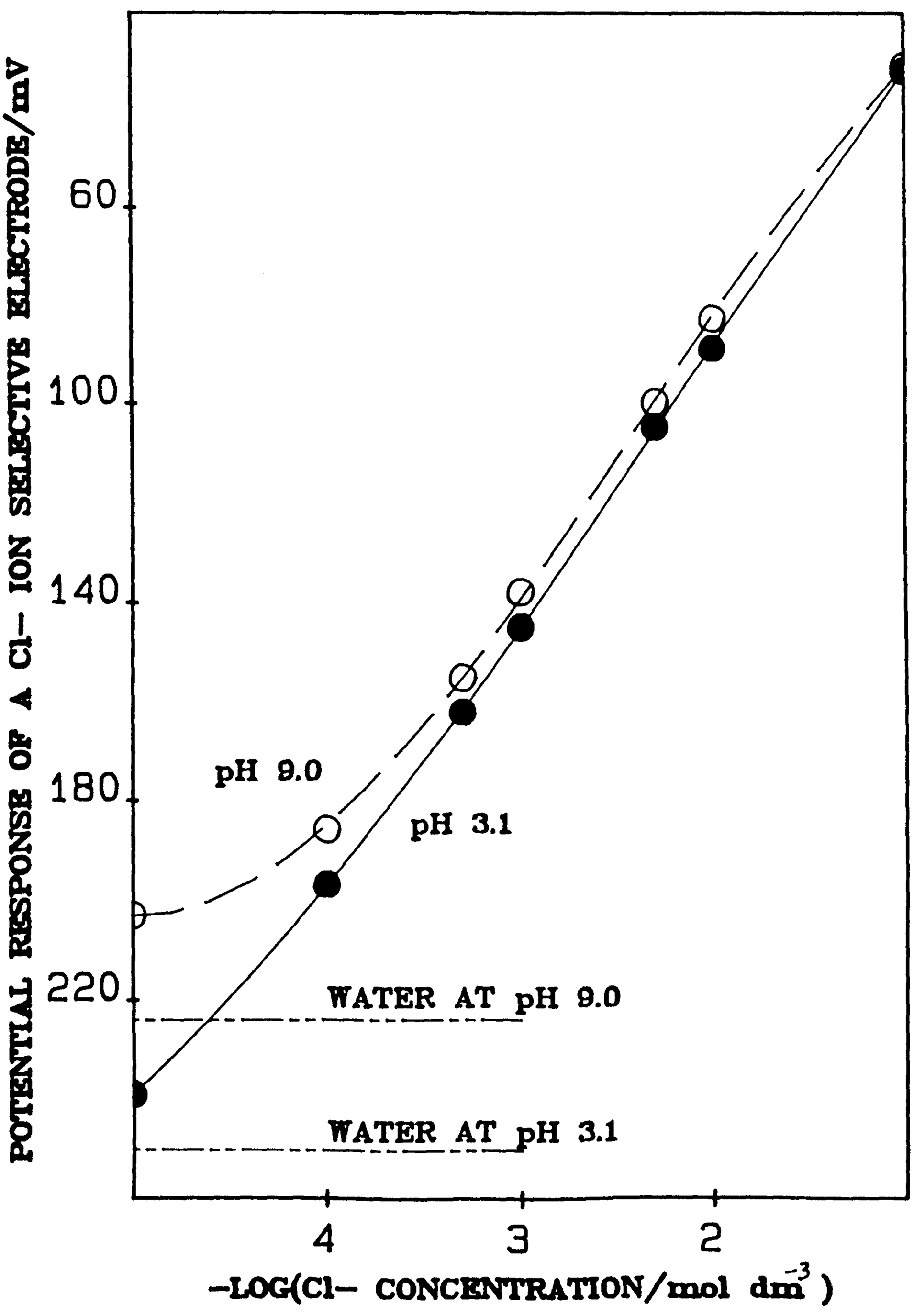

FIGURE A.2

APPARENT DECREASE IN Cl– CONCENTRATION (AS MEASURED BY A Cl– ISE) CAUSED BY THE ELEVATION OF pH FROM ca. pH 3 TO A HIGHER VALUE AS A FUNCTION OF THE POTENTIAL RESPONSE OF THE ISE AND pH.

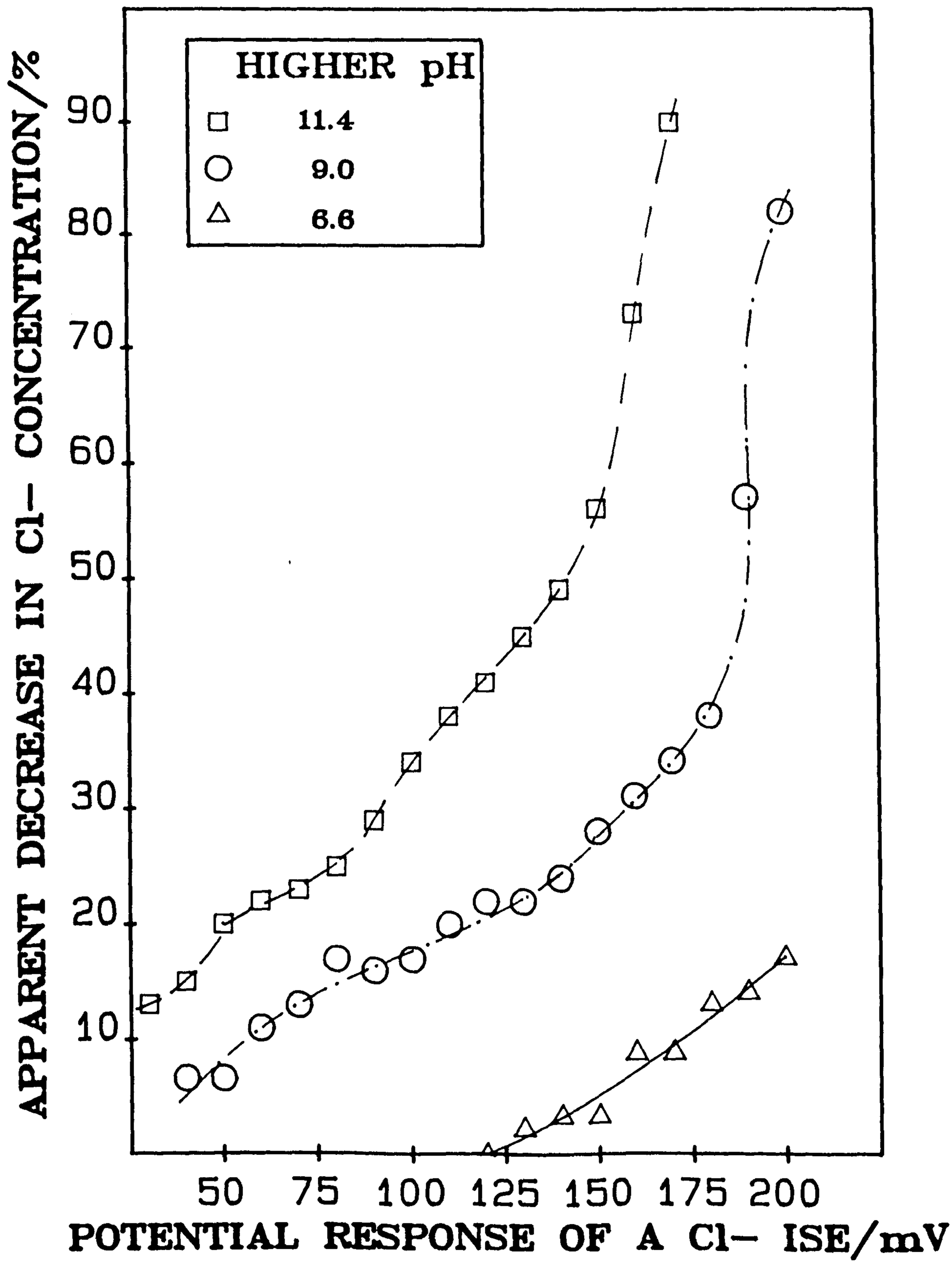

A value of K_{ClOH}, designated †, was calculated using eqn. A.2. Calculated values of K_{ClOH} and -log (K_{ClOH} $[OH^-]$) are given in Table A.1. The variation of the E_{Cl^-} of water at pH_B with -log (K_{ClOH} $[OH^-]$) is shown in Fig. A.3.

5. CONCLUSION

The presence of OH^- ions causes a significant interference of the E_{Cl^-} of a chloride ISE. This interference is most prevalent at high $[OH^-]$ and low $[Cl^-]$, and causes an apparent reduction in the evaluated $[Cl^-]$ of a solution whose pH > 6 (compared to that evaluated at a low pH). Thus, the lowest level of Cl^- ion activity that can be measured with confidence is a variable parameter which depends on solution pH. This Cl^- ion detection limit is shifted to higher values with increasing $[OH^-]$; indeed, at pH > 7 there will be detectable OH^- ion interference even at 0.01 mol dm^{-3} Cl^- aq..

The method of determing K_{ClOH} usually employed by chloride ISE manufacturers, involving unrealistically high $[Cl^-]$ and $[OH^-]$ values, yields an apparently favourable value for K_{ClOH} (<< 1). However, when K_{ClOH} is evaluated within the allowed experimental working conditions of a chloride ISE (pH 1 to 10) K_{ClOH} values are obtained that obviously declare the significant interferance of OH^- ions on the E_{Cl} of a chloride ISE. The validity of the method for evaluating K_{ClOH} involving a $[OH^-]$ that is outside the specified working conditions of a chloride ISE is questionable.

TABLE A.1

Values of the OH^- chloride ISE selectivity constant, K_{ClOH}, and the lowest level of Chloride activity that can be measured with confidence, $-\log (K_{ClOH} \times [OH^-])$, at different $[OH^-]$.

pH_B	K_{ClOH}	$-\log (K_{ClOH} \times [OH^-])$
13.0	0.0041‡	3.39
11.4	0.112	3.55
10.8	0.532	3.48
9.6	1.78	4.15
9.0	2.24	4.65
6.8	776	4.31
6.6	661	4.58

FIGURE A.3

Cl– ISE POTENTIAL RESPONSE OF WATER AT VARIOUS HIGH pH VALUES AS A FUNCTION OF THE LOWEST LEVEL OF Cl– ION ACTIVITY THAT CAN BE MEASURED WITH CONFIDENCE.

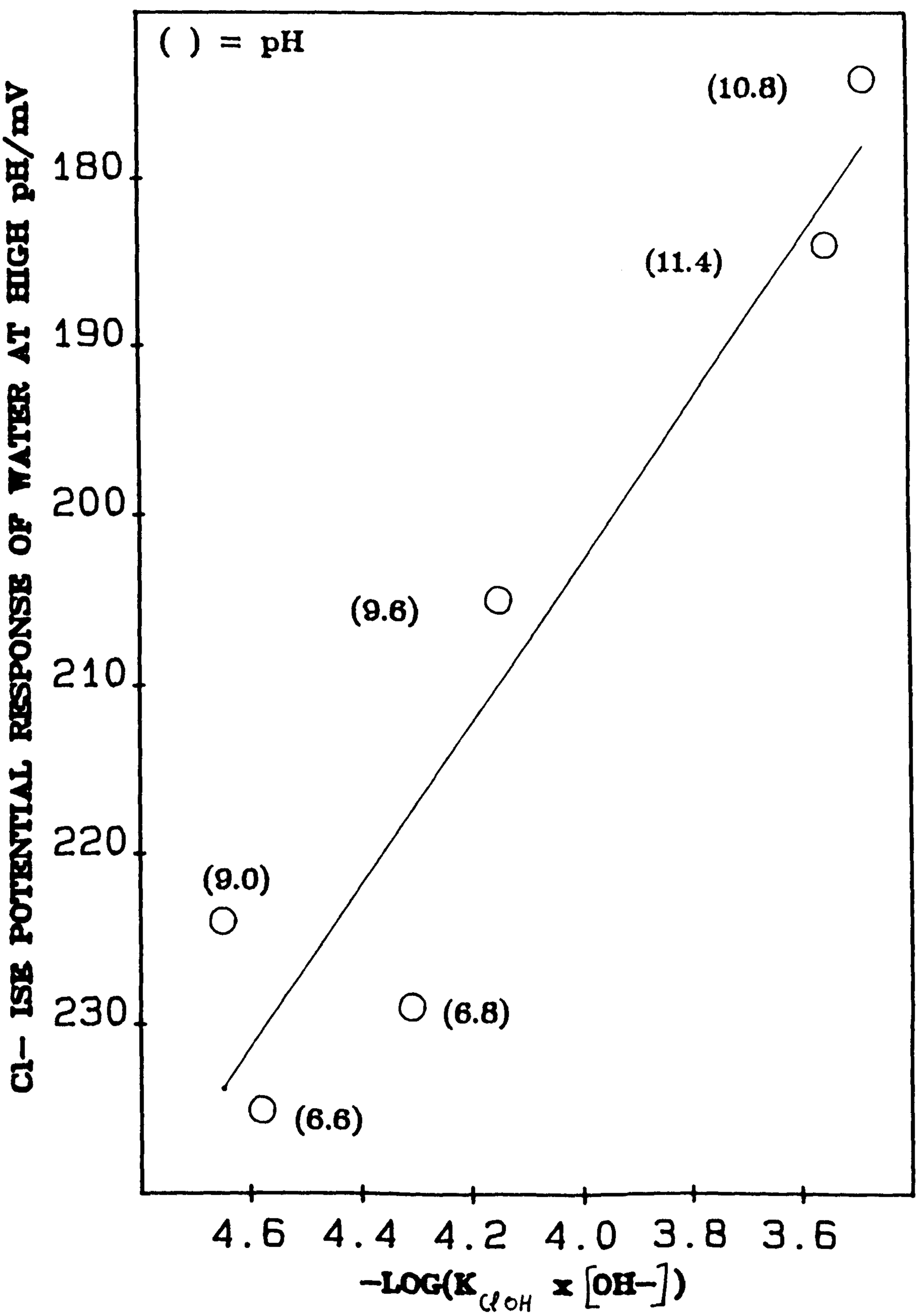

REFERENCES

Eisenman, G., Ann. New York Acad. Sci., 148, 5 (1968),

Moody, G. J. and Thomas, J. D. R., Talanta, 19, 623 (1972).

"Philips Guide to the use of Ion Selective Electrodes".

APPENDICES

APPENDIX A

Experimental procedures.

1. Standardisation of the pH electrode system (performed daily).

Before use, the outer compartment of the double junction reference electrode was filled with the outflowing electrolyte. The manual temperature compensation control (tpc) of the pH meter was adjusted to 25°C and the two buffer solutions maintained at this temperature using a thermostated water resevoir. The pH electrode system was then standardised at 25°C using the two buffer solutions. The precise pH value of each buffer solution at this temperature, used in the standardisation, was that given in the standard literature (British Standards, BDH Standard Reference). After standardisation the tpc of the pH meter was turned to the temperature of the solution under test.

2. Particle microelectrophoresis (see Chapter B1).

2.1. Platinisation of the (reversible) platinum metal electrodes.

The platinum metal electrodes were thoroughly cleaned in detergent water using a small brush and rinsed with hot tap water. The electrodes were then immersed in chromic acid cleansing solution (conc. and hot) for 30 minutes and rinsed with distilled water. The electrodes were immersed in the platinising solution and connected to the power supply whereupon electrodeposition from the solution onto the anodic electrode occurred. The polarity of the electrodes was reversed every 30s and within 30 minutes both electrodes were coated with an even, thin layer of black platinum.

2.2. Stationary levels within the particle microelectrophoresis cell.

Microelectrophoresis measurements are complicated by the simultaneous occurrence of electro-osmosis (Shaw). The internal surfaces of the cell are generally charged, and the applied electric field causes not only electrophoretic migration but also an electro-osmotic flow of liquid near to the tube walls together with a compensating return flow of liquid with maximum velocity at the centre of the tube. This results in a parabolic distribution of liquid speeds with depth, and the true electrophoretic velocity is only observed at the so-called "stationary levels" in the cell where the electro-osmotic flow and return flow of liquid cancel. For cylindrical cells, the electro-osmotic effect by itself gives rise to a velocity v_{EO} across the cross-section of the cell towards the electrode of the same polarity as the charge on the cell wall.

The reverse flow is, according to Poiseuille's law,

$$v_L = v_{EO} - \Omega (a^2 - r^2) \qquad \text{AA.1}$$

where v_L is the liquid velocity at a distance r from the centre of the tube of radius a, and Ω is a constant.

For zero overall liquid transport

$$\int_0^a v_L (2\pi r)\, dr = 0 \qquad \text{AA.2}$$

The solution of these expressions gives

$$c = \frac{2v_{EO}}{a^2} \qquad \text{AA.3}$$

so that

$$v_L = v_{EO} \left(\frac{2r^2}{a^2} - 1\right) \qquad \text{AA.4}$$

The stationary level (i.e., $v_L = 0$) is, therefore, located at

$$\frac{2r^2}{a^2} - 1 = 0 \qquad \text{AA.5}$$

$$\text{i.e.,} \quad \frac{r^2}{a^2} = \tfrac{1}{2} \qquad \text{AA.6}$$

$$\text{or,} \quad \frac{r}{a} = (\tfrac{1}{2})^{\frac{1}{2}} \qquad \text{AA.7}$$

$$\text{thus,} \quad r = a(\tfrac{1}{2})^{\frac{1}{2}} \qquad \text{AA.8}$$

Or, in terms of the distance (^1r) from the inside surface of the cell and the diameter (d) of the cell, we have

$$r = a - {}^1r = a(\tfrac{1}{2})^{\frac{1}{2}} \qquad \text{AA.9}$$

i.e., $$^{1}r = a(1 - (\tfrac{1}{2})^{\frac{1}{2}}) \qquad \text{AA.10}$$

hence, $$^{1}r = \frac{d}{2}(1 - (\tfrac{1}{2})^{\frac{1}{2}}) \qquad \text{AA.11}$$

2.3. Determination of inter-electrode (platinum wires) distance (ℓ_C) within the particle microelectrophoresis cell.

The cell was filled with KCl aq. (0.1 mol dm^{-3}) and immersed in the auxillary water bath. The universal conductance bridge was connected to the platinum wires of the cell and the conductance (G) of the electrolyte solution measured. From a knowledge of the conductivity (K_C) of 0.1 mol dm^{-3} KCl aq. at 25°C, and the cross-sectional area (A_{CS}) of the cell, ℓ_C was determined using the expression

$$\ell_C = \frac{K_C \, A_{CS}}{G} \qquad \text{AA.13}$$

where $K_C = 1.2856 \text{ S m}^{-1}$ (Jones and Bradshaw)

$$A_{CS} = \frac{\pi(1708 \times 10^{-6})^2}{4} \text{ m}^2$$

and $G = 3.47 \times 10^{-5}$ S

hence, $\ell_C = 8.489$ cm .

2.4. Absolute viscosity (η) of NaCl aq. at 25°C in the concentration range $0 < [NaCl] < 0.5$ mol dm^{-3}.

A comprehensive literature search was undertaken, and a compilation derived of the absolute viscosity of NaCl aq. solutions at 25°C and within the concentration range $0 < [NaCl] < 0.5$ mol dm^{-3}. a regression analysis was performed on the compiled data and the closeness of the fit of the computed polynomial to the data noted. Regression analyses were performed on several combinations of data from different source authors and the closeness of the fit of each resulting polynomial to its accompanying input data recorded. Eventually, a set of data from a particular combination of source authors was found that yielded a polynomial which fitted this final data selection exceedingly well; that is, an average percentage deviation of the fitted regression line from the final data selection of 0.01%.

2.5. The time required, prior to particle velocity measurements, for αFeOOH particles to become fully equilibrated with NaCl aq. solutions.

It was demonstrated that, for αFeOOH particles in a particular NaCl aq. solution at a chosen pH, the measured particle velocity increased slightly with time t. [t being the length of time allowed to elapse between addition of αFeOOH to the NaCl aq. solution and measurement of particle velocity.] After approximately 1 to 2 days it was observed that measured particle velocity became independent of time. In the light of this experiment it was decided to leave αFeOOH/NaCl aq. dispersions at pH 7 for 7 days (t = 7 days) before conducting particle velocity measurements.

2.6. The minimum weight concentration of αFeOOH dispersed in NaCl aq. solutions, required for weight independent particle velocity measurements.

It was demonstrated that, for αFeOOH particles dispersed in a particular NaCl aq. solution at a chosen pH value, the measured particle velocity increased slightly with weight concentration of αFeOOH. It was observed that the measured particle velocity became independent of the weight concentration of αFeOOH when this concentration was > 0.40 g in 200 cm^3. Consequently, particle velocity measurements were conducted using αFeOOH/NaCl aq. dispersions having an αFeOOH weight concentration of 0.40 g per 200 cm^3 NaCl aq..

3. Ion chromatography (see Chapter B2).

The experimental set-up is shown in Plate AA.1.

3.1. Operational settings of the ion chromatographic HPLC system.

a) Pump flow-rate = 1.5 cm^3 min^{-1}

b) Sample injection loop volume = see Table AA.1.

c) UV detector

i) wavelength = 265nm

ii) range = 0.16A

iii) back-off = 10

iv) output filter = 0.5 s

PLATE AA.1

Experimental set-up for ion chromatography.

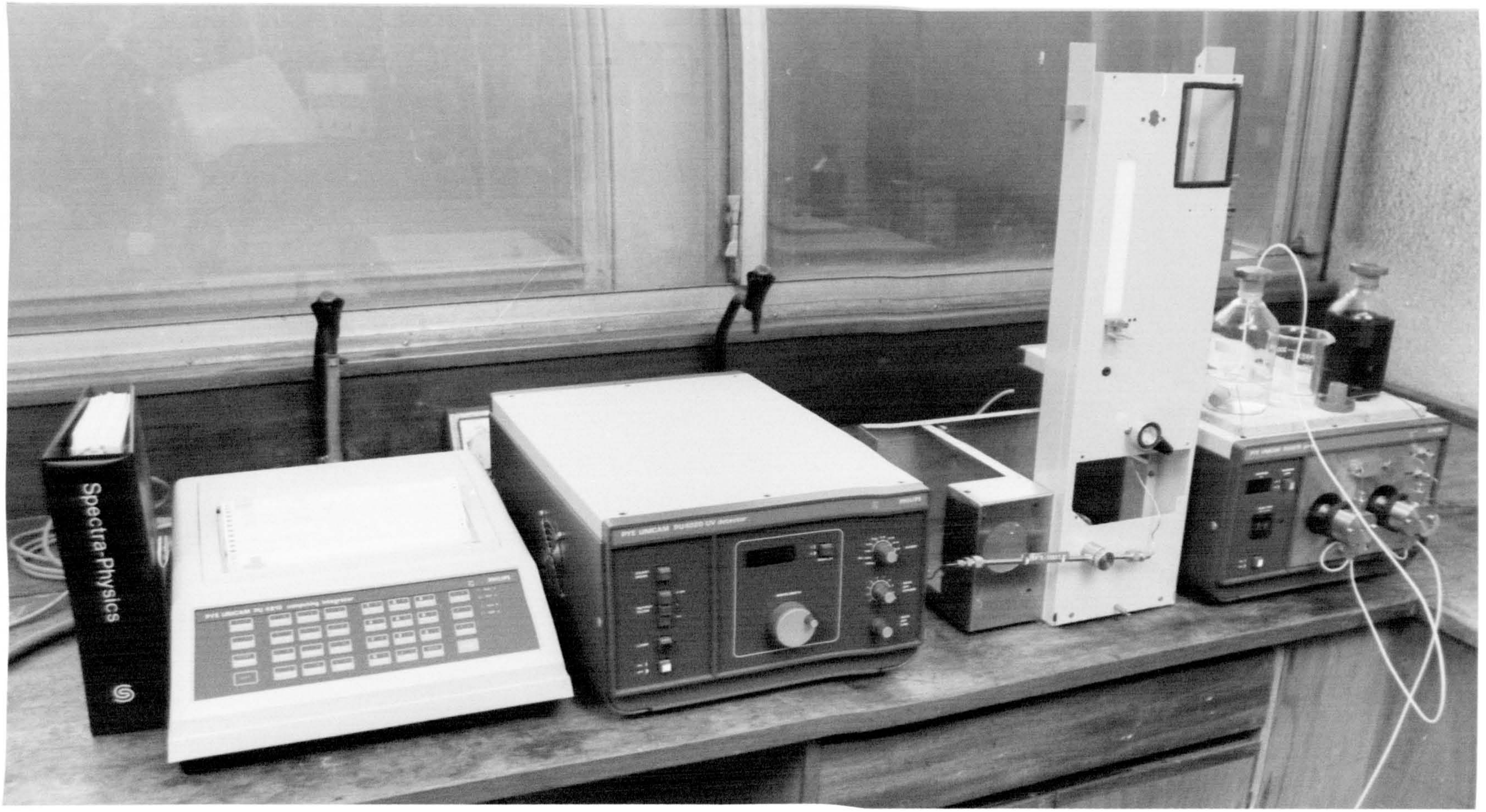

Table AA.1

[NaCl]	Attenuation (AT).	Peak Width (PW).	Sample injection loop volume.	Filtered sample volume.	Chloride ion contamination of filtered sample, due to leaching from Acro LC13 filter.
mmol dm^{-3}			mm^3	mm^3	µmol dm^{-3}
0.5	128	6	100	164	20.38
1.0	128	6	100	164	20.38
5.0	128	6	20	114	20.10
10.0	256	6	20	114	20.10
25.0	512	8	20	114	20.10
50.0	512	8	10	114	20.10
100.0	512	10	10	114	20.10

d) Computing integrator

i) chart speed (CS) = 1cm min^{-1}

ii) attenuation (AT) = see Table AA.1

iii) peak markers (PM) enabled = 0s (never disabled).

iv) auto-zero (AZ) enabled = 0.5s (never disabled).

v) integration inhibit (II) enabled = 2.5 minutes.

vi) integration inhibit (II) disabled = prior to chloride peak.

vii) method number (MN) = 0

viii) peak detection threshold = automatically set by depression of PT EVAL key (value usually in the range 500 to 1500).

ix) peak width (PW) = see Table AA.1.

3.2. Syringe loading.

The volume of solution withdrawn into the syringe was either 150 mm^3 for [NaCl] < 1mmol dm^{-3} or 100 mm^3 for [NaCl] > 1mmol dm^{-3}, a small volume of air (approximately 10 mm^3 to 50 mm^3) was also withdrawn into the syringe ahead of the solution.

3.2.1. αFeOOH - free solutions.

The needle was securely attached and the volume of solution withdrawn into the syringe.

3.2.2. Sample solutions.

[Immediately prior to a sample being withdrawn into the syringe, the syringe was flushed with double distilled water and dried.] A water-purged Acro LC13 filter was attached to the syringe and a sample of the αFeOOH/NaCl aq. suspension withdrawn through the filter into the syringe. The filter was discarded, the end of the syringe wiped clean and the needle attached.

3.3. Injection.

The injection valve was turned to load and the contents of the syringe, volume of air first, slowly injected, via the injection valve, into the sample loop until fluid exuded from the waste port; care was taken not to inject any air bubbles in the middle of the volume of solution, and

a small volume of solution was always retained in the syringe. Simultaneously, the solution contained in the sample loop was quickly discharged into the mobile phase stream, and the INJ.A key of the computing integrator depressed. The injection and subsequent discharging of the solution into the mobile phase stream was carefully timed so that the generated chloride peak would occur in isolation, far removed from any CO_3^{2-} peak (and, in the case of a filtered sample solution, far removed from any NO_3^- peak) originating from a previous injection. [Under the particular HPLC operational settings employed, the divalent CO_3^{2-} ion (and monovalent NO_3^- ion), unavoidably present in aqueous solutions, generated a chromatographic peak with a retention time (RT) of approximately 30 minutes (RT $\simeq$ 10 minutes for NO_3^-.]

3.4. Peak acceptance criteria.

The integrated area of a generated chloride peak was recorded if the peak complied with the following criteria:- i) the baseline before and after the peak was stable. ii) integration of the peak, as displayed by the position of the peak markers, began and finished at the start and end of the peak, respectively. iii) the peak occurred in isolation far removed from any other peak.

3.5. Preparation of calibration curve.

Six integrated areas were recorded of acceptable chloride peaks generated by the injection of NaCl aq. solutions of concentration [NaCl], 3[NaCl]/4 and [NaCl]/2 mol dm^{-3} (two integrated areas per concentration). A linear regression analysis of the six integrated areas against $[Cl^-]$ was performed and the coefficient of the straight line, constrained to pass through the origin, noted.

4. Potentiometric and salt titrations (see Chapter B3).

The experimental set-up is shown in Plate AA.2

200 cm^3 of double distilled water, or a NaCl aq. solution, was pipetted into the reaction vessel. The magnetic stirrer, controlling the teflon coated flea inside the reaction vessel, was turned on and the solution stirred at an appropriate speed to avoid excessive turbulence. The glass and reference electrodes were inserted through two inlet/outlet ports in the top of the reaction vessel, and their heights within the vessel

PLATE AA.2

Experimental set-up for potentiometric and salt titrations.

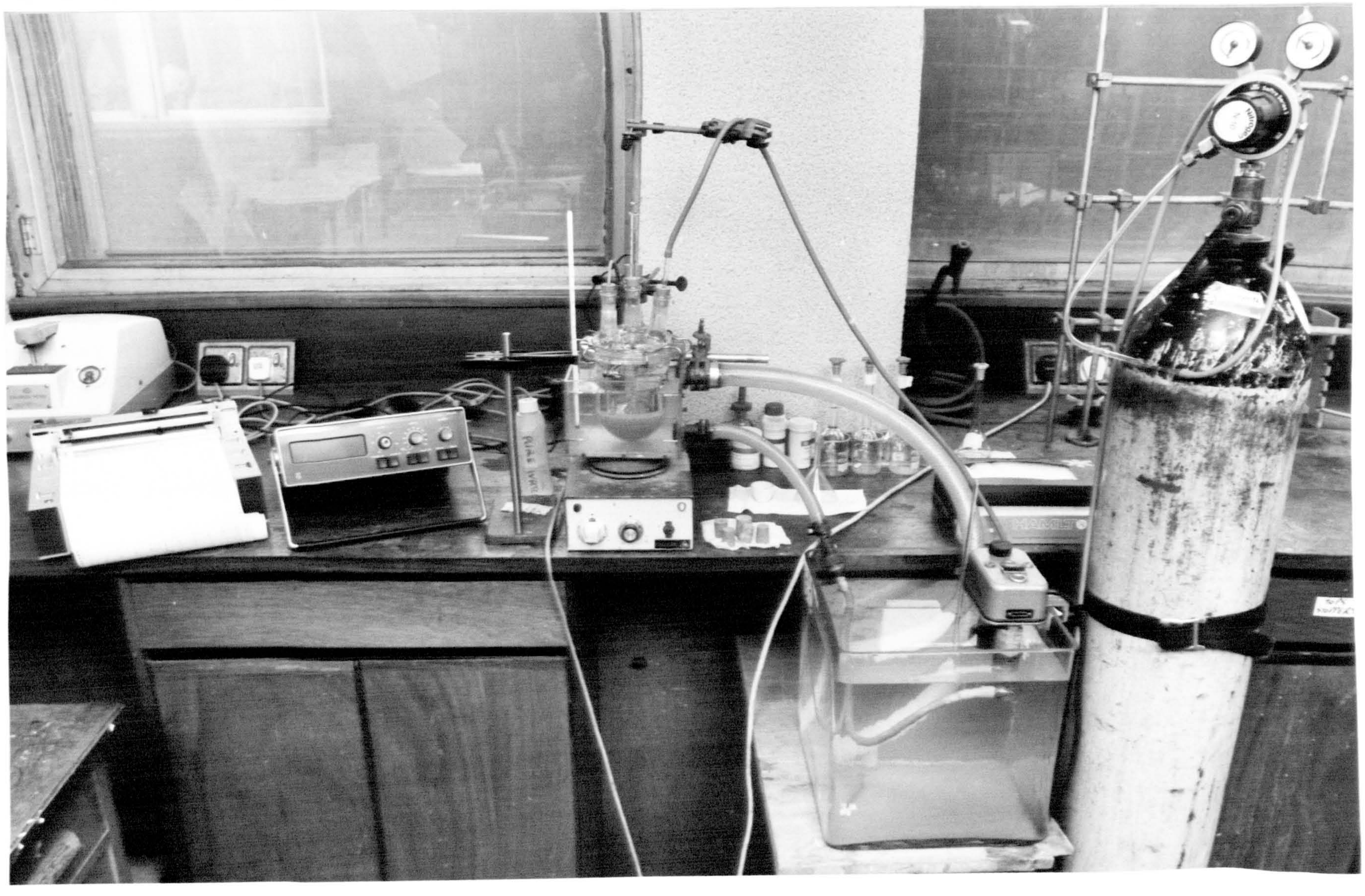

adjusted so that their spherical membrane and liquid junction, respectively, resided well within the stirred solution. The pH of the solution was displayed on the digital pH meter and recorded on the chart recorder. N_2 gas was bubbled (ca. 50 cm^3 min^{-1}) into the solution via a pasteur pipette inserted through an inlet/outlet port. As the pH of the solution approached 7 the N_2 gas bleed was slowed down. When the pH of the solution was 7.00 ± 0.01, 1.0000g ± 0.0005g of αFeOOH was quickly added to the stirred solution through a warm glass funnel positioned in the centre inlet/outlet port. At the same time the length of the pasteur pipette, through which the N_2 gas flowed, inside the reaction vessel was reduced so that its tip resided just above the surface of the suspension. In this way, the suspension was continuously blanketed by an inert atmosphere of nitrogen, thus prohibiting the absorption by the suspension of CO_2.

The stirred αFeOOH aq. suspension was left to stabilise for ca. 2 hrs (acid/base titration) or ca. 24 hrs (salt titration). In the case of a potentiometric titration the pH was raised using base to about pH 9.4, approximately 10 to 15 minutes prior to titration. For a salt titration the pH was adjusted to a required value with acid, and/or base, ca. 2 hrs prior to titration. Titration was only commenced, after such pH alteration, when the pH was virtually (i.e., pH drift < 0.01 min^{-1}) or absolutely constant, for acid/base and salt titration, respectively. The suspension was then titrated in the reversible cell

glass electrode	aqueous suspension of αFeOOH; (electrolyte NaCl)	aqueous KNO_3 salt bridge (0.1 mol dm^{-3}	saturated calomel electrode

the pH of the suspension being recorded before each addition of titrant and at the completion of a titration. Titrant addition was achieved by microlitre syringe and was effected as soon as the pH drift was < 0.01 $minute^{-1}$ (about every 5 minutes and 25 minutes for acid/base and salt titration, respectively). For potentiometric titrations the volume of titrant added was adjusted to give a change in pH of about 0.2 unit. In the vicinity of the equivalence point (pH 7) this titrant volume was 25 mm^3, while as extreme pH values were approached progressively larger titrant volumes were required (50 mm^3, 75 mm^3, 100 mm^3 and 125 mm^3) to effect

the same pH change. The particular series of titrant volumes added to effect a change in pH away from an extreme pH value were purposely made the same, as far as possible, as the series of titrant volumes added to effect a change in pH towards an extreme pH value. The pH range covered was kept relatively small, usually less than 5pH units.

The titrant HNO_3 aq. (0.1 mol dm^{-3}) was standardised with Na_2CO_3 using methyl orange as indicator, and the tirant NaOH aq. (0.1 mol dm^{-3}) was standardised with potassium hydrogen phthalate using phenol phthalein as indicator. A portion of each standardised solution was kept in a small volumetric flask (50 cm^3) ready for its easy and quick loading into the syringe. This standardisation procedure was repeated, for each stock solution, about every two weeks.

APPENDIX B

Apparatus.

Chart recorder.
Chessell Ltd. two pen chart recorder set at 100mV full-scale deflection (10mV/pH unit).

Chemical surface analyser (from Na onwards).
Jeol JSM 8040 scanning electron microscope in conjunction with a Link Systems 860 Series II X-ray microanalyser, using a non-conducting (carbon stud) and carbon (Dag) glue.

Cl^- ion selective electrode.
Philips, solid state AgCl membrane
(model IS 550).

Computer hardware.

i) Texas instrument TI53 constant memory programmable calculator.
ii) Commodore PET 2001 series microcomputer.
iii) BBC microcomputer.
iv) DEC System 2060 mainframe computer.

Dialysis membrane.
Medicell International Limited dialysis tubing; visking size 5-24/32", pore size 2.4 nm.

Differential scanning calorimeter.
Du Pont (model 910).

Digital voltmeter.
Advance instuments (model DVM4A).

Dispersion containers.
250 cm^3 flat-bottomed flasks with B34 ground-glass short necks and ground glass stoppers.

Gas chromatograph - Mass spectrometer.
Finnigan Mat (model 1020).

Infrared spectrophotometers.
Perkin Elmer (model 298) over the range 4000 cm^{-1} to 600 cm^{-3}, and Pye Unicam (model SP1200) over the range 1300 cm^{-1} to 400 cm^{-1}.

Ion chromatographic HPLC system (reversed-phase, ion-pair).
comprising:- Pye Unicam pump (model PU4010), stainless steel tubing (0.254mm bore), Rheodyne Inc. injection valve (model 7120 with appropriate sample loop (see Table AA.1), Phase Separations spherisorb S50DS column (10500 plates m^{-1} efficiency with fluorene), Pye Unicam UV detector (model PU4020) with air-cooled deuterium arc lamp, and Pye Unicam computing integrator (model PU4810). In compliance with the manufacturers recommendation (Philips), the pump and other HPLC components were subjected to regular maintenance: The four check valve filter cartridges of the pump were cleaned every 4 to 6 weeks as follows:- the cartridges were placed in a beaker containing HNO_3 aq. (1.5 mol dm^{-3}) and the beaker positioned in the ultrasonic water bath. After 15 minutes the cartridges were removed, rinsed with distilled water and placed in a beaker containing methanol, this beaker was also placed in the ultrasonic water bath for 15 minutes. The two piston seals of the pump were checked every 3 months and, if necessary, replaced according to the method of Philips. The pump and other HPLC components were flushed with methanol at the conclusion of an analysis, before being switched off.

Magnetic stirrer.
Gallenkamp; controlling a 2 cm teflon coated flea.

Nuclear magnetic resonance spectrometer (fourier transform).
Joel (model JNM-GX270).

Particle microelectrophoresis apparatus.
Rank Brothers (model MKII) with auxillary water bath receiving water from, and returning water to, a thermostated water reservoir. The length, ℓ_g, of one division of the eyepiece graticule within the observing microscope was calibrated to be 2.76×10^{-5} m.

Particle microelectrophoresis cell (van Gils, thin-walled cylindrical; incorporating platinum wires).
Rank Brothers; internal diameter and wall thickness measured to be 1708 μm and 80 μm, respectively. At the end of each working day the cell was rinsed with distilled water and left overnight containing HCl aq. (conc.) to dissolve any remaining αFeOOH particles.

pH electrode.
Philips Pye Unicam pH glass electrode (type 201, membrane HA).

pH meter.
Philips Pye Unicam high impedance voltmeter (model PW9409) with manual temperature compensation control and an IEC integral mains filter (RS Components Ltd. Stock No. 238-514) designed to filter mains borne interference.

Platinum electrodes.
Rank Brothers.

Power supply.
Farnell (model E30/2); operating at ca. 5V and 10mA.

Reaction vessel and lid.
Fisons, cylindrical (reference number FR700F) capacity 700 cm^3, flange bore 100 mm, height 135 mm. Fisons multi-socket/flat flange lid (reference number MAF 2/32) flange bore 100 mm, four sockets:- centre socket 19/26 and side sockets 19/26 (parallel), 24/29 (5°), 19/26 (10°).

Reference electrode.
Philips Pye Unicam double junction reference electrode with moveable ground glass sleeve (type RE3/DJ/NS). KNO_3 aq. 0.1 mol dm^{-3} was used as the outflowing electrolyte (leakage rate approximately 1 cm^3/24 hr at 25°C (Pye Ingold). In compliance with the manufacturers recommendation the outer-compartment of the electrode was drained of electrolyte at the end of each working day.

Sample preparation filters (for liquid chromatography samples).
Gelman Sciences Inc. Acro LC13 filter (product number 4450), with 13mm diameter fluoropolymer filter media of 0.2 µm pore size and a low hold-up volume of 14 mm^3; female luer lock inlet and "mini spike" outlet. It was discovered that the passage of 164 mm^3 of double distilled water through an Acro LC13 filter, into the previously cleaned and dried syringe, caused the leaching of Cl^- ions from the filter into the water, resulting in 164 mm^3 of a chloride solution of concentration 0.2 mmol dm^{-3}. Such chloride contamination was also observed from Acro LC13 filters into dilute chloride solutions. It was found that by repeated purging of the

filters with double distilled water, this chloride contamination could be reduced to an acceptable level. Consequently, all Acro LC13 filters were repeatedly purged with double distilled water and dried in a vacuum desiccator before use. The chloride contamination of a chloride solution passed through a previously water-purged and dried Acro LC13 filter was determined to be 20.10 μmol dm^{-3}, for the passage of 114 mm^3 of solution, and 20.38 μmol dm^{-3}, for the passage or 164 mm^3 of solution (see Table AA.1). It would seem plausible to suggest that the fluoropolymer filter media of an Acro LC13 filter contains leachable Cl^- ions possibly remaining from the preparation of such filter media by a Ziegler-Natta catalyst (eg. $TiCl_4$).

Scanning electron microscope.
JEM-1200 EX with scanning attachment. The particles of a specimen, commonly in a high degree of aggregation, were disengaged into free particles by their dispersion into double distilled water followed by the immersion of this suspension in the ultrasonic water bath for 30 minutes. The dried, deaggregated specimen was attached to a brass support using silver (Dag) glue, and sputter coated with gold by means of a Polaron SEM coating unit E5000.

Surface area and pore volume analyser.
Micromeritics Instrument Corporation (model 2100D Orr) physical adsorption analyser, using a 15 cm^3 glass specimen bulb (Coulter Electronics Limited, part number 9961055); computations were performed on the microcomputers. The 'dead-space' of the empty sample tube connected to the surface area and pore volume analyser was determined to be 18.331 cm^3.

Syringes.
Hamilton, precision (50 to 200 mm^3)

Thermogravimetric balance.
Stanton automatic thermo-recording balance.

Ultrasonic water bath.
Sonicor Instrument Co. (model SC-50-22T).

Universal conductance bridge.
Wayne Kerr (model B224).

Water reservoir I.
22 dm^3 of tap-water thermostatically maintained at 25 ± 0.2°C was continuously pumped into, by a BTL CIRCON heater and pump, and drained out of the particle microelectrophoresis cell water bath.

Water reservoir II.
22 dm^3 of water thermostatically maintained at 25 ± 0.2°C was continuously pumped into, by a BTL CIRCON heater and pump, and drained out of a small perspex bath surrounding the reaction vessel.

X-ray diffractometer.
Philips PW 1700 X-ray powder diffraction system comprising X-ray diffractometer, a DEC PDP 11 series mini-computer and the Philips ADP 1700 software package.

X-ray fluorescence spectrometer.
Philips PW1400 system comprising a rhodium X-ray tube, a collimator, three analysing crystals (see Table AB.1), a goniometer, radiation detectors, a DEC PDP 11 series microcomputer and the Philips ADP 1400 software package; chart speed 1°/min., full scale deflection 1 x 10^4, continuous scan at 1°/min. Samples were diluted with sodium tetraborate (sample concentration usually 5% or 10% w/w) and pressed into a pellet prior to analysis.

Table AB.1

Philips PW 1400 system

Crystal Analysers (XRD)

Crystal	Reflection plane	2d spacing nm	Lowest atomic number detectable	Reflection efficiency
LiF220	220	0.2848	23 (V)	High
Pentacrythritol (PET)	002	0.8742	13 (Al)	High
Potassium hydrogen phthalte (TLAP)	$10\bar{1}1$	2.64	8 (O)	Average

APPENDIX C

Materials.

$BaCl_2$.
BDH general purpose reagent.

Buffer solutions (pH values 4.0, 7.0 and 9.2; at 20°C).
Prepared using BDH buffer tablets and distilled water (1 table/100 cm^3). Care was taken to avoid prolonged exposure of buffer solutions to the atmosphere, and fresh solutions were prepared weekly. It was noted that the pH of freshly prepared buffer solutions did vary with time and only attained a constant value after several hours; consequently, buffer solutions were prepared approximately one day prior to use.

Buffer tablets (pH values 4.0, 7.0 and 9.2; at 20°C).
BDH buffer tablets 4.0.

$CHCl_3$. Analar reagent grade.

Chromic acid cleansing solution (conc. and hot).
Prepared by carefully adding H_2SO_4 aq. (90% w/w) to $Na_2Cr_2O_7$ aq. (5% w/w) (Vogel (Organic)).

Distilled water.
Distilled from tap-water; conductivity ca. 36 $\mu S\ m^{-1}$ at 25°C.

Double distilled water.
Distilled water, at pH 12.5 (using KOH) and containing $KMnO_4$ (1% w/w), was redistilled, under an atmosphere of nitrogen, through a 2 m vertical glass column incorporating a spray trap and packed with raschig rings (Hughes); conductivity ca. 20 $\mu S\ m^{-1}$ at 25°C.

$FeSO_4$.
Analar reagent grade.

HCl aq..
BDH general purpose reagent grade, 36% (w/w) HC1.

HgO.
Oakes Eddon general reagent.

HNO_3 aq..
Aristar reagent grade.

H_2O_2.
Analar reagent grade.

H_2SO_4 aq..
BDH general purpose reagent grade; 90% w/w H_2SO_4.

I_2.
BDH general purpose reagent.

Indicators.
Methyl orange and Phenol phthalein.

KI.
Analar reagent grade.

$KMnO_4$.
BDH analar reagent grade.

KNO_3.
Analar reagent grade.

KOH.
Analar reagent grade.

K_2PtCl_6
BDH Analar reagent grade.

$La(NO_3)_3$.
BDH general purpose reagent.

Magnesium metal.
BDH laboratory reagent.

Methanol.
BDH Analar reagent grade.

Mobile phase for ion chromatography.
1.3 cm^3 of tetra-n-butylammonium hydroxide aq. (40% w/v) was carefully pipetted into a 2 dm^3 volumetric flask and degassed, double distilled water added up to the mark, this gave a tetra-n-butylammonium hydroxide concentration of approximately 1 mmol dm^{-3}. The pH of this solution was lowered from about pH 11 to about pH 7.0 by the addition of ca. 20 cm^3 potassium hydrogen phthalate (0.1 mol dm^{-3}), this gave a phthalate concentration of approximately 1 mmol dm^{-3}. To avoid destruction of the stationary phase the pH of the mobile phase was measured again and adjusted, if necessary, to pH 7.0 $\pm$ 0.5 by the further addition of phthalate.

Mounting compound.
Fazaplas polyester resin.

N_2.
BOC white spot grade.

$Na_2B_4O_7 \cdot 10H_2O$.
BDH Analar reagent grade.

NaCl.
Analar reagent grade heated to 210°C and allowed to cool in a desiccator (Vogel (Inorganic)).

Na_2CO_3.
Analar reagent grade heated to 260-270°C and allowed to cool in a desiccator (Vogel (Inorganic)).

$Na_2Cr_2O_7$.
BDH general reagent grade.

NaOH.
Analar reagent grade.

NH_3 aq..
BDH general purpose reagent; specific gravity 0.880.

NH_4Cl.
Oakes Eddon general reagent.

NH_4NO_3.
BDH laboratory reagent.

$(NH_4)_2\ MoO_4$.
Fisons analytical reagent.

$Pb(CH_3COO)_2$.
Analar reagent grade.

Platinising solution.
Prepared using K_2PtCl_6 (2% w/w) and Pb $(CH_3COO)_2$ (0.02% w/w) in HCl aq. (25 mmol dm^{-3}) (Findlay).

Potassium hydrogen phthalate.
Analar reagent grade heated to 120°C and allowed to cool in a desiccator [2].

Resorcinol.
BDH laboratory reagent.

Silver (Dag) glue.
Agar Aids quick drying silver paint.

Steam (100°C).
Produced from boiling, distilled water at pH 13.5 (using KOH) and containing $KMnO_4$ (1% w/w).

Tetra-n-butylammonium hydroxide aq. (40% w/v).
BDH general purpose reagent grade.

REFERENCES

British Standards No. 1647, (2), 3.

BDH Standard Reference: pH values and their determination, 7th Edition, 1961.

Shaw, D.J., "Electrophoresis", Academic Press, London, 1969.

Jones, G. and Bradshaw, B.C., J. Amer. Chem. Soc., 55, 1780 (1933).

"Philips Pye Unicam PU4010 Pump Users Manual".

Vogel, A., "Testbook of Practical Organic Chemistry", 4th Edition, Longman, New York, 19 78.

Hughes, R.C., Murau, P.C. and Gundersen, G., Anal. Chem., 43, (6), 692 (1071).

Vogel, A., "Textbook of Quantitative Inorganic Analysis", 4th Edition, Longman, New York, 1978.

Findlay, A., "Practical Physical Chemistry", 8th Edition, Longmans Green and Co., New York 1954.

"Pye Ingold pH and Redox Electrodes".